

THE STRUCTURE AND RHEOLOGICAL PROPERTIES
OF LIQUEFIED NATURAL GAS GELLED WITH
WATER AND METHANOL CLATHRATES

by

Lucile M. Shanes

B.S., Washington University (May, 1972)

Submitted in Partial Fulfillment
of the Requirements for the
Degree of Doctor of Philosophy

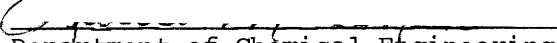
at the

MASSACHUSETTS INSTITUTE OF TECHNOLOGY

August, 1977

Signature of Author:

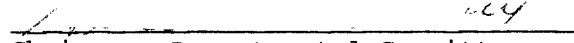
VOL I


Department of Chemical Engineering

Certified by:

Professor R. C. Reid
Thesis Supervisor

Accepted by:


Chairman, Departmental Committee on
Graduate Theses



Abstract

THE STRUCTURE AND RHEOLOGICAL PROPERTIES
OF LIQUEFIED NATURAL GAS GELLED WITH
WATER AND METHANOL CLATHRATES

by

Lucile M. Shanes

Submitted to the Department of Chemical Engineering on August 16, 1977, in partial fulfillment of the requirements for the degree of Doctor of Philosophy.

Liquefied natural gas has been gelled using two different gelants, water and methanol, by a vapor condensation technique which produces fine crystalline particles. These gelant particles were analyzed both experimentally and theoretically to assess the nature of the gel structure. X-ray diffraction, composition determination and microscopic observation provided substantial evidence that the particles were crystalline clathrate solids rather than pure solids. Subsequent theoretical analysis of the attractive interactions indicated that the van der Waals attraction is fairly weak and that hydrogen bonding between the particles is likely to be responsible for the observed gel structure.

The rheological (both elastic and viscous) properties of the gels were determined using an oscillating shear technique, and the behavior was found to be consistent with the proposed structure of the gels. The results showed non-linear viscoelasticity and the observed behavior appeared to be primarily a transient response. Analysis of the transient response and extrapolation to steady state indicate an apparent Bingham plasticity at the low shear rates studied.

A primary incentive for this study was the possible use of LNG gel as a safer form in which to transport natural gas. If an accidental spill were to occur, the rapid spread and vaporization of the LNG could produce flammable mixtures several miles from the spill site. To assess whether gelation would indeed provide a

safety benefit, an experimental study was done on the rate of vaporization of LNG gel from a water surface. It was found that the gels boiled at a rate which was one-half to one-third that of LNG. Also, a numerical technique was used to predict the spreading behavior (based on the results of the rheological study). The combined decrease in spread rate and vaporization indicated that a gel of yield stress 500 dynes/cm^2 could reduce the estimated maximum distance for flammable mixtures by a factor of five.

Thesis Supervisor:

Robert C. Reid
Professor of Chemical Engineering

-4-

Department of Chemical Engineering
Massachusetts Institute of Technology
Cambridge, Massachusetts 02139

August, 1977

Professor Irving Kaplan
Secretary of the Faculty
Massachusetts Institute of Technology
Cambridge, Massachusetts 02139

Dear Professor Kaplan:

In accordance with the regulations of the Faculty, I herewith submit a thesis, entitled "The Structure and Rheological Properties of Liquefied Natural Gas Gelled with Water and Methanol Clathrates," in partial fulfillment of the requirements for the degree of Doctor of Philosophy in Chemical Engineering at the Massachusetts Institute of Technology

Respectfully submitted,

Lucile M. Shanes

Dedicated to my Family

ACKNOWLEDGEMENTS

I wish to acknowledge with deepest gratitude the guidance and encouragement which my thesis supervisor, Professor Robert C. Reid, gave throughout my stay here. Certainly there have been numerous difficult times, and his constant support and advice have been most appreciated. Thanks also go to all of the other professors in the Chemical Engineering Department, particularly Professor K. S. Smith and Dr. Elizabeth Drake (currently at A. D. Little), who have offered valuable comments and suggestions during my thesis work.

The American Gas Association made funds available for this research, and their support is gratefully acknowledged.

I am also deeply indebted to the many people at Charles Stark Draper Laboratory who made it possible for me to study the rheological properties of my gels using their oscillating viscometer. In particular, Phil Gilinson has been a constant source of assistance, and is primarily responsible for making this opportunity possible. Others, Bob Dauwalter and Paul Halloran, have also helped in various aspects of my thesis.

I would also like to thank all of the students who have made my stay here enjoyable. In particular, Kent Griffis, who has been a constant friend as well as having assisted me in all aspects of my experimental work and final thesis preparation. Many other rewarding friendships, Ross Wilcox, Michael van Eek, et al., have been made during my stay here. I would also like to gratefully acknowledge the

assistance of Jay Dweck in the composition analysis study.

Most of all, I would like to thank my parents for their continued confidence and support throughout my schooling. Finally, to my husband, John, goes my unlimited gratitude for his continuous understanding and patience.

Lucile M. Shanes
Cambridge, Massachusetts
August, 1977

TABLE OF CONTENTS

1. Summary	18
1.1 The Gelation Process	20
1.2 The Gelant Particles	25
1.2.1 Crystal Structure Analysis	28
1.2.2 Particle Composition Analysis	32
1.2.3 Microscopic Observation	35
1.2.4 Attractive Forces Between Particles	38
1.3 Vaporization of LNG Gels on Water	39
1.4 Gel Rheology	40
1.5 Safety Benefit Analysis	51
2. Gels and the Gelation Process	60
2.1 Flocculation of Lyophobic Colloidal Particles	61
2.1.1 Van der Waals Forces	65
2.1.1.a Microscopic Theory	65
2.1.1.b Macroscopic Theory	71
2.1.2 Electrostatic Interactions	80
2.1.3 Other Repulsive Interactions	83
2.2 Formation of Colloidal Particles	86
2.3 Procedure for Gelling LNG	88
2.3.1 Jet Flow	90
2.3.2 Condensation by Nucleation and Particle Growth	92
2.3.2.a Nucleation	98
2.3.2.b Particle Growth	102
2.3.2.c Application to Present Condensation Process	103
2.4 Further Considerations on the Nature of the Gelant Particles	106
3. Gel Structure Analysis	120
3.1 Crystal Structure of Gelant Particles	120

3.1.1	Analysis of Powder X-ray Diffraction Data	121
3.1.2	The Formation and Structure of Ice	126
3.1.3	The Formation and Structure of Solid Methanol	141
3.1.4	Clathrate Hydrates	147
3.1.5	Methanol Clathrates	160
3.1.6	X-ray Diffraction of Gels	167
3.2	Thermodynamic Stability of the Gelant Particles	169
3.3	Microscopic Observation of the Gelant Particles	174
3.4	Solid Phase Composition Analysis	179
4.	Rheology of LNG Gels	192
4.1	General Rheological Behavior of Gels	192
4.2	Structural Model of Rheological Behavior	206
4.3	Time Dependency	220
4.4	LNG Gel Rheology	227
4.4.1	Oscillatory Behavior	229
4.4.2	Static Yield Stress	256
5.	Vaporization of LNG Gels on Water	262
5.1	General Boiling Behavior	262
5.2	Characteristics of Liquid Methane and LNG Boiling on Water	268
5.3	Boil-off Behavior of LNG Gels on Water	273
5.4	Further Qualitative Aspects of Boiling LNG	281
5.5	Conclusions on Gel Vaporization Behavior	290
6.	Experimental Equipment and Procedures	293
6.1	Gelation Apparatus	293
6.2	Solid Phase Analysis	301
6.3	Powder X-ray Diffraction	305
6.4	Microscope Analysis	308
6.5	Boil-off Rate Apparatus	311
6.6	Viscometer	312
6.7	Gel Concentration Measurements	321
7.	Industrial Scale Application of LNG Gels	322
7.1	Assessment of Safety Benefit	325
7.2	Spill Behavior	341
7.3	The Gelation Process	342

8. Conclusions and Recommendations	347
------------------------------------	-----

Appendices

A. London's Attractive Force	349
B. Calculation Using Hamaker's Expression	354
C. Approximation for Dielectric Susceptibility	356
D. Calculations Based on the Lifshitz Expression	358
E. Surface Potential of Ice in Liquid Methane	361
F. Energy of Repulsion for Ice Double Layers	363
G. Equilibrium Criterion Based on Variation of Nucleus Radius and its Effect on Availability	364
H. Estimation of Supersaturations	365
I. Nucleation Rates During Cooling of Vapor Mixture	366
J. Particle Growth History Based on Condensation and Coalescence	367
K. Scattering of X-rays	368
L. Diffraction From a Finite One-dimensional Array	372
M. Scattering From a 3-Dimensional Array	376
N. Abberations in Peak Position due to Absorption and Flat Specimen	379
O. X-ray Diffraction Data for LNG Gels	381
P. Estimation of Diffusion Effects	386
Q. Bingham Yield Stress Functionality	388
R. Maximum Shear Force Measured by Buildup on a Disk	389
S. Boil-off Data for LNG Gels	391
T. LNG Gel Modeled as a Vaporizing Solid	404
U. Estimation of Frothing Capability	406
V. Vapor Dispersion	408
W. Analysis of Plug Flow Assumption	411
X. Numerical Technique Used to Assess the Spreading Behavior of LNG Gels	412
Bibliography (Addendum on last page)	414
Location of Original Data	427
Biographical Note	428

LIST OF FIGURES

1-1	Gelation Apparatus	22
1-2	Outlet Tube	24
1-3	Phase Diagram for Methane + Water	26
1-4	Pentagonal Dodecahedron with Enclathrated Carbon Dioxide Molecule	27
1-5	Unit Cell for Hexagonal Ice	29
1-6	Structure of 12 A Cubic Gas Hydrates	31
1-7	Basic Cage for Methanol Clathrate	33
1-8	Vaporization of LNG Gel on Water	41
1-9	Steady-state Rheological Behavior for Gels	44
1-10	Shear Stress Response for LNG Gels Under an Applied Sinusoidal Shear	46
1-11	Comparison of Responses for the Constant Shear Rate Portion of a Sinusoidal Input and an Equivalent Shear Rate Sawtooth Input	48
1-12	Rheological Behavior of LNG Gels	49
1-13	Static Yield Stress Variation With Gel Composition	52
1-14	Numerical Results for Breaking-Dam Model Using LNG and a Free-Slip Boundary Condition	54
1-15	Numerical Results for Breaking-Dam Model Using LNG Gel and a No-Slip Boundary Condition	55
1-16	Numerical Results for Breaking-Dam Model Using LNG Gel and a Free-Slip Boundary Condition	56
1-17	Spreading and Vaporization of 10^7 Kg LNG and LNG Gel	58
2-1	Types of Gel Networks	62
2-2	Particle-Particle Interaction Energies	64

2-3	Frequency Ranges which Contribute to the van der Waals Interaction	77
2-4	Particle-Particle Energies of Interaction for the Combination of van der Waals Attraction and Short-range repulsion	85
2-5	Compact Particle Aggregates with Loose Chain Links	89
2-6	Formation of LNG/Methanol Gel	91
2-7	Constant Velocity Profile for Gas Jet into Quiescent Methane at 113 K	93
2-8	Appearance of Vapor Jet During the Gelation of LNG	93
2-9	Natural Gas Jetting into LNG	94
2-10	Pentagonal Dodecahedron with Enclathrated Carbon Dioxide Molecule	108
2-11	Phase Diagram for Methane + Water	109
2-11	Phase Diagram for Ethane + Water	110
2-12	Phase Diagram for Propane + Water	111
2-13	Isothermal Cross Section of the System $H_2O-CH_4-C_3H_8$	118
3-1	Phase Diagram for Ice	127
3-2	Unit Cell for Hexagonal Ice	129
3-3	3-Dimensional Packing in Hexagonal Ice	130
3-4	Powder X-ray Diffraction Patterns for Ice	132
3-5	Structure of Cubic Ice	133
3-6	High-Temperature Solid Methanol Structure	142
3-7	Bimolecular Unit Cell for Low Temperature Form of Solid Methanol	143

3-8	Polyhedra Commonly Found in the Clathrate Hydrates	148
3-9	Structure of 12 A Cubic Gas Hydrates	149
3-10	Arrangement of Pentagonal Dodecahedra in 17 A Cubic Gas Hydrate Structure	151
3-11	Powder X-ray Diffraction Patterns for Structure I Hydrates	157
3-12	Powder X-ray Diffraction Patterns for Structure II Hydrates	158
3-13	Basic Cage for Phenol Clathrate	162
3-14	Possible Packing Arrangement for Methanol Clathrate Cages with $R\bar{3}$ Space Group.	163
3-15	Possible Packing Arrangement for Methanol Clathrate Cages with $P\bar{3}$ Space Group	164
3-16	Transformation of X-ray Powder Diffraction Pattern as Liquid Evaporates from Gel	168
3-17	Low-Temperature Clathrate Equilibrium Apparatus	171
3-18	Methane/Water Gelant Agglomerate	177
3-19	Typical Adsorption/Desorption Isotherm for a Porous Solid	186
4-1	Models for Time Independent Flow Behavior	193
4-2	Typical Steady-State Rheological Behavior for Gels	195
4-3	Shear Stress Response for an Applied Constant Rate of Shear	196
4-4	Shear Stress Behavior for Varying Constant Shear Rates	198
4-5	Thixotropic Behavior	199
4-6	Typical Rheogram for a Rheopectic Fluid	200

4-7	Creep Curves for Lard and Shortening	203
4-8	Compact Particle Aggregates with Loose Chain Links	209
4-9	Transient Response for an Applied Constant Rate of Shear	222
4-10	Reduced Viscosity versus Time	224
4-11	Oscillating Parallel Plates	230
4-12	Typical Shear Stress Responses for a Sinusoidal Shear Input	231
4-13	Shear Stress Response for a Bingham Plastic Subjected to a Sinusoidal Shear Oscillation	233
4-14	Shear Stress Response for LNG Gels and Cab-O-Sil Gels Under an Applied Sinusoidal Shear	234
4-15	Shear Stress Response for a Bingham Body with Zero Relaxation Time and Single Yield Stress	237
4-16	Shear Stress Behavior for Modified Bingham Body	238
4-17	Sequence of Hysteresis Loops for Bentonite/Water Dispersions	242
4-18	Shear Stress Response for Disperse Systems of Polystyrene Solution and Styrene-divinyl Benzene Copolymer Particles	247
4-19	Comparison of Responses for the Constant Shear Rate Portion of a Sinusoidal Input and an Equivalent Shear Rate Sawtooth Input	248
4-20	Rheological Behavior of LNG Gels	252
4-21	Static Yield Stress Variation with Gel Composition	258
5-1	Characteristic Boiling Curve	263
5-2	Boiling Curves for Methane and LNG	265
5-3	Film Boiling Model	267

5-4	Vaporization of Liquid Methane on Water	269
5-5	Vaporization of LNG Gel on Water	274
5-6	Vaporization of Methane-Methanol Gels on Water	275
5-7	Vaporization of Methane-Methanol Gels on Water	276
6-1	Gelation Apparatus	294
6-2	LNG Gelation Apparatus	295
6-3	Outlet Tube	298
6-4	Apparatus for Solid Phase Composition Analysis	302
6-5	Cold Stage for X-ray Diffractometer	306
6-6	Microscope Cold Stage	309
6-7	Electronic Feedback Loop	313
6-8	Cross-Sectional View of Cup and Bob	315
6-9	Cross-Section of Viscometer Parts Inside Plexiglass Chamber	317
7-1	Physical Models for the Spreading of One Fluid on Another	327
7-2	Numerical Results for Breaking-Dam Model Using LNG and a Free-Slip Boundary Condition	334
7-3	Numerical Results for Breaking-Dam Model Using LNG and a No-Slip Boundary Condition	335
7-4	Numerical Results for Breaking-Dam Model Using LNG Gel and a Free-Slip Boundary Condition	336
7-5	Numerical Results for Breaking-Dam Model Using LNG Gel and a No-Slip Boundary Condition	337
7-6	Spreading and Vaporization of 10^7 Kg LNG and LNG Gel	339

LIST OF TABLES

2-1	Dissociation Pressures for Gas Hydrates at 273 K	116
3-1	Crystal Systems	124
3-2	Hexagonal Ice - X-ray Diffraction Data	134
3-3	X-ray Diffraction Data for High Pressure Ice Forms	137
3-4	X-ray Diffraction Data for Solid Methanol at 163 K	144
3-5	X-ray Diffraction Data for the Low-Temperature Form of Solid Methanol	146
3-6	Structure I Hydrate Formers which have been Studied by X-ray Diffraction	152
3-7	Structure II Hydrate Formers which have been Studied by X-Ray Diffraction	153
3-8	Dimensions of Clathrate Cages	154
3-9	Hydrate Structures for Peralkylated Cation Clathrate Hydrates	155
3-10	X-ray Diffraction Data for Methane-Water Gel	159
3-11	X-ray Diffraction Data for Methane-Methanol Gels and Calculated Values for Proposed Structure	166
4-1	Mechanical Models for Viscoelastic Fluids	205
4-2	Proposed Relations for Pseudoplastic Behavior	211
4-3	Elastic and Viscous Properties of LNG Gels	254
4-4	Static Yield Stress for Cab-O-Sil Gels	259

4-5	Static Yield Stress for Liquid Methane- Methanol Gels	261
7-1	Spread Distances for LNG and LNG Gel Based on a Breaking-Dam Model	338

CHAPTER 1 - SUMMARY

The primary incentive for this study was the possible use of gelled liquefied natural gas (LNG) as a safer form in which to transport natural gas. For oceanic transport, natural gas (composed primarily of methane but includes small amounts of heavier hydrocarbons such as ethane and propane) is presently converted to its liquid form (boiling point 110 K at 1 bar). This has a volumetric advantage over shipment in the gas form, as the liquid density is 0.42 g/cm^3 while the gas is 0.02 g/cm^3 at 30 bar. Economic considerations have, therefore, shown that liquid transport in large insulated tankers is preferred to gas transport in thick-walled vessels. A concern associated with such cryogenic transport is the possibility of a tanker accident resulting in an LNG spill. With its low viscosity (0.12 cp) and high volatility, LNG will readily flow out of a ruptured tank, spread, and vaporize. As the cold, newly vaporized natural gas mixes with air, a vapor cloud forms above the spreading pool of LNG. This vapor cloud may travel a considerable distance before there has been sufficient dilution to reduce the natural gas concentration below its lower flammability limit (5 mole percent in air).

The magnitude of the hazard associated with any major LNG spill is directly related to the quantity spilled and thus dependent on tanker capacities. Thirty-five natural gas tankers with an average capacity of 46,000 cubic meters are now in operation. Future tankers (those either under construction or in the design stage) will average

124,000 cubic meters in capacity. Although such tankers are designed with a large safety factor (they generally consist of five or six separate storage tanks which are separated from the hull by greater than a meter thickness of insulation), there is, nevertheless, concern due to the large quantities being transported. It has been estimated that the spill from a single inner storage tank could result in flammable gas mixtures several miles from the spill site. Thus it is still desirable to reduce this hazard should a feasible means be available.

In order to obtain such a safety benefit, one would like to significantly reduce any or all of the following rates: the spill rate, the spreading rate, and the rate of boil-off per unit area. The first two rates are affected primarily by the rheological properties of the fluid, and a gel would have two desirable properties--a yield stress and a high viscosity. The high viscosity should reduce the rate of spreading while the yield stress will halt the spreading altogether once its height can be supported by the gel structure. The third factor, the rate of boil-off per unit area (on water) is dependent on the boiling curve (heat flux versus $\Delta T = T_{\text{boiling liquid}} - T_{\text{water surface}}$) for nucleate and film boiling. LNG has previously been studied in confined spill tests and the results showed an increase in boil-off rate with time. This has been interpreted as a shift from film to nucleate boiling. Thus it is desirable to alter the boiling curve in such a way as to prevent this shift to nucleate boiling.

The present study has investigated LNG gel properties related to this possible safety benefit and has also considered properties which will be important in any future assessment of industrial-scale feasibility. Initially, a laboratory procedure was developed for gelling LNG with either water or methanol. The choice of these two gelants was based on a previous study by Vander Wall (1971) on liquid methane gels. The resulting LNG gels were then investigated to determine their structural and rheological properties. The structural analysis consisted of a theoretical analysis of the gelant particle interactions and a detailed experimental analysis of the nature of the actual gelant particles, which included crystal structure determination, composition analysis, and thermodynamic stability analysis. The rheological study included an experimental determination of both the elastic and viscous properties of the gels. For this particular application of LNG gels, the most important rheological parameters measured were the yield stress and the steady-state shear stress as a function of rate of shear. These rheological properties were then used to assess the possible safety benefit associated with the transport of LNG gels, and the structural properties were considered in relation to possible large-scale production and use.

1.1 The Gelation Process

The present laboratory technique for gelling LNG used a nucleation/particle growth sequence to form colloidal size (generally 1 nm to 1 μ m) gelant particles. This produces a lyophobic gel (i.e. one

in which the colloidal particles have little or no affinity for the dispersion medium) which derives its semi-solid structure from inter-particle attractive forces. The gelation procedure was similar to that used by Vander Wall in his study of liquid methane gels. A vapor mixture of natural gas with a small amount of gelant (≤ 2 mole percent water or methanol) was jetted under the surface of the LNG. The contact of the cryogenic liquid with the warm vapor produced rapid heat exchange. Temperature measurements within the jet indicated that the exit vapor cooled from 273 K to 110 K in less than 0.1 ms, thus producing nucleation and particle growth in the vapor phase. Some of these particles will then reach the vapor-liquid interface by diffusion and convection and will be retained in the liquid. After continual addition of such gelant particles, the gelant concentration will eventually be high enough to form a structure throughout the liquid, thus forming a gel.

A diagram of the gelation apparatus used in this study is shown in Figure 1-1. Two separate lines were used. The first line carried methane gas which was subsequently condensed (by contacting the bottom surface of a preparation beaker which was situated in a bath of liquid nitrogen) to form the initial charge of liquid methane. In the second line, the natural gas/gelant mixture was produced by splitting a natural-gas stream, saturating one of the streams with gelant, and subsequently mixing it with the unaltered bypass stream. This mixture was then jetted into the previously prepared charge of liquid methane by means of an outlet tube with a 0.159 cm (1/16") exit hole (Figure

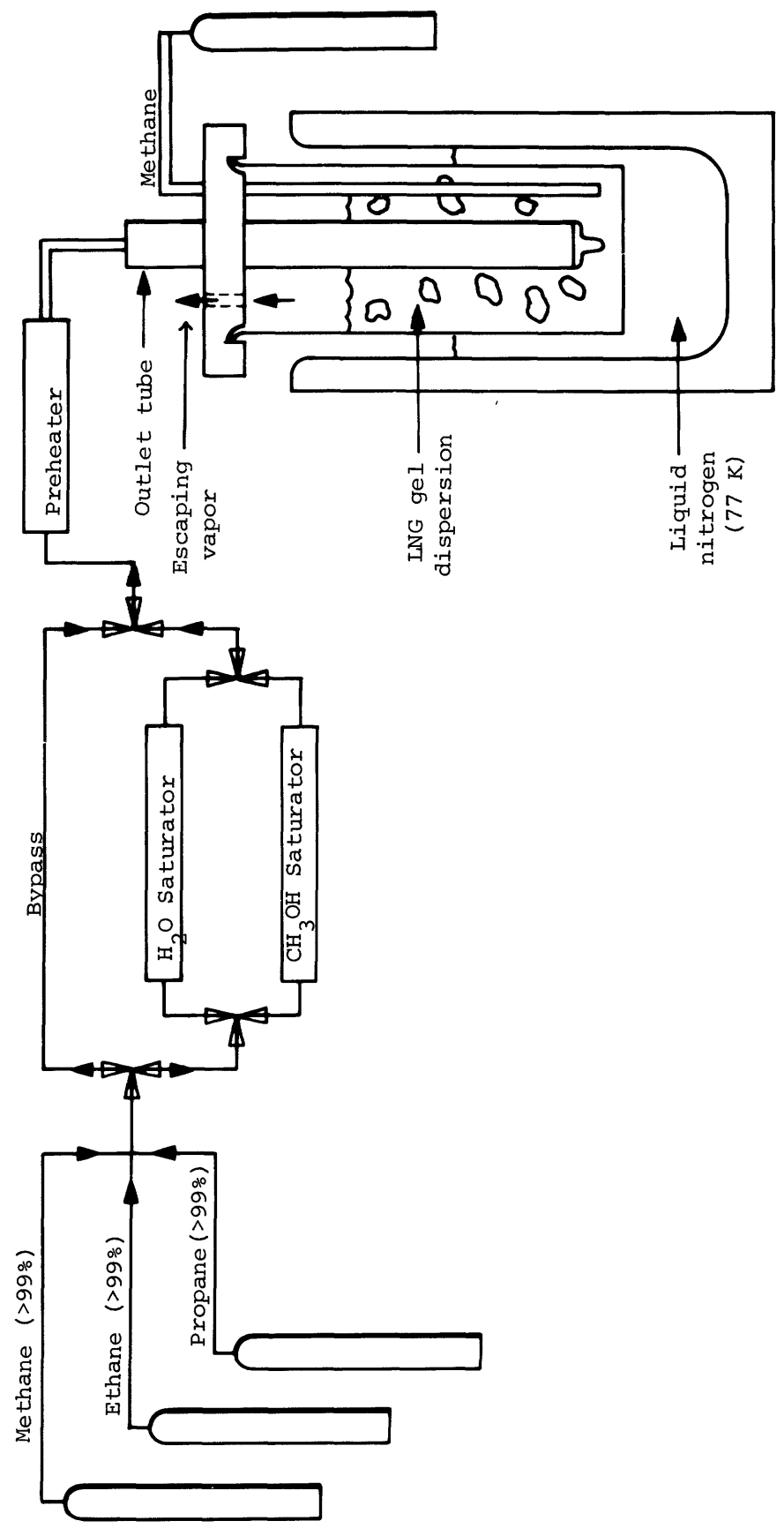
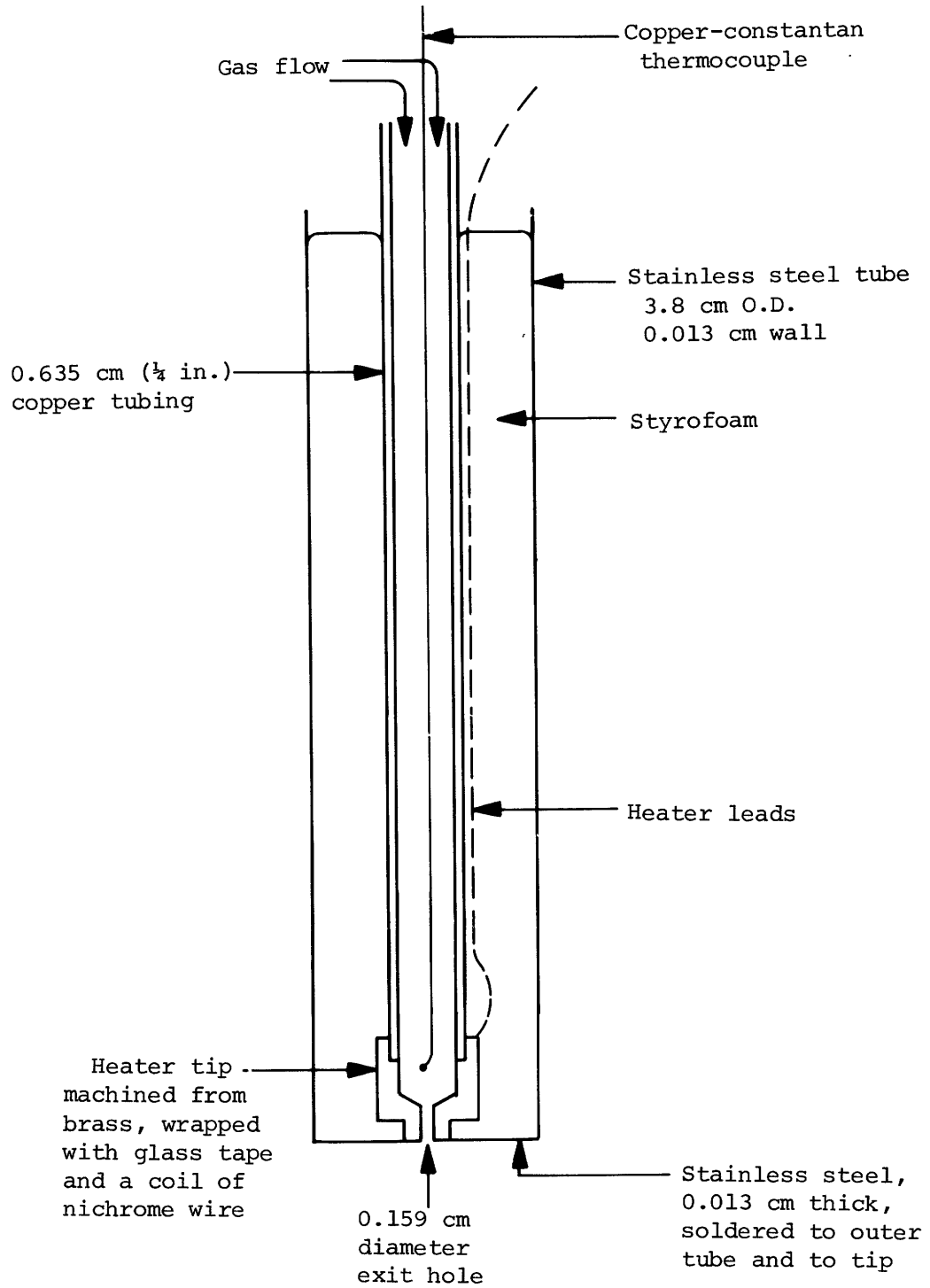


Figure 1-1 Gelation Apparatus

1-2). Insulation and heating capabilities were required in the outlet tube to prevent condensation of the gelant prior to contact with the liquid methane. The gas flow rate for this vapor mixture was $110 \text{ cm}^3/\text{s}$ (at 273 K, 1 bar), and gelation time ranged from two to four hours. During the entire process, liquid nitrogen was used as a coolant to keep the gel from vaporizing and to provide the necessary cooling for condensation of the gelant. Natural gas mixtures ranging from a "heavy" composition of 80/15/5 mole percent methane/ethane/propane to pure methane were gelled with this apparatus. When a mixture (as opposed to pure methane) was used, the heavier components, ethane and propane, would condense out, mixing with the initial charge of liquid methane to form a final LNG composition which was dependent on the run time.

The rigidity of the final gel is strongly dependent on the particle size, and, for a given gelant concentration, the smaller the particles, the more rigid (higher yield stress) will be the gel. Thus, the process which controls the final particle size will be particularly important. In the present case, nucleation and particle growth were thought to be the controlling processes. Nucleation rates were calculated using the classical expression for condensation from a vapor (Becker and Doring, 1935; Zeldovich, 1942). Particle growth was assumed to follow the gas-kinetic theory, with each collision resulting in a fusion of the colliding species. Assuming a linear temperature change over a time interval of 10^{-4} s, and restricting nucleation and particle growth to the vapor phase (i.e. once a particle

Figure 1-2 Outlet Tube



has been entrained by the liquid, no further particle growth will occur), results in an estimated final particle size of ≈ 1000 A (radius) for an average vapor phase residence time of 100 ms. However, calculations based on the gel yield stress (Section 1.4) indicate that the particle size is closer to $r = 150$ A. This suggests that either the average residence time in the vapor is $\approx 10^{-4}$ s or that evaporation rates are significant (i.e. only a small fraction of the collisions result in a fusion of the two species).

1.2 The Gelant Particles

The solid gelant particles are formed at approximately atmospheric pressure within the temperature range of 273 to 113 K. In the case of H_2O as a gelant, this temperature range not only covers a region in which ice is stable, it also includes a lower temperature region in which a natural gas-water clathrate is stable (Figure 1-3). Clathrates may be considered solid solutions in which a cage-like host structure is formed by hydrogen bonding of the water molecules. This host lattice, which by itself is unstable, becomes stabilized by the inclusion of the second component, methane, ethane, or propane in this case. A typical clathrate cage is the pentagonal dodecahedron shown in Figure 1-4.

If these LNG gels are to be produced and used on an industrial scale, it will be important to know whether these gelant particles are indeed clathrates and whether they are thermodynamically stable. There is a substantial amount of information already available on

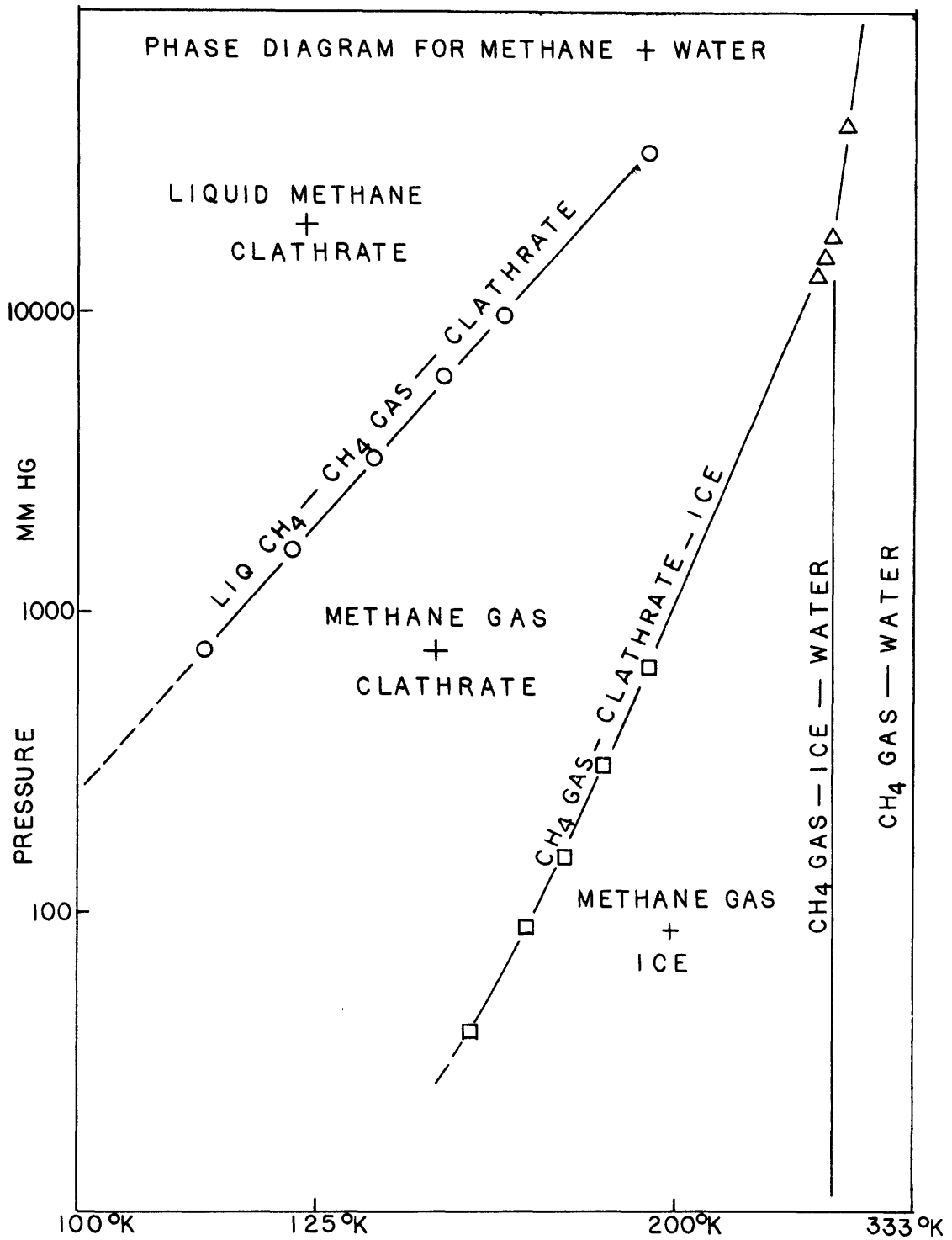


Figure 1-3

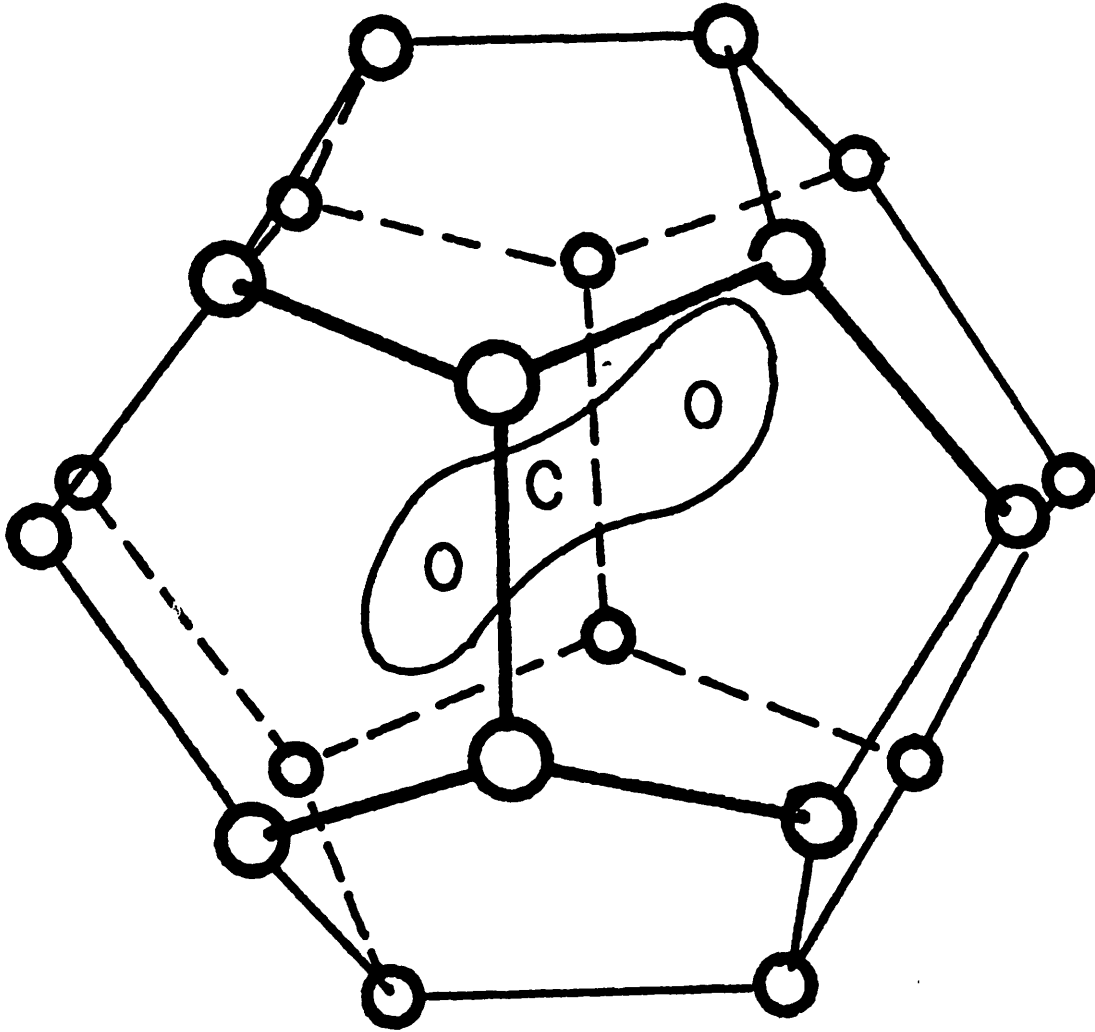


Figure 1-4 Carbon Dioxide molecule encaged in a pentagonal dodecahedron formed by hydrogen bonding of the water molecules. Oxygen atoms are represented by O's. Hydrogens lie along pentagon edges.

methane-, ethane-, and propane-water clathrates (commonly referred to as hydrates) including composition, crystal structure, and equilibrium data. Methanol, on the other hand, has not been previously reported to form clathrate structures, but the ability to form hydrogen bonds suggests that this is certainly a possibility. Several different types of experiments were, therefore, performed in order to establish whether the gelant particles were clathrates and further to determine the thermodynamic stability of the methanol gelant particles.

1.2.1 Crystal Structure Analysis

The crystal structure of the gelant particles was studied using a powder x-ray diffractometer with a liquid nitrogen-cooled sample stage. Past studies have described the various structures for ice, solid methanol, and numerous water clathrates, thus providing a basis for distinguishing between the pure crystalline solids and the crystalline-clathrate structures. For the methanol clathrate, however, there was no reported knowledge of its existence or its crystal structure, although several similar compounds (i.e. those containing a single OH group available for hydrogen bonding) are known to form clathrates and whose crystal structures have been determined.

Initially samples of ice and solid methanol were studied. Ice is known to form several different structures, but the hexagonal ice form (Figure 1-5) is most likely to occur under the temperature and pressure conditions in the present study (i.e. 110 K and 1 bar).

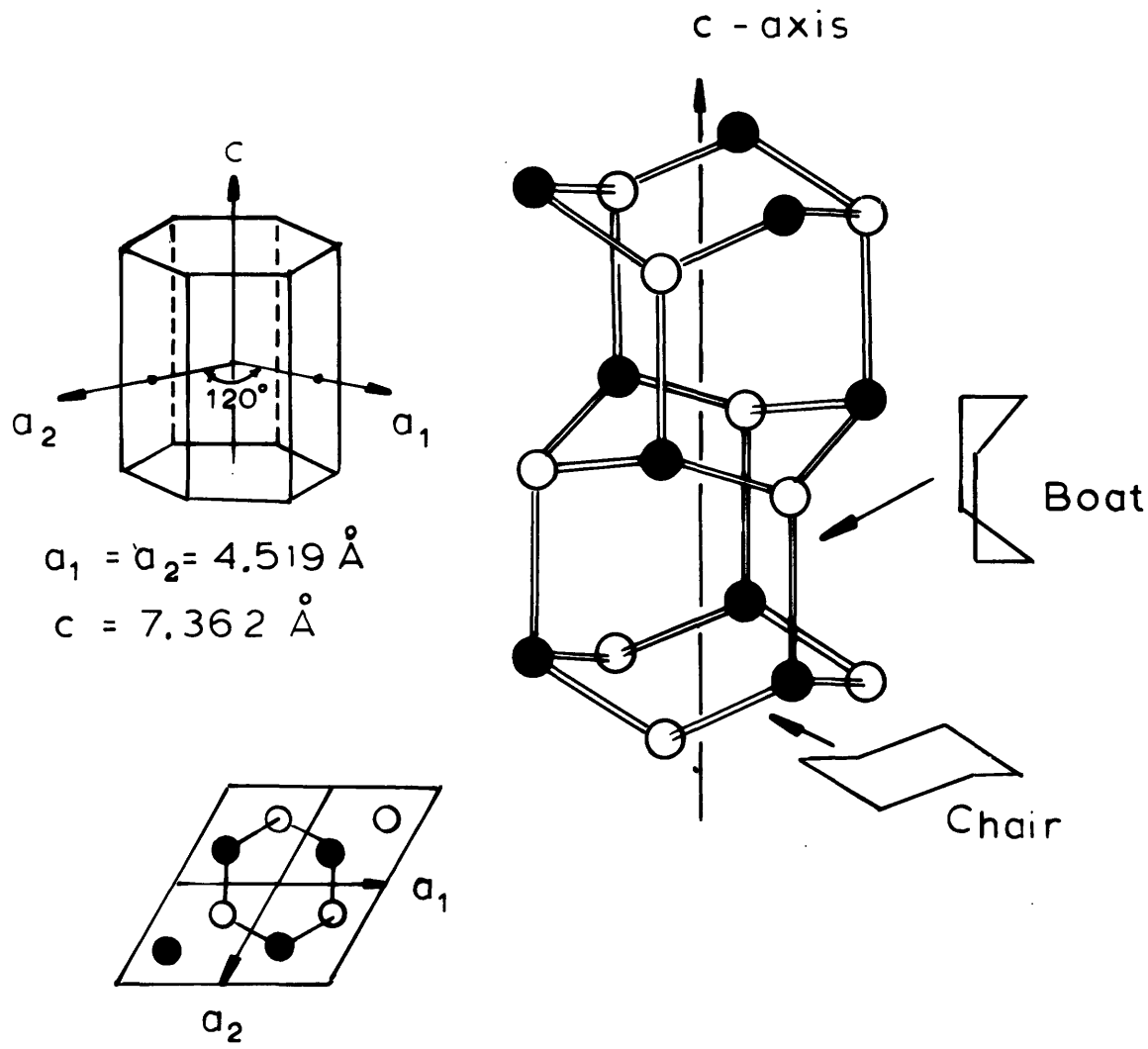


Figure 1-5 Unit cell for hexagonal ice, I_h . Spheres (both solid and open) represent oxygen atoms of water molecules. The unit cell consists of two puckered rings stacked along the c axis but differing by a 60° rotation. Adding a third puckered ring shows the ABAB sequence of hexagonal ice.

Methanol is known to form two different solid phases with the transition point being 158 K. (The general structure is a zigzag line of hydrogen bonds, the lines being packed in parallel.) Thus, hexagonal ice and the low temperature form of solid methanol were analyzed, and the x-ray diffraction results were in excellent agreement with those previously reported. The gelant particles were then analyzed by placing a fairly rigid gel sample on the cold stage. The methane was subsequently allowed to partially vaporize from the sample, exposing dry particles at the surface which could then be impinged with an x-ray beam to obtain the powder diffraction pattern. The results for the water gels were not clearly distinguishable as any known ice or clathrate structure. Methane, due to its small molecular size, was expected to form a 12 Å cubic clathrate crystal structure (Figure 1-6), but the data could not be fit to such a structure, nor any combination (i.e. a mixture of solid phases) of this plus ice. However, the observed x-ray pattern was quite reproducible and similar patterns were found for other low-temperature crystals ($\text{CO}_2/\text{H}_2\text{O}$, $\text{N}_2/\text{H}_2\text{O}$, and air/ H_2O) formed under clathrate-stable conditions. This suggests that the low temperature may cause a slightly different structure than originally expected. Analysis of the data indicated that the observed peaks could, however, be accounted for by a unit cell of dimension $a = 14.8 \text{ Å}$ or a tetragonal unit cell with dimensions of $a = 11.9 \text{ Å}$, $c = 10.1 \text{ Å}$. No smaller unit cell was possible. Although larger unit cells were certainly possible, the small number of peaks observed indicated that this was unlikely. This minimum unit

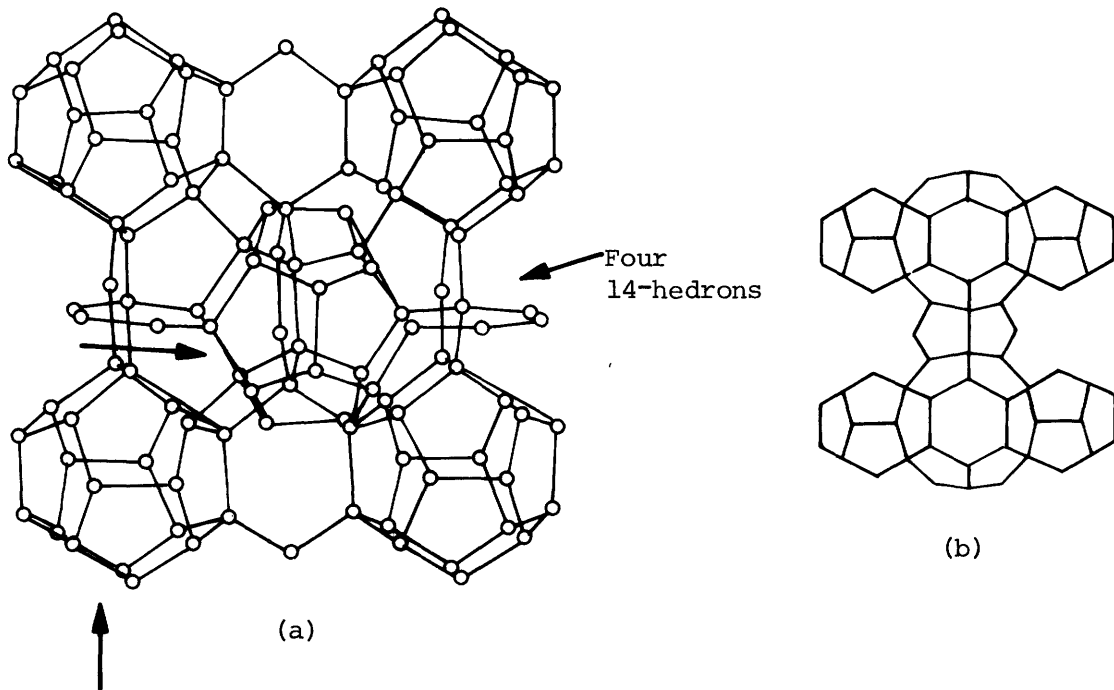


Figure 1-6 Structure of 12 A cubic gas hydrates

- a) Structure composed of 14-hedrons (12 pentagons and 2 hexagons): 2 sharing hexagon faces in middle of front face of cube; 2 with hexagons on top and bottom edges of front face; combination of four 14-hedrons at left and right faces (with planes perpendicular to paper). Unlabeled arrows indicate locations of pentagonal dodecahedrons.
- b) Pentagonal dodecahedrons lie at the eight corners of cube and in center.

cell size is still large in comparison to those for the various ice structures, and would, therefore, indicate that a clathrate structure is present, possibly a distortion of the 12.0 Å cubic or a completely new structure. Due to the complexity of water-clathrate structures, no attempt was made to determine the exact unit cell and atomic positions for this case.

For the methanol-methane gels, the x-ray diffraction data also indicated that a structure quite different from the pure solid was present. These results were tested for their consistency with a variety of possible clathrate structures (similar to those for other single OH compounds), and a fair agreement was found for the structure shown in Figure 1-7. Further single crystal diffraction data, however, would be necessary to confirm this structure.

1.2.2 Particle Composition Analysis

To confirm further the clathrate nature of the solid gelant particles, an experimental technique was designed to analyze the composition of these particles. Here a pure solid phase should be clearly distinguishable by its absence of natural gas. As the gelant particles are formed by nucleation and particle growth from a vapor phase, there is little likelihood that dissolved gas would be frozen into the pure solid. On the other hand, if the solid is a crystalline clathrate phase, a significant amount of natural gas will be encaged in the clathrate structure. For the natural gas components, methane, ethane, and propane, their hydrate compositions have been studied

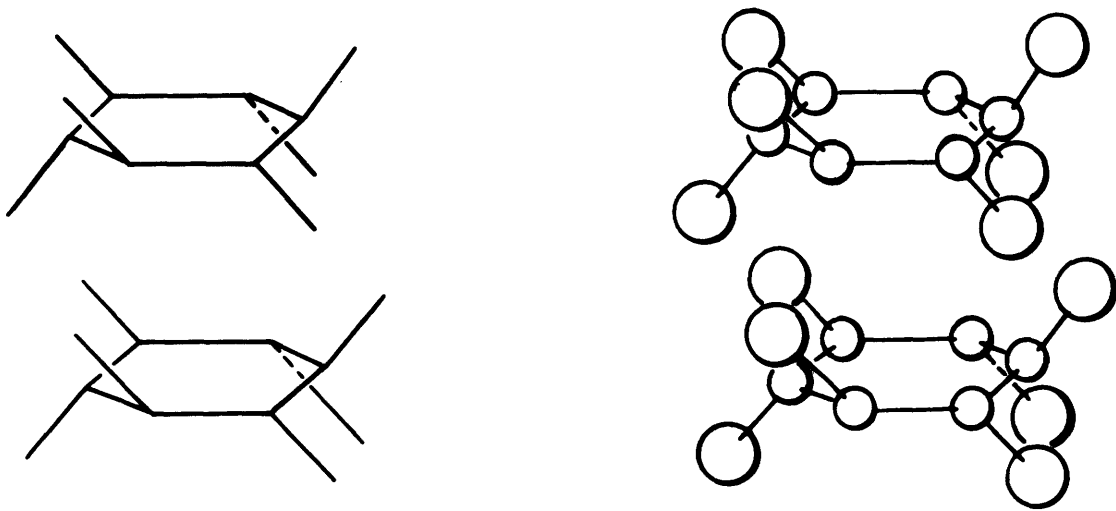


Figure 1-7 Basic cage for methanol clathrate. OH groups bond in hexagon rings with methyl groups alternating up and down from plane of hexagon. Identical rings stack together to form a cage. Two OH rings are shown above.

previously and determined to be $\text{CH}_4 \times 7.1\text{H}_2\text{O}$; $\text{C}_2\text{H}_6 \times 8.2\text{H}_2\text{O}$ and $\text{C}_3\text{H}_8 \times 18.0\text{H}_2\text{O}$ (Frost and Deaton, 1946). These differ slightly from the ideal formulas (i.e. based on the known crystal structure with all cages filled)-- $\text{CH}_4 \times 5.75\text{H}_2\text{O}$, $\text{C}_2\text{H}_6 \times 7.67\text{H}_2\text{O}$, and $\text{C}_3\text{H}_8 \times 17.0\text{H}_2\text{O}$, indicating that not all of the cages need to be occupied to make the structure thermodynamically stable.

To determine the composition of the liquid methane gelant particles (only pure, ≥ 99.95 percent, methane was used in these experiments), an initial separation of the solid particles from the liquid medium was required. This was accomplished by placing the gel sample under a slight vacuum (33 kN/m^2). Also, the sample was kept in a cryogenic temperature-controlled bath with the selected temperature being well above the methane boiling point but below the expected clathrate decomposition temperature, i.e. the temperature at which the clathrate converts to ice. This decomposition temperature was known for methane hydrate, but could only be estimated for the methanol clathrate. Another important experimental consideration was the porosity of the gelant particle structure which remains after vaporization of methane from the gel. To avoid residual methane trapped in these pores, the ratio p/p^* (p is the pressure of the vapor under operating conditions and p^* is the liquid vapor pressure at the temperature of the experiment) must be less than ~ 0.3 . For the water-methane gel, the sample was maintained at 163 K and 33 kN/m^2 , which gives a favorable p/p^* of 0.015 . For this low ratio, only fractional coverage is expected, and a previous ice-nitrogen adsorption study

(Adamson et al., 1967) indicated that the fraction is less than or equal to 0.5.

Once the gel sample ceased to evolve gas (total desorption took approximately two hours), the gelant particles were assumed to be dry except for this small residual methane adsorption. The sample was then isolated and warmed. As the particles decomposed and melted the escaping vapor was collected and measured. The weight of the remaining liquid gelant was also measured and a composition was thus determined.

Two runs were made on water-methane gel samples yielding compositions of $\text{CH}_4 \times 6.7 \pm .5 \text{H}_2\text{O}$ and $\text{CH}_4 \times 5.9 \pm .5 \text{H}_2\text{O}$. The accuracies reported here are the maximum experimental errors. Due to residual adsorbed methane, a maximum error of 20 percent may have occurred (methane in excess). If this adsorbed methane is accounted for, the resulting composition would be $\text{CH}_4 \times 7.4 \text{H}_2\text{O}$ to $\text{CH}_4 \times 8.4 \text{H}_2\text{O}$. For both cases, the results are within the expected composition range for the clathrate, and thus tend to substantiate the clathrate theory.

For the methane-methanol gels it was not possible to determine the composition of the gelant particles as their decomposition temperature was too low. Attempts to analyze these gels indicated a decomposition temperature of $\sim 135 \text{ K}$ at 33 kN/m^2 . Thus, the sample could not be kept at a temperature high enough to avoid capillary effects without decomposing the solid.

1.2.3 Microscopic Observation

The microscope study was originally designed with three

objectives: 1) to determine whether the particles behaved as clathrate crystals or pure solid crystals; 2) if the behavior proved to be consistent with the clathrate theory, to determine further the decomposition temperature (at atmospheric pressure) for the clathrate crystals; and 3) to determine the size and shape of the primary particles and whether there was a change in size with a change in gelant concentration of the initial vapor mixture from which the gelant particles were formed.

A light microscope with a suitable sample cold stage was used in this investigation, and samples of very dilute gels were used so that gelant particle agglomerates could be isolated. It was found that the majority of the individual particles were not distinguishable under a light microscope, indicating that the principal dimension was less than 1 μm . Thus, no further information on the actual size and shape of the primary gelant particles could be obtained without the use of an electron microscope. Due to the cryogenic-temperature requirements, no attempt was made to use such a technique. However, the light microscope proved to be useful in observing the behavior of the gelant particles with changes in temperature. In general, the following sequence occurred as the gelant agglomerate was warmed at atmospheric pressure.

1) As the liquid methane boiled off, the agglomerate became compact, eventually leaving only a thin layer of liquid around the agglomerate. This remaining liquid vaporized as the temperature was increased, and the agglomerate appeared dry when the temperature was

~10 K above the cryogen boiling point.

2) At a temperature well below the pure solid melting point, the agglomerate became dark. With a further increase of 10 to 20 K, the agglomerate sometimes took on a skeleton-like appearance (as if fusion of the particles were occurring). During this time, new crystals appeared on the surface of the microscope slide and continued to grow, while the agglomerate appeared to shrink.

The microscopically observable transformation (i.e. when the agglomerate visibly darkened) in the water-methane system occurred at 178 ± 5 K which is in agreement with the known decomposition temperature of 183 K. This indicated that the present technique was adequate for determining decomposition temperatures, and analysis of the methane-methanol agglomerates yielded a decomposition temperature of 145 ± 5 K. This initial transformation appears to be due to either controlled vaporization or a popping of the clathrate crystals releasing H_2O into the vapor phase. The new ice crystals then formed at appropriate nucleation sites on the microscope slide.

3) As the temperature was further increased (but still held below the pure solid melting point), the agglomerate appeared to melt and recrystallize. This indicated that at higher temperatures, the solid-solid transformation probably occurred with a rupture of the clathrate crystal leaving the water molecules briefly in a random subcooled liquid form until such molecules could reorient to crystallize as a pure solid.

4) Final melting of the remaining agglomerate and the new

crystals occurred at the known melting point within ± 5 K.

1.2.4 Attractive Forces Between Particles

The microscopic observations along with the results of the composition analysis and x-ray diffraction have provided substantial evidence that the gelant particles have a crystalline clathrate structure. The advantage of having such clathrate particles, with respect to gelation, was then considered from a theoretical point of view. The only two attractive forces which would be present in such a system are van der Waals attraction between the particles and hydrogen bonding between surface hydroxyls. The van der Waals attractive force between two polymolecular particles is dependent on the particle size and separation distance. For spherical particles with a radius, r , which is much larger than the separation distance, D , the expression is

$$V_v = \frac{Ar}{12D} \quad (1-1)$$

where V_v = van der Waals attractive energy
 A = Hamaker constant (Hamaker, 1937) or Hamaker-Lifshitz function (Lifshitz, 1956)

In the present calculations, "A" was assumed to be constant, and the Lifshitz expression (Lifshitz, 1956) for small separation distances was used to determine its value. For water clathrate particles, a value of 2.1×10^{-14} ergs was calculated for "A". This is quite low

and suggests that for very small particles (< 200 A radius) hydrogen bonding may be important in producing the observed gel structure. Also, there was no distinction between the van der Waals force for ice crystals and water clathrate crystals as their spectral absorption data were quite similar. It is not known whether a gel could actually be formed if ice particles equivalent in size to the present clathrate particles could be produced. However, surface characteristics will, no doubt, play an important role in determining whether two particles in contact with each other will stick together, and if so whether a relatively weak linkage such as that formed by cage bridging will occur, or whether surface planes will match and coalescence result. For gelation, it is important to avoid coalescence as this eventually produces a single solid mass. Also, particle-particle linkages must be reversible under shear if the rheological behavior is to be consistent with that for a gel.

For the methanol gelant particles, van der Waals attraction was assumed to be the same as that for pure solid methanol particles, and "A" was estimated to be $2 \times 10^{-14} \leq A \leq 10^{-13}$ ergs (a more precise value could not be obtained due to insufficient data on the properties of solid methanol). This too is a fairly low value, and hydrogen bonding between particles is again likely to produce the observed gel structure.

1.3 Vaporization of LNG Gels on Water

To ascertain whether LNG gels would provide a significant safety advantage, it was necessary to know whether gelation affected the rate

of boil-off per unit area on a water surface. Confined spill studies were performed to measure this quantity. The procedure involved spilling a quantity of the gel onto water which was held in an insulated container. The quantities spilled were always sufficient to cover the entire water surface with an initial cryogen head of ≥ 0.5 cm. The weight of the container plus water and cryogen was then measured as a function of time to obtain the mass vaporized per second. Also, a thermocouple was placed in the vapor space above the boiling cryogen to determine whether the escaping vapor was substantially superheated, i.e. at a temperature above the atmospheric boiling point of the cryogen. For the LNG gels, it was found that the boil-off behavior was significantly different from that of LNG. LNG boiled at a rate which initially increased with time. This has been explained as a shift from film to nucleate boiling. Also, no superheating of the vapor was measured, which is typical for nucleate boiling. The LNG gels, on the other hand, boiled at a lower fairly steady rate (Figure 1-8), and the vapor was generally quite superheated (between 30 K and 90 K) which might be expected for film boiling. In general, the gels boiled at an average rate which was two to three times lower than LNG of the same composition.

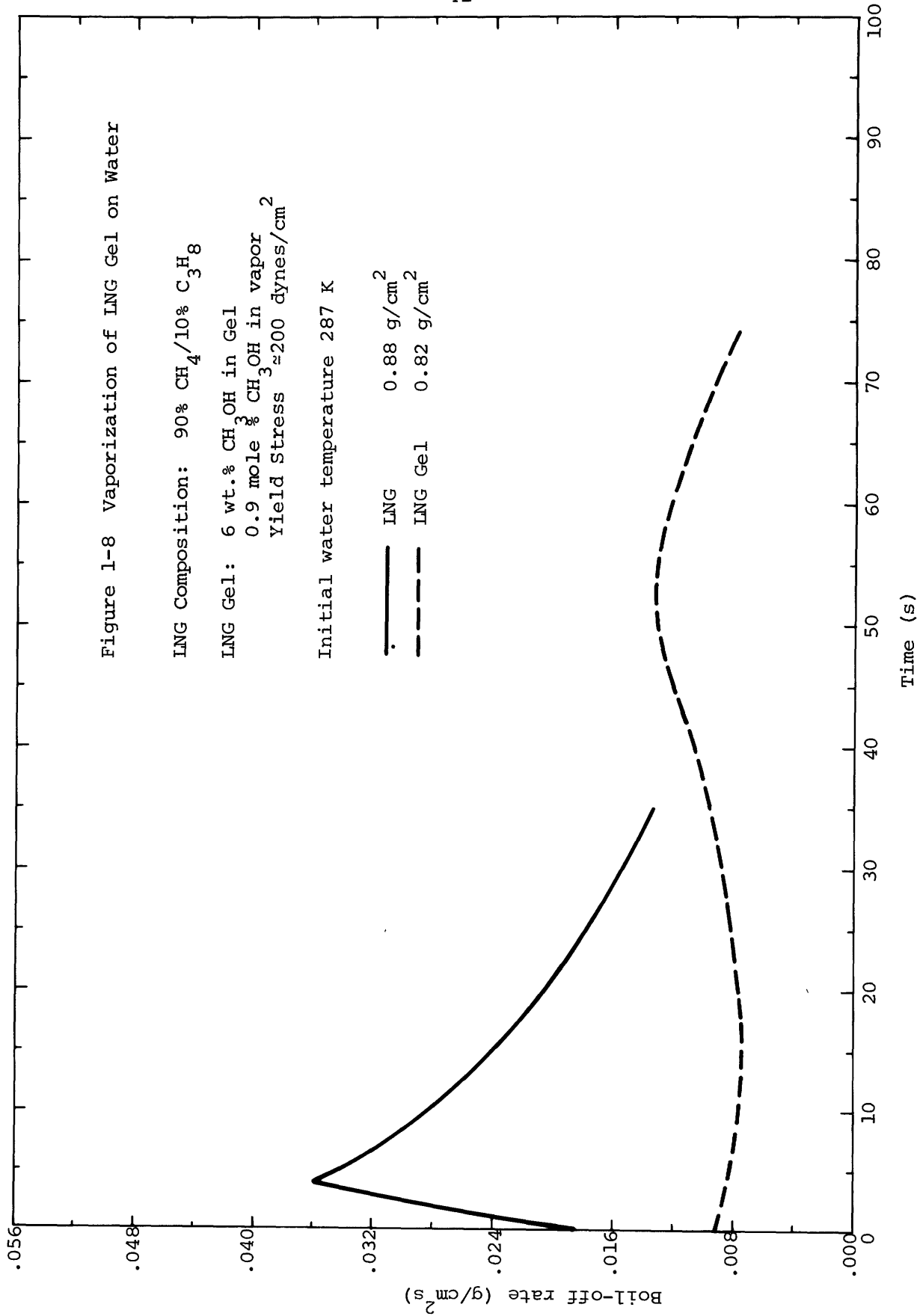
1.4 Gel Rheology

Past studies on different types of gels have shown their rheological behavior to be non-Newtonian and time dependent. In general, the simplest expression which can be used with such floc-

Figure 1-8 Vaporization of LNG Gel on Water

LNG Composition: 90% CH₄/10% C₃H₈
LNG Gel: 6 wt.% CH₃OH in Gel
0.9 mole % CH₃OH in vapor
Yield Stress ≈ 200 dynes/cm²

Initial water temperature 287 K



culated dispersions is an expression proposed by Oldroyd (1958), but modified to include a yield stress.

$$\tau - \tau_y + \lambda_1 \left(\frac{\delta \tau}{\delta t} \right) = \eta_p \left(\frac{dv}{dx} + \lambda_2 \left(\frac{\delta}{\delta t} \left(\frac{dv}{dx} \right) \right) \right) \quad (1-2)$$

where τ = shear stress
 dv/dx = shear rate
 t = time
 λ_1, λ_2 = relaxation times for shear stress and shear rate respectively
 η_p = plastic viscosity coefficient

This relation defines the behavior above the yield stress, τ_y . Below the yield stress, the gel will behave as an elastic solid.

$$\tau = G\gamma \quad (1-3)$$

where G = linear elasticity (or elastic modulus)
 γ = shear $\Delta l/l$



According to these expressions, if a gel, initially at rest, is instantaneously subjected to a constant rate of shear, the shear stress response will be an initial elastic response until a critical shear (i.e. that which corresponds to the yield stress) is reached. At this point the shear stress will continue to increase, but will do so exponentially, thus approaching a steady-state value of shear stress. Some of the previously reported data for this type of rheological experiment agreed quite closely with this model. However, under certain conditions, the shear stress response was found to peak and then decay to a steady-state value. Jachimiak (1974) has developed a criterion for the occurrence of such peaks--when $\dot{\gamma}/\lambda_1 < 1$ (where $\dot{\gamma} = d\gamma/dt$), no peak will be observed.

The fact that a steady-state value is approached for each rate of shear indicates that a steady-state curve exists for shear stress as a function of rate of shear. Equation 1-2 yields a Bingham plastic relation for steady-state behavior. This, however, is known to be an oversimplification for most gels, although it may be applicable for specific ranges of shear rate. In general, gels behave as shown in Figure 1-9. At high shear rates ($\geq 1000 \text{ s}^{-1}$) gel behavior has been adequately described with a Bingham plastic model. At low shear rates ($\leq 1 \text{ s}^{-1}$) the behavior may also be that of a Bingham plastic, but this region has received little attention in the past. At moderate shear rates, however, gels will display a pseudoplastic behavior. The low shear rate data can be extrapolated to zero shear rate to obtain a steady-state yield stress. However, it has been found that a gel can resist flow even at shear stresses much greater than this steady-state value. If the gel is subjected to increasing shear stress until flow occurs, the maximum observed shear stress is generally referred to as a static yield value. For the present application of LNG gels to a safety benefit analysis, the yield stress will be a particularly important parameter, as it determines when an LNG gel will cease spreading due to the gel structure being able to support the residual gel height. Here the steady-state value will provide a conservative estimate while the static yield will provide a maximum. The steady-state curve for shear stress versus shear rate was also desirable for future estimation of the increased pumping requirements.

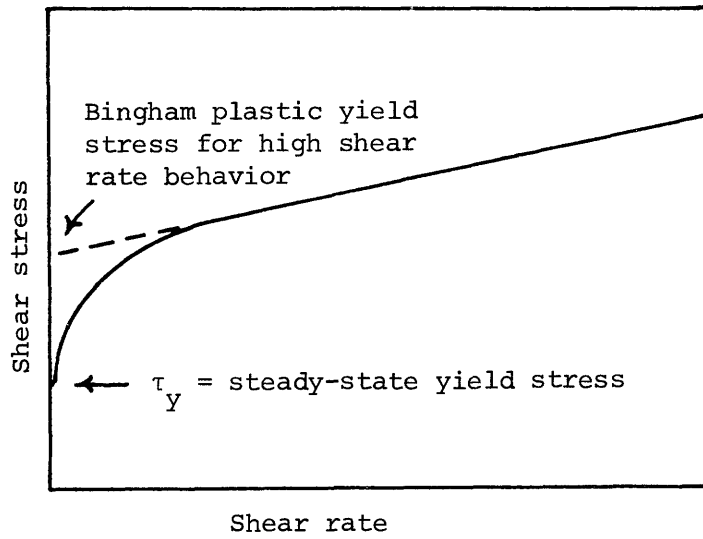
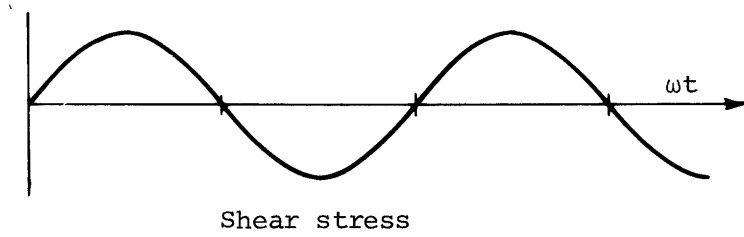
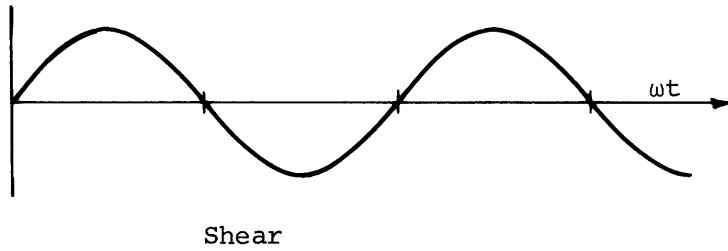


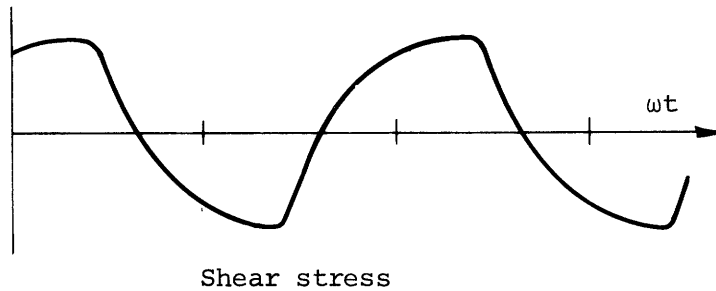
Figure 1-9 Steady-state rheological behavior for gels.

In this study, an oscillating viscometer was used to study the rheological behavior of the gels. The geometry was Couette (coaxial rotational) with a forced oscillation, i.e. the gel was subjected to a shear oscillation such as a sinusoid and the torque was measured. The response to such a sin wave input was a function of the frequency and the amplitude of the oscillation (Figure 1-10). Starting with a sample at rest, if a sin oscillation at low frequency (≤ 0.5 Hz) and low amplitude (≤ 0.01 shear) was applied, the behavior was elastic, and variation of the amplitude showed a linear correlation of shear stress with shear, i.e. it was Hookean elastic. This response was representative of the static structure below its yield stress. At low frequencies and higher amplitudes (up to $\gamma = 0.15$, the maximum shear attainable on the present instrument), a distinctive non-linear viscoelasticity response was observed. This behavior indicated that the yield stress had been exceeded, and the response was typical of transient behavior under an applied rate of shear. At higher frequencies and maximum amplitude, the response was again elastic with the same elastic modulus as shown at the low frequencies. This response is probably due to insufficient time for particle-particle bonds to break during each half cycle.

To determine the steady-state shear stresses, the non-linear viscoelastic responses were used. Similar shear stress responses have been observed by previous investigators, but the methods of analysis have differed greatly. Some investigators have fit the response to a Fourier series to obtain a spectrum of relaxation times. Others have



Elastic response at low frequency-low amplitude shear and at high frequency-all amplitudes shear



Non-linear viscoelastic response at low frequency-high amplitude shear

Figure 1-10 Shear stress response for LNG gels under an applied sinusoidal shear.

defined new rheological functions whose relation to the desired steady-state values is unknown. Probably the most appropriate method of analysis was that of Elliott and Green (1972) who suggested using a modified Bingham body expression (this is Oldroyd's expression without the shear rate relaxation term) to fit the observed responses. Although such a model will produce curves somewhat similar to those actually observed for LNG gels, it is not certain whether the shear rate relaxation term is actually negligible under such conditions. To analyze the present data a slightly different method was used. For a sinusoidal input, the actual cup (shear) oscillation was quite linear over much of the region around the inflection point (Figure 1-11), and the observed shear stress response for this region showed the same steep initial elastic response followed by a slow relaxation which is typical of the transient responses for an applied constant shear rate. Thus, the oscillation and resulting shear stress behavior were similar to one alternating between two steady shear rates. When compared with a sawtooth input (one which exactly alternates between two constant shear rates), the responses matched. Thus, to obtain the desired steady-state values, the slowly-relaxing portion of the response was fitted to an exponential and the value for this function at infinite time was assumed to be equal to the steady-state shear stress. The results for the different LNG gels are shown in Figure 1-12, and all displayed a Bingham plastic response at the low shear rates studied.

Although no exact correlation exists for τ_y as a function of

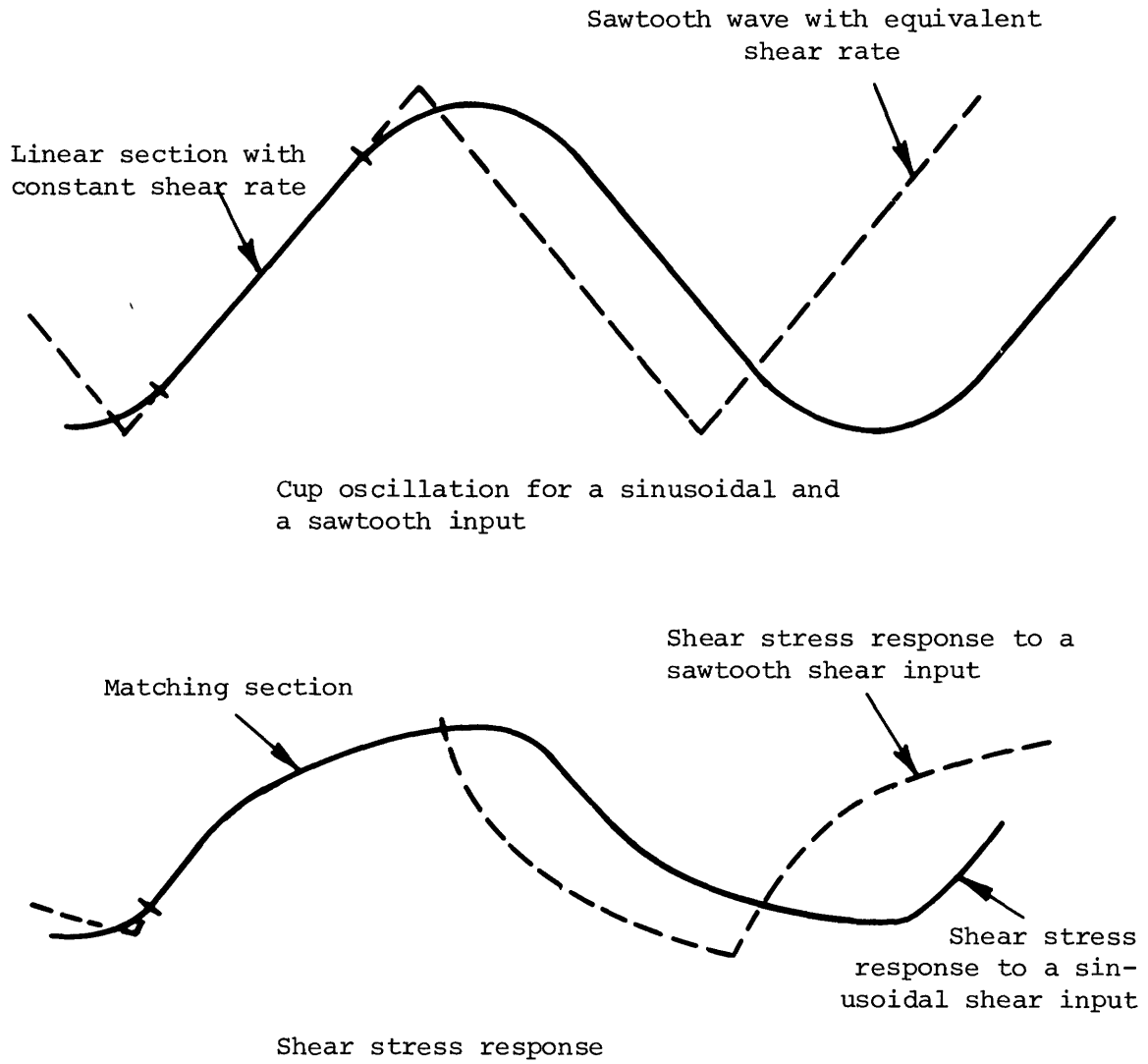


Figure 1-11 Comparison of responses for the constant shear rate portion of a sinusoidal input and an equivalent shear rate sawtooth input.

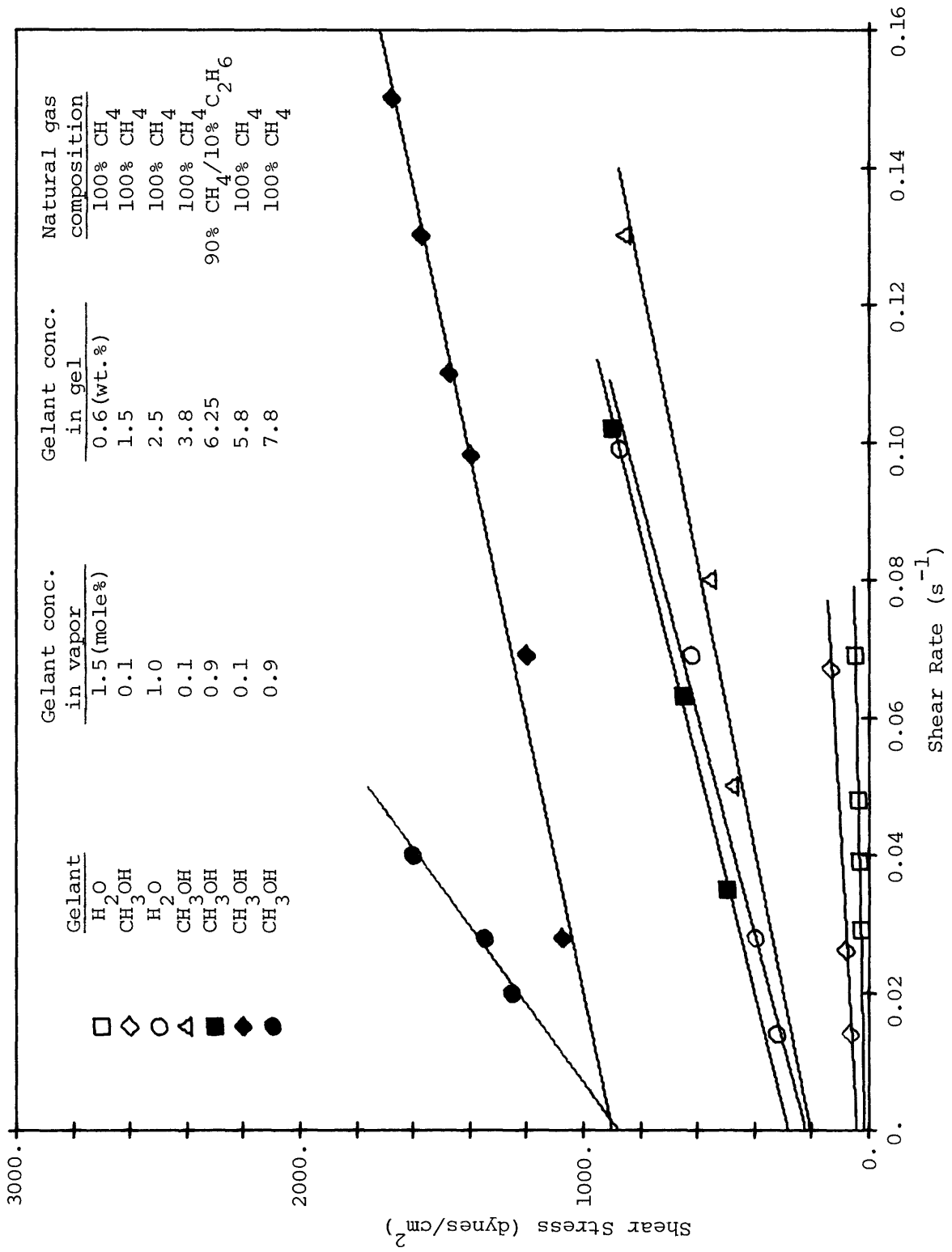


Figure 1-12 Rheological behavior of LNG gels

known parameters, past investigations have suggested that the following proportionality exists.

$$\tau_y \propto \frac{A\phi_p^3}{Dr^2} \quad (1-4)$$

where A = Hamaker constant
 D = separation distance between particles
 ϕ_p = volume fraction of particles
 r = particle radius

Based on previous experimental data (Thomas, 1961), the constant of proportionality for this expression ranges from 5 to 20. This relation includes a proportionality with the particle-particle van der Waals attractive force. For very small LNG gelant particles, hydrogen bonding will be the dominant interaction force, and the resulting proportionality will be

$$\tau_y \propto \frac{n(E_{HY})\phi_p^3}{r^3} \quad (1-5)$$

where E_{HY} = hydrogen bond energy
 n = number of hydrogen bonds formed between two particles

The constant of proportionality for this expression ranges from 50 to 250. This expression gives a calculated radius ranging from 100 A to 200 A (assuming 1 to 3 hydrogen bonds) for all of the LNG gelant particles, which is quite small and well below the range where van der Waals forces dominate.

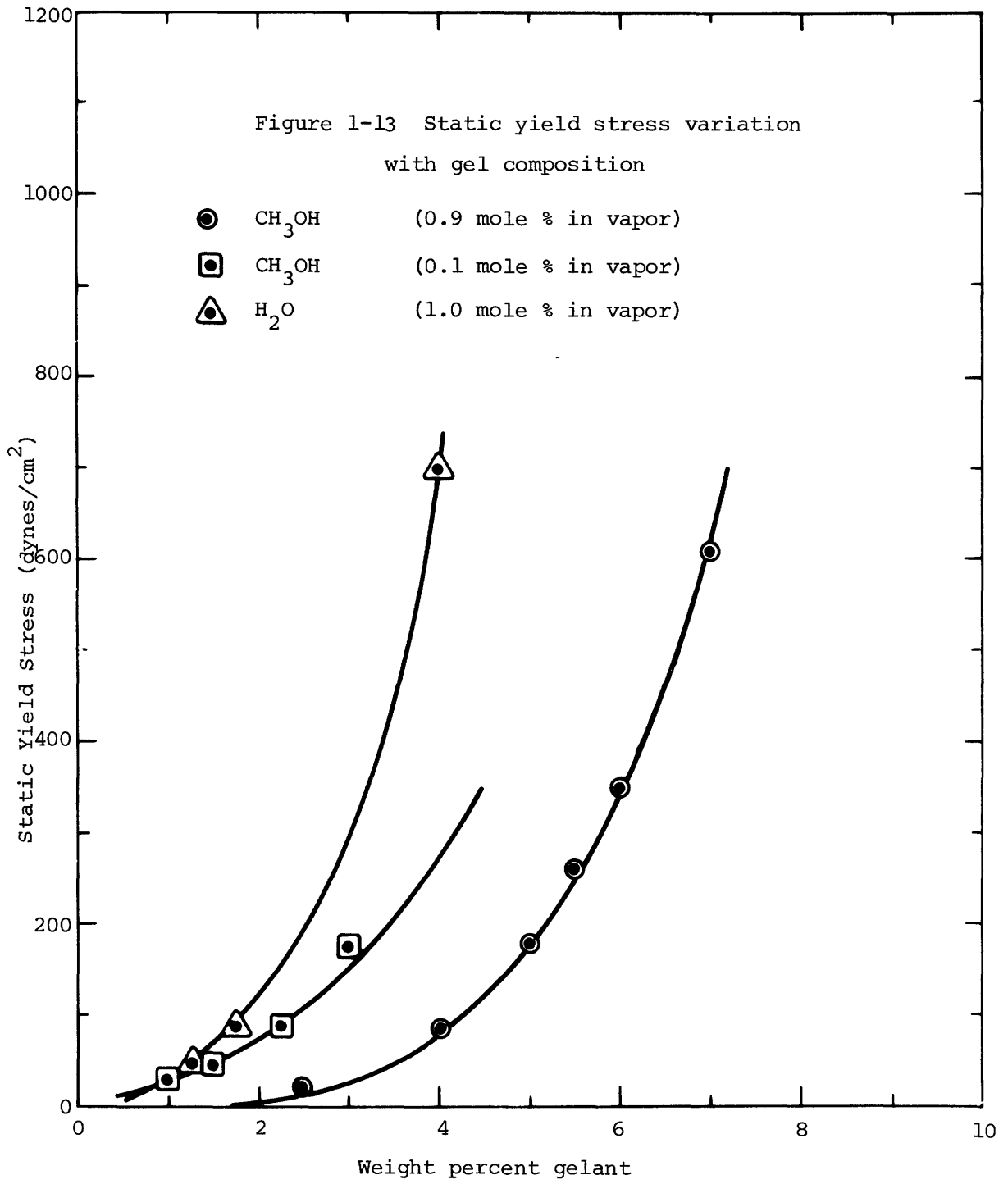
The results for the methanol gels clearly showed that changing the gelant concentration in the initial vapor mixture (i.e. the gas

mixture from which the gelant was condensed) affected the final gel rigidity. Lower gelant concentrations in the vapor produced higher yield stress gels (for the same final gel composition), suggesting that smaller particles were formed. However, for the observed variation in yield stress with vapor gelant concentration, the estimated difference in radius was only 30 percent. Although the water gels did not show a similar variation in yield stress, this may have been due to the small concentration range studied. The gelant concentration in the vapor mixture was only varied by a factor of two, whereas in the methanol gels it was varied by a factor of 9.

The static yield stresses for the LNG gels were determined primarily by measuring the height of gel buildup which remains on a suspended disk which has been submerged in the gel and gradually withdrawn. An initial study using Cab-O-Sil gels showed a correlation of $\tau \approx (1/3)\rho gh$, where ρ is the gel density and h is the peak height. In a few cases, further confirmation of the LNG gel static yield stresses was made using a Brookfield Synchro-Lectric Viscometer. The resulting variation of static yield with gelant and gelant concentration is shown in Figure 1-13.

1.5 Safety Benefit Analysis

The primary incentive for gelling LNG was to reduce the hazard associated with an accidental LNG spill by decreasing the maximum travel distance for flammable gas mixtures. According to the available



vapor dispersion expressions, this distance is approximately proportional to the overall rate of vapor generation. Thus, to estimate this maximum distance requires knowledge of the maximum pool radius which, in turn, is dependent on the rate of spread and boil-off.

Although analytical models have been derived to describe both low viscosity (such as LNG) and high viscosity liquids spreading on water, a number of assumptions have been made which do not seem appropriate. Also, the available expressions suggest that there is no advantage in having a fluid more viscous than water, which intuitively would not seem to be the case. Thus, an alternative technique was necessary to determine whether the high viscosity of the gel would indeed reduce the rate of spread. For this purpose a numerical technique (developed by Amsden and Harlow, 1970, which uses the complete Navier-Stokes equations) was used. This computer program was not designed to handle two different fluids nor to allow for any loss of fluid by boil-off. However, the effect of gelation could still be adequately demonstrated using the simple case of a breaking dam. As the Navier-Stokes equations pertain only to Newtonian fluids, the gel was modelled as a highly viscous Newtonian fluid of viscosity 500 poise (for a gel of yield stress 500 dynes/cm^2 , the apparent viscosity at 1 s^{-1} would be ≥ 500 poise). Several cases were considered for the breaking dam model. Both a free-slip (shear stress equals zero) and a no-slip (velocity equals zero) surface were used, and both LNG and LNG gel were analyzed. The results for these different numerical cases are shown in Figures 1-14, 1-15, and 1-16.

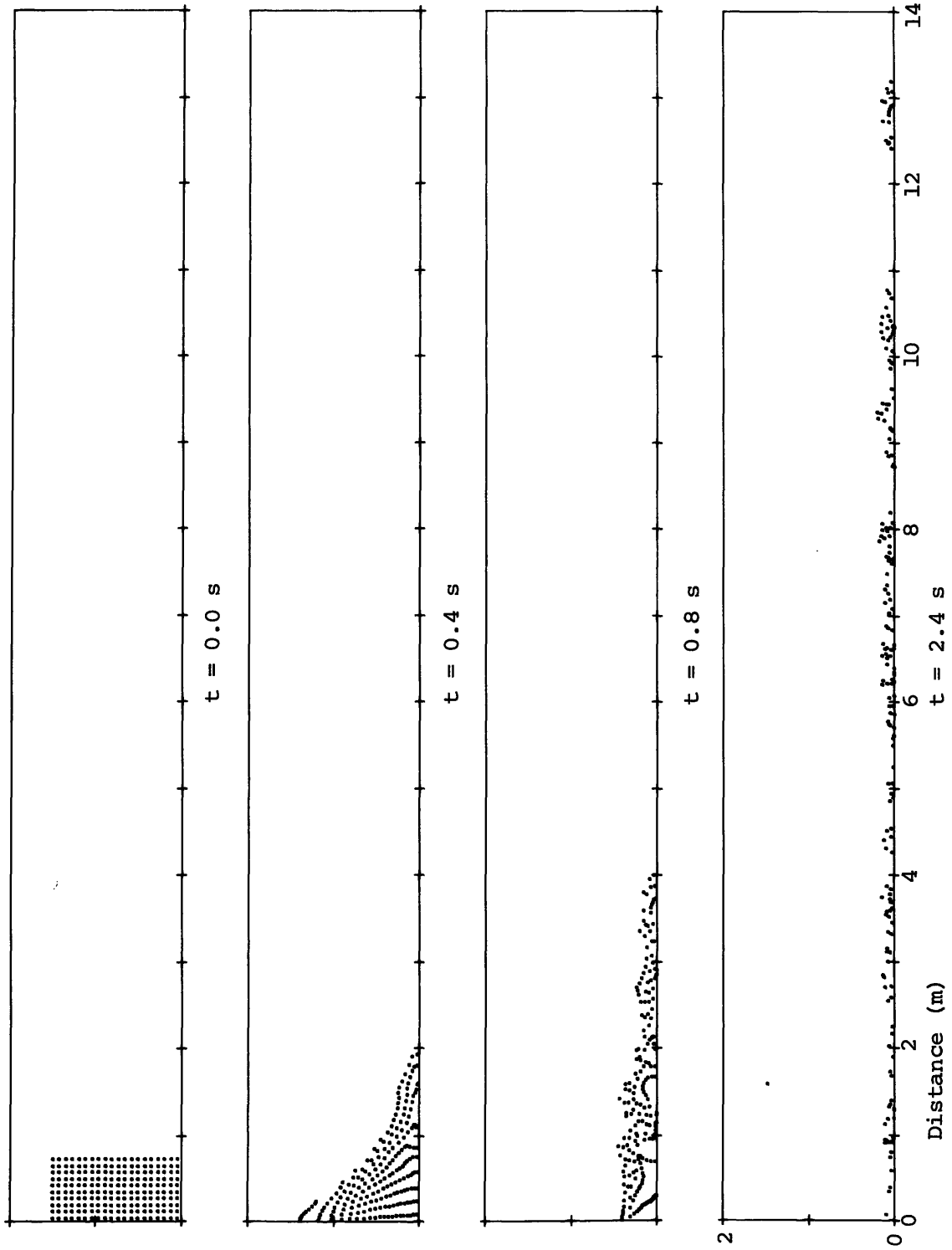


Figure 1-14 Numerical results for breaking-dam model using LNG and a free-slip boundary condition

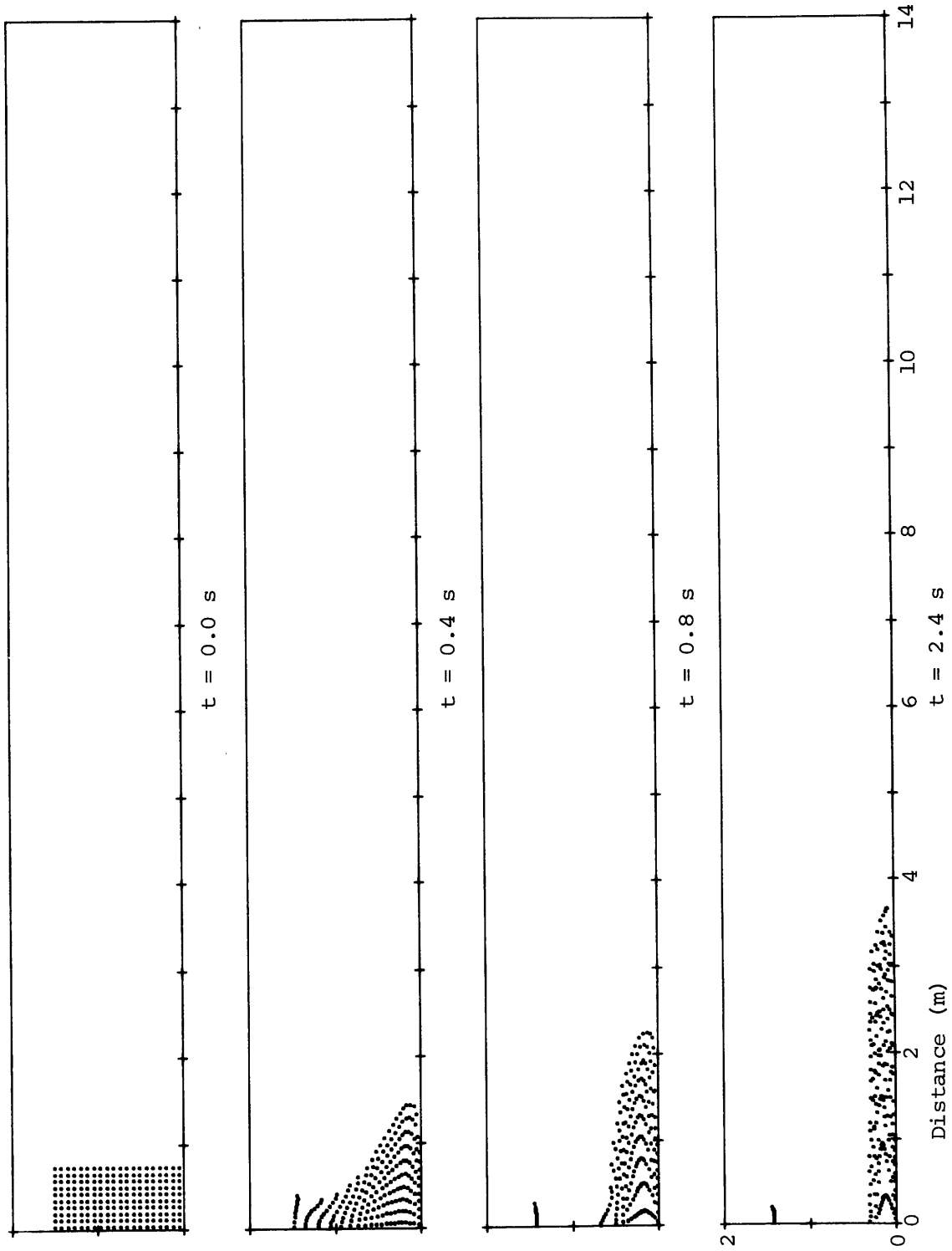


Figure 1-15 Numerical results for breaking-dam model using LNG gel and a no-slip boundary condition

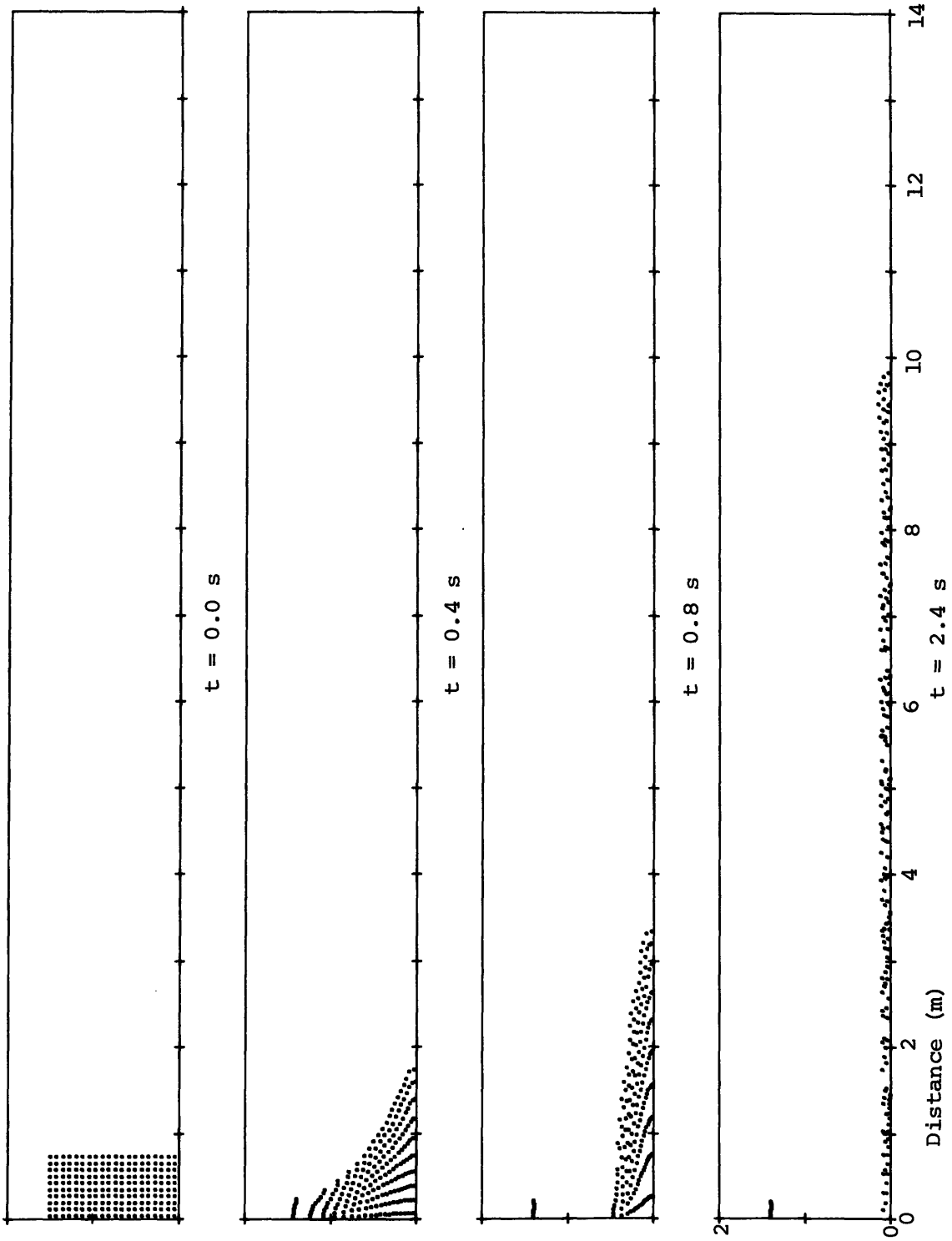


Figure 1-16 Numerical results for breaking-dam model using ING gel and a free-slip boundary condition

The spreading behavior of the LNG gel for the free-slip boundary condition showed a small decrease in rate of spread, approximately 2/3 that of LNG (both free-slip and no-slip were similar for LNG). On the other hand, the spreading rate for the gel under a no-slip boundary condition was significantly lower (approximately 1/8 that of LNG). However, the spreading behavior of LNG gel in an actual spill on water is likely to be somewhere in between these two rates. To model large LNG and LNG gel spills of 10^7 kg each (this is approximately equal to that in a single storage tank on a tanker), constant radial spread rates and boil-off rates were assumed. For LNG, the spreading rate was assumed to be 0.8 m/s (this is slightly higher than has been observed in small instantaneous spills, but lower than that found for the previous breaking dam case), and for LNG gel the rate was assumed to be 40 percent lower (i.e. 0.3 m/s). Average values for the boil-off rates (taken from the previously discussed vaporization data) were used--0.2 g/cm²s for LNG and 0.1 g/cm²s for LNG gel. Under these conditions, the spreading and vaporization of the two cryogenes will be as shown in Figure 1-17. If the gel yield stress and concentration change with time are also taken into account, the gel (assuming an initial $\tau_y = 500$ dynes/cm²) would spread until the gel height is ≈ 10 cm (this includes the buoyancy effect). The overall effect will be to reduce the maximum rate of vapor generation by a factor of 5, and, in turn, to reduce the maximum travel distance for flammable mixtures by approximately the same factor.

Thus, if a sufficiently rigid gel is transported, the safety

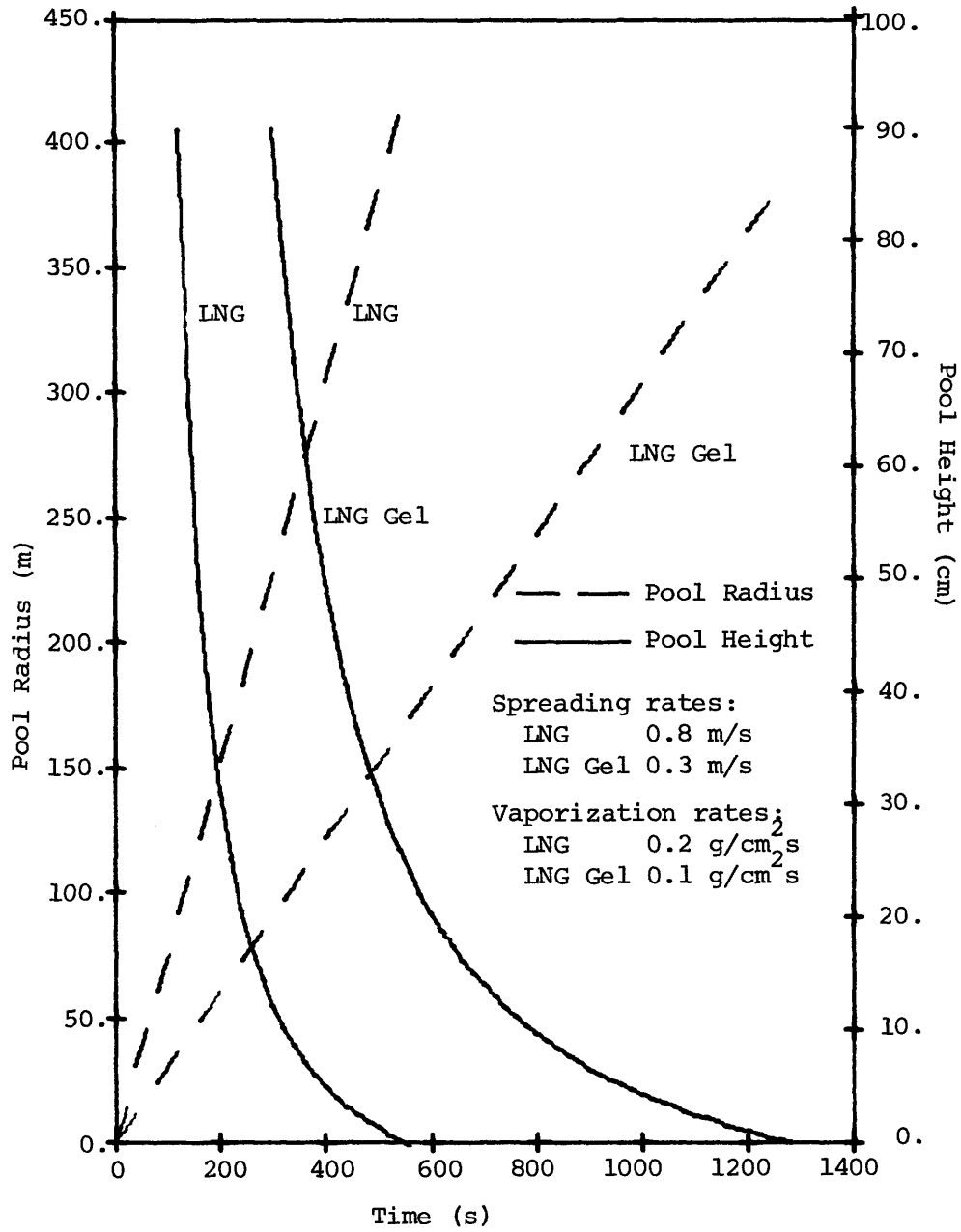


Figure 1-17 Spreading and Vaporization of 10^7 kg
LNG and LNG Gel

hazard may be significantly reduced. However, the feasibility of industrial-scale use is still uncertain. The small clathrate particles may be difficult to produce efficiently. Both methods for producing colloidal size particles, by comminution of larger particles or by a condensation sequence of nucleation and particle growth (as used in this study), have drawbacks. The grinding of larger crystals has a limit as to the minimum size which can be produced ($\sim 1 \mu\text{m}$), and the required gelant concentration for this size particle (based on Equation 1-4) will be approximately 80 weight percent (63 volume percent) to produce a gel with $\tau_y = 500 \text{ dynes/cm}^2$. On the other hand, a condensation process requires rapid cooling to avoid undesired condensation on vessel walls, as well as to produce the desired small particle size. One possibility might be to expand a natural gas-gelant vapor mixture using a supersonic jet (extremely fine particles of $\sim 50 \text{ \AA}$ radius have previously been produced by this method), with subsequent condensation of the surrounding natural gas. However, even if a feasible means of producing LNG gels is found, there may be other problems associated with industrial-scale usage. In particular, the revaporization of the gels may pose problems due to the increasing yield stress during natural gas boil-off. Further study is therefore necessary before any feasibility assessment can be made.

CHAPTER 2 - GELS AND THE GELATION PROCESS

In the literature, "gels" come under the broad topic of "colloid chemistry". A preliminary discussion of the nature of colloidal systems will therefore be helpful in clarifying the term "gel". Some relevant definitions include:

Colloid Science - the science which deals with a) kinetic units which are large in comparison with atomic dimensions yet visibly small (usually includes 1 nm to 1 μ m) and b) systems containing these kinetic units or structures derived from them.

Colloidal particles - the kinetic units described above.

Colloidal system (Colloid) - a material system which is composed of colloidal particles (or derived structures) along with smaller kinetic units such as a liquid.

Here it is customary to distinguish between two different classes of colloidal systems which have distinctively different behavior-- lyophilic and lyophobic. In lyophilic colloids it is assumed that there is a strong affinity between the particles and the molecules of the dispersion medium, while in lyophobic colloids such affinity is either weak or absent. The kinetic units of lyophobic colloids are rigid polymolecular particles (either amorphous or crystalline) or small liquid droplets (emulsion). Lyophilic colloids, on the other hand, are distinguished by their kinetic unit "particle" which consists of either a single large molecule or a cluster of such molecules dissolved in the dispersion medium. A "gel" is then defined as a colloidal system (either lyophobic or lyophilic) with a solid-like character, in which the colloidal particles somehow constitute a coherent structure

which is interpenetrated by smaller kinetic units, usually a liquid. The nature of the coherent structure varies with the type of colloid. In lyophobic gels, the structure is formed by the flocculation or aggregation of the particles. Examples of lyophobic gels include clays, Cabosil, vanadium pentoxide, silica gel, etc. (See Figure 2-1) In lyophilic gels the coherent network may be formed by ordered crystalline regions of the macromolecules dispersed throughout the liquid, but which are mutually united by single macromolecular chains. Another possible structure consists of single macromolecules bound together at certain points by cohesion forces or stronger chemical bonds. An example of the former type of lyophilic structure is gelatin which forms ordered regions of triple helices. Examples of the latter structure are the chemically bonded structures of vulcanized rubber, protein elastin, cross-linked polystyrene networks, etc.

2.1 Flocculation of Lyophobic Colloidal Particles

Lyophobic colloids are often discussed as to whether they remain individually dispersed or flocculate, those systems which remain individually dispersed being considered stable. The terms flocculation, aggregation, and coagulation are generally used interchangeably and refer to the interaction of particles to form clusters whereby the particles have maintained their individuality, but are held together at a few points only by comparatively weak forces. From a thermodynamic sense, lyophobic colloids are never stable, as a large crystal will not spontaneously dissociate into colloidal particles (as will lyophilic

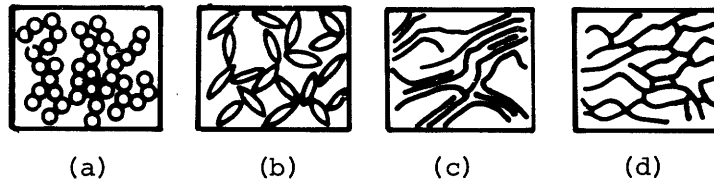


Figure 2-1 Types of Gel Networks

- a) Lyophobic spherical particles
- b) Lyophobic rod-like particles
- c) Lyophilic with crystalline regions
- d) Lyophilic with covalent bonding between branches

colloids). Work must be supplied due to the required increase in the crystal-liquid interfacial area. However, with respect to flocculation, lyophobic particles may be stable, and such a stable system of colloidal particles dispersed in a liquid is commonly referred to as a "sol".

The interparticle forces which affect the stability of lyophobic colloids include electrostatic repulsion (also attraction in a few cases), steric (entropic) repulsion, and van der Waals attraction. Summation of these effects will give an interaction potential curve such as in Figure 2-2. If the repulsive forces are minimal, the net interaction will be an attraction at close range. When Brownian motion plus external forces bring two particles into close proximity, the attractive force will be stronger than the kinetic energy of the particle (kT) and the two particles will stick together. Once in contact, other short range forces such as hydrogen bonding may be important. In the present study on the gelation of liquefied natural gas, two different gelants, water and methanol, have been used, both of which exist in a frozen state at the temperature of LNG (freezing point of methanol, 183 K). With the present gelation technique, fine crystalline gelant particles are produced and dispersed in the LNG, thus forming a lyophobic colloid. The forces affecting the stability of lyophobic colloids will, therefore, be applicable to the present systems. Particularly important will be the combination of forces which result in a net particle-particle attraction (producing flocculation) and the nature and magnitude of the adhesive force once flocculated. Detailed discussions will therefore be given as to the nature of these forces and procedures for estimating

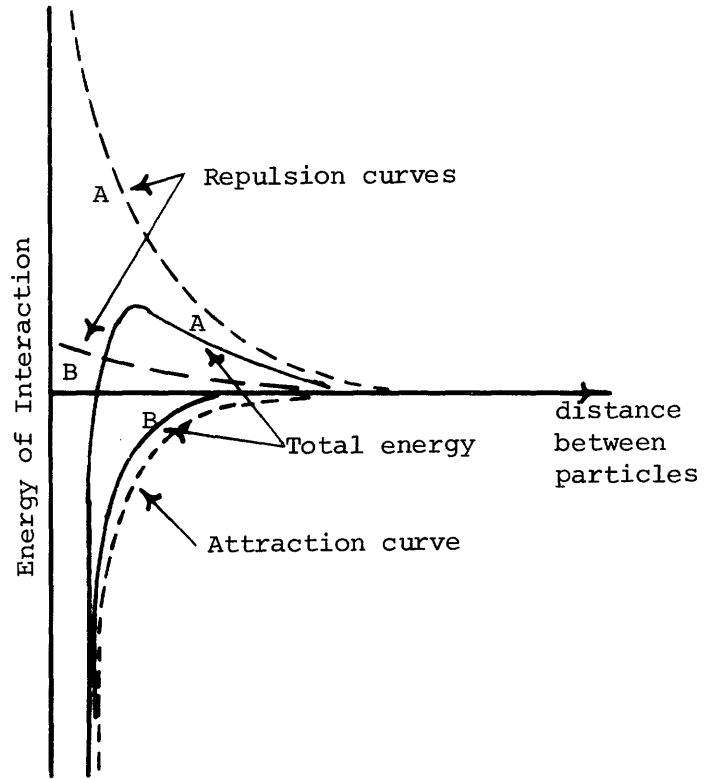


Figure 2-2 Particle-particle Interaction Energies.
A combination of one attraction curve with
two repulsion curves of different height
is shown.

their magnitudes.

2.1.1 Van der Waals Forces

Two identical colloidal particles will have a general attraction for each other similar to the van der Waals molecular attractive forces. To analyze these forces, two distinct theoretical approaches have been developed, the first based on microscopic properties, and the second based on macroscopic properties.

2.1.1.a Microscopic Theory

The microscopic approach is based on the interactions of the individual molecules and assumes that these forces are additive (i.e. that the total force is the sum of the interactions of all molecules in one particle with all of the molecules in the other particle). For two neutral molecules there are three sources of attraction (commonly lumped together as van der Waals attraction): a Debye interaction (induction); a Keesom interaction (orientation); and a London interaction (dispersion). The Debye and Keesom interactions only occur when the molecule has a permanent dipole while the London interaction is a general attractive force possessed by all molecules.

The Keesom attractive force is based on the interaction between two permanent dipoles. This depends on the mutual orientations of the dipoles and is determined by taking a statistical mean (based on a Boltzmann distribution) over all possible orientations. The result is

an attractive force due to the preponderance of attractive orientations over the repulsive ones.

$$\begin{aligned}
 V_K &= \frac{\mu_1 \mu_2 f}{D^3} \\
 V_K &= \frac{\int V_K \exp(-V_K/kT) d(\text{orient})}{\int \exp(-V_K/kT) d(\text{orient})} \\
 &= \frac{\int V_K (1 - V_K/kT) d(\text{orient})}{\int (1 - V_K/kT) d(\text{orient})} \\
 &= \frac{\int V_K d(\text{orient})}{\int d(\text{orient})} - \frac{1}{kT} \frac{\int (\mu_1^2 \mu_2^2 / D^6) f^2 d(\text{orient})}{\int d(\text{orient})} \\
 &= 0 - \frac{2\mu_1^2 \mu_2^2}{3kTD^6} \tag{2-1}
 \end{aligned}$$

where μ_1, μ_2 = dipole moment of molecule 1 and 2 respectively
 k = Boltzmann's constant
 T = absolute temperature
 D = distance between two molecules
 V_K = Keesom interaction energy
 f = function of dipole orientations and is of order unity

The Debye force is based on the interaction of a permanent dipole in one molecule and the dipole which it induces in another molecule. An attractive force always results as the induced dipole is always anti-parallel to the inducing one. For a dipole moment in one molecule, μ_1 , and a polarizability, α_2 , in the second molecule, the interaction can be derived as follows. The electric potential, ϕ_d , due to μ_1 is

$$\phi_d = \frac{\mu_1 \cos\theta}{D^2} \tag{2-2}$$

where D = separation distance between molecules
 θ = angle between dipole and radius vector

The corresponding electric field, $E = d\phi/dD$, is

$$E_d = \frac{2\mu_1 \cos\theta}{D^3} \quad (\text{in direction of } D) \quad (2-3)$$

The energy of interaction with a molecule of polarizability α_2 is

$$\begin{aligned} V_d &= -(1/2)\alpha_2 E_d^2 = \frac{-2\alpha_2 \mu_1^2 \overline{\cos^2\theta}}{D^6} \\ &= \frac{-\alpha_2 \mu_1^2}{D^6} \end{aligned} \quad (2-4)$$

where V_d = Debye interaction energy

Finally, the London force is based on the premise that molecules without permanent dipoles may still attract each other due to instantaneous fluctuations in their respective electron distributions. From quantum mechanics Eisenschitz and London (1930) derived an expression for this attractive energy, V_L , for two complex atoms or molecules.

$$V_L = \frac{-B_{12}}{D^6} = \frac{-3h\alpha_1\alpha_2}{2D^6} \frac{\nu_1\nu_2}{\nu_1+\nu_2} \quad (2-5)$$

where α_1, α_2 = polarizability of molecules 1 and 2 respectively
 h = Planck's constant
 ν_1, ν_2 = chief dispersion frequency (s^{-1}) taken from the dispersion spectrum for molecule 1 and 2 respectively
 B_{12} = London constant

London (1937) suggested replacing $h\nu$ with the ionization potential of the atom or molecule.

$$B_{12} = \frac{3}{2} \frac{\alpha_1 \alpha_2}{I_1 + I_2} \frac{I_1 I_2}{I_1 + I_2} \quad (2-6)$$

where I_1, I_2 = ionization potential for molecules 1 and 2 respectively

Several assumptions were made to obtain this expression and further details of the derivation are given in Appendix A. Other relations for the London constant have been proposed by various people (Slater and Kirkwood, 1931; Moelwyn-Hughes, 1961; Neugebauer, 1937) all of which result in values of B larger than that from the London expression.

Visser (1972) has compared recent theoretical and experimental results and concludes that the London expression and the Slater-Kirkwood expression (which differs from the London expression by a factor of \sqrt{Z} , where Z is the number of electrons in the outer shell of one molecule) are the most satisfactory for determining particle-particle attractive forces.

Comparing the three interaction potentials, Debye, Keesom, and London, all are proportional to $1/D^6$. However, in general, the London force will dominate the van der Waals attraction except where very strong dipoles (such as H_2O , NH_3) are present. Accordingly, the microscopic approach to particle-particle van der Waals attraction (Hamaker, 1937) has dealt solely with the London interaction.

To obtain the total attractive interaction between two colloidal particles, Hamaker (1937) derived expressions for the interaction

between two spheres and two semi-infinite plates. Hamaker has considered only the London dispersion force and assumed the additivity of this force. For colloidal interactions the Debye and Keesom interactions are not additive, as the electrical field strength acting on an atom is the vectorial sum of the separate strengths generated by each of the atoms. The resulting total energy due to these forces is usually much smaller than the sum of the separate energies, and the range of action will always be extremely small (<a few molecular diameters). Thus, the neglect of the Debye and Keesom forces is satisfactory when the interaction distance of interest is large with respect to molecular dimensions (> 50 A). Also, the assumption of additivity of the London forces is not precisely correct. Spaarnay (1959) has shown that the deviation from additivity varies from case to case and is not known a priori. In the cases he considered, 5 and 7 atom particles, deviations ranged from 10 to 30 percent.

The resulting expression for the interaction between two semi-infinite plates of substance 1 and 2 (Hamaker, 1937) is

$$E_v = \frac{-A_{12}}{12\pi D^2} \quad \text{and} \quad A_{12} = \pi^2 q_1 q_2 B_{12} \quad (2-7)$$

where E_v = van der Waals interaction energy per unit area
 q_1, q_2 = number of molecules per unit volume for molecule 1 and 2 respectively
 D = separation distance
 A_{12} = Hamaker constant
 B_{12} = London constant

For two spheres of equivalent radius the expression is (Hamaker, 1937)

$$V_v = \frac{-A_{12}}{6} \left(\frac{2}{s^2 - 4} + \frac{2}{s^2} + \frac{\ln(s^2 - 4)}{s^2} \right) \quad (2-8)$$

and $s = 2 + D/r$

where D = separation distance - equal to shortest distance between the two surfaces
 r = radius of sphere
 A_{12} = Hamaker constant (as defined above)
 V_v = total van der Waals attractive energy

When the particle size is much larger than the separation distance (i.e. $r \gg D$), the expression reduces to

$$V_v = \frac{-A_{12}r}{12D} \quad (2-9)$$

The above relation for the Hamaker constant is based on the interaction of two colloidal particles in a vacuum. If the particles are separated by some medium, (3), such as a liquid, the desired Hamaker constant is (Hamaker, 1937)

$$A_{132} = A_{12} + A_{33} - A_{13} - A_{23}$$

According to Berthelot's principle (Berthelot, 1898), $B_{12} = \sqrt{B_{11}B_{22}}$,

and therefore

$$A_{12} = \sqrt{A_{11}A_{22}} \quad (2-10)$$

Krupp (1967) has shown that this relation holds for a variety of substances when the macroscopic theory (discussed in next section) is used to determine the interaction constants. Thus, the principle seems

to be applicable to the interaction between polymolecular particles. If two identical particles are separated by medium 3, the resulting expression for the Hamaker constant will therefore be

$$A_{131} = (A_{11}^{\frac{1}{2}} + A_{33}^{\frac{1}{2}})^2 \quad (2-11)$$

Although the use of the Hamaker relations is straightforward and requires a minimum amount of information about the particular substances, significant inaccuracies can occur. Ionization potentials have commonly been used to represent the characteristic energies in the expression for the London constant. The corresponding frequency ($h\nu=I$) for an energy of this order of magnitude (≈ 10 eV) is generally in the ultraviolet frequency range. To determine particle-particle interactions, however, one should consider all characteristic frequencies. This includes strong adsorption bands in the infrared, dielectric relaxation at low frequencies, etc. Although the ultraviolet frequencies may be dominant in some colloidal systems, other spectral regions have been shown to dominate in the present interaction between LNG gelant particles. Further discussion of this is given under the macroscopic theory.

2.1.1.b Macroscopic Theory

Lifshitz and coworkers (Lifshitz, 1956; Dzyaloshinskii et al., 1959) considered only macroscopic properties and derived expressions for the interaction between two semi-infinite media separated by a planar slab. Based on quantum theory they suggested that the electrons of an electrically neutral solid do not occupy fixed states of a

sharply defined minimum energy, but rather are subject to random excitations into states of higher energy. By definition, the absorption spectrum represents the extent to which charges within a body will change energy in response to an incident wave. Thus, the frequencies at which absorption occurs are the same natural frequencies at which charges will spontaneously move when transmitting and receiving electrical signals with neighboring charges. It is this spectrum of charge fluctuations which determines the resulting van der Waals force. For the attractive force per unit area between two semi-infinite media of substance 1 separated by a planar slab of substance 2, Dzyaloshinskii et al. have derived the following expression.

$$F(D) = \left(\frac{kT}{\pi c^3}\right) \sum_0^{\infty} \epsilon_2^{3/2} \xi_n^3 \int_0^{\infty} p^2 \left[\left(\left(\frac{s+p}{s-p} \right)^2 \exp\left(\frac{2p\xi_n D \epsilon_2^{1/2}}{c}\right) - 1 \right)^{-1} + \left(\left(\frac{s\epsilon_2 + p\epsilon_1}{s\epsilon_2 - p\epsilon_1} \right)^2 \exp\left(\frac{2p\xi_n D \epsilon_2^{1/2}}{c}\right) - 1 \right)^{-1} \right] dp \quad (2-12)$$

$$\text{and } s = (\epsilon_1/\epsilon_2 - 1 + p^2)^{1/2}$$

$$\epsilon = \epsilon(i\xi_n)$$

$$\xi_n = 4\pi^2 nkT/h$$

where

- k = Boltzmann's constant
- T = absolute temperature
- c = speed of light
- ϵ = dielectric susceptibility which is a function of the imaginary frequency component $i\xi_n$
- 1,2 = subscripts representing substances 1 and 2 respectively

The symbol \sum_0^{∞} indicates that the zero term must be multiplied by 1/2.

The range of validity for this expression is similar to that of the Hamaker expression. The gap width must be larger than atomic dimensions in order to specify dielectric properties for three separate media. Also, Lifshitz has assumed smooth interfaces which physically may or may not be true. However, if the gap width is large compared to surface defects, the above expression will be valid. Both the Hamaker and Lifshitz expressions are limited to gap widths ≤ 500 A, as the gap must be small compared to the wavelengths which contribute to the attractive force. Otherwise a retardation will occur due to the finite time required for the electromagnetic wave to travel from one particle to the other. This alters the third power proportionality for separation distance to a fourth power proportionality in both the Lifshitz and the Hamaker expressions for the attractive force.

Both frequency and dielectric susceptibility are complex quantities, $\omega = \omega_n + i\xi_n$ and $\epsilon(\omega) = \epsilon'(\omega) + i\epsilon''(\omega)$. The desired quantity is $\epsilon(i\xi_n)$. According to Landau and Lifshitz (1960) $\epsilon(i\xi_n)$ is real and decreases monotonically from a finite positive value (or $+\infty$ for metals) at $\xi_n = 0$ to 1 at $\xi_n \rightarrow \infty$. In principle the entire dielectric susceptibility function $\epsilon(i\xi_n)$ for imaginary frequencies can be obtained from the real component of frequency using the Kramers-Kronig relation.

$$\epsilon(i\xi_n) = 1 + \frac{2}{\pi} \int_0^{\infty} \frac{\omega_n \epsilon''(\omega_n)}{\omega_n^2 + \xi_n^2} d\omega_n \quad (2-13)$$

In practice, it is possible to approximate the function $\epsilon(i\xi_n)$ knowing the major absorption frequencies and indices of refraction by fitting

constants to the general form for a damped linear oscillator (Ninham and Parsegian, 1970a).

$$\epsilon(i\xi_n) = 1 + \frac{C_{mw}}{1 + \xi_n/\omega_{mw}} + \sum \frac{C_j}{1 + (\xi_n/\omega_j)^2 - \gamma_j \xi_n} \quad (2-14)$$

where C_{mw} = constant proportional to oscillator strength for Debye relaxation (dipole reorientation) at microwave frequencies. The value for this constant is equal to the change in dielectric susceptibility which occurs at the relaxation frequency, ω_{mw} . (Example in Appendix B)

C_j = constant proportional to oscillator strength for Lorentz electron dispersion in infrared through mid-ultraviolet frequencies.

ω_{mw}, ω_j = resonance (primary absorption) frequencies for microwave and infrared through mid-ultraviolet frequencies respectively (determined from measurements on the real frequency axis $\omega = \omega_n$)

The damping term $\gamma_j \xi_n$ will have a negligible contribution as bandwidths are always much less than absorption frequencies (Ninham and Parsegian, 1970b). At very high frequencies the dielectric dispersion has the limiting form

$$\epsilon(i\xi_n) = 1 + \frac{4\pi N e^2}{m \xi_n^2} \quad (2-15)$$

where e = electron charge
 m = mass of electron
 N = number of electrons per volume

For components with similar electron densities, the contribution from this frequency range will be negligible.

The general form given for the van der Waals attraction is mathematically complex and several simplifying assumptions are often made which yield a more tractable expression. Integration of the original equation with respect to D gives the corresponding van der Waals free energy of interaction per unit area (taking $E_v = 0$ at $D = \infty$).

$$E_v(D,T) = \left(\frac{kT}{8\pi D^2} \right) \sum_0^{\infty} I(\xi_n, D)$$

$$\text{and } I(\xi_n, D) = \left(\frac{2\xi_n D \epsilon_2^{1/2}}{c} \right)^2 \int_1^{\infty} p \left[\ln \left(1 - \Delta^2 \exp \left(\frac{-2p\xi_n D \epsilon_2^{1/2}}{c} \right) \right) \right. \\ \left. + \ln \left(1 - \Delta^2 \exp \left(\frac{-2p\xi_n D \epsilon_2^{1/2}}{c} \right) \right) \right] dp \quad (2-16)$$

$$\bar{\Delta} = \frac{s\epsilon_2 - p\epsilon_1}{s\epsilon_2 + p\epsilon_1} \quad \Delta = \frac{s - p}{s + p}$$

Here it is convenient to define a "Lifshitz-Hamaker function"

$$E_v(D,T) = \frac{-A(D,T)}{12\pi D^2}$$

$$\text{and } A(D,T) = 1.5kT \sum_0^{\infty} I(\xi_n, D) \quad (2-17)$$

where $A(D,T)$ = Lifshitz-Hamaker function

For the limiting case of $D \rightarrow 0$, "A" converges to

$$A(0,T) = 1.5kT \sum_0^{\infty} \int_0^{\infty} x \ln \left[1 - \left(\frac{\epsilon_2 - \epsilon_1}{\epsilon_2 + \epsilon_1} \right)^2 e^{-x} \right] dx \quad (2-18)$$

This expression is satisfactory for $D \leq 50 \text{ \AA}$.

Another limiting case is $T \rightarrow 0$. Even at zero temperature each solid body contains local electric fields of a wide range of frequencies. These originate from the spontaneous polarizations of the constituent molecules. (At $T > 0$ there are additional contributions from thermal excitations.) To evaluate the interaction energy at the limit $T \rightarrow 0$, kT is replaced by $h\xi$ and from the definition of ξ the Σ now becomes an integral yielding

$$A(0,0) = \frac{3h}{4\pi} \int_0^{\infty} \left\{ \frac{\epsilon_2 - \epsilon_1}{\epsilon_2 + \epsilon_1} \right\} \left\{ \frac{\epsilon_3 - \epsilon_1}{\epsilon_3 + \epsilon_1} \right\} d\xi \quad (2-19)$$

This expression holds for $kT \ll h\xi_n$. Parsegian and Ninham (1971) have performed calculations on a hydrocarbon/water system to demonstrate the effect of these two approximations. The neglect of temperature gave attractive energies which were much lower ($\approx 1/2$) than those calculated using the general formula (Equation 2-16). A comparison of $A(0,T)$ with $A(D,T)$ indicated that for separation distances less than $\approx 20 \text{ \AA}$, $A(0,T)$ will deviate from the actual value by no more than 10 percent. They also compared the contributions of the various frequency regimes to the total energy of interaction based on the exact formulation and found the contributions from the previously ignored microwave and infrared regimes to be significant (Figure 2-3). It is clear, however, from the expressions for van der Waals interaction, that this attractive force is dependent on the differences in dielectric susceptibility between the attracting substance and the separating medium. Only for those values of ξ_n for which there is a significant

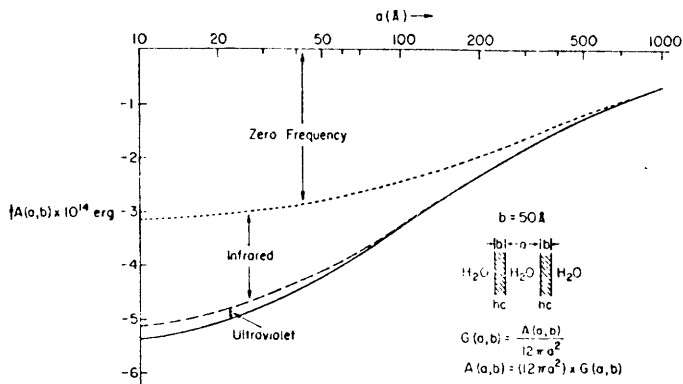


Figure 2-3 Frequency Ranges which Contribute to the van der Waals Interaction. The full energy coefficient (Equation 2-16) for two thin hydrocarbon layers separated by water (Ninham and Parsegian, 1970a) is broken into contributions from zero through microwave frequency fluctuations, infrared frequencies, and electromagnetic fluctuations in the ultraviolet. At all separation distances the low-frequency contribution is most important. The ultraviolet is always small and negligible after $a = 100 \text{ \AA}$. Infrared fluctuations are significant for $a < 500 \text{ \AA}$. ($a =$ separation distance)

difference between $\epsilon_1(i\xi_n)$ and $\epsilon_2(i\xi_n)$ will there be a major contribution to the overall attractive interaction.

The expression for the interaction of two spheres has been derived by Mitchell and Ninham (1972). It is equal in complexity to that for the interaction of two planar slabs. However, for two identical spherical particles with a separation distance that is small compared to the particle radius ($D/r \gg 1$), the expression reduces to

$$V_v = \frac{-A(0,T)r}{12 D} \quad (2-20)$$

which has the same geometric functionality as the Hamaker expression (Equation 2-9). Thus, for small separations, a single Lifshitz-Hamaker constant is necessary to determine the resulting van der Waals attraction.

A number of previous investigations have attempted to test the above theory by actually measuring van der Waals forces. In several of these studies, large gap widths were used (Derjaguin et al., 1956; Van Silfhout, 1966; Kitchener and Prosser, 1957), thus corresponding to the fully-retarded force region. For comparison with these experimental values, Gregory (1969) calculated van der Waals interaction constants using both the Hamaker and the Lifshitz expressions. The results, however, did not indicate that either expression was more accurate than the other, but, in fact, showed fair agreement for both expressions.

In the unretarded region, Tabor and Winterton (1969) succeeded in measuring the attraction between cleaved surfaces of mica in a

vacuum at separations as low as 50 Å. Their data were consistent with a Hamaker constant of $\approx 10^{-19}$ joules (10^{-12} ergs). Gregory calculated values from available dispersion data for mica and obtained a value of 1.13×10^{-19} joules using the Hamaker expression and a value about 20 percent lower using the Lifshitz expression. Here the approximation $A(0,0)$ was used, which could have produced inaccurate values.

For the case of a liquid separating the particles, little experimental data are available on the van der Waals attractive forces. Ninham and Parsegian (1970b) calculated Hamaker constants (actually functions) for a hydrocarbon/water system based on the Lifshitz expression and compared their values (5.5×10^{-14} to 7.1×10^{-14} ergs) to experimental values (Haydon and Taylor, 1969, 4.7×10^{-14} ergs; and Srivastava and Haydon, 1964, 1.6×10^{-13} ergs). Although no calculation was made based on the Hamaker expression, it is estimated to be similar to that calculated for ice/liquid methane ($\approx 3.5 \times 10^{-15}$ ergs), and is therefore an order of magnitude lower than the measured values. This indicates that the values obtained from the Lifshitz expression are, in general, more reliable, although in some cases both expressions will give similar values. Also, the peculiarities of the dispersion spectra for the present substances (i.e. the large permanent dipole of one component, ice, and zero dipole of the other, methane) suggest that the Hamaker expression will not give an appropriate estimate in this case.

In the present study, calculations of the Hamaker and Lifshitz-Hamaker constants were made for the interaction between two particles of ice in liquid methane and two particles of solid methanol in liquid

methane (Appendices B, C, and D). These two systems are thought to be representative of the present LNG gelant particles even though further studies have indicated that the solid particles are probably crystalline clathrates. The infrared spectrum for the water clathrates of structure I are very similar to ice (Bertie et al., 1973; Bertie and Whalley, 1964) as are the dielectric properties in the low frequency range (Gough and Davidson, 1973). Both methane and H₂O have identical ionization potentials, and thus the contribution from the ultraviolet frequencies is not likely to be significant. The interaction between two clathrate particles should, therefore, be very close to that of two pure solid particles.

In the calculations for ice particle interaction based on the macroscopic theory ($A(0,100\text{ K}) = 2.1 \times 10^{-14}$ ergs), the zero and microwave frequency terms were found to be quite important (Appendix D). Since the original Hamaker expression includes only the ultraviolet contribution, the resulting energy of interaction ($A = 3.5 \times 10^{-15}$ ergs) was an order of magnitude lower than that obtained by Lifshitz's formulation. The higher value is believed to be more accurate. Due to insufficient information on the properties of solid methanol, the constants for the methanol gelant particles could only be estimated ($2 \times 10^{-14} < A(0,100\text{ K}) < 10^{-15}$ ergs and $10^{-17} < A < 10^{-15}$ ergs).

2.1.2 Electrostatic Interactions

Many stable lyophobic colloids owe their stability to electrostatic repulsion between the particles. This occurs when the particles have net charges. In a sol of identical spherical particles, the particles will be similarly charged and tend to repel each other. In clays, where the particles may be platelike, the edges may appear to

have a charge opposite to the face, resulting in a face-to-edge attraction. According to van Olphen (1963) the particle charge may be created in two different ways. Imperfections within the interior of the crystal lattice may cause a net positive or negative lattice charge. This occurs in clays due to isomorphous replacement (such as Si^{+4} being replaced by Al^{+3}). However, van Olphen indicates that this mechanism of particle charge is comparatively rare in hydrophobic colloids. In the majority of lyophobic sols, the particle charge is created by the preferential adsorption of specific ions (referred to as "peptizing" ions) on the particle surface. This adsorption may be either chemical or physical. However, irrespective of the mechanism of formation, the net surface charge will be balanced by an equivalent ionic charge in the liquid immediately surrounding the particle. This combination of surface charge with compensating ions in the immediately surrounding liquid layers is referred to as the electrical double layer, and the resulting sol stability is due to double layer repulsion.

Neither of the above mentioned charge-creation mechanisms seems likely to exist in the LNG gels, as neither ice nor liquid methane is ionic. Liquid methane has an extremely low electrical conductivity ($\leq 10^{-17} \Omega^{-1} \text{cm}^{-1}$) (White, 1975) indicating that the concentration of ions is likely to be $\leq 3 \times 10^3$ ions/cm³ (calculations in Appendix E). The electrical conductivity of ice has been postulated to involve the ionization mechanism $\text{H}_2\text{O} \leftrightarrow \text{H}^+ + \text{OH}^-$ (discussion in Onsager, 1973) with ion concentrations of $\approx 10^5$ ions/cm³ (Appendix F). This, however, would still not account for a net surface charge unless either the positive

or negative ion predominated in the surface layer, or contaminating ions were incorporated into the ice lattice. Based on the conductivities and ionic concentrations, it was estimated that the surface potential (if it exists) is $\leq 6 \times 10^{-6}$ mvolt (Appendix F). This is an extremely low potential, and the associated double layer can therefore be described by the following expression (Verwey and Overbeek, 1948).

$$\sigma = \epsilon \epsilon_0 \kappa \phi_0 \quad \kappa = \frac{2z^2 F^2 c}{\epsilon \epsilon_0 RT} \quad (2-21)$$

where

- σ = surface charge density, equivalent to the integrated charge density in the solution phase
- ϵ = dielectric constant of medium
- ϵ_0 = dielectric permittivity of a vacuum
- F = Faraday's constant
- c = ion concentration
- z = ionic charge
- T = absolute temperature
- R = ideal gas law constant
- $1/\kappa$ = double layer thickness
- ϕ_0 = surface potential

The electrical repulsion between two spheres of equal surface potential (for small surface potentials and small κr) is (Verwey and Overbeek, 1948)

$$V_R = 4\pi \epsilon \epsilon_0 r^2 \phi_0^2 \alpha \frac{\exp(-\kappa D)}{2r + D} \quad (2-22)$$

where

- r = particle radius
- D = minimum distance between sphere surfaces
- α = numerical factor which varies between 0.6 and 1.0; depends on whether repulsive interaction is based on a constant surface potential (as in the case of peptizing ions) or on a constant

$$V_R = \begin{array}{l} \text{surface charge (inherent} \\ \text{lattice charge)} \\ \text{energy of repulsion} \end{array}$$

The repulsive energy calculated for two spherical particles, each with radius 5×10^{-6} cm, on close approach, 10^{-7} cm gap, was 2.0×10^{-26} ergs.

This is negligible compared to the corresponding van der Waals attractive energy. Also, it is considerably lower than the thermal energy of the particles, 1.38×10^{-14} ergs. The double layer repulsive force can therefore be neglected in determining the LNG gelant particle interactions.

2.1.3 Other Repulsive Interactions

Recent investigations (Napper and Netschey, 1971) have shown that another significant repulsive force is present in some lyophobic colloids. This is an entropic repulsion which occurs when macromolecules are adsorbed on the particle surface. Thermodynamically, there is a positive free energy associated with the interpenetration of the molecular chains as the particles approach one another. If the gain in free energy exceeds the van der Waals attractive energy the particles will remain separated, thus producing a stable sol. This, however, can only occur when macromolecules or polymers are available for adsorption onto the particle surface, and therefore does not pertain to the present LNG gels.

On close approach there is thought to be a short-range repulsion, to which van Olphen (1963) suggested two possible contributions. The first is a Born repulsion which occurs when protruding lattice regions

come into contact. The repulsion is due to the interpenetration of the electron shells of two atoms, thus resisting the interpenetration of the two lattices. The second short-range repulsion results from the adsorption forces between the crystal lattice and the molecules of the liquid medium. There may be one or two monomolecular layers of the liquid bound to the particle surface. For the interparticle distance to become less than the thickness of the two adsorbed layers, the liquid must be desorbed. The energy required for the desorption thus results in a short-range repulsive force. Also, if the liquid has a strong dipole, the adsorption may result in oriented dipoles which also tend to repel on close particle approach. To account for these short-range repulsive interactions, van Olphen suggests a dominant repulsive force beginning at ≈ 10 A as shown in Figure 2-4.

If the flocculated gelant particles in the LNG gels are separated by at least two monomolecular layers of adsorbed methane, the lattices will not be close enough to form bridging by hydrogen bonds, and van der Waals attraction will dominate. Calculation of this van der Waals attraction for ice particles of various sizes and separation distances yields the following results.

<u>D(A)</u>	<u>r(A)</u>	<u>V_v (ergs)</u>
10	100	1.8×10^{-14}
10	200	3.5×10^{-14}
10	500	8.8×10^{-14}
10	1000	1.8×10^{-13}
5	100	3.5×10^{-14}
5	200	7.0×10^{-14}
5	500	1.8×10^{-13}
5	1000	3.5×10^{-13}
1	100	1.8×10^{-13}
1	200	3.5×10^{-13}
1	500	8.8×10^{-13}
1	1000	1.8×10^{-12}

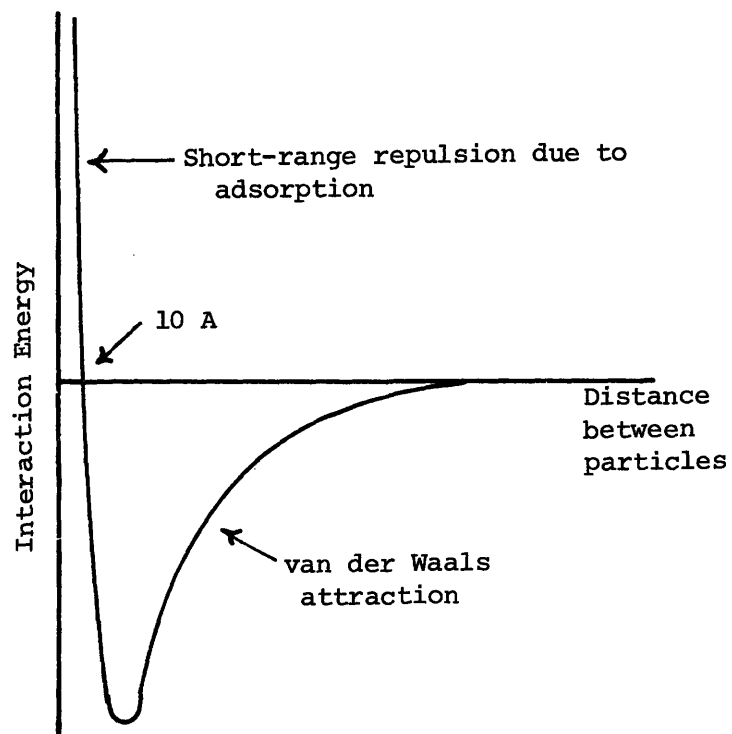


Figure 2-4 Particle-particle energies of interaction for the combination of van der Waals attraction and short-range repulsion.

If the particles are indeed separated by two liquid layers (i.e. $D \approx 10A$) the attractive energies will be fairly low, and a comparison with the thermal energy of the particles (1.4×10^{-14} ergs) indicates that the particle radius must be greater than $\approx 150 A$ (i.e. several kT) if flocculation is to occur. Later calculations based on rheological data (Chapter 4), however, suggest that the particle radius is between $100A$ and $200A$, and that flocculated particles are actually in contact. Such lattice contact between the particles allows for a combination of van der Waals attraction plus hydrogen bonding (bond energy = 3.5×10^{-13} ergs), thus producing a stronger attractive interaction. Although the expressions for van der Waals attractive energy have assumed separation distances of $\geq 50 A$, these expressions have also been applied to cases of adhesion ($D \approx 4A$) and were found to predict adhesion forces which were in fair agreement with measured values (Krupp, 1967; Visser, 1976).

2.2 Formation of Colloidal Particles

Colloidal size particles can be formed by two techniques -- either comminution of larger particles or a condensation sequence such as reaction/nucleation/particle growth. Several types of instruments such as colloid mills and micronizers exist for grinding larger particles, but the minimum average particle size attainable by such mechanical techniques is $\approx 1 \mu m$. This is at the upper size limit for colloidal particles, and in cases where smaller particles are desired, a condensa-

tion technique must be used.

For the production of a gel, it is desirable to have particles smaller than 1 μm . The rigidity (yield stress) of a gel depends on the number of particle/particle linkages per unit volume and the strength of this interparticle bond. For a given weight (or volume) percent gelant, the yield stress can be increased by reducing the size of the particle. Although two effects occur due to the decreased size - the van der Waals attractive force is reduced and the particle number concentration is increased, the latter effect will dominate and thus result in a higher yield stress. A smaller particle size will therefore reduce the amount of gelant necessary to produce the gel. Commercially available gelants range in size from 100 A diameter spherical particles (Cab-O-Sil, a product of Cabot Corporation) to 1400 A average size rods (Attagel, a product of Engelhard Minerals and Chemicals). Cab-O-Sil, chemically SiO_2 , is produced by a reaction/nucleation/particle growth process. It is sold commercially as a powder, and is commonly used to gel non-polar substances. Due to van der Waals attraction plus surface hydroxyls available for hydrogen bonding, a rigid gel can be obtained with approximately 2 volume percent. Daney and Rapial (1969) studied the gelation of liquid nitrogen and liquid hydrogen with Cab-O-Sil (diameter 700A). For a fairly rigid gel with a yield stress of 500 dynes/cm^2 , they found that liquid nitrogen required 6 wt. percent gelant while liquid hydrogen required 36.5 wt. percent. The density of Cab-O-Sil is 2.2 g/cm^3 which gives approximately 2 vol. percent for both gels. This is equivalent to $8.2 \times 10^9 \text{ particles/cm}^3$ Cab-O-Sil can also be used to gel liquid methane.

However, the required concentration would be ≈ 12 weight percent (2 volume percent), for a yield stress of 500 dynes/cm².

Although the primary factors influencing the yield stress are the bond strength and the particle concentration, the degree of dispersion will also have an effect. The degree of dispersion refers to the uniformity of the particle distribution throughout the liquid. If compact aggregates of particles are loosely flocculated to form the gel structure, the aggregate may act as a particle, and the aggregate/aggregate contacts thus define the gel structure (See figure 2-5). A more uniform chainlike structure is therefore desired for rigidity and requires a lower minimum concentration for gelation. Also, the more irregular in shape (deviation from spherical) the lower the required concentration (Van Ophen 1963).

2.3 Procedure for Gelling LNG

In the present study a condensation process was used to form small particles. A jet of natural gas vapor containing a small percentage of gelant, ≤ 2 mole % water of methanol, was discharged below the surface of the LNG. The contact of liquid and vapor produced rapid heat exchange, cooling the vapor from 0°C to -160°C, thus resulting in nucleation and particle growth in the vapor phase. (The nature of the solid particles formed is discussed in a subsequent section.) As the particles form, they diffuse to the vapor-liquid boundary. Assuming particle wetta-

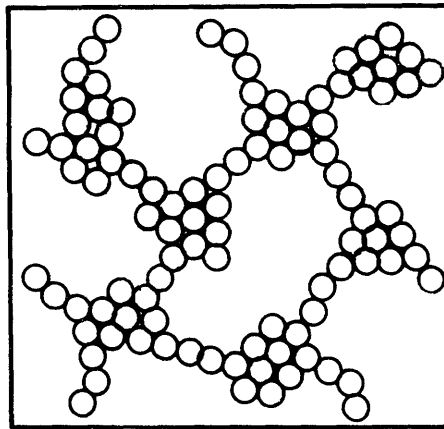


Figure 2-5 Compact particle aggregates with loose chain links--represents poor dispersion and a relatively weak network.

bility, those particles which come into contact with the liquid will likely be retained in the liquid phase. If part of the natural gas vapor also condenses (i.e. if ethane and propane are present, or the system is subcooled liquid methane) particles may also become entrained in this manner. Once a sufficient number of particles have been entrained by the liquid, the particles will begin to collide with each other producing flocculation. To form the gel, the process is continued until enough particles are present to form a semi-rigid network throughout the liquid (Figure 2-6).

The sequence of jet flow, heat transfer, nucleation and particle growth is quite difficult to characterize quantitatively due to the extreme temperature conditions and lack of accurate expressions for the separate processes. However, since these processes determine the final particle size, each will be discussed in more detail and rate estimates made when possible.

2.3.1 Jet Flow

The jet configuration, here, is vertical exiting downward into the LNG. Simple jets such as those of gas into gas have been well-characterized and discussed in detail by Abramovich (1963). If the present jet conditions of 0.16 cm diameter orifice and exit velocity of 60 m/s (at 273 K) were applied to a vapor jet exiting into quiescent methane gas at 110 K, the velocity and temperature profiles would be as

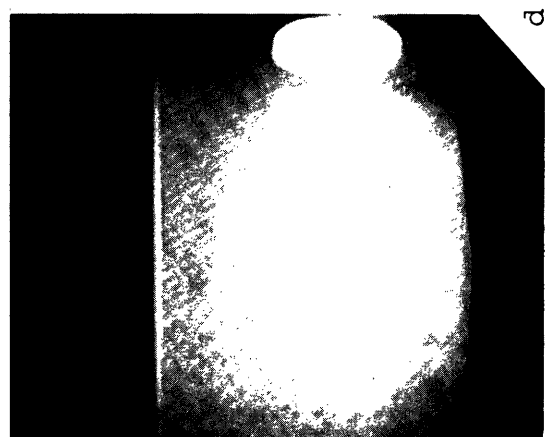
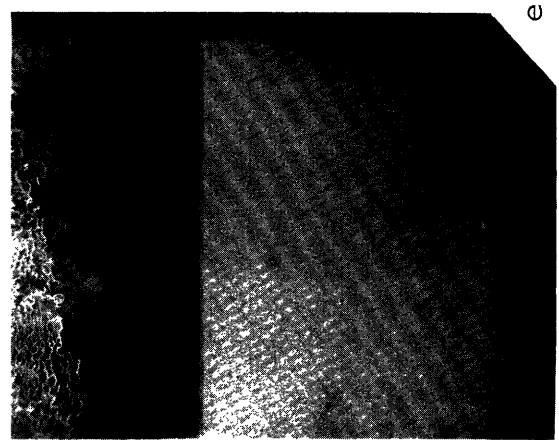
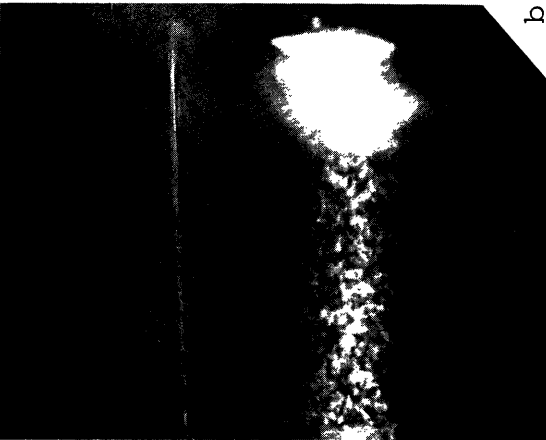
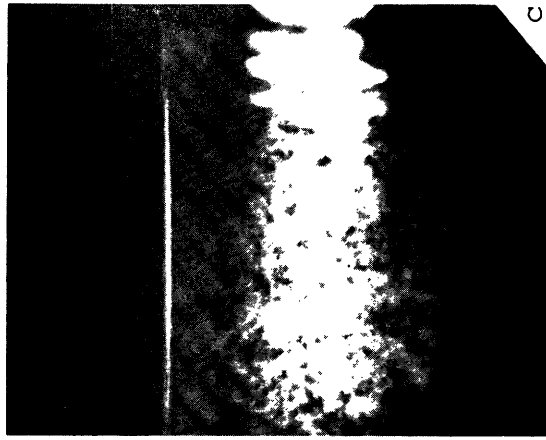


Figure 2-6 Formation of LNG/Methanol Gel

- a) Clear liquid CH_4 prior to gelation
- b) Observed flocculation after ≈ 2 min. of adding gelant, i.e. ≈ 0.1 g methanol in ≈ 100 g CH_4
- c) ≈ 0.2 g methanol in ≈ 100 g CH_4
- d) & e) ≈ 0.5 g methanol in ≈ 100 g CH_4

shown in Figure 2-7. The present system, however, appears quite different due to the buoyancy effect forcing the gas back up around the perimeter of the jet (Figures 2-8 and 2-9). The buoyancy effect has been treated analytically by Abramovich for the case of a gas exiting into a more dense gas. His resulting correlation indicates that the midpoint of the jet would reach zero velocity at 5 mm from the exit. This formulation, however, neglects the effect of the gas flowing in the opposite direction at the jet edge. Also, the most important factor, the rate of heat transfer, will depend on the amount of entrainment of drops of liquid methane within the jet. Kennedy and Collier (1974) measured significant liquid entrainment in a horizontal supersonic vapor jet of air discharging into water. Liquid entrainment began at the initiation of the jet boundary layer and increased along the length of the jet. Appropriate expressions for estimating the amount of entrained droplets and droplet size are not available for the present subsonic system, and experimental temperature measurements within the jet were, therefore, thought to give the best estimate of the temperature history of the gas stream. Using a thermocouple probe, the results indicated that the temperature decrease was extremely rapid. Within 2 mm from the exit, the temperature was that of the surrounding methane. This is equivalent to a drop in temperature of 160 K within 0.1 ms.

2.3.2 Condensation by Nucleation and Particle Growth

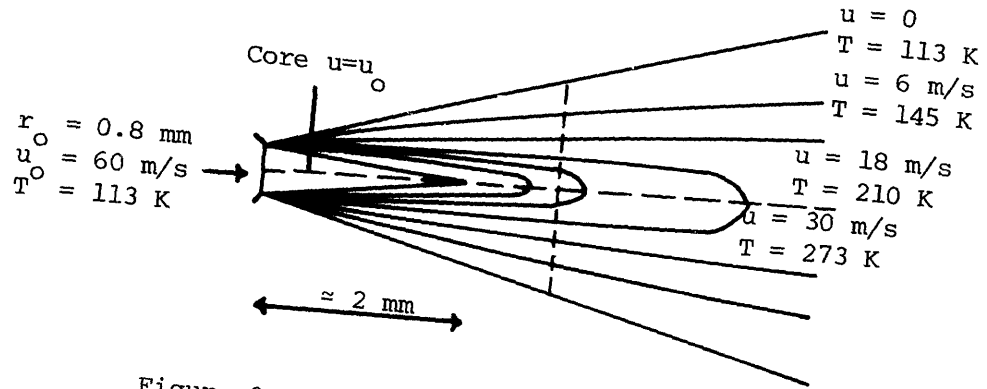


Figure 2-7 Constant velocity profile for gas jet into quiescent methane at 113 K.

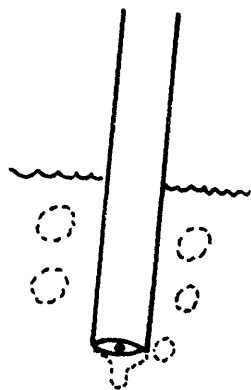


Figure 2-8 Appearance of vapor jet during the gelation of LNG (see also Figure 2-9).

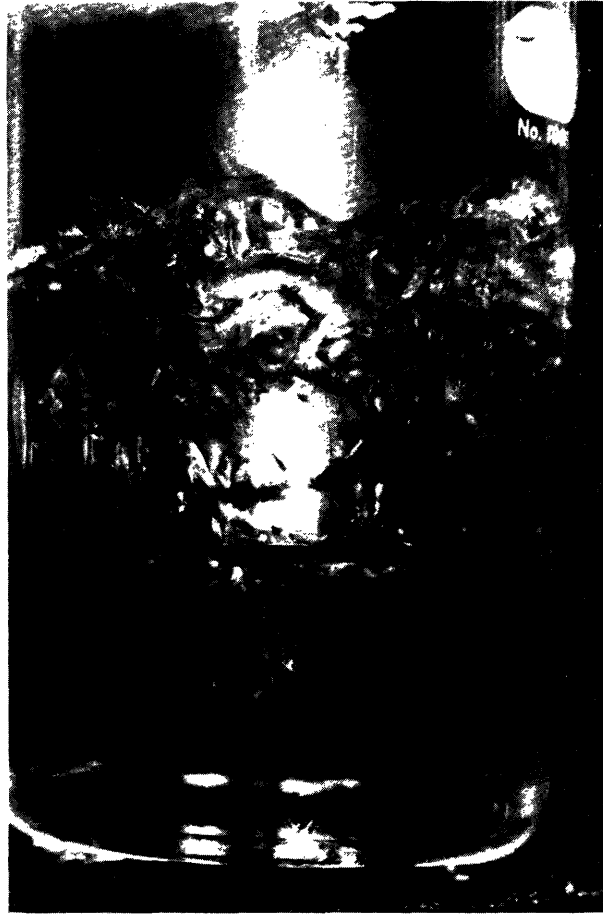
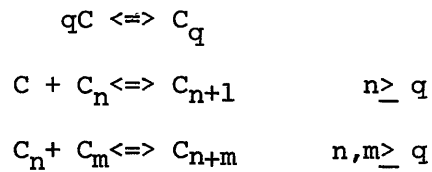


Figure 2-9 Natural gas jetting into LNG. During gelation, the natural gas vapor stream shown will also contain a small percentage of vaporized gelant.

Nucleation and particle growth can be described by a sequence of reactions as follows.



The first reaction is considered the nucleation reaction in which several molecules are converted into a stable product (i.e. one which will grow). C_q is referred to as the critical size nucleus, indicating that it is as likely to grow as to decay. Particles smaller than C_q tend to revert to the molecular species of C. The reaction C with any particle C_n ($n \geq q$) represents a condensation step, i.e. one which leads to particle growth without changing the number of particles. The third reaction depicts coalescence of two particles. This differs from coagulation as previously defined (although many authors use this term to describe coalescence). In coagulation (or flocculation) the particles are united at point contacts and the total surface area of the aggregate is essentially the sum of the individual particle surface areas. Whereas, in coalescence, there is a broad area of contact and the two particles fuse together. (It is possible that the reaction is not as simple as defined in the equation. Flocculation may occur initially with further condensation onto the aggregate resulting in a fusion of the original two particles.) The mechanism of coalescence of solid particles has apparently not been fully described in previous literature.

The basis for the existence of a critical-size cluster necessary for spontaneous growth has been developed from thermodynamics. The

traditional approach considered the free energy of forming an embryo or cluster, the critical size corresponding to the maximum in the free energy versus cluster radius curve. However, for such an isothermal system with varying pressure, the appropriate thermodynamic function is availability, α , which is a minimum function for stable equilibrium.

(2-23)

$$\alpha = U - T_0 S + P_0 V$$

where

U = specific internal energy at T_0, P_0 .

S = specific entropy at T_0, P_0 .

V = specific volume at T_0, P_0 .

T_0 = absolute temperature.

P_0 = pressure.

Prior to embryo formation the system will be homogeneous with N_i^α moles of the α phase.

(2-24)

$$a_i = N_i^\alpha (U^\alpha - T_0 S^\alpha + P_0 V^\alpha)$$

α = superscript representing α phase.

i = subscript representing initial condition.

When N^β moles form an embryo of a new phase β , the total availability of this new system must include three components, the availabilities for the remaining α phase, and the new β phase, and the surface phase.

(2-25)

$$\alpha_f = (N_i^\alpha - N^\beta) (U^\alpha - T_0 S^\alpha + P_0 V^\alpha) + N^\beta (U^\beta - T_0 S^\beta + P_0 V^\beta) + \underline{U}^s - T_0 \underline{S}^s$$

where s = superscript representing surface phase.

\underline{U} = total internal energy

\underline{S} = total entropy.

Using Euler's equations for U^α , U^β , \underline{U}^S

$$U^\alpha = T_o S^\alpha - P_o V^\alpha + \mu^\alpha \quad (2-26)$$

$$U^\beta = T_o S^\beta - P^\beta V^\beta + \mu^\beta$$

$$\underline{U}^S = T_o S^S + \sigma S$$

where σ = specific surface free energy of the interface between the embryo and phase.

and assuming a spherical embryo, the change in availability becomes

(2-27)

$$\Delta\alpha = N^\beta (\mu^\beta - \mu^\alpha) + (P_o - P^\beta) (4/3) \pi r^3 + 4\pi\sigma r^2$$

where

r = radius of embryo.

μ^α = chemical potential of phase α at P_o , T_o .

μ^β = chemical potential of phase β at P^β , T_o .

The equilibrium criterion for varying r at constant mass $\{[\partial(\Delta\alpha)/\partial r]_{N^\beta}\}$ yields the familiar Laplace equation (See Appendix G for derivation)

(2-28)

$$r = 2\sigma / (P^\beta - P_o)$$

Further, if the embryo has reached its equilibrium size, the two chemical potentials can be shown to be equal.

(2-29)

$$\mu^\beta(T_o, P^\beta) = \mu^\alpha(T_o, P_o)$$

For a single component system at T_o , there exists an equilibrium pressure such that

$$(2-30)$$

$$\mu^\beta(T_o, P_{eq}) = \mu^\alpha(T_o, P_{eq})$$

Since $d\mu = VdP$, subtracting equation (2-30) from (2-29) yields

$$(2-31)$$

$$\int_{P_{eq}}^{P^\beta} V^\beta dP = \int_{P_{eq}}^{P_o} V^\alpha dP$$

For a supersaturated ideal vapor at T_o, P_o , and an incompressible phase

$$(2-32)$$

$$V^\beta(P^\beta - P_{eq}) = RT_o \ln(P_o/P_{eq})$$

$$(P^\beta - P_o) = [(RT_o/V^\beta) \ln(P_o/P_{eq})] - (P_o - P_{eq})$$

The second term on the right hand side is usually negligible. Thus,

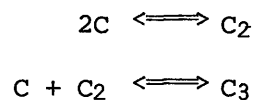
$$(2-33)$$

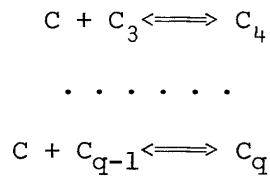
$$r = 2\sigma/(P^\beta - P_o) = (2\sigma V^\beta/RT_o)/\ln(P_o/P_{eq})$$

Which is equivalent to the expression derived on the basis of free energy.

2.3.2.a Nucleation

The nucleation reaction can be broken down into the following sequence of reactions.





Clusters C_i ($i < q$) are termed embryos and are more likely to vaporize than to grow. The process of nucleation may be described as follows. The vapor phase is in a state of constant transformation, embryos rapidly growing and decaying. At any given instant there will be embryos of many sizes present. Frenkel (1939) derived an expression for the equilibrium concentration of an embryo of i molecules assuming the number of embryos of all sizes to be very much smaller than the number of atoms of the unassociated molecules and also assuming ideal mixing

(2-34)

$$\frac{N_V^R}{N_V^0} = \exp(-\Delta G^R/kT)$$

where R = size of embryo of i molecules

N_V^R = number of embryos of size R
per unit volume

N_V^0 = number of unassociated molecules per unit volume.

The free energy change should, more accurately, be the change in availability, but the resulting expression is equivalent for the critical size embryo.

(2-35)

$$\Delta G^* = \Delta a^* = \frac{16\pi\sigma^3 (V_m^0)^2}{3[RT \ln(p/p_{eq})]^2}$$

* = superscript representing critical size.
 V_m^β = molar volume of β phase.

The concentration of critical nuclei N_V^* will be

(2-36)

$$(N_V^*/N_V^0) = \exp(-\Delta G^*/kT)$$

Expressions for estimating nucleation rates are based on the above sequence of reactions. A variety of assumptions, however, can be made as to which steps in the sequence are fast, slow, at equilibrium, etc. and thus a number of expressions have been proposed. The original formulation for nucleation rates was proposed by Volmer and Weber (1926). It was based on three assumptions. First, all steps in the reaction sequence are fast except $C_n + C \rightleftharpoons C_{n+1}$, and the concentration of critical nuclei is therefore characteristic of equilibrium. Second, the backflux of supercritical nuclei can be neglected. Third, the rate can be appropriately defined using gas kinetic theory. With these assumptions, the rate of nucleation becomes

(2-37)

$$J = v_C A^* N_V^* \quad v_C = P / (2\pi m k T)^{\frac{1}{2}}$$

where v_C = collision frequency of single molecules with nuclei per unit area of the nuclei.

A^* = surface area of critical nuclei.

m = molecular mass.

J = rate of formation of nuclei per unit volume.

P = partial pressure of nucleating species.

For spherical nuclei

(2-38)

$$J = \frac{4\pi R^* N_V^0 P}{(2\pi mkT)^{\frac{1}{2}}} \exp(-\Delta G^*/kT)$$

Later Becker and Doring (1935) removed the assumption of no backflux, deriving an expression for the net rate of growth of clusters to critical size. The mathematics were further simplified by Zeldovich (1942) to give the following expression

(2-39)

$$J = \frac{v N_V^0 P}{kT} \left(\frac{6\sigma}{m\pi} \right)^{\frac{1}{2}} \exp(-\Delta G^*/kT)$$

v = molecular volume in embryo

A number of previous investigators (katz and Ostermeier, 1967; Katz, 1970; Heist and Riess, 1973) have used a diffusion cloud-chamber technique to determine critical supersaturations (assumed to be the supersaturation corresponding to a nucleation rate of 1 to 100 nuclei/cm³s) for various compounds including water and methanol. Their results were in good agreement with the values predicted from this so-called classical (Becker-Doring) theory. Jaeger et al. (1969) have also studied the homogeneous nucleation of H₂O using a different experimental technique (a supersonic nozzle) and found good agreement with the classical theory.

Other modifications of the nucleation theory have been proposed (Frenkel, 1955; Goodrich, 1964; Courtney, 1962) all of which yield lower nucleation rates and generally require computer solutions. In

general, very little experimental work has been done in which nucleation rates were measured-- most experiments have measured only critical supersaturations. However, Allen and Kassner (1969) reported data for water nucleation from both an argon and a helium atmosphere. Comparison of their data with nucleation theory indicated that the Becker-Doring theory was not satisfactory. At supersaturations ≥ 5 , the model predicts nucleation rates which are orders of magnitude higher than those observed. Thus, it is very difficult to obtain accurate estimates for nucleation rates, but the Becker-Doring relation may be used to obtain an upper limit when dealing with high supersaturations. It will later be shown that the rate of nucleation in the present gelation process has a negligible effect on the final particle size.

2.3.2.b Particle Growth

For small clusters ($r < 10^{-5}$ cm) or individual molecules in a vapor phase, the gas kinetic theory gives a collision frequency of

(2-40)

$$Z_{12} = [8\pi kT(m_1+m_2)/m_1m_2]^{\frac{1}{2}}(r_1+r_2)^2 C_1C_2$$

where m_1, m_2 = mass of clusters 1 and 2
respectively.
 r_1, r_2 = radius of clusters 1 and 2.
 C_1, C_2 = #concentration of clusters
1 and 2.

Z_{12} = collision rate, #collisions/cm³s

If each collision results in a fusion between the two colliding species, this expression can be used as is to describe condensation and coalescence. However, if only a fraction of the collisions are successful, the collision frequency must be multiplied by this fraction to obtain the desired rates for particle growth. For solid particles (less than 10⁻⁵cm) experimental data indicate that this coefficient will be close to unity (Pound, 1972).

Larger particles ($r \geq 10^{-5}$ cm) will be affected by viscosity, and Stokes Law must be used to determine the rate at which the two species collide. This relation has been developed by von Smoluchoski(1916).

(2-41)

$$Z_{12} = \frac{8kT}{3\eta} C_1 C_2$$

where η = viscosity of surrounding fluid.

2.3.2.c Application to Present Condensation Process

The condensation process in the present study is unusual in that the temperature change is particularly large (160K) and the estimated supersaturation (Appendix H) is extremely high (7x10¹⁵). The existence of such a high supersaturation, however, is highly questionable. Certainly from a physical standpoint, one could argue that an absolute maximum superaturation must exist, as the size of the nucleus decreases with increasing supersaturation. Once this nuclei size approaches the

size of a single molecule, supersaturation can no longer exist, as even unassociated molecules will be stable species. This concept of a maximum supersaturation has been previously suggested by Scherbakov et al. (1961) based on free energy considerations. They further derived an expression for this maximum supersaturation based on the following criteria.

First, as the nucleus becomes smaller and smaller, the actual interfacial tension will be less than the bulk surface tension. Second, as supersaturation increases, the nucleus will eventually become so small that the free energy of formation of the nucleus will be zero.

The resulting expression:

(2-42)

$$(\rho/M)^{2/3} (T/\sigma_\infty) \log(S^{**}) = B$$

where σ_∞ = bulk surface tension.

S^{**} = maximum supersaturation
(p/p_{eq})

ρ = density of nucleating phase.

M = molecular weight of nucleating phase.

T = absolute temperature

B = constant ranging from .45 to 165 (based on experimental data)

The derivation of this relation required the following proportionality,

(2-43)

$$\sigma = \sigma_\infty \Psi(r/r_0)$$

where r_0 = radius at which surface tension goes to zero.

Ψ = function of r/r_0 .

with $\Psi(r^{**}/r_0)$ a universal constant.

r^{**} = radius of nuclei corresponding to S^{**} .

Several different relations have been suggested for the functionality of σ (Scherbakov, 1958; Kirkwood and Buff, 1949) the most common one being

(2-44)

$$\sigma = \sigma_{\infty}(1 - 2/\delta r)$$

where $1/\delta$ = coefficient ranging from 0.2×10^{-7} to 0.5×10^{-7} cm.

This does not, however, fit the expected criterion -- $\lim_{r \rightarrow 0} \sigma = 0$, but such an expression is meaningless for any radius less than that of the individual molecule, and should only be used when $r > r_0$.

Experimental data on maximum supersaturations were reported by Bykov and Teverovskii (1949). Scherbakov et al. (1961) used these data to calculate the value for the constant B which was found to vary from .45 (water) to .65 (glycerine). Although not precisely constant, this is close enough to give appropriate order of magnitude estimates of absolute maximum supersaturation for the present water and methanol nucleating systems. Here Scherbakov's expression yields maximum supersaturation values of $S_{H_2O}^{**} = 12$ and $S_{CH_3OH}^{**} = 4$ respectively. During the cooling history of the natural gas/gelant vapor, nucleation and particle growth may occur until this maximum supersaturation is reached. At this point, there is no longer a slow nucleation step, i.e. all species will spontaneously grow and the processes controlling the final particle size

will then be only condensation and coalescence.

To estimate the final particle size for the present systems, it was assumed that the temperature change of the natural gas/gelant vapor was linear over a time interval of 10^{-4} sec. Appropriate nucleation and particle growth rates are given in Appendix I. The calculations show that the maximum supersaturation is reached after $\approx 10^{-5}$ sec, and a negligible number of nuclei have formed at this time. As the vapor cools further and condensation and coalescence occur, the final particle size can be estimated by assuming that particle growth occurs only in the vapor phase and the average residence time is 100ms. This results in an estimated particle size of $\leq 1000\text{\AA}$ (Appendix J). Calculations based on the gel yield stress (See Chapter 4) indicate that the particle size is closer to $r = 150\text{\AA}$. This suggests that the average residence time in the vapor is $\approx 10^{-4}$ sec or evaporation rates are significant. Evaporation rates are generally included in the accommodation coefficient (fraction of successful collisions), and, in this case, the result suggests that the coefficient may be much less than unity.

2.4. Further Considerations on the Nature of the Gelant Particles

The solid gelant particles are formed at approximately atmospheric pressure within the temperature range of 273 to 113 K. In the case of H_2O as gelant, this temperature range not only covers a region in which ice is stable, it also includes a lower temperature region in which a

natural gas/water clathrate is stable. Clathrates may be considered solid solutions in which a cage-like-host structure is formed by hydrogen bonding of the water molecules. This host lattice, which by itself is unstable, becomes stabilized by the inclusion of the second component, methane, ethane, or propane in this case. A typical clathrate cage is the pentagonal dodecahedron shown in Figure 2-10. (Further discussion of clathrate structures is given in Chapter 3).

Such clathrate compounds are most commonly formed at high pressures and moderate temperatures. In particular, the natural gas hydrates (clathrates in which the host lattice is constructed of water molecules) were found to clog natural gas pipelines and much attention was subsequently directed towards predicting such formation conditions (Carson and Katz, 1941; Katz, 1945; Nagata and Kobayashi, 1966), as well as methods for alleviating the problem (Hammerschmidt, 1936; Piëroen, 1955). However, natural gas is also known to form clathrates at low temperatures and a substantial amount of equilibrium data are presently available covering a wide range of temperature and pressure. The phase equilibrium diagrams for the natural gas components--methane, ethane, and propane -- with water are given in Figures 2-11, 2-12, and 2-13. The lines designate 3-phase equilibrium, and by the phase rule allow one degree of freedom. When the critical temperature of the solute is above room temperature (as in ethane and propane), the 3-phase line, HL_2G (hydrate-liquid hydrocarbon-gas) is intersected by the 3-phase line HL_1G (hydrate-water-gas), representing an invariant point of 4-phase equilibrium. This intersection point also represents the temperature above which no hydrate

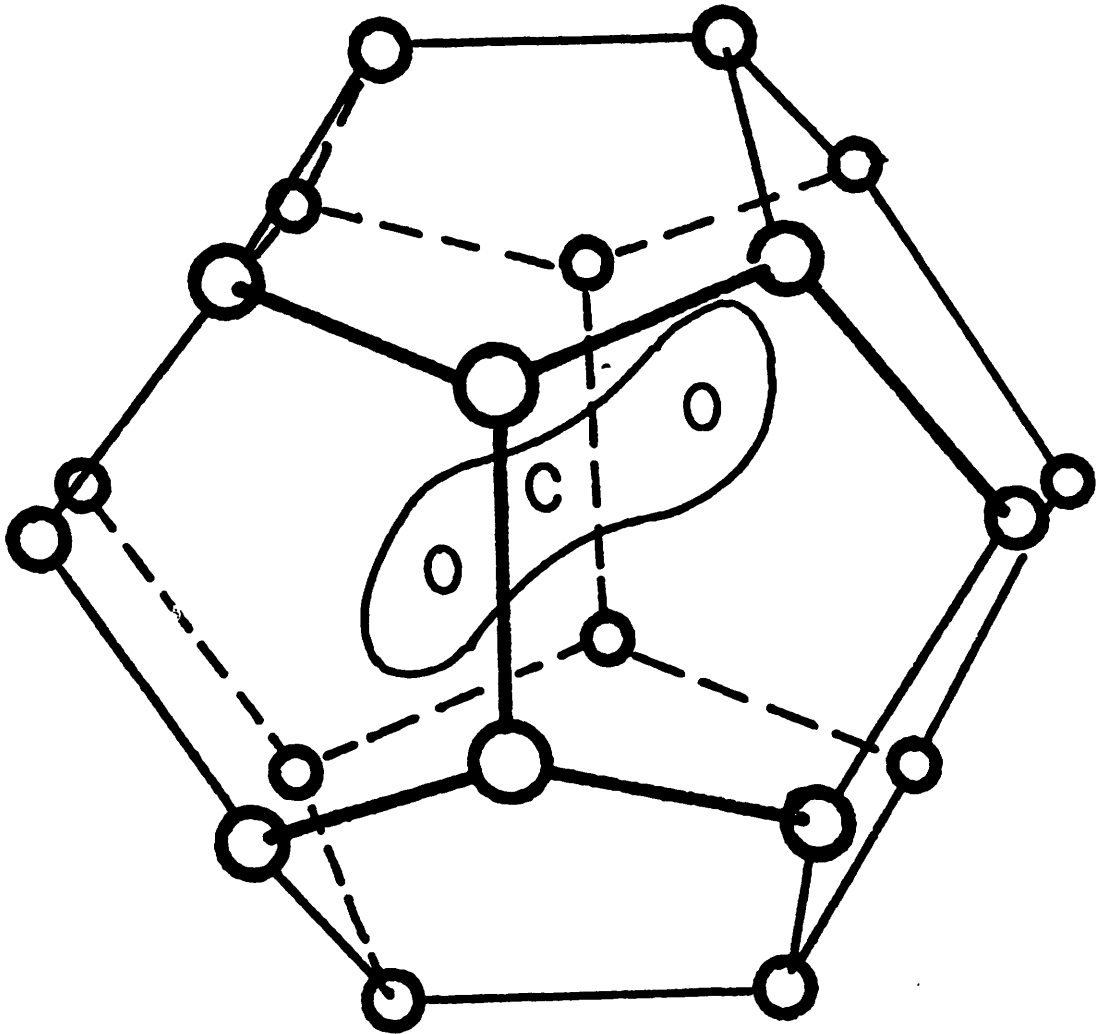
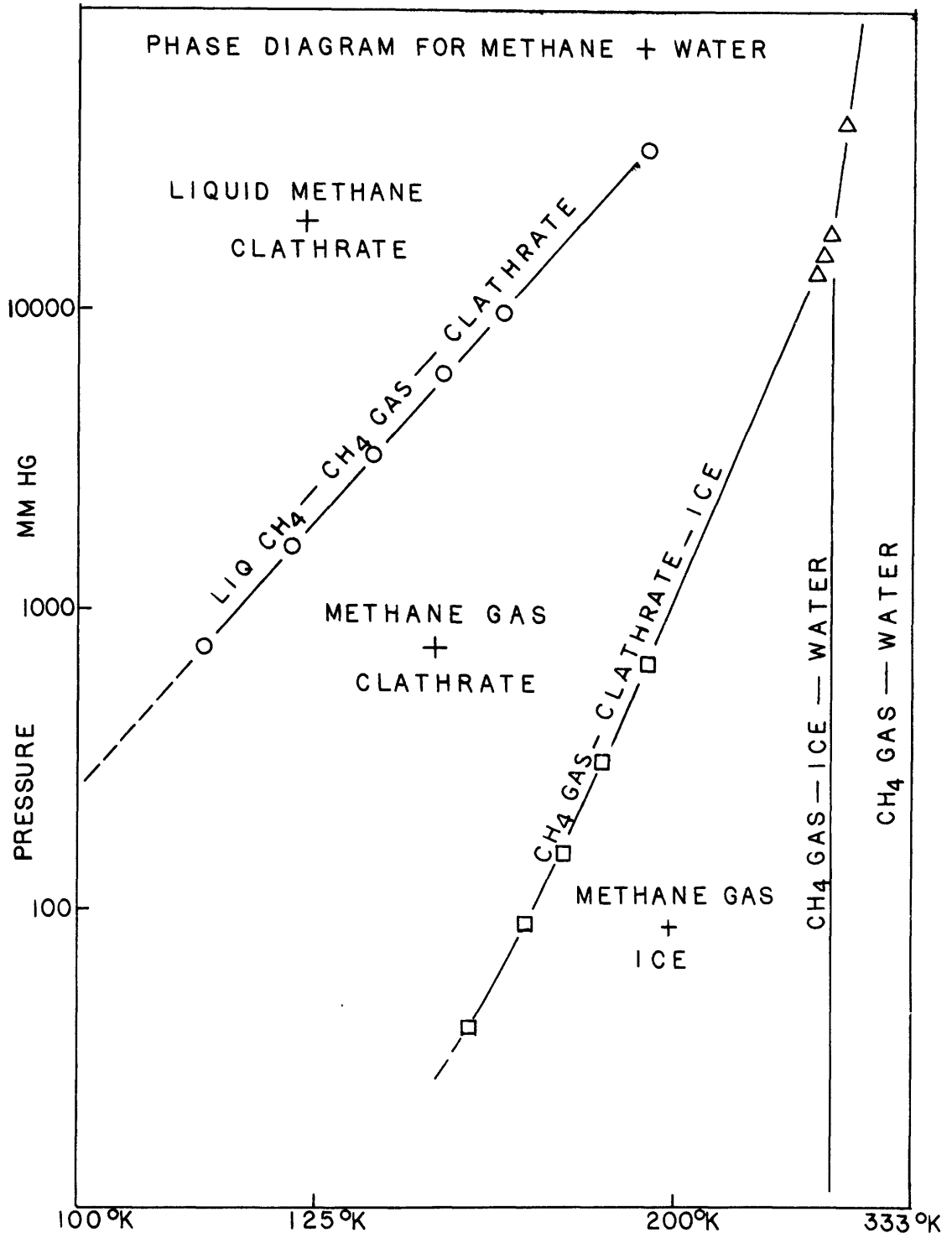


Figure 2-10 Carbon Dioxide molecule encaged in a pentagonal dodecahedron formed by hydrogen bonding of the water molecules. Oxygen atoms are represented by O's. Hydrogens lie along pentagon edges.

Figure 2-11



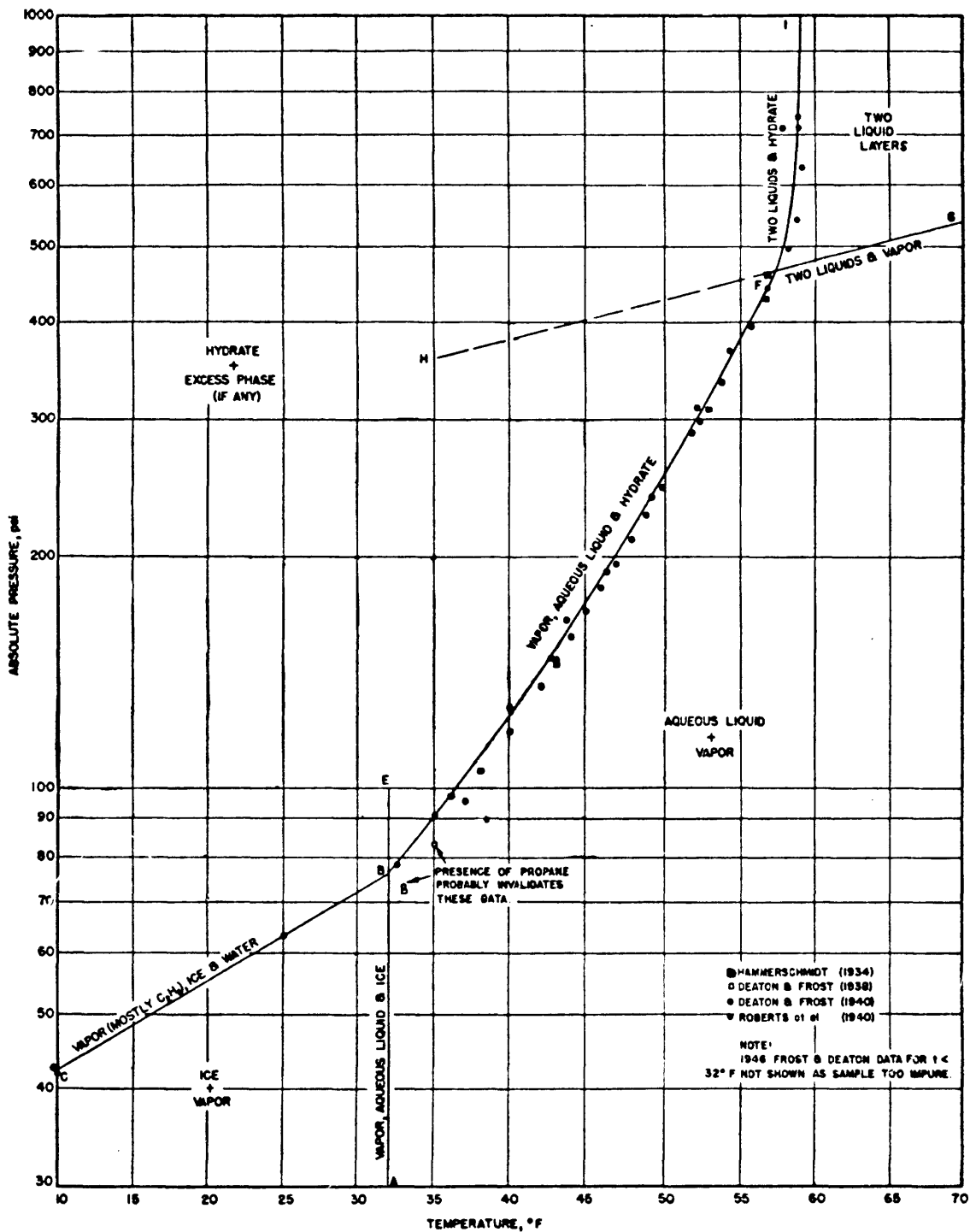


Figure 2-12 Phase Diagram for Ethane + Water

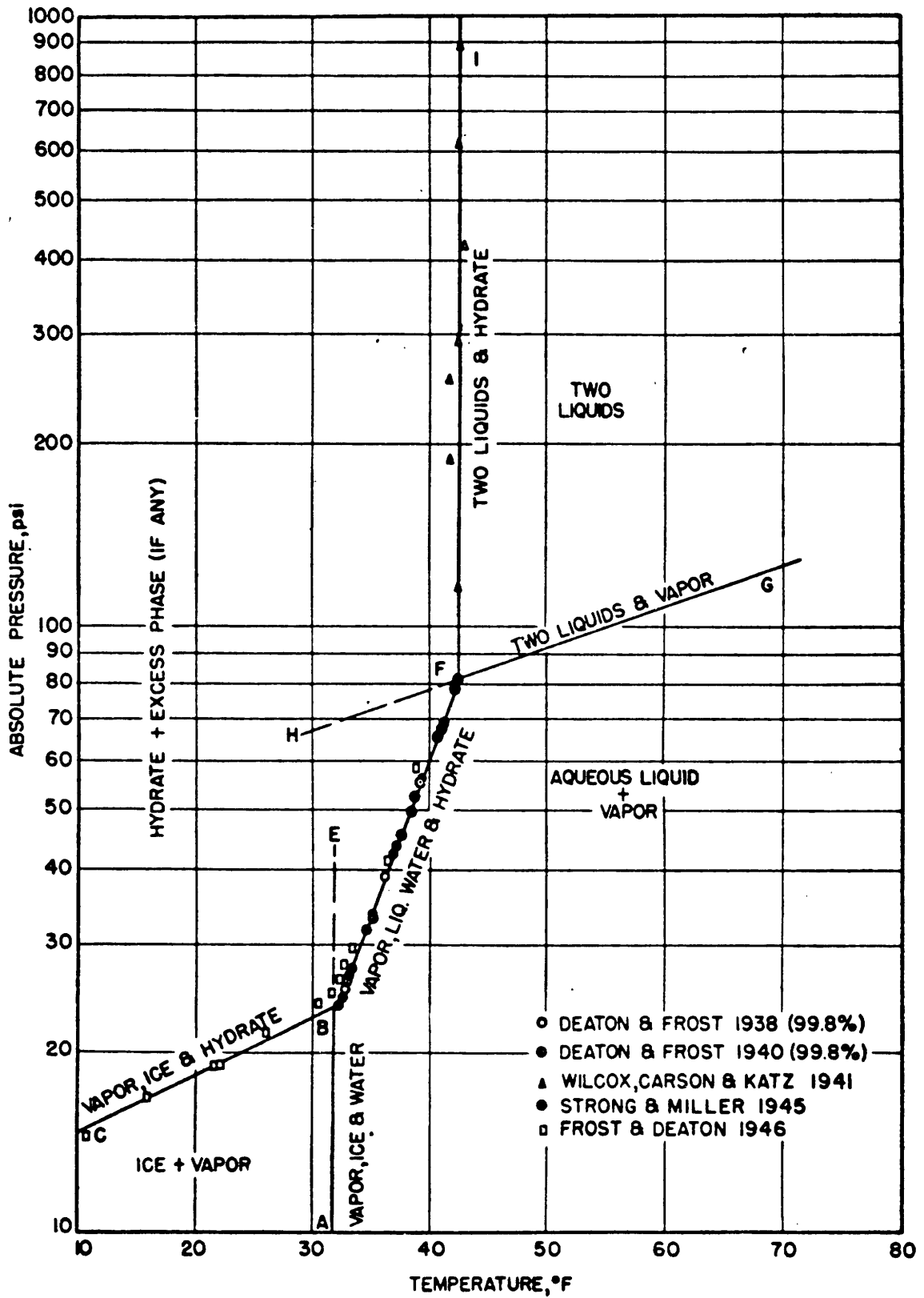


Figure 2-13 Phase Diagram for Propane + Water

exists. Here, van der Waals and Platteeuw (1959) argue that the line HL_1L_2 is very steep because the volume change accompanying the formation of the hydrate from the two liquids is quite small. They do, however, recognize the possibility that ΔV could be negative and the line would then extend to temperatures higher than this quadruple point. On the other hand, if the critical temperature of the solute is below room temperature, there is no restricting temperature above which the hydrate cannot exist. The 3-phase equilibrium lines representing hydrate stability, HIG (hydrate-ice-gas), HL_1G , and HL_1L_2 are often referred to as the loci of clathrate decomposition points. Here decomposition refers to clathrate conversion to ice and gas, water and gas, or water and hydrocarbon liquid respectively.

The phase diagram shown in Figure 2-11 represents a system in which Methane (the encaged species) is in excess. For a system with H_2O in excess, the vapor-liquid equilibrium line for the guest species will not be present, and the water-ice equilibrium will extend upward defining a region (to the left of this line) in which hydrate and ice coexist.

Van der Waals and Platteeuw (1959) have successfully described the phase behavior of clathrates on the basis of a solution theory with the following assumptions. 1) The contribution of the solute molecules to the free energy is independent of the mode of occupation of the cavities. This excludes clathrates in which the encaged molecule is large enough to distort the host lattice. 2) The encaged molecules are localized in the cavities and a cavity can never hold more than one solute molecule.

3) The mutual interaction of the solute molecules is neglected. Partition functions were used to derive the composition and chemical potential of solvent in the clathrate phase, assuming that the vapors of the solutes behave as ideal gases. The following expressions were obtained.

(2-45)

$$P_K = (1/C_{Ki}) [y_{Ki}/(1 - Y_i)]$$

(2-46)

$$\text{and } \Delta\mu = [\mu^\beta - \mu^\alpha]_{T,P} = -kT \sum_i v_i \ln(1 - Y_i)$$

where K = guest species

P_K = partial pressure of species K (if not ideal gas must be fugacity)

v_i = ratio of the number of cells of type i to the number of water molecules

Y_i = probability that a type i cell is occupied. $= \sum_j y_{ji}$ where j includes all species available for filling a type i cage

y_{ji} = probability that a type i cell is occupied with species j

μ = chemical potential of solvent (superscript designates phase)

α = pure solid phase

β = empty clathrate lattice

The expression for partial pressure is analogous to a Langmuir isotherm and the Langmuir constants are given as

(2-47)

$$C_{Ki} = (1/kT) \int_{V_{cell}} \exp(-U_K/kT) dV$$

This expression assumes that the internal degrees of freedom of the entrapped guest molecule are the same as those in the gas phase. The integral represents the configurational contribution of the guest-host interaction and is referred to as the free volume integral.

Evaluation of these expressions requires that the clathrate structure be known. To date, several different water clathrate structures have been identified, and a number of these have been completely characterized by x-ray diffraction. A common structure (referred to as structure I and discussed in more detail in Chapter 3) occurs when the guest species is small (molecular radius < 2.8 Å, which includes methane and ethane) and was found to consist of two different cages, a pentagonal dodecahedron and a hexakaidecahedron. This particular structure will be considered in the subsequent discussion.

In this study the most important 3-phase equilibrium curve is that of the pure solid-clathrate-gas equilibrium. Here the chemical potential of the host former in the clathrate phase, μ , must equal that of the pure solid, μ^α . The region on the phase diagram above this line therefore represents $\mu < \mu^\alpha$, and from Equation 2-46 it follows that

$$\Delta\mu = \mu^\beta - \mu^\alpha < -kT \sum_i v_i (1 - Y_i) \quad (2-48)$$

To estimate dissociation pressures, the interaction potential and the chemical potential difference, $\Delta\mu$, must be known. Tester et al. (1972) studied a variety of gas hydrates, and for $\Delta\mu$ they assumed that the molar volume difference between the empty lattice (β) and ice, Δv , was independent of pressure.

$$\Delta\mu(273\text{K},P) = \Delta\mu(273\text{K},P=0) + \Delta v(P)$$

Here Δv can be determined from knowledge of the structure and density of the two phases. Von Stackelberg and Muller (1954) give a value of $3.0 \text{ cm}^3/\text{mole}$ for the structure I hydrate. To evaluate the total guest-host interaction potential, two different techniques have been used. In both cases the Lennard-Jones 6-12 potential was used for the individual interaction between the guest and each host molecule. Van der Waals and Platteeuw (1959) then used a Lennard-Jones and Devonshire summation for the total interaction, which assumed the cage molecules to be evenly distributed over the surface of a sphere. In contrast, Tester, et al. (1972) used the known positions of the host molecules in the cage structure, and the total interaction was taken as the sum of the individual interactions of the guest with each host molecule. A Monte Carlo technique was then used to vary the position and orientation of the guest molecule to obtain an ensemble average. Calculated values from both studies are given in Table 2-1 and compared with experimentally determined dissociation pressures. For non-spherically symmetric guests Tester et al. (1972) also used a Kihara potential which gave quite satisfactory results.

When the gas phase consists of more than one component, the equilibrium becomes more complex. For two species such as methane and propane which form different clathrate structures, either a clathrate of one structure only may occur (i.e. $\text{CH}_4 + \text{H}_2\text{O}$ and $\text{C}_3\text{H}_8 + \text{H}_2\text{O}$ form a solid solution referred to as a mixed hydrate) or both structures

Table 2-1 Dissociation Pressures
for Gas Hydrates at 273°K

<u>Guest</u>	<u>Observed Fugacity (bars)</u>	<u>Calculated Fugacity (L-J-D) [☒] (bars)</u>	<u>Calculated Fugacity (Monte Carlo) [☑] (bars)</u>
Argon	97.0 ^Δ	95.5	97.0
Krypton	14.2 ^Δ	15.4	13.3
Xenon	1.45 ^O	1.0	.83
Methane	24.8 [☐]	19.0	24.3*
Ethane	5.2 ^Δ	1.1	
Carbon Dioxide	12.6 [#]		12.9*
			12.4**
Nitrogen	157.5 [≠]	90	46.0
			161.9**
Oxygen	111.9 ^{☐≠}	63	60.9
			103.9**

☒ Vander Waals and Platteuw (1959)

☑ Tester, et al. (1972)

Δ Barrer and Edge (1967) and von Stackelberg and Muller (1954) (Note-ethane data found only in von Stackelburg & Muller)

O Parrish and Prausnitz (1972)

☐ Saito, et al. (1964)

≠ van Cleeff and Diepen (1965)

Unruh and Katz (1949)

* spherically symmetric Kihara Potential

** non-spherically symmetric Kihara Potential

may occur simultaneously. Van der Waals and Platteeuw investigated the methane-propane system and found regions of stability for both of these cases (Figure 2-13). The curves drawn in this figure represent the calculated values and fit the experimental results quite well.

A number of investigators (Wilcox, Carson & Katz, 1941; Carson & Katz, 1941; Hammerschmidt, 1934) considered the compositions of such mixed hydrates and experimentally determined that the less volatile component had a greater mole fraction (relative to the total number of guest molecules) in the clathrate phase than in the gas phase. Also dissociation pressures were determined for such mixtures and found to decrease with the addition of a less volatile component (Deaton & Frost, 1937; Wilcox, Carson, and Katz, 1941). Holder and Hand (1977) recently studied the multiple phase equilibria for mixtures of methane, ethane, propane, and water at temperatures above 0° C. Although the phase diagrams were more complex, the general behavior with a change in gas phase composition showed the same trend in dissociation pressures (which in this case refers to the conversion of clathrate to vapor plus water).

A significant number of clathrate equilibrium studies have been done on a variety of guest species, but the majority of these deal with temperatures at or above 0°C. Obtaining satisfactory data for the clathrate-pure solid-gas equilibrium is particularly difficult, as it requires a solid-solid transformation. However, a few such studies have been reported (Barrer and Edge, 1967; Falabella and Vanpee, 1974; Barrer and Ruzicka, 1962; Roberts et al., 1940). In general, observable reaction rates for solid-solid transformations are often difficult to

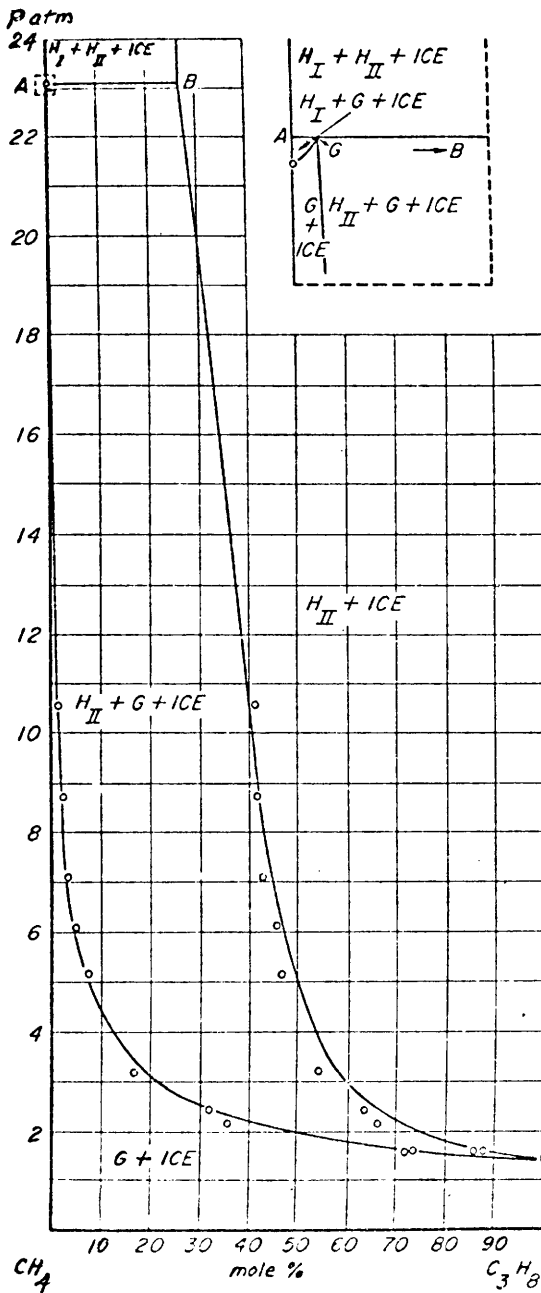


Figure 2-13 Isothermal cross section of the system $H_2O-CH_4-C_3H_8$ on a water-free basis at 270 K. The points represent experimental results and the curves were obtained from a theoretical analysis (van der Waals and Platteeuw, 1959). H_I and H_{II} represent hydrates of structure I and II respectively, H_I contains only methane.

obtain, as such transformations are thought to be controlled by a nucleation (here the free energy of formation must include a strain energy term) and particle growth sequence. (Fisher et al., 1948) For temperatures and pressures at or near the equilibrium point the rate of nucleation may be negligible. However, for the clathrate-ice conversion the reaction may also take place from the vapor phase, as the vapor pressure of the ice will be high enough to cause the clathrate to form at suitable solid surface nucleation sites. In this case, the finer the ice crystals, the larger will be the surface area available for vaporization. On the other hand, Barrer and Edge postulated that the ice reacted at the surface and continuous bombarding with steel balls was necessary to clear the surface of the newly-formed clathrate. (Further discussion of the technique used in this previous study will be given in Chapter 3).

As indicated by the number of publications, there is considerable interest in clathrates, and many compounds other than water have, in fact, been found to form such cage-like structures. However, there are apparently no previously reported incidences of the formation of methanol clathrates, but the availability of OH groups for hydrogen bonding certainly suggests clathrate formation as a possibility.

CHAPTER 3 - GEL STRUCTURE ANALYSIS

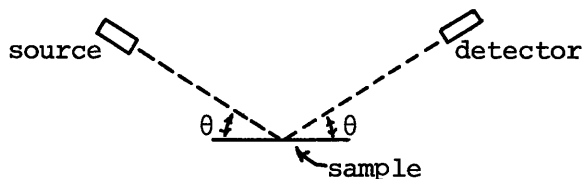
3.1 Crystal Structure of Gelant Particles

The crystal structure of the gelant particles was studied using powder x-ray diffraction, the objective being to distinguish whether the particles were pure crystalline solids (ice or solid methanol) or crystalline clathrate structures. Past studies have provided considerable information on the structures of ice, solid methanol and various water clathrates. The methanol clathrate, however, has not been previously reported, and some effort was made to determine its structure. Also due to the anomalous results of the x-ray diffraction pattern obtained from the water/methane gels, all of the possible ice and clathrate structures will be considered here, with detailed descriptions provided for the most probable structures.

This section will be divided into several parts. In the first, a discussion is given of the equations used in the analysis of the x-ray diffraction data. Next are descriptions of the pure solid crystals including techniques for the formation of the various phases and confirmation of previously reported x-ray diffraction data. These sections are followed by separate discussions on water and methanol clathrates and are concluded with some considerations on the effect of using a gel-like sample.

3.1.1 Analysis of Powder X-ray Diffraction Data

The powder x-ray diffraction technique used in this study consisted of a flat sample with the impinging x-rays perpendicular to the axis of rotation. The angle (θ) formed by the x-ray beam and the sample was equal to the angle formed by the detector and the sample, and the diffractometer maintained this equality as θ was varied.

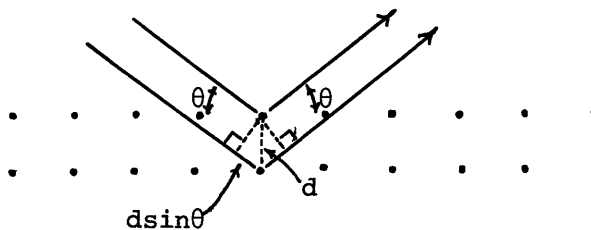


Major peaks in intensity should therefore be observed at angles which obey Bragg's Law.

$$\lambda = 2d \sin\theta \quad (3-1)$$

where λ = wavelength of impinging x-ray
 d = spacing between reflecting planes
 θ = angle between x-ray beam and sample surface

A two-dimensional arrangement of atoms indicates the basis for Bragg's law. Two waves constructively interfere when the difference in the distance traveled by the two waves is a multiple of the wavelength of the x-ray beam. A three-dimensional derivation of Bragg's law is given in Appendices K, L, and M.

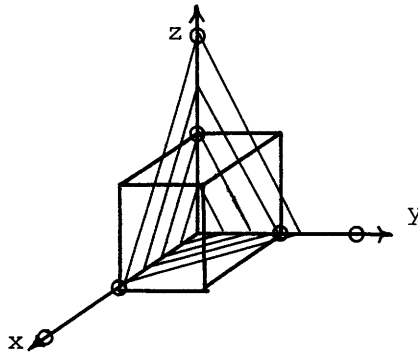


Each recorded intensity peak represents a set of diffracting planes with an interplanar spacing "d". These sets of planes are commonly referred to by their Miller indices (hkl) which satisfy the equation for a plane in space.

$$hx + ky + lz = 1 \quad (3-2)$$

$$\begin{aligned} \text{and } h &= 1/a \\ k &= 1/b \\ l &= 1/c \end{aligned}$$

where x, y, z = coordinates along the 3 axes describing the unit cell.
 a, b, c = $x, y,$ and z axis intercepts, respectively. These are fractional values of the unit cell edge lengths.



Example. Family of planes (432) with unit cell

The values for $h, k,$ and l are always integers, 0 and negative numbers being permissible. Fractional values can never produce reflecting sets of planes as the repeating nature of the crystal produces destructive interference. When the symmetry of the unit cell is great, there may be nonparallel planes which have the same atomic distribution and equivalent "d" spacings. For example, in the cubic crystal, sets of planes (100), (010), (001), (001), (010), (100) are all crystallographically equivalent. Equivalent planes are represented by one of

the sets of planes, $\{100\}$, and are said to have a given multiplicity, six in this case.

The "d" spacing represents the perpendicular distance between each plane in that particular set (hkl). If the unit cell is cubic (see Table 3-1 for definitions of this and other crystal systems), the relation between the Miller indices and the angles of intensity peaks is

$$\sin^2 \theta = \frac{\lambda^2}{4a^2} (h^2 + k^2 + l^2) \quad (3-3)$$

$$\text{thus} \quad \frac{1}{d^2} = \frac{1}{a^2} (h^2 + k^2 + l^2)$$

If the unit cell is hexagonal, the equation is

$$\sin^2 \theta = \frac{\lambda^2}{3a^2} (h^2 + hk + k^2) + \frac{\lambda^2}{4c^2} (l^2) \quad (3-4)$$

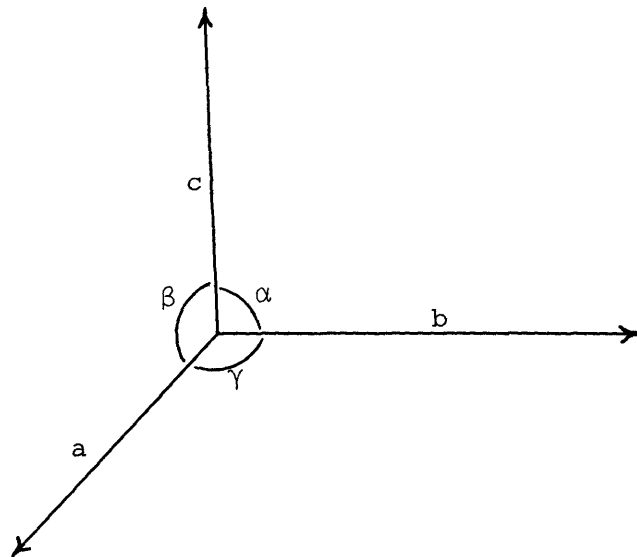
$$\text{or} \quad \frac{1}{d^2} = \frac{1}{3a^2} (h^2 + hk + k^2) + \frac{1}{4c^2} (l^2)$$

When the unit cell contains a large number of atoms, it is possible that not all of the sets (hkl) will give prominent intensity peaks. In general, the planes which give major reflections will be those which are atom rich, as atoms between reflecting planes destructively interfere. The observed intensity is primarily dependent on the particular types of atoms and their positions within the unit cell. The following proportionality relates the observed intensity to these factors, including appropriate correction terms.

Table 3-1

Crystal Systems

<u>System</u>	<u>Unit Cell</u>	
Cubic	$a = b = c$	$\alpha = \beta = \gamma = 90^\circ$
Tetragonal	$a = b \neq c$	$\alpha = \beta = \gamma = 90^\circ$
Hexagonal	$a = b \neq c$	$\alpha = \beta = 90^\circ \quad \gamma = 120^\circ$
Trigonal	$a = b = c$	$\alpha = \beta = \gamma \neq 90^\circ$
Orthorhombic	$a \neq b \neq c$	$\alpha = \beta = \gamma = 90^\circ$
Monoclinic	$a \neq b \neq c$	$\alpha = \gamma = 90^\circ \quad \beta \neq 90^\circ$
Triclinic	$a \neq b \neq c$	$\alpha \neq \beta \neq \gamma$



$$I_{\{hkl\}} = \left(\frac{1 + \cos^2 2\theta}{\sin^2 \theta \cos \theta} \right) (P) |F_{\{hkl\}}|^2 \quad (3-5)$$

$$\text{and } |F_{\{hkl\}}|^2 = \left(\sum_i f_i \cos \theta_i \right)^2 + \left(\sum_i f_i \sin \theta_i \right)^2$$

$$\theta_i = 2\pi(hx_i + ky_i + lz_i)$$

where $I_{\{hkl\}}$ = integrated intensity
 $F_{\{hkl\}}$ = unit cell structure factor for family of planes $\{hkl\}$
 P = multiplicity of $\{hkl\}$
 x_i, y_i, z_i = coordinates of atom i referred to unit cell axes
 f_i = scattering factor for atom i . This is dependent on atom type and scattering angle. Values tabulated in International Table for X-Ray Crystallography

(See Appendix M for derivations of the above equations)

The trigonometric term $\frac{(1 + \cos^2 2\theta)}{(\sin^2 \theta \cos \theta)}$ is a correction factor which accounts for (1) the partial polarization of the relected beam, (2) the variations in the time spent in a reflecting position, and (3) the probability that a particular set of planes will pass through the reflecting position.

Powder diffraction techniques can lead to certain systematic errors due to preferential orientation of particles, nonhomogeneity of sample, particle size and adsorption effects. Powder diffraction requires small (ideally around 1 micron in size) randomly oriented crystals so as to provide a sufficient number of crystals with the

appropriate planar orientation for each reflection angle. If the crystals are too large or preferentially oriented, resulting peak intensities may be quite misleading. Non-random crystal orientation may even result in missing peaks. Nonhomogeneity in particle size (and composition if sample contains particles of different crystal structures) can also result in errors in intensity measurements. Absorption effects may also occur. As the geometry used in this study was a reflecting one (as opposed to transmitting through the powder as in Debye Scherrer) it is desirable to have high absorption to minimize the possibility of reflections from planes below the surface. If the latter occurred, there would be a tendency to shift the position of the reflection to smaller angles. The use of a flat sample (as opposed to the ideally-curved sample with a changing arc appropriate to each reflection angle) will also tend to shift peaks to lower angles. These effects, however, can be estimated (see Appendix N) and are negligible for all of the cases studied here.

3.1.2 The Formation and Structure of Ice

Several crystalline forms of ice exist, and their regions of thermodynamic stability are shown in Figure 3-1. As indicated in this diagram, only the hexagonal phase (I_h) is likely to form at 1 bar and 273 to 113 K (the conditions during the gelation process). However, two other forms of ice, cubic ice (I_c) and vitreous ice, have been formed at low temperatures by vapor condensation under vacuum. These three ice forms will therefore be considered in detail.

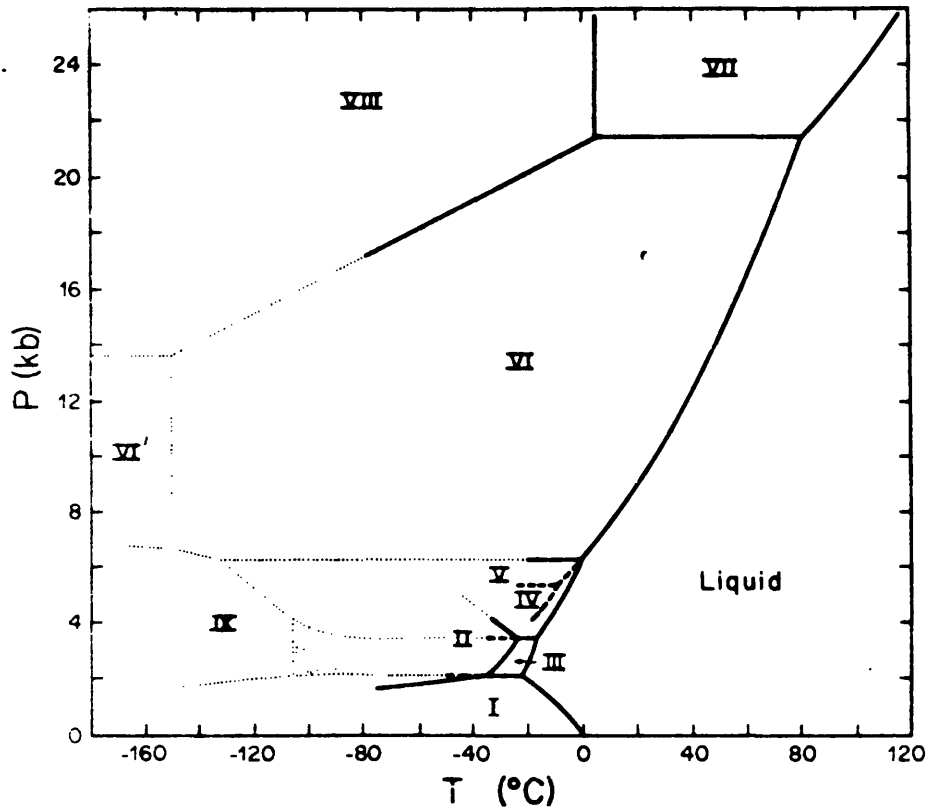


Figure 3-1 Phase Diagram for Ice (Kamb, 1973)

- Experimentally established phase boundaries
- Experimentally established phase boundaries which are prolonged metastably or involve metastable phases
- Inferred phase boundaries

The structure of hexagonal ice (I_h) can be visualized as arrays of hexagons. Six H_2O molecules link together to form either a puckered "chair" or a "boat" configuration while preserving the desired tetrahedral bond angles. In hexagonal ice (Figures 3-2 and 3-3), layers of the puckered chair rings stack together, each layer being the mirror image of the layer preceding it. (Boat configurations result from this stacking sequence.) This results in a tetramolecular hexagonal unit cell with dimensions $a = 4.519 \text{ \AA}$, $c = 7.362 \text{ \AA}$ at atmospheric pressure and 263 K. The observed change in these dimensions with temperature is $.0004 \text{ \AA/K}$ (Owston, 1958).

Hexagonal ice has been produced by freezing water at atmospheric pressures and temperatures between 273 and 73 K. Some past techniques have ground ice into powder form under liquid nitrogen using a mortar and pestle or used vapor deposition of ice onto a cold sample plate maintained at 143 K. In the present study several methods were used. Initially, samples were ground under liquid nitrogen. Although finely ground samples could be produced this way, the sample would not pack and stick together in the sample indentation. (Also, this technique may result in nitrogen clathrate formation which will be discussed later.) A more satisfactory technique was to impinge a fine mist of water onto the sample indentation, while maintaining the stage temperature between 223 and 143 K. Dowell and Rinfret (1960) had previously reported producing hexagonal ice by this method. The x-ray diffraction results using this technique were quite good, indicating that this method was satisfactory for producing fine

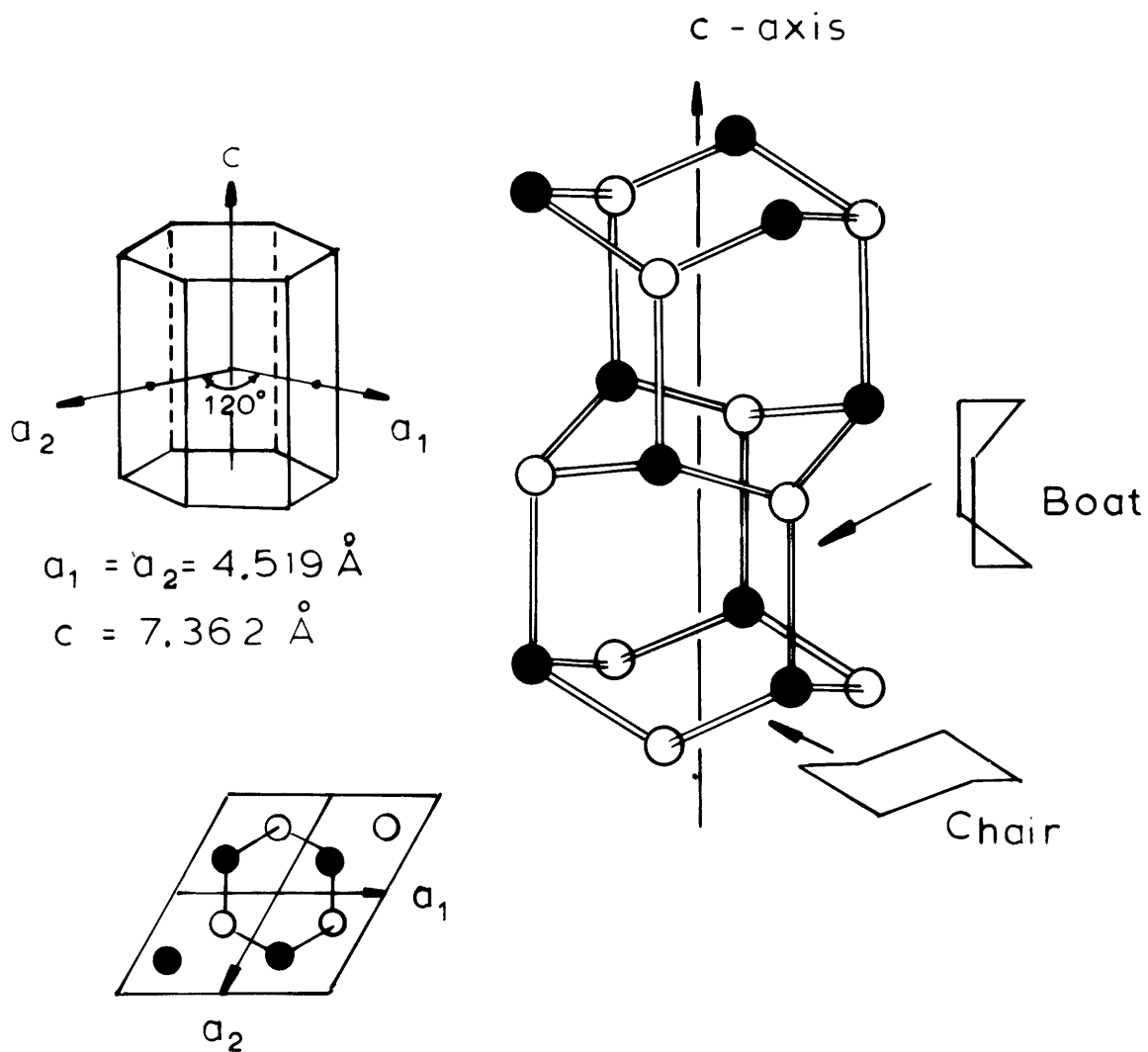


Figure 3-2 Unit cell for hexagonal ice, I_h . Spheres (both solid and open) represent oxygen atoms of water molecules. The unit cell consists of two puckered rings stacked along the c axis but differing by a 60° rotation. Adding a third puckered ring shows the ABAB sequence of hexagonal ice.

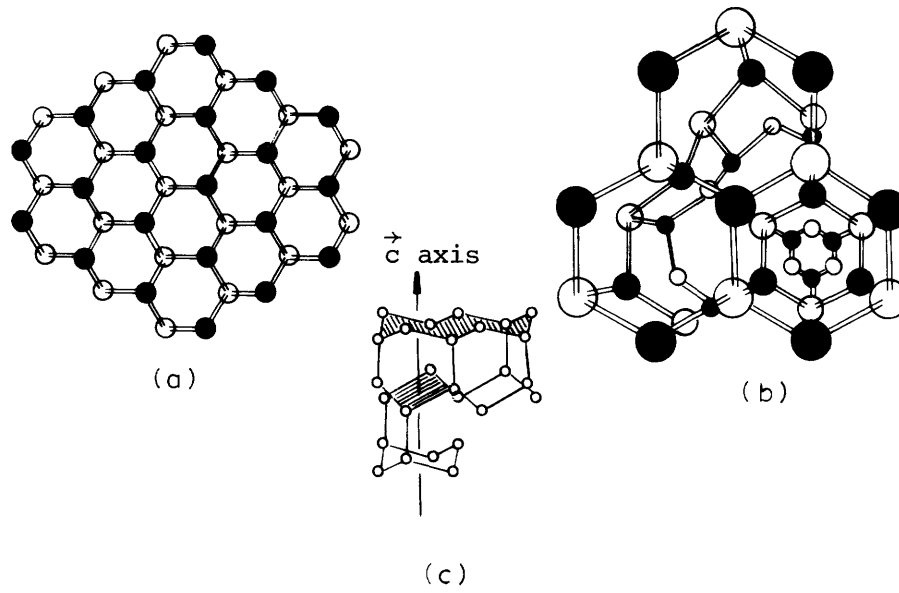


Figure 3-3 3-Dimensional packing in hexagonal ice

- a) Single layer of puckered rings
- b) Hexagonal channels viewed parallel to \vec{c} axis
- c) View of stacking perpendicular to \vec{c}

crystal grains in random orientation. Frost formed from atmospheric moisture on a cold stage at ≥ 153 K also produced hexagonal ice x-ray diffraction patterns. However, when the stage was maintained at colder temperatures ≤ 123 K conversion to another structure, presumably an air (nitrogen and oxygen) hydrate structure, was observed. Although the surface temperature of the sample was not measured (because of possible interference of the thermocouple with the x-ray beam), the transition temperature is likely to be around 143 K, the decomposition temperature for nitrogen hydrate (Section 3.3). Due to the presence of oxygen, however, the temperature may be slightly greater than 143 K. The reflections observed for the hexagonal ice were in excellent agreement with those reported by Dowell and Rinfret (1960) (Table 3-2). A typical recorder output is shown in Figure 3-4. Table 3-2 also includes a comparison of observed intensities with the intensities calculated for the known structure. This is based on the atomic positions of the oxygen atoms only, as the hydrogen atoms contribute negligibly to the x-ray diffraction results. The positions for the oxygen atoms are $\pm(1/3, 2/3, 1/16)$ and $\pm(1/3, 2/3, 7/16)$ as reported by Owston (1958) resulted in a confidence factor $\sum (I_{\text{obs}} - I_{\text{cal}}) / \sum I_{\text{cal}} = 0.18$ which is quite good for powder x-ray diffraction data.

Cubic ice also consists of layers of hexagonal ring networks. However, each successive layer is identical to the preceding one but shifted one-half the diameter of the hexagonal ring (Figure 3-5). This results in an ABCABC... stacking sequence and a cubic unit cell

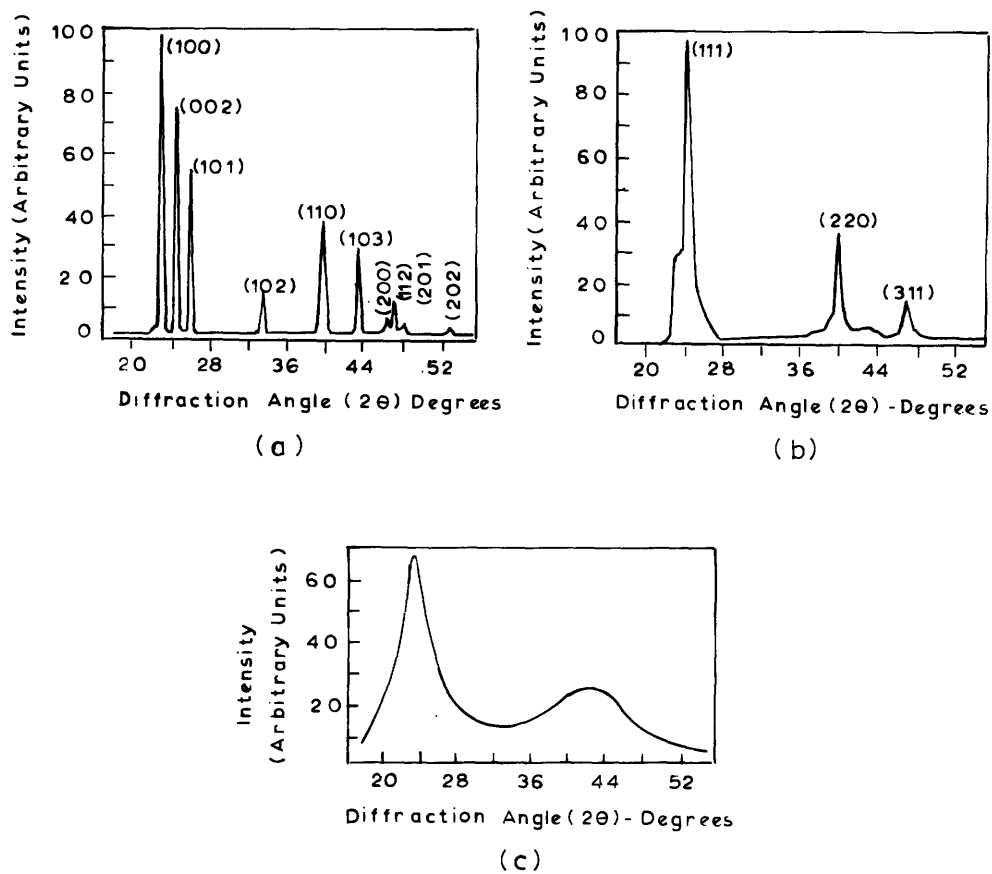


Figure 3-4 Powder X-ray Diffraction Patterns for
a) Hexagonal Ice
b) Cubic Ice
c) Vitreous Ice
from Dowell and Rinfret (1960).
Numbers in parentheses are the Miller indices for that particular reflection.

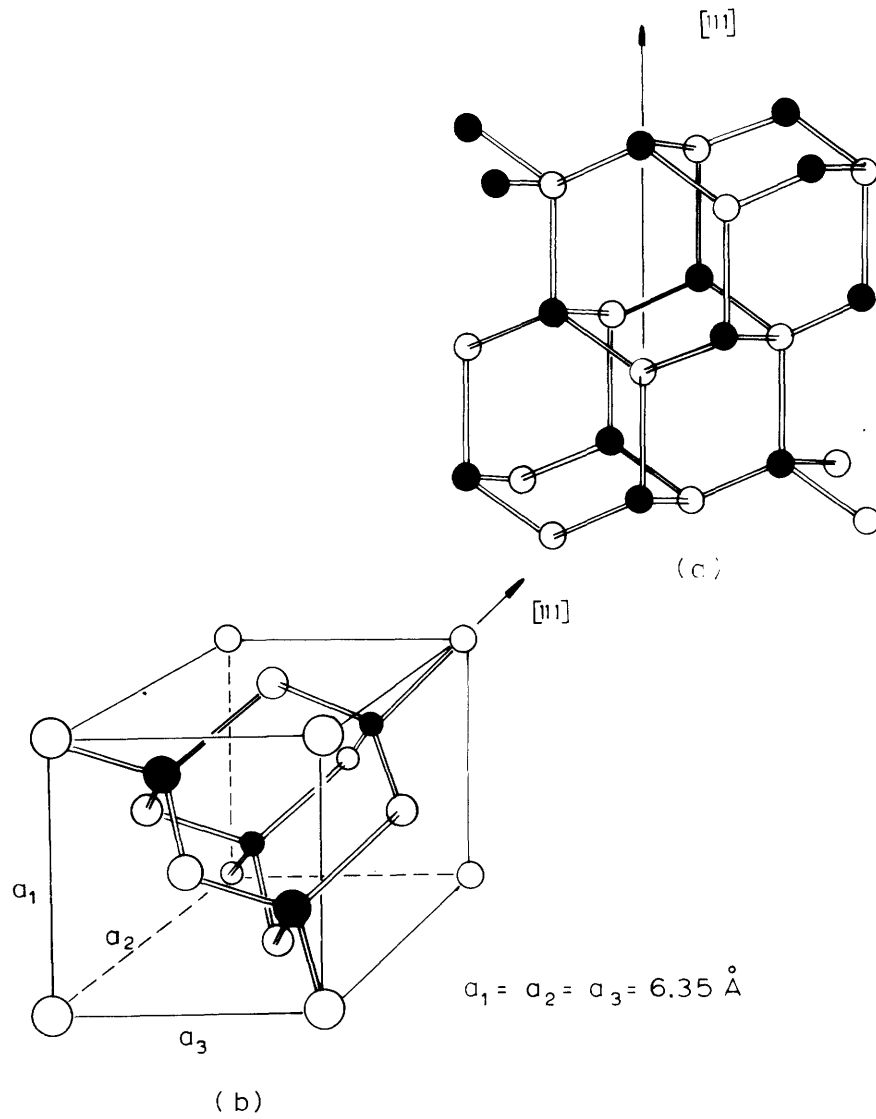


Figure 3-5 Structure of Cubic Ice

- (a) Identical Layers of Puckered Rings
Stack in ABCABC Sequence with each
Succeeding Layer Shifted $\frac{1}{2}$ the Distance
of a Puckered Ring
- (b) Unit Cell for Cubic Ice

Table 3-2

Hexagonal Ice

<u>hkl</u>	<u>2θ (degrees)</u>		<u>Intensity (I/I_{max})</u>			<u>d(A)</u>
	<u>Calc.</u>	<u>Obs.</u>	<u>Calc.</u>	<u>Obs.*</u>	<u>Obs.**</u>	
100	22.8	22.9	100	100	100	3.896
002	24.2	24.4	57	75	53	3.673
101	25.9	25.9	62	53	51	3.436
102	33.5	33.6	33	17	22	2.672
110	40.0	40.0	72	39	69	2.251
103	43.6	43.7	67	30	40	2.073
200	46.6	46.7	10	4	7	1.947
112	47.4	47.4	38	18	24	1.916
201	48.3	48.3	8	3	4	1.882
202	53.2	53.4	6	2	2	1.720

* Dowell and Rinfret (1960). These values are probably peak heights as opposed to areas.

** Integrated intensities from H₂O sprayed onto cold stage.

with dimension $a = 6.358 \text{ \AA}$ at 88 K. Two techniques have been used by past researchers to produce this form of ice, the most common one being vapor condensation under vacuum. Phase stability has been correlated with temperature, but not with pressure. Blackman and Lisgarten (1957) used $\approx 5 \times 10^{-5}$ mm Hg in their experiments and were able to produce vitreous ice when the base temperature was between 93 K and 133 K, and cubic ice when the base was between 133 K and 153 K. A mixture of cubic and hexagonal forms was produced between 153 K and 173 K, and hexagonal ice alone was formed above this temperature. Dowell and Rinfret (1960) used a stream of wet nitrogen gas with a continuous flow impinging on the cold stage. Ice deposited on the surface while the nitrogen was continuously pumped off, thus maintaining the chamber under vacuum during formation. The actual pressure, however, was not reported. They too were able to form deposits of vitreous and cubic ice. However, their reported temperatures were slightly lower than Blackman and Lisgarten. Beaumont et al. (1961) reported temperature ranges (again pressure conditions were not reported) in agreement with Blackman and Lisgarten and suggested that Dowell and Rinfret may have had heat leak inaccuracies in their experiments which resulted in the lower observed temperatures. Although past researchers did not consider the possibility of clathrate formation, the formation of ice under vacuum and low temperature conditions is consistent with the previously discussed thermodynamic stability of gas/water systems.

Cubic ice has also been produced starting with a high pressure form of ice (II, III, or V) (Bertie, Calvert, and Whalley, 1963). The pressure and temperature of the sample were subsequently reduced to 1 bar and 90 K. Upon warming, the high pressure form converted to the cubic form at ~ 160 K and further converted to the hexagonal form at 170 K. However, the temperature at which the rate of formation of hexagonal ice was detectable varied with the thermal history of the sample, and appeared to be dependent on the presence of hexagonal ice nuclei. In this case the cubic form is probably a metastable phase. However, the ability to form cubic ice directly from water vapor under vacuum indicates that this phase may have a region of thermodynamic stability. These conditions, however, require a vacuum, and thus the cubic phase is not likely to form at the conditions used in the present gelation process. No attempt was made to reproduce this form of ice. However, x-ray diffraction peaks for cubic ice and several of the high pressure forms of ice are listed in Table 3-3 for comparison with the data obtained in this study on the methane-water gels.

The structure of vitreous ice has not been precisely determined. Allen (1973) has reviewed the available data and has suggested possible models. One of these models consists of a random stack of sheets held apart by van der Waals repulsion. Each sheet has the same conformation as a single layer of I_c or I_h but consists of only a few rings. This is consistent with observed x-ray diffraction data (Figure 3-4) provided the OHO bond length is 2.62 to 2.63 Å which is shorter than that found in I_c or I_h , 2.67 Å. Another possible

Table 3-3

X-ray Diffraction Data for High Pressure Ice Forms*

II		III		V	
$2\theta^\circ$	I/I_{\max}	$2\theta^\circ$	I/I_{\max}	$2\theta^\circ$	I/I_{\max}
6.4	100				
10.9	40	10.5	10	13.5	80
11.6	5				
12.6	25	12.0	4	14.5	100
13.6	80	13.5	100	15.4	100
14.7	100	14.7	40	16.8	30
16.1	60	17.0	4		
16.7	80			17.9	20
17.2	50	18.0	13	18.7	8
18.3	5				
19.6	12	19.0	15	20.0	20
		20.1	7		
20.5	15	20.9	13	20.9	30
21.3	15	21.9	15	21.8	30
22.4	15	22.6	3		
23.4	10	24.1	5	23.0	15
24.3	10	25.7	7		
24.9	5	26.5	3	23.8	15
25.5	20	28.2	2		
26.5	10	28.6	5	25.2	8
27.2	20	29.8	1		
28.8	15	31.2	4	26.3	10
29.4	10	32.5	7		
32.5	5	33.3	3	27.6	8
34.7	5	34.7	1	28.6	10
35.7	5	36.7	1	29.8	10
37.7	5	38.1	1	32.0	5
41.6	5	41.6	1		

* From Bertie et al. (1963)

model is a combined amorphous microcrystalline phase of cubic ice, the microcrystals of the cubic ice being responsible for the peak broadening in the powder diffraction pattern.

As the observed reflections for the gel crystals did not precisely fit the pattern for the expected clathrate structure, all possibilities were considered. Past techniques for producing ice were checked for the possibility of unknowingly producing a clathrate or unknown ice structure instead of the desired ice structure, and whether erroneous results had occurred. Shallcross and Carpenter (1957) attempted to produce cubic ice by condensing moisture from the atmosphere onto an aluminum wire. The wire was fastened inside a 5 ml Dewar filled with liquid nitrogen and extended above the Dewar into the x-ray beam. After some ice had condensed, a stream of cold nitrogen gas at 143 K was directed onto the wire to maintain a low temperature and prevent further condensation. This technique was reported to have produced primarily hexagonal ice; in only 25 percent of the attempts were they able to produce cubic ice. It is possible that this technique may have produced some nitrogen clathrate (which was mistakenly identified as hexagonal ice) but its decomposition temperature at atmospheric pressure is around 143 K. Thus, quite likely hexagonal ice was actually formed.

Powder samples were often produced by grinding ice (of the desired structure) under liquid nitrogen using a mortar and pestle. This clearly allows for the possibility of nitrogen clathrate formation, and the rate of conversion is rapid enough to be observable. Bertie

et al. (1963) used this grinding technique in the study of high pressure ice forms. They reported that a white powdery material accumulated in the liquid nitrogen bath. From its x-ray pattern, they assumed it to contain some hexagonal ice. This was probably a nitrogen-water clathrate which was mistakenly identified as hexagonal ice because the x-ray patterns are somewhat similar. However, no record of the indexed x-ray pattern for this crystalline form was indicated.

Although the evidence suggests that ice dispersed in liquid nitrogen may convert to nitrogen clathrate, this transformation is thought to be a surface reaction rather than a solid-solid transformation (see Sections 2.4 and 3.3). This is consistent with the supposed difficulty of incorporating the gas molecules into an already formed ice structure. The water molecules are packed together so tightly that a gas molecule would have difficulty diffusing into the structure. The transformation can thus proceed by two possible mechanisms. The H_2O molecules may dissolve in the liquid nitrogen with subsequent clathrate crystal growth at a separate location and/or the surface molecules may rearrange to form a coating of clathrate crystals around the ice particles (which in turn would halt the former dissolving process). Both types of surface reactions have been observed in previous clathrate studies (Hartgerink et al., 1977), and it is not certain which is the primary mechanism for this particular case.

High-pressure forms of ice were made by compressing water in a piston and subsequently freezing it at an appropriate temperature. One research group (Arnold et al., 1971) did, however, study ice under helium pressure. Although he noted some differences in transition temperatures for the various crystalline phases, he did not observe any anomalous x-ray diffraction patterns. The helium molecule is so small, with a van der Waal radii of .9 A, that quite likely it could not be confined in any of the cage structures known to clathrates.

A review of the literature on the high pressure forms of ice indicated one unexplained anomaly in the reported x-ray diffraction data. MacFarlan (1936a & b) reported separately on the formation and study of type II and type III ice which later researchers found somewhat erroneous. His type II was in fair agreement with the type III produced in later studies (Bertie et al., 1963; Kamb and Prakash, 1968), while his type III conforms to no other reportedly observed structure. Details of his formation technique were not complete, however, and ice structure conversions may have taken place. Also clathrate formation may have occurred during grinding in liquid air with possible further conversion in the x-ray chamber. However, their reported data do not conform to any known clathrate x-ray diffraction pattern, to any known ice structure data, or to the presently obtained data. One can only guess that the sample may have been a non-homogeneous mixture of more than one ice phase with or without possible oriented clathrate crystal growth during the x-ray diffraction data collection.

3.1.3 The Formation and Structure of Solid Methanol

Methanol is known to form two different solid phases with the transition point being 158 K. Tauer and Lipscomb (1952) have studied pure solid methanol at 163 K and 113 K using single-crystal x-ray diffraction. Their technique for forming such single crystals involved distilling purified methanol into thin-walled capillary tubes (0.5 mm diameter). The methanol was subsequently frozen using liquid nitrogen, and the capillary sealed under vacuum. Apparently, this technique produced the higher-temperature form, (i.e., although liquid nitrogen was used to freeze the methanol they apparently did not cool the crystal down to the boiling point of liquid nitrogen) as they report having produced the lower-temperature phase by subsequent cooling (with liquid nitrogen) of this prior phase. Such cooling caused the destruction of the single crystal by twinning; however, they were still able to obtain satisfactory x-ray diffraction results, and thus were able to determine the crystal structure.

The high-temperature modification of pure solid methanol consists of infinite zigzag chains of hydrogen bonded methanol molecules (Figure 3-6). The observed reflections are listed in Table 3-4. The zigzag chains lie parallel to each other, but alternate as to the direction of the methyl group. This results in a tetramolecular unit cell. In the low temperature form, each chain is exactly like the preceding chain (Figure 3-7), and the resulting unit cell therefore contains only two molecules. Murti (1959) did a further study of the

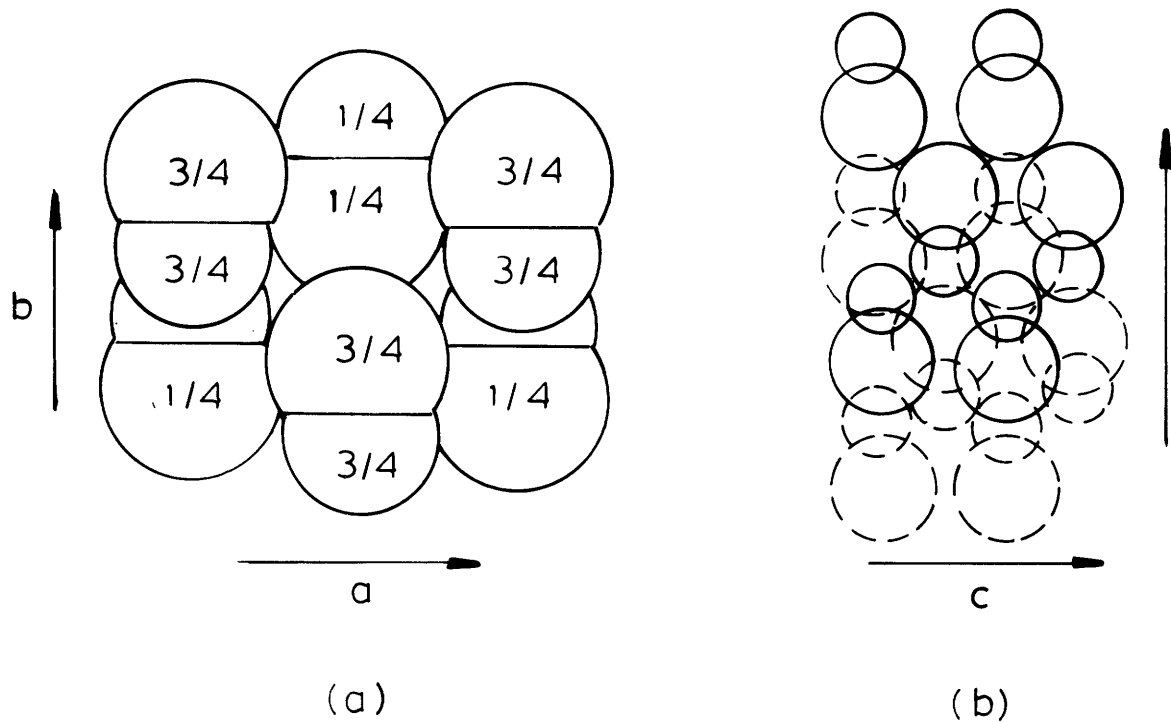


Figure 3-6 High-temperature Solid Methanol Structure

Smaller circles represent oxygen atoms.
Larger circles represent methyl group.

- a) Projection on \vec{ab} plane--fractions give position along \vec{c} axis
- b) Projection on \vec{bc} plane shows zig-zag chain of OHO bonds. Dashed groups represent succeeding layer in \vec{a} direction.

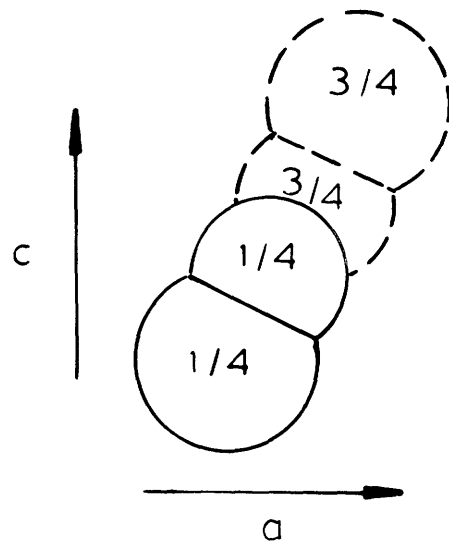


Figure 3-7 Bimolecular Unit Cell for Low Temperature Form of Solid Methanol. Zigzag of OHO Bonds in Direction Perpendicular to Plane of Paper.

Table 3-4

X-ray Diffraction Data for Solid Methanol at 163 K*

<u>hkl</u>	<u>2θ (degrees)</u>	<u>Intensity</u> <u>(I/I_{max})</u>
110	18.4	44
002	38.5	15
111	26.6	100
200	27.8	43
112	43.1	4
11 $\bar{3}$	62.7	2
021	31.2	9
202	48.2	6

* From Tauer and Lipscomb (1952)

low-temperature form at 93 K. He found that the space group D_{2h}^{17} remained the same as in the slightly higher-temperature (113 K) form produced by Tauer and Lipscomb, but that the unit cell dimensions changed slightly to $a = 4.59$ A, $b = 4.68$ A, $c = 4.92$ A and $\beta = 97^\circ 30'$. Murti used a powder sample, but his technique was not clearly described (Murti and Sen, 1956). Grinding, however, was apparently done using a mortar and pestle at cryogenic temperatures with subsequent transfer of the sample to a glass tube. No mention was made as to whether the tube was sealed. Cooling inside the camera was accomplished by dripping liquid oxygen onto the specimen. Due to the handling and grinding at atmospheric pressure, plus the questionable conditions used during the x-ray photography, it might have been possible to form an oxygen-methanol clathrate. Also his grinding procedure is quite uncertain, as it is extremely difficult, if not impossible, to grind solid methanol in liquid nitrogen with a mortar and pestle. However, his data are in close agreement with those observed at 113 K, and his sample was therefore presumed to be, primarily, pure solid methanol.

In this study, pure solid methanol was produced by spraying a fine mist of methanol onto the precooled x-ray diffraction stage maintained at 93 K to 77 K. The results are listed in Table 3-5 along with those of Tauer and Lipscomb and Murti. The observed peaks fit most closely to the 93 K data of Murti. However, he did not determine atomic positions to see if his data were in agreement with a structure appropriate to his unit cell. The differences in

Table 3-5

X-ray Diffraction Data for the Low-Temperature
Form of Solid Methanol

hkl	Monoclinic 113 K*			Monoclinic 93 K**		Present study < 93 K	
	$2\theta^\circ$	(I/I_{\max})	$ F _{\text{obs}}$	$2\theta^\circ$	I_{obs}	$2\theta_{\text{obs}}^\circ$	I_{obs}
001	18.1	21	<4	18.1	m	18.2	16
100	19.3	30	9	19.5	w	19.3	5
10 $\bar{1}$	26.5	61	18	24.9	vw		
011	26.2	56	18	26.3	s	26.5	88
110	27.2	100	24	27.3	vs	27.0	100
101	26.5	2	18	28.5	m	28.2	11
002	36.5	1	5				
11 $\bar{1}$	32.8	-		31.5	w	31.5	2
111	32.8	10		34.5	w	34.7	2
020	38.4	23		38.4	m	38.6	100
20 $\bar{1}$	43.4	3	8	} 39.5	w		
200	39.3	4	5				
021	42.7	4	<4	42.8	w		
210	43.9	10	6	} 44.3	w	43.5	5
102	41.6	1	8				
21 $\bar{1}$	47.8	16		} 45.8	vw		
201	43.4		9				
121	47.3		8	} 48.6		47.4	2
112	46.0	5				w	48.6
12 $\bar{1}$	47.3	17					
211	47.8	1		50.1	w		
022	54.0		4	54.6	w		
21 $\bar{2}$	58.3		7				
220	56.1	2	4	56.4	vw		

* Tauer and Lipscomb (1952)

** Murti (1959)

intensity, particularly the peak at 38.4 may have been due to large crystal grains and/or crystal orientation. In spite of slight inaccuracies in intensity, the major peaks were quite clear, and the diffraction pattern was reproducible.

3.1.4 Clathrate Hydrates

Although water-clathrate compounds were observed as early as 1810 by Davy, the nature of bonding in these compounds was not understood until x-ray diffraction techniques became available to elucidate their cagelike structure. Initial powder x-ray diffraction studies by von Stackelberg and Muller (1951, 1954) indicated that there were two types of gas hydrates (structure I and II). Although von Stackelberg was able to suggest a structure for the structure I hydrate, the OHO bond length and angles required by this structure were inappropriate, and further modeling by Pauling and Marsh (1952) produced a structure which gave a much better fit to the data. Claussen (1951) apparently proposed the same structure independently and at about the same time. This structure is formed by the combination of pentagonal dodecahedrons and tetrakaidecahedrons (Figures 3-8 and 3-9). Face-sharing between the polyhedra produce a cubic unit cell with cell dimension $a = 12 \text{ \AA}$. Using molecular models, the correct structure for the structure II hydrates was guessed by Claussen (1950) and subsequently supported by x-ray diffraction measurements (von Stackelberg and Muller, 1954, using powder diffraction techniques and by Mak and McMullan, 1965,

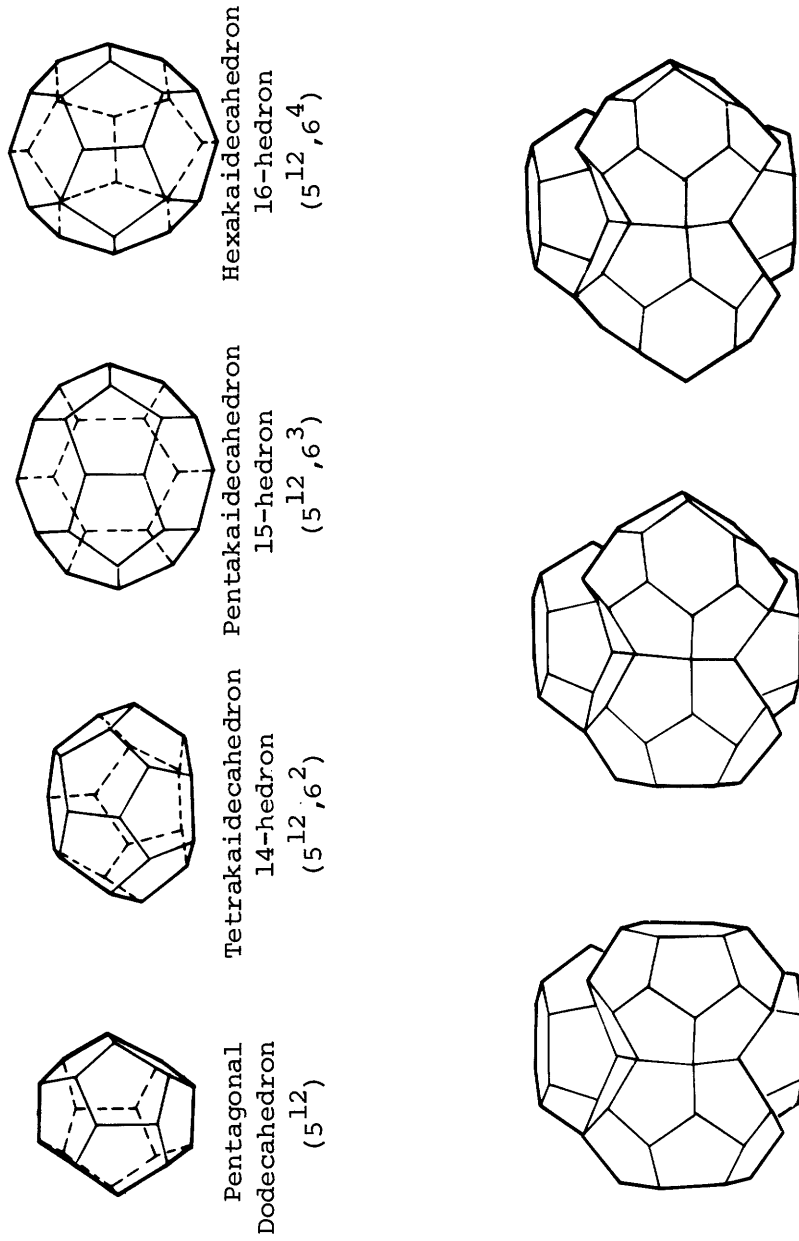


Figure 3-8 Polyhedra Commonly Found in the Clathrate Hydrates

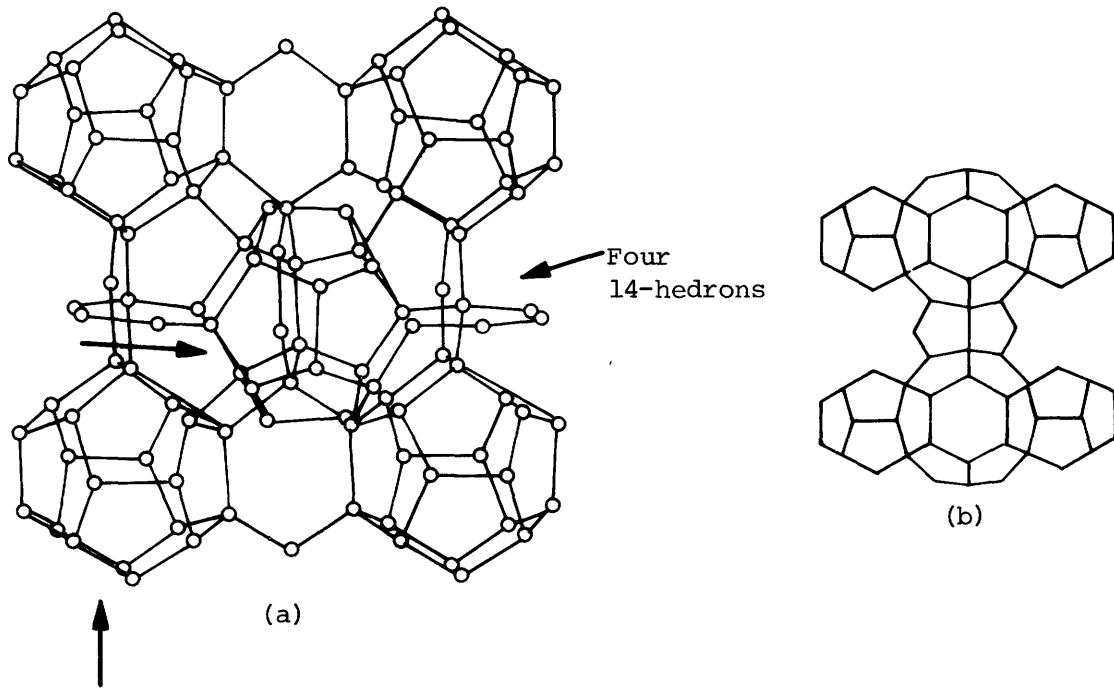


Figure 3-9 Structure of 12 A cubic gas hydrates

- a) Structure composed of 14-hedrons (12 pentagons and 2 hexagons): 2 sharing hexagon faces in middle of front face of cube; 2 with hexagons on top and bottom edges of front face; combination of four 14-hedrons at left and right faces (with planes perpendicular to paper). Unlabeled arrows indicate locations of pentagonal dodecahedrons.
- b) Pentagonal dodecahedrons lie at the eight corners of cube and in center.

using single crystal diffraction). This structure can be defined solely by building pentagonal dodecahedrons together with face-sharing as shown in Figure 3-10. This stacking arrangement produces a second larger cavity, a hexakaidecahedron. This is a slightly larger cage than the tetrakaidecahedron, and this clathrate structure consequently has been observed to form when the included guest species is too large for the tetrakaidecahedron.

Table 3-6 and 3-7 list the different gas species which have been observed to form clathrates of structures I and II, respectively, along with the unit cell size as determined by x-ray diffraction. In general, the largest molecular dimension of the included guest molecule has been an appropriate measure to determine which structure would form (Table 3-8), and the methane hydrate has therefore been assumed to form the structure I clathrate filling all cages, ethane to form structure I filling only the larger cages, and propane forming structure II filling only the larger cages. None of these, however, have been previously studied by x-ray diffraction, either at low temperatures or high pressures.

Since the work of von Stackelberg, Claussen, etc., many other water clathrate structures have been observed. In particular, the amines form a variety of structures. A list of the known structures is given in Table 3-9. All of these structures have quite large cages, as required by the particular encaged molecule and would, therefore, seem unlikely possibilities for the methane hydrate. On the other hand, anomalies have occurred, as in the case of the Bromine hydrate.

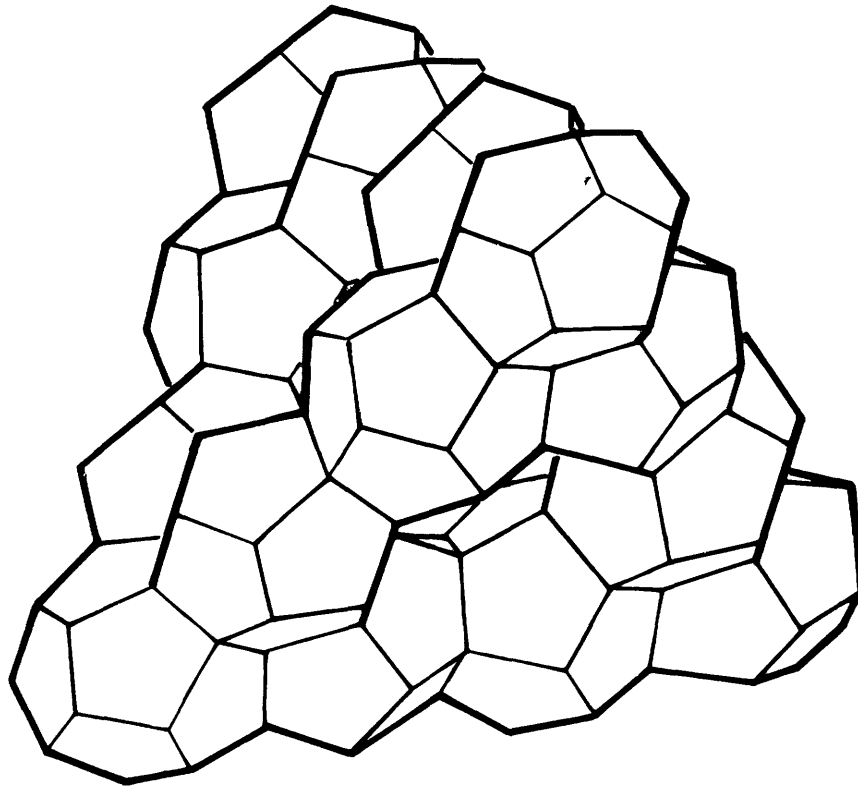


Figure 3-10 Arrangement of Pentagonal dodecahedra in 17 A cubic gas hydrate structure. The central cavity defined by this arrangement is a 16-hedron.

Table 3-6

Structure I Hydrate Formers which have been
Studied by X-ray Diffraction^a

<u>Hydrate Former</u>	<u>Unit Cell Size (Å)</u>
Xe	11.97
H ₂ S	12.00
H ₂ Se	12.06
N ₂ O	12.03
CH ₃ Cl	12.0
Cl ₂	12.03; 11.82 ^b
CH ₃ Br	12.09
CH ₃ SH	12.12
BrCl	12.09
CO ₂	12.04
SO ₂	11.94
Trimethylene oxide ^c	
Ethanol ^c	
Cyclopropane ^d	
Br ₂ ^e	
(CH ₂) ₂ O ^f	12.03

- a data from von Stackelberg (1954) unless otherwise specified
b Pauling and Marsh (1952)
c Sargent and Calvert (1966)
d Hafemann and Miller (1969)
e Allen and Jeffrey (1963) (also forms in tetrahedral structure)
f McMullan and Jeffrey (1965)

Table 3-7

Structure II Hydrate Formers which have been
Studied by X-ray Diffraction^a

<u>Hydrate Former</u>	<u>Unit Cell Size (Å)</u>
$(\text{CH}_3)_3\text{CH}$	17.53
$\text{C}_2\text{H}_5\text{Cl}$	17.30
CH_2Cl_2	17.31
CHCl_3	17.30
1,3-Dioxolane ^b	17.10
Ethanol ^b	
Trimethylene Oxide ^b	17.10
Cyclopropane ^c	
Tetrahydrofuran ^b	
Acetone ^d	17.16
Tetrahydrofuran ^b	17.13
2,5-Dihydrofuran ^b	17.2
Cyclobutanone ^b	17.09
Propylene Oxide ^b	17.10

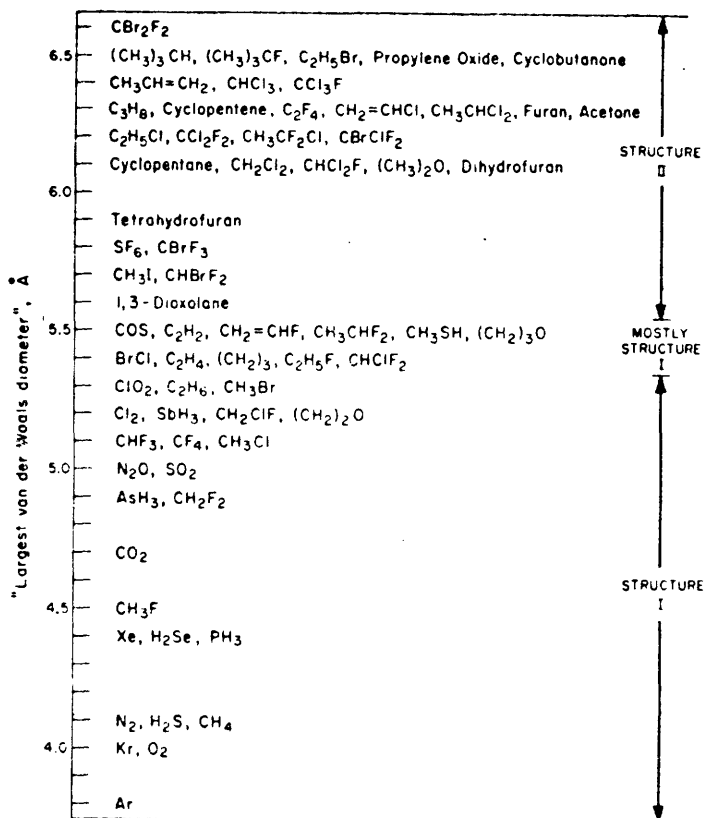
- a from von Stackelberg (1954) unless otherwise specified.
Numerous gas mixtures also form this clathrate structure.
(See Figure 3-10)
- b Sargent and Calvert (1966)
- c Hafemann and Miller (1969)
- d Quist and Frank (1961)

Table 3-8

Dimensions of Clathrate Cages

Radii in A from center of polyhedron to nearest and furthest vertex*

	<u>Minimum</u>	<u>Maximum</u>
Dodecahedron	3.85	3.95
14-hedron	4.05	4.60
15-hedron	4.45	4.90
16-hedron	4.65	4.75



Known hydrate formers with experimentally determined or assumed structure compared with molecular dimensions.

* Effective radii of space available for included species requires subtracting out van der Waal radii of oxygen atom (1.4 A)

Table 3-9

Hydrate Structures for Peralkylated Cation Clathrate Hydrates

		<u>Cell Dimensions (Å)</u>	<u>Example</u>
I. Orthorhombic	no. of vertices = 80 (H ₂ O molecules)	a = 21.1	$R_4^+ N_4^+ F^- \times 32.8H_2O^*$
	no. of Pent. dod. = 6	b = 12.7	
	no. of large voids = 8	c = 12.4	
II. Tetragonal	no. of vertices = 172	a = 23.6	$R_4^+ N_4^+ nC_4H_9COO^- \times 39.5H_2O^{**}$
	no. of pent. dod. = 10	c = 12.4	
	no. of 14-hedra = 16		
	no. of 15-hedra = 4		
III. Cubic	no. of vertices = 368	a = 24.6	$[R_4^+ N_4^+]_2 C_2 O_4^{=} \times 57.3H_2O^{***}$
	no. of pent. dod. = 16		
	no. of large voids = 48		
IV. Cubic (truncated octahedron)	no. of vertices = 12	a = 7.68	$HPF_6 \times 6H_2O^{****}$

* McMullan et al. (1963)

** Bonamico et al. (1962)

*** Beurskens et al. (1963)

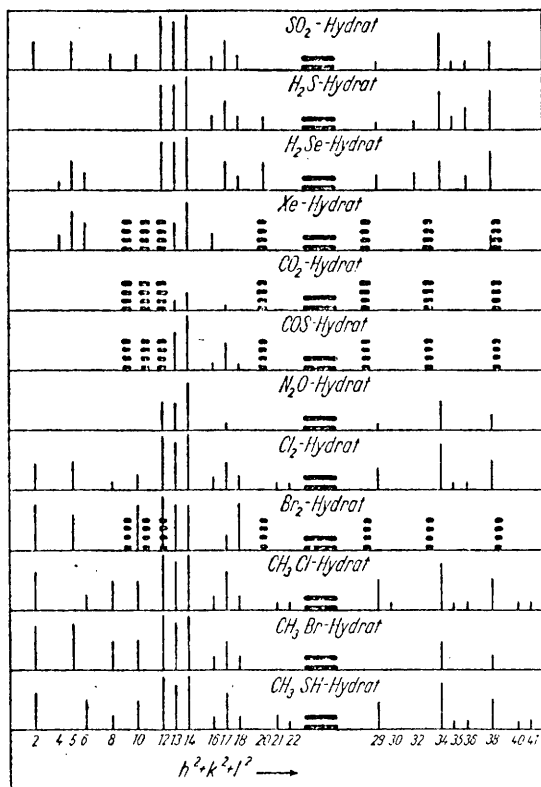
**** Bode and Teufer (1955)

With a van der Waal diameter of 5.68 Å, bromine was expected to form a structure I clathrate. However, single crystal x-ray diffraction by Allen and Jeffrey (1963) showed that a tetragonal unit cell was formed with dimensions and symmetry similar to that in the amines.

Other hydrates have been observed to form both structures I and II depending on the temperature and pressure conditions during formation. Cyclopropane, ethanol, and trimethylene oxide are examples of compounds which have been reported to form both structures (Sargent and Calvert, 1966; Hafemann and Miller, 1969).

The powder diffraction patterns obtained by von Stackelberg for various structure I and II clathrates are shown in Figures 3-11 and 3-12. Although the different gas hydrates do vary as to the major reflections observed, this may be due partly to the difference in scattering capability of the included guest species. Some differences may also have resulted from crystal orientation. The patterns are nevertheless distinctive, and a comparison with the water/methane gel data (Table 3-10 and Figure 3-16) indicates that the structure of the gelant crystals is probably neither structure I or II. A comparison of these data with all of the data for the various ice structures also produced no apparent match. Due to these anomalous results, several other systems ($\text{CO}_2 + \text{H}_2\text{O}$, $\text{N}_2 + \text{H}_2\text{O}$, and air + H_2O) were also studied. Samples (presumably clathrate crystals) were formed by adding a small amount of H_2O vapor to the gas stream and subsequently impinging the vapor onto the liquid nitrogen-cooled sample stage (maintained at a temperature appropriate for clathrate formation). All of these

Figure 3-11 Powder X-ray Diffraction Patterns for Structure I Hydrates

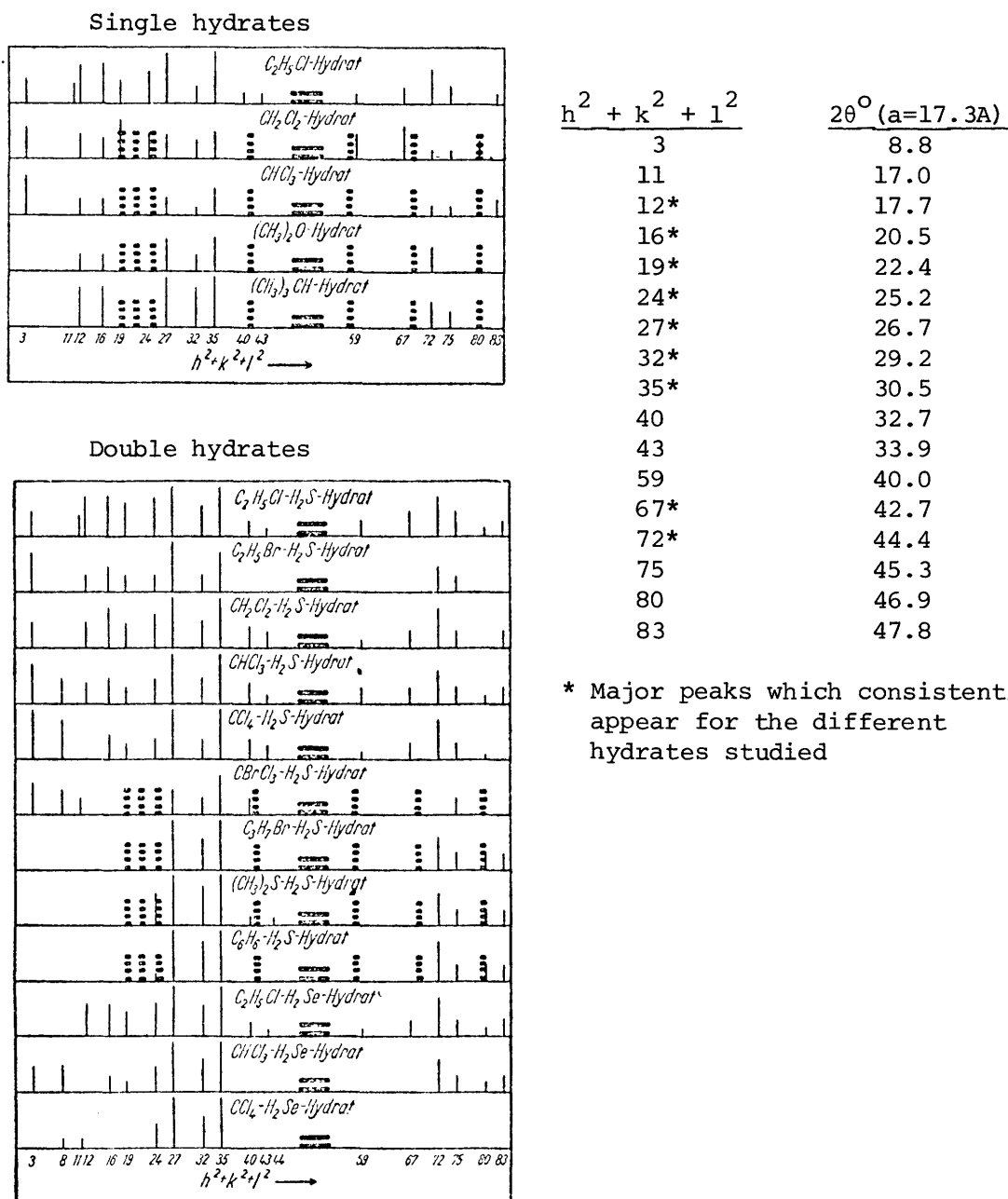


$h^2 + k^2 + l^2$	$2\theta^\circ$ (a=12Å)
2	10.4 ^o
4	14.7
5	16.5
6	18.1
8	20.9
10	23.4
12*	25.7
13*	26.8
14*	27.8
16	29.7
17	30.7
18	31.6
20	33.4
21	34.2
22	35.0
29	40.4
30	41.2
32	42.6
34*	43.9
35	44.6
36	45.3
38*	46.6
40	47.9
41	48.5

Small dashed lines represent ice peaks. Long dashed lines represent diffuse peak due to included species. From von Stackelberg (1951)

* Major peaks which consistently appear for the different hydrates studied

Figure 3-12 Powder X-ray Diffraction Patterns for Structure II Hydrates



Small dashed lines represent ice peaks. Long dashed lines represent diffuse peak due to included species. From von Stackelberg (1951)

Table 3-10

X-ray Diffraction Data for Methane-Water Gel

<u>2θ (degrees)</u>	<u>Relative Intensity (I/I_{max})</u>
22.5	100
23.9	55
25.5	45
28.4	6
29.3	10
31.1	3
39.5	19
42.5	74
49.5	45

clathrates were produced and analyzed at cryogenic temperatures, and the results were similar to that of the methane/water gel. The highest temperature sample used ($\text{CO}_2 + \text{H}_2\text{O}$ at 200 K) gave a pattern slightly different from the rest and more closely approaching that observed by von Stackelberg for structure I clathrates. This suggests that the low temperature may cause a slightly different structure than originally expected. These gelant crystal data were, therefore, indexed separately and found to fit reasonably well to either a cubic unit cell of dimension $a = 14.8 \text{ \AA}$ or a tetragonal unit cell with dimensions $a = 11.9 \text{ \AA}$, $c = 10.1 \text{ \AA}$. No smaller unit cell was possible for the observed data. Although larger unit cells would certainly be possible, the small number of peaks would indicate that this is unlikely. The probable unit cell size seems large in comparison to those for the various ice structures, and would, therefore, indicate that a clathrate structure is present, possibly a distortion of the 12 \AA cubic or a completely new structure.

3.1.5 Methanol Clathrates

A host of compounds other than water are also known to form clathrate compounds. Examples include hydroquinone (whose structure was deduced prior to the hydrates), phenol, Dianin's compound, etc. (Palin and Powell, 1945, 1947, 1948ab; Mak et al., 1976; Flippen et al., 1970; von Stackelberg, 1956; Powell and Wetters, 1955; Hardy et al., 1976). These compounds have OHO type hydrogen bonding and can be

considered in two groups, those having two OH groups for hydrogen bonding and those having a single OH group. Although methanol has not previously been shown to form a clathrate structure, the possibility certainly exists, and the structure would likely be similar to those formed by other compounds containing a single OH group. The basic cage structure for all of these compounds is a hexagon ring of OHO bonds with the remaining portion of each of the six molecules alternating at some angle above and below the plane of the hexagon (Figure 3-13). Identical hexagons stack one on top of the other to form a cage stabilized by the presence of a guest molecule inside the cage. The infinite stacks must then pack together in some orderly arrangement. All of the reported compounds have displayed an $R\bar{3}$ space group which occurs when the packing is hexagonal but the OHO hexagons do not lie side by side in the same plane (Figure 3-14). This space group was thought to be a likely possibility for the methanol clathrate. Also, because of the small symmetrical methyl group, a $P\bar{3}$ and a $P6$ space group were also considered (Figure 3-15). Both of these space groups have the hexagons in the same plane. However, within these space groups, several packing arrangements are still possible: the hexagons which lie side by side in the same plane may have a point-to-point, an edge-to-edge, or even a shifted edge arrangement. Also, the OHO hexagons may be flat or puckered, and the methyl groups may either alternate up and down from the hexagon at some angle or lie flat in the same plane. All of these structures were thought to be possible. Using the packing dimensions calculated from the atomic

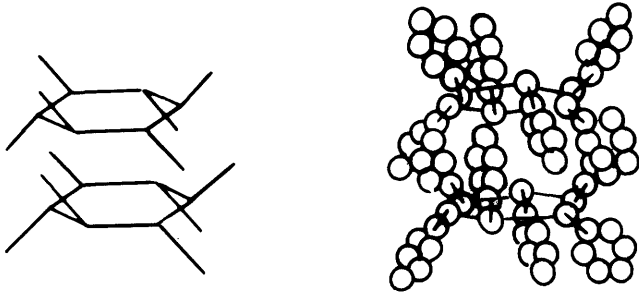


Figure 3-13 Basic Cage for Phenol Clathrate
OH Groups Bond in Hexagon Rings
with Benzyl Group Alternating up
and down from Plane of Hexagon.
Identical Rings Stack together to
Form Cage. Two OH Rings are Shown
Above.

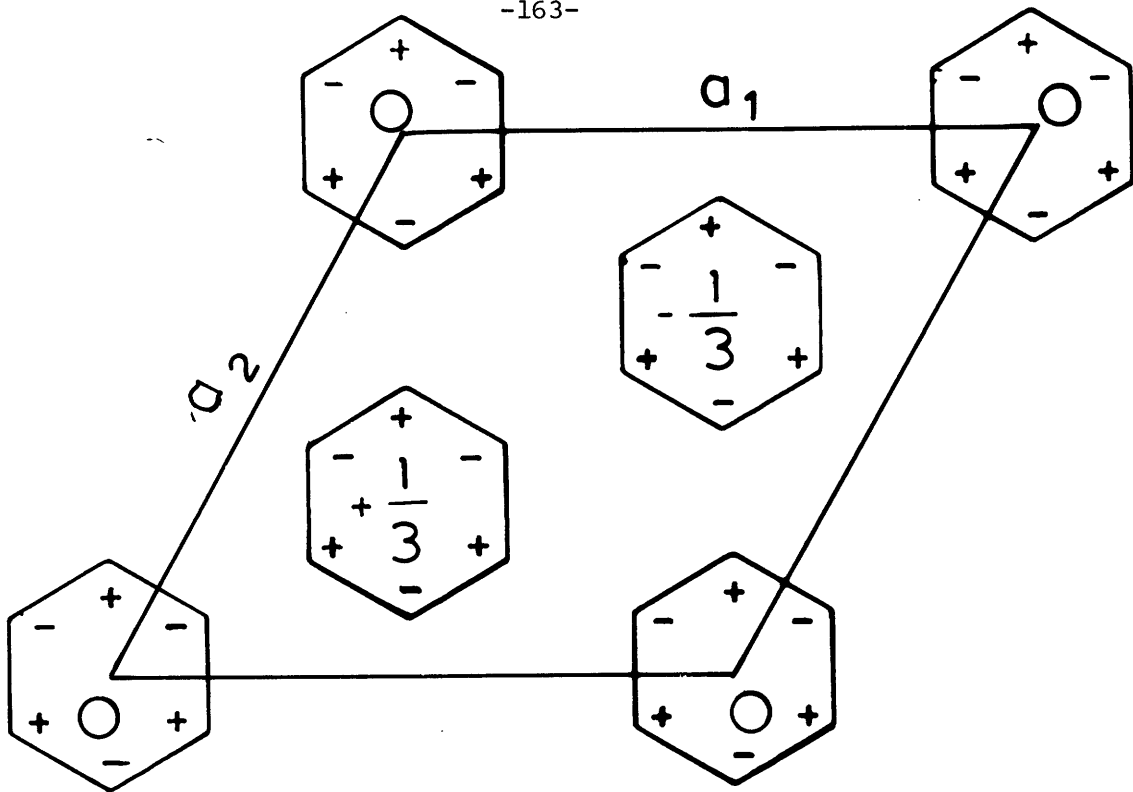


Figure 3-14 Possible packing arrangement for methanol clathrate cages with $R\bar{3}$ space group. Numbers in the centers of the hexagons refer to the plane in which the hexagon lies with respect to the c axis, i.e. the "0" plane is the plane of the paper; the "+1/3" plane is above and parallel to the plane of the paper with a shift of 1/3 the distance of the length of a cage (as in Figure 3-13). The + and - signs refer to the direction of the methyl group, whether it projects above or below the plane of the paper.

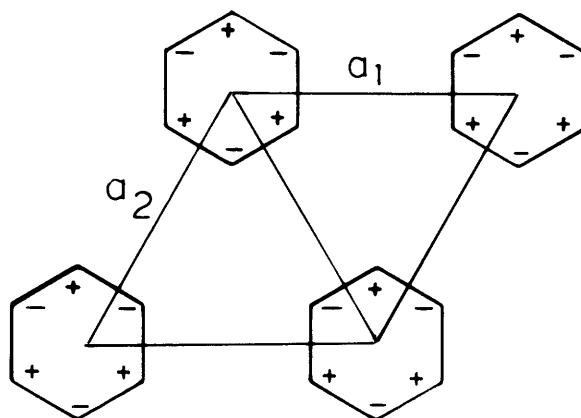
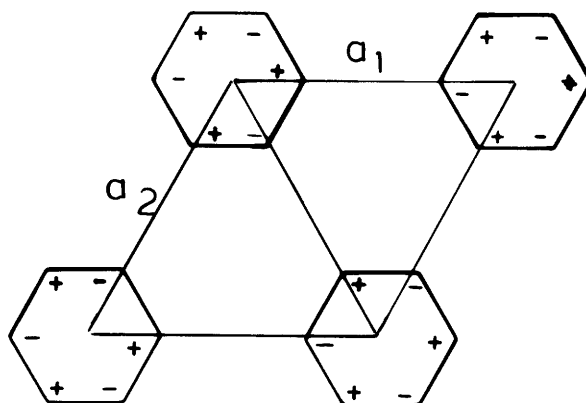


Figure 3-15 Possible Packing Arrangements for Methanol Clathrate Cages Where Hexagons of OHO Bonds Lie in Same Plane. $P\bar{3}$ Space Group Results. The + and - Signs Refer to the Direction of the Methyl Group, Whether it Projects Above or Below the Plane of the Paper.

spacings in solid methanol ($r_{\text{CH}_3} = 1.8 \text{ \AA}$, C-O bond length = 1.4 \text{ \AA}, O-H-O bond length = 2.62 \text{ \AA}), appropriate unit cell dimensions were determined for each of the structures suggested above. Due to possible variation in angle of the methyl group, a range of a and c dimensions were possible and several combinations gave reasonable fits for the data. For the $\overline{\text{P3}}$ or P6 space group, possible dimensions were $a = 8.9$, $c = 4.8$; $a = 10.3$, $c = 4.1$; and $a = 10.1$, $c = 4.45$. For the $\overline{\text{R3}}$ space group, the data could be indexed to a unit cell with $a = 17.0$, $c = 4.6$. The $\overline{\text{R3}}$ space group has systematic absences in reflection peaks--the only possible reflections being those for $-h + k + l = 3n$. This was taken into account when indexing the peaks. Atomic positions were then determined for the different packing arrangements, and expected intensities computed. The expected intensities were then compared with those observed. Major peaks can only occur when the atomic structure yields a large relative intensity. On the other hand, if the atomic structure predicts major peaks other than those observed, one can only make a value judgement as to whether severe orientation of the crystals could have occurred or that the structure is inappropriate. Taking these factors into consideration, the best fit was a $\overline{\text{P3}}$ with points of the hexagons matching and unit cell dimensions $a = 8.9$ and $c = 4.8$. This packing arrangement is a very compact one, and drawings using appropriate dimensions for the atoms would indicate that the methyl groups must, therefore, be at $\sim 60^\circ$ angles and project slightly off-center in a pinwheel fashion. Table 3-11 gives the indexed peaks relative to this unit cell along with the expected and observed intensities based on this atomic arrangement.

Table 3-11

X-ray Diffraction Data for Methane-Methanol Gels and
Calculated Values for Proposed Structure

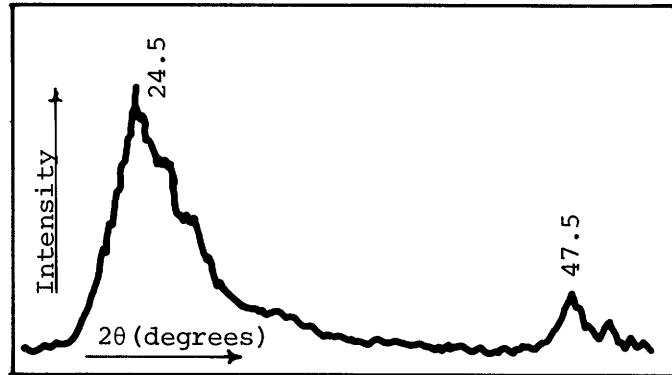
<u>$\sin^2 \theta$</u>	<u>Angle</u>	<u>Obs. rel. Intensity</u>	<u>Obs. rel. $F ^2$</u>	<u>Cal. rel.* $F ^2$</u>
.178	20.5	66	34	27
.234	27.1	100	71	100
.302	35.2	33	31	70
.344	40.2	85	95	28
.362	42.4	22	26	0.8
.379	44.5	43	55	3
.407	48.0	28	40	4
.418	49.4	10	15	-
.438	52.0	8	12	4
.454	54.0	9	15	8
.487	58.3	54	100	46
.528	63.8	9	20	3

* for $P\bar{3}$ $a = 8.9$ A, $c = 4.8$ A (structure discussed in text)

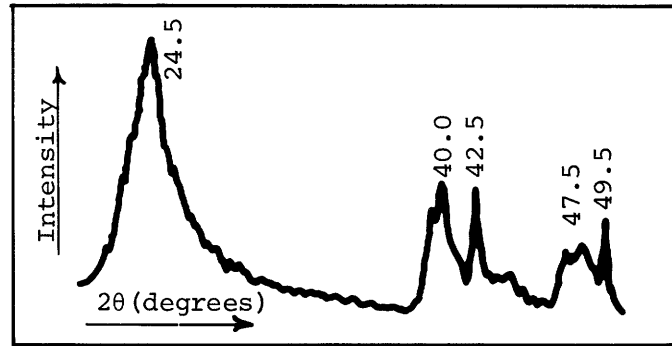
3.1.6 X-ray Diffraction of Gels

Very little research has been done on the study of gels using x-ray diffraction. However, the gel itself consists of dispersed flocculated crystalline particles in a liquid. In the gel form, one would, therefore, expect to see diffraction peaks corresponding to the crystalline structure of the particles superimposed on the broad diffraction peaks corresponding to molecular distances in the liquid phase. As the liquid is vaporized from the sample leaving only the crystalline particles, the broad liquid peaks should disappear leaving only the sharp peaks due to their crystalline structure. The observed peak changes during drying of the methane/water gel are shown in Figure 3-16.

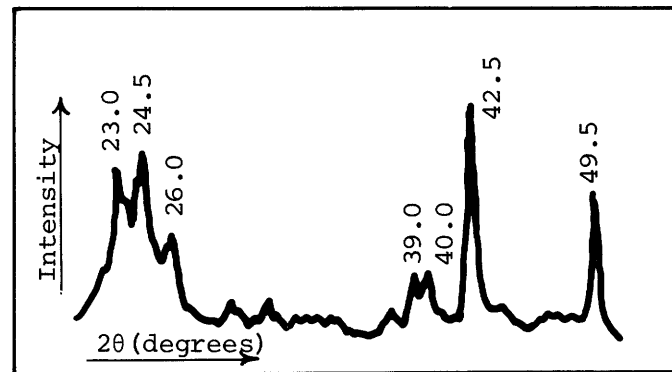
Petz (1965) studied the structure of liquid methane and found that two peaks were observed, a major peak at 24° and a small peak at 47° . Both of these peaks were observed in the gel data. However, as methane was vaporized from the gel sample, another broad peak appeared at 40° . This corresponds with x-ray diffraction data reported by McLennan and Plummer (1929) for solid methane. It also corresponds to the broad peak in cubic ice. However, if this peak were due to a cubic ice type bonding between the particles, the peak would be expected to persist even when the liquid methane peaks are no longer observed. This, however, did not occur, and the peak disappeared with further methane evaporation. Probably this peak represents a somewhat ordered liquid methane entrapped in the gel structure.



(a)



(b)



(c)

Figure 3-16 Transformation of x-ray powder diffraction pattern as liquid evaporates from gel
(a) Liquid methane peaks
(b) Liquid/solid methane peaks + crystal peaks
(c) Primarily crystal peaks, but further drying sharpens peaks

Although the water/methane gels demonstrated the sequence quite clearly, the methanol methane gels could not be easily freed from the presence of the liquid methane peaks. The crystal peaks, however, were easily identifiable (Appendix O).

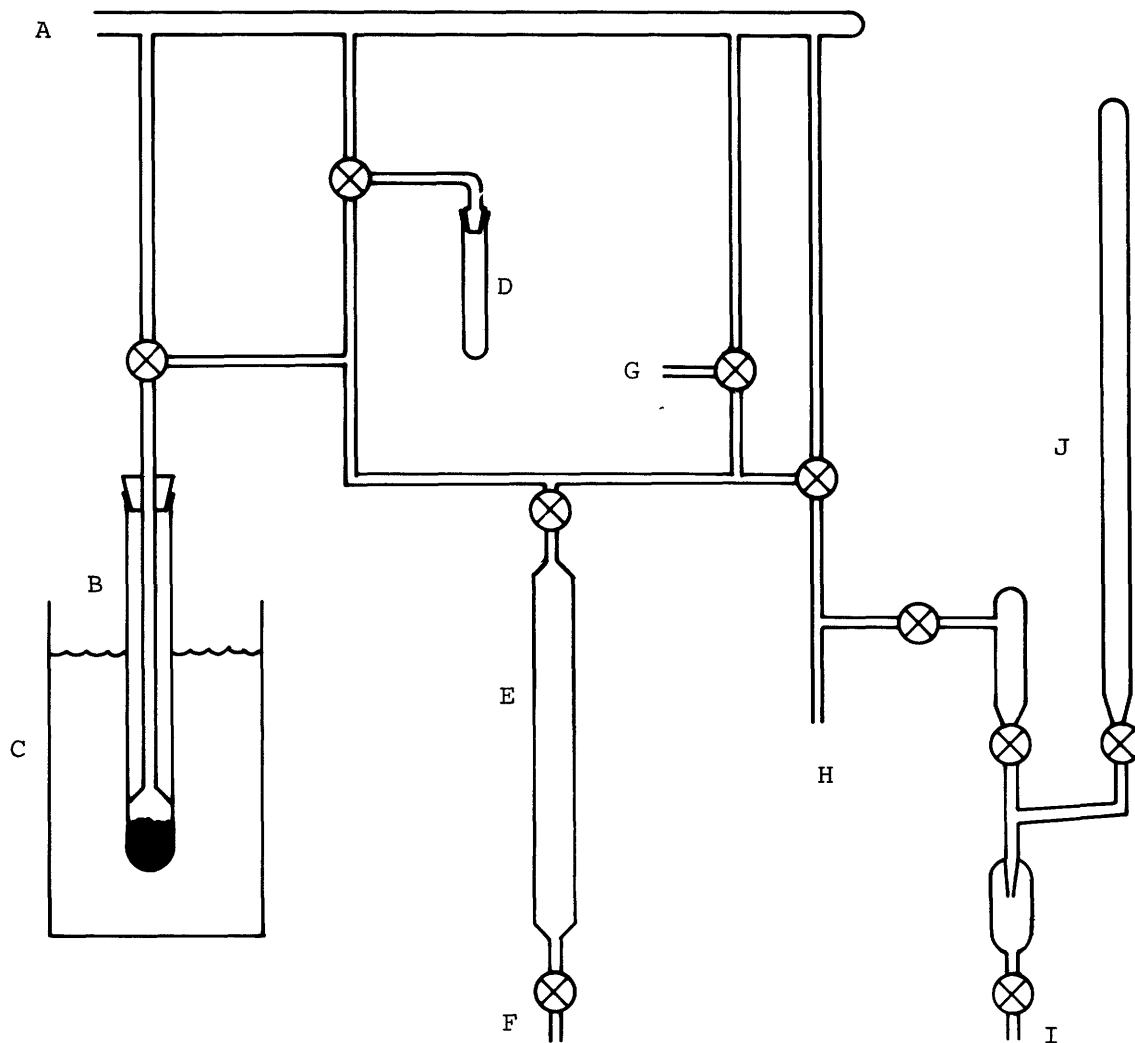
3.2 Thermodynamic Stability of the Gelant Particles

As the previous evidence suggested that the gelant particles were solid clathrates, an important industrial scale consideration is the region of thermodynamic stability for such solid crystals. This will be of interest in designing any industrial scale process for producing the fine gelant particles, and also will indicate at what conditions they will dissociate during gel revaporization. The natural gas components, methane and ethane, have previously been studied at the low temperatures and moderate pressures of interest here (See discussion in Chapter 2), and their region of thermodynamic stability has been well established. At cryogenic temperatures the conversion is $\text{clathrate} \rightleftharpoons \text{ice} + \text{gas}$, and the decomposition pressures are generally ≤ 1 atm. This requires a vacuum apparatus with provisions for making very fine ice crystals. In an investigation by Falabella and Vanpee (1974), such an apparatus was built and used to study the methane and ethane hydrate stability in the ranges 150 K to 190 K for methane and 200 K to 240 K for ethane. (A similar apparatus had been used previously by Barrer and Edge (1967) in their study of inert gas

hydrates.) After completion of their experimental investigation (Fallabella and Vanpee) were kind enough to allow us to use this apparatus to study methanol clathrate stability. The experimental procedure, however, was not entirely adequate for such an investigation, and the reason for this will be discussed after a brief description of the apparatus and procedure.

The apparatus consisted of a reaction vessel with a cryogenic temperature-controlled bath, a vacuum distillation section for producing fine ice crystals, and a section for monitoring the pressure and volume. (See Figure 3-17) The experimental sequence was as follows: 1) The reaction vessel was evacuated down to ≤ 0.05 newtons/m² (3 μ m Hg). 2) From the vacuum distillation section (D), a degassed sample of ice at 93 K (also under vacuum ≤ 0.05 newtons/m²) was allowed to warm. As the vapor pressure of the ice increased, the water vapor was caused to flow into the reaction vessel (B). During this time, the reaction vessel (which was filled with 0.32 cm diameter steel balls) was maintained at 93 K. The water vapor nucleated and grew into fine ice particles on the surface of the steel balls. 3) After a sufficient number of ice crystals had been formed, the reaction vessel was placed in the cryogenic temperature bath which had previously been stabilized at the temperature to be investigated. An appropriate amount of the desired gas was then added to the reaction vessel. The actual amount was chosen such that the resulting pressure was well above that for the expected ice-hydrate equilibrium. At this point, the ice would react with the gas to form clathrate and a decrease in system pressure would

Figure 3-17 Low-Temperature Clathrate Equilibrium Apparatus



- | | |
|--|-----------------------------|
| A) To vacuum pump | F) To mercury leveling bulb |
| B) Reaction vessel filled with steel ball bearings | G) To gas supply |
| C) Cryogenic temperature-controlled bath | H) To McLeod Gauge |
| D) Sample bulb for pure solid-- | I) To mercury leveling bulb |
| source for vacuum distillation | J) Mercury manometer |
| E) Burette used for measuring volume change | |

be detected. However, to obtain such observable reaction rates, it was particularly important to have very fine ice crystals, and often it was even necessary to bombard the crystals with steel balls (accomplished using a mechanical shaker on the reaction vessel). It is not certain whether the conversion proceeded with the surface molecules reacting to form clathrate and thus coating the particles. Barrer and Edge (1967) postulated this mechanism, suggesting that bombardment acted to grind off the clathrate coating on the particles. It is also possible that the reaction proceeded in the vapor phase with H_2O evaporation and subsequent clathrate formation on separate nucleation sites. Here bombardment with steel balls would increase the total surface area available for evaporation. 4) After approximately 50 percent or more of the pure solid had converted to clathrate, the system pressure was gradually lowered until a noticeable reverse reaction (increase in pressure) occurred, indicating conditions favorable to ice formation. Subsequent cycling above and below the equilibrium point, using decreasing pressure increments, gave further accuracy in pinpointing the ice-clathrate equilibrium decomposition pressure for that particular reactor temperature. To initiate the original clathrate conversion invariably required subjecting the ice crystals to a pressure well in excess of that required for ice-clathrate equilibrium. However, once the solid had been seeded with clathrate crystals, the reactions proceeded readily in accordance with the thermodynamic stability of the solid phase present.

When this apparatus and procedure were used to study the thermodynamic stability of methanol clathrates, difficulties were encountered

in forming the fine crystals of pure solid methanol. Methanol has a very low vapor pressure at its freezing point (estimated to be 1 μ m Hg) For the nucleation and growth of fine methanol crystals, the partial pressure of the methanol must be kept below this value during the vacuum distillation procedure. This can be accomplished by controlling the temperature of the degassed sample of solid methanol, maintaining it at or below its freezing point. However, the vapor pressure is then so low that only diffusion will transport the methanol molecules into the reaction vessel. Such a procedure would require an excessive length of time (estimated to be \approx 10 hours) due to the long capillary connecting lines. This was not considered feasible with this particular apparatus due to the non-negligible vacuum leakage which would result over such a long time span. Also there were difficulties in keeping the reaction vessel walls and connecting lines warm enough to avoid nucleation and particle growth at these locations. (For best results the ice particles should be formed on the steel balls.) In an effort to find a more suitable technique for forming fine solid methanol particles, two other procedures were tested. Methanol vapor was added to a helium carrier gas and subsequently projected onto a cold collecting surface. Again, at partial pressures above the pure solid vapor pressure, nucleation of liquid droplets occurred with further freezing into a single solid mass. At the very low partial pressures, heat transfer was not rapid enough (for reasonable flow rates) to form any solid. A second, cryogrinding, procedure was also tried. Here a mortar and pestle were used in an attempt to grind solid methanol under liquid nitrogen. However, solid

methanol at such temperatures is particularly hard, and it proved impossible to break up the solid mass with any reasonable amount of force. Although the procedure for studying clathrate-pure solid equilibrium might still be feasible with some equipment modifications to improve the vacuum distillation technique, the temperature control of the various solid surfaces would still be critical. Because of such difficulties, this technique was not pursued further. Two other experimental studies, microscopic observation of the gelant particles and solid phase composition analysis, were instead designed to obtain further evidence that the gelant particles were, indeed, clathrate crystals, and to determine further how stable such crystals were to temperature and pressure changes.

3.3 Microscopic Observation of the Gelant Particles

The microscope study was originally designed with three objectives:

- 1) to determine whether the particles behaved as clathrate crystals or pure solid crystals;
- 2) if the behavior proved to be consistent with the clathrate theory, to further determine the decomposition temperature (at atmospheric pressure) for the clathrate crystals; and
- 3) to determine the size and shape of the primary particles and whether there was a change in size with a change in gelant concentration of the initial vapor mixture (i.e. the natural gas/gelant mixture which contacts the LNG and

through rapid cooling causes nucleation and growth of fine gelant particles).

In the study of Falabella and Vanpee (1974), the three-phase equilibrium temperature for methane-ice-hydrate at one atmosphere was found to be 183 K. Thus, if a particle agglomerate of a methane/water gel could be isolated and gradually warmed, a microscopically observable transformation is likely to occur between 183 K and 273 K provided the particles are indeed clathrate crystals. Further, if a distinct change occurs near 183 K, then such a microscopic technique should be suitable for determining the atmospheric decomposition point for the methane/methanol clathrate.

Experimentally, it was possible to isolate agglomerates if dilute gels were used (See apparatus discussion). Actually, these were dispersions, as the concentration was well below the minimum concentration for gelation. However, the majority of the individual particles were not distinguishable under a light microscope, indicating that the principal dimension was less than $1\mu\text{m}$. Four systems were studied: methane/water, methane/methanol, nitrogen/water, and nitrogen/methanol. The dilute gels of liquid nitrogen were prepared using the same procedure as the liquid methane gels, but liquid nitrogen was used in place of LNG and nitrogen was used as the diluent gas in the vapor mixture. These liquid nitrogen systems were studied primarily because they provided a cheaper and safer system with which to develop and perfect the microscope cold-stage technique. However, they also provide evidence that other cryogenics can be gelled in a similar manner.

In general, the following sequence occurred as the gelant agglomerate was warmed at atmospheric pressure (Figure 3-18).

1) As the liquid (methane or nitrogen) boiled off, the agglomerate became compact, eventually leaving only a thin layer of liquid around the agglomerate. This remaining liquid vaporized as the temperature was increased, and the agglomerate appeared dry when the temperature was $\approx 10\text{K}$ above the cryogen boiling point. Although release of entrapped liquid is likely to occur up to 30 K above this point, it was not visibly detectable.

2) At a temperature well below the pure solid melting point, the agglomerate became dark. With a further increase of 10 to 20 K, the agglomerate sometimes took on a skeleton-like appearance (as if fusion of the particles were occurring). During this time, new crystals appeared on the surface of the microscope slide and continued to grow, while the agglomerate appeared to shrink somewhat. However, in the methanol system, new particles were only occasionally observed, as the small temperature difference between the transformation and melting points did not allow sufficient time for them to grow to a detectable size. Also, it was more difficult to isolate methanol gel agglomerates, as they had less tendency to adhere to the microscope slide. This reduced the amount of vaporized methanol available in the immediate vicinity to form the new crystals of pure solid.

The microscopically observable transformation (i.e. when the agglomerate visibly darkened) in the water/methane system occurred at $178 \pm 5\text{ K}$ which is in agreement with the known decomposition temperature

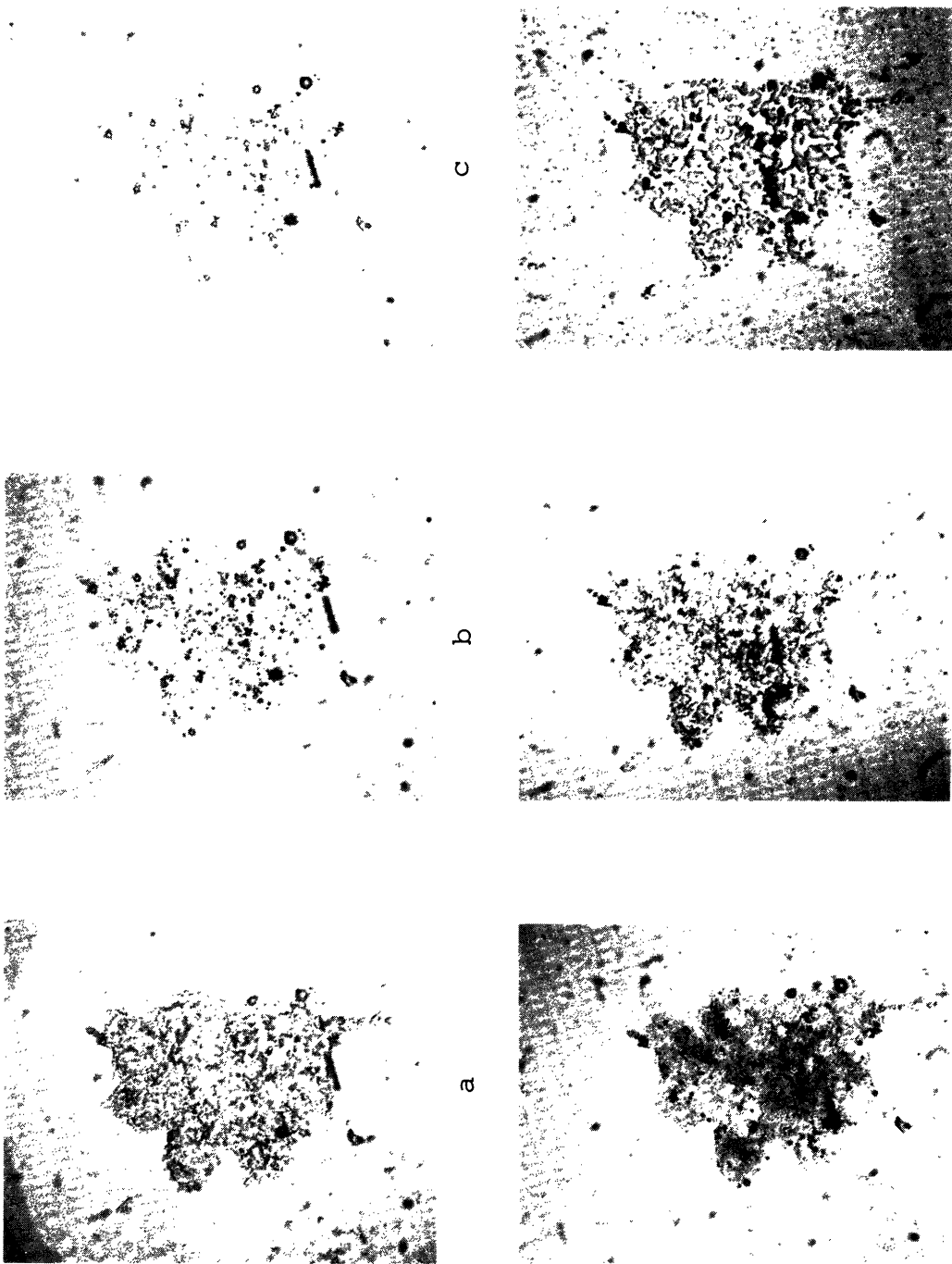
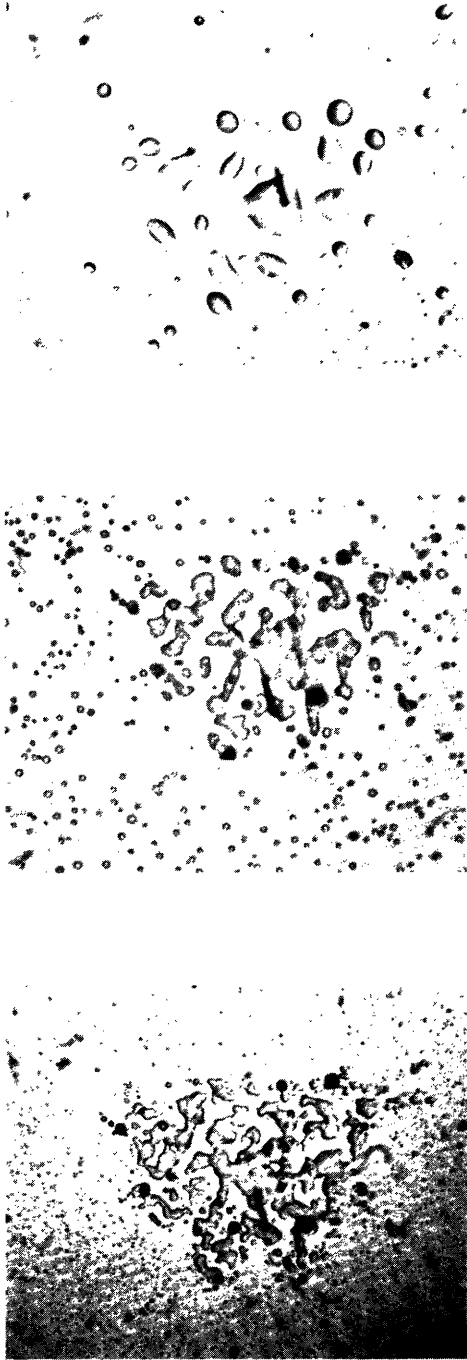


Figure 3-18 (Continued on next page)



i

h

g

Figure 3-18 Methane/Water Gelant Agglomerate
a) 113 K - Liquid methane has vaporized leaving a compact agglomerate. Agglomerate is still saturated with liquid methane at this point.
b) 120 K - Agglomerate drying.
c) 140 K - Agglomerate dry.
d) 180 K - Agglomerate darkening as clathrate decomposes.
e) 200 K - Skeleton-like formation as particles fuse together. New particles of pure solid beginning to appear.
f) 210 K; g) 220 K; h) 250 K - Melting with recrystallization. New particles of pure solid growing larger.
g) 273 K - Melted.

of 183 K. This indicated that the present technique was adequate for determining decomposition temperatures, and an analysis of the other three systems yielded the following results.

<u>Clathrate Compound</u>	<u>Clathrate Decomposition Temp. at Atm. Press.</u>
nitrogen/water	145±5 K
nitrogen/ methanol	115±5 K
methane/methanol	145±5 K

This initial transformation appears to be due to either controlled vaporization or a popping of the clathrate crystals releasing H₂O into the vapor phase. The new ice crystals then formed at appropriate nucleation sites on the microscope slide.

3) As the temperature was further increased (but still held below the pure solid melting point), the agglomerate appeared to melt and recrystallize. This indicates that at higher temperatures, the solid-solid transformation probably occurs with a rupture of the clathrate crystal leaving the water molecules briefly in a random subcooled liquid form until such molecules can reorient to crystallize as a pure solid.

4) Final melting of the remaining agglomerate and the new crystals occurred at the known melting point within ±5 K.

3.4 Solid Phase Composition Analysis

To further confirm the clathrate nature of the solid gelant parti-

cles, an experimental technique was designed to analyze the composition of these particles. Here a pure solid phase should be clearly distinguishable by its absence of natural gas. As the gelant particles are formed by nucleation and particle growth from a vapor phase, there is little likelihood that dissolved gas would be frozen into the pure solid. On the other hand, if the solid is a crystalline clathrate phase, a significant amount of natural gas should be encaged in the clathrate structure. For the natural gas components, methane, ethane, and propane, their hydrate compositions have been studied previously by a number of investigators (Roberts et al., 1940; Frost and Deaton, 1946; Hammerschmidt, 1934). A brief discussion of the techniques used and the results of these studies will indicate the difficulties which can occur in such analyses as well as the accuracy of these previously reported compositions.

Several methods have been used to analyze gas hydrate compositions, but all except one of these have involved indirect calculations from experimentally derived quantities, such as heats of formation. Both methane and ethane hydrate compositions, however, have been determined by direct experimental analysis (Frost and Deaton, 1946). The technique used was as follows. Initially the gas hydrates were formed by bubbling the gas through water in a pressure cell (maintained at a temperature pressure condition favorable to the formation of the clathrate). Once the chamber was filled with a honeycomb mass of hydrate, the excess water was drained from the cell. The cell was then maintained at clathrate favorable conditions for several days to insure that any residual liquid

water would have converted to clathrate. The solid clathrate was then allowed to warm, and the gas released during decomposition was measured along with the amount of residual liquid. The runs were all made above 273 K, but the actual temperature and pressure conditions of hydrate formation were not reported. The compositions for the various runs were as follows.

Methane (99.7% pure)	$\text{CH}_4 \cdot 7.11 \text{H}_2\text{O}$
	$\text{CH}_4 \cdot 7.04 \text{H}_2\text{O}$
Ethane (98.3% pure)	$\text{C}_2\text{H}_6 \cdot 8.06 \text{H}_2\text{O}$
	$\text{C}_2\text{H}_6 \cdot 8.13 \text{H}_2\text{O}$
	$\text{C}_2\text{H}_6 \cdot 8.54 \text{H}_2\text{O}$
	$\text{C}_2\text{H}_6 \cdot 8.33 \text{H}_2\text{O}$

These are all slightly enriched in water compared with the ideal structural formulas (based on known crystal structure and assuming that each cage is filled with a single guest molecule) of $\text{CH}_4 \cdot 5.75\text{H}_2\text{O}$ and $\text{C}_2\text{H}_6 \cdot 7.67 \text{H}_2\text{O}$. This could be due to either a thermodynamic stabilization with less than 100% of the cages filled, or also there could be an experimental problem of not being able to convert all of the excess liquid water. Comparison with theoretical predictions (as discussed in Chapter 2) are not conclusive. Van der Waals and Platteeuw (1959) obtained compositions similar to the experimental values, but Tester et al. (1972) predicted values closer to the ideal formulas.

Two indirect calculational procedures have also been used, the first being based on the following relation.

$$n = \frac{\Delta H_2 - \Delta H_1}{\Delta H_{\text{fusion}}} \quad (3-6)$$

where n = the number of water molecules per molecule of guest species

ΔH_2 = standard heat of reaction for the formation of hydrate from gas and ice.

ΔH_{fusion} = heat of fusion for ice (1437 cal/gmole)

ΔH_1 = standard heat of reaction for formation of hydrate from gas (guest species) and water.

To obtain values for ΔH_1 and ΔH_2 , decomposition pressure versus temperature data can be used along with the Clausius-Clapeyron relation.

$$(3-7)$$

$$dP/dT = \Delta H/T\Delta V$$

Both the ice-hydrate and water hydrate equilibrium curves generally fit nicely to an equation of the form.

$$(3-8)$$

$$\log(P) = A + B/T$$

Combining these two equations gives

$$(3-9)$$

$$\Delta H = \frac{-B(\Delta V)P}{(.4343)T}$$

To determine the composition (i.e. the value of n) requires that both heats of formation be at the same temperature. Thus, a composition can only be determined for 273°K. (Although heat capacity data could be used to extrapolate to other temperatures, the required hydrate heat

capacity values are not available.) Frost and Deaton (1946) obtained sufficient data to calculate the following compositions for the natural gas hydrates: $\text{CH}_4 \cdot 7.18\text{H}_2\text{O}$; $\text{C}_2\text{H}_6 \cdot 8.25\text{H}_2\text{O}$; $\text{C}_3\text{H}_8 \cdot 17.95\text{H}_2\text{O}$ (ideal structural formula $\text{C}_3\text{H}_8 \cdot 17\text{H}_2\text{O}$)

Another indirect method, the "Miller-Strong" (Miller and Strong, 1945,1946) method can be used to determine compositions at different temperatures, but is limited to the 3-phase equilibrium gas-water-hydrate. This procedure uses a salt solution and is based on the following relations.

(3-10)

$$\frac{1}{K} = \frac{[a_{\text{H}_2\text{O}}]^n [a_A]}{[a_{\text{A} \cdot n\text{H}_2\text{O}}]} = \frac{[a_{\text{H}_2\text{O}}]^n [a_A]}{[a_{\text{A} \cdot n\text{H}_2\text{O}}]} \text{ salt solution}$$

pure water

$$\text{or } a_p^n f_p = a_s^n f_s \quad n = \ln(f_s/f_p)/\ln(a_p/a_s)$$

where f_p = fugacity of the guest species at T in the pure water-hydrate system

f_s = the fugacity of the guest species at T in the NaCl aqueous solution-hydrate system

a_p = the activity of water at T in the pure water-hydrate system; assumed to obey Raoult's law

$$a_p = x_{\text{H}_2\text{O},p} = 1 - x_{A,p}$$

a_s = the activity of water at T in the NaCl aqueous solution-hydrate system; assumed to be

$$a_s = a_s^* x_{\text{H}_2\text{O},s} = a_s^* (1 - x_{A,s})$$

a_s^* = the activity of water in NaCl aqueous solution with out any dissolved guest species (A) (available from literature, Bozzo, 1967)

A = guest species

To obtain a value for n , thus, required a knowledge of the equilibrium fugacity (estimated from the decomposition pressure) for the hydrate in pure water and for the hydrate in salt solution. Although this method has not been used for the analysis of methane, ethane, and propane hydrates, Vlahakis et al. (1972) did use this method to study carbon dioxide hydrate and obtained a composition of $\text{CO}_2 \cdot 7.3 \pm .13 \text{H}_2\text{O}$ for the temperature range 273 to 283 K. This composition is significantly different from the value which they also calculated using the Clausius-Clapeyron relation (i.e., $\text{CO}_2 \cdot 5.93 \text{H}_2\text{O}$). Vlahakis et al. further suggest that the Miller-Strong method is more accurate for this case due to the questionable accuracy of the ice-hydrate gas equilibrium curve near 273 K. With regard to this they say only that such equilibrium is difficult to obtain.

Another technique for direct experimental analysis has been used to study hydroquinone clathrates, but as yet has not been applied to hydrates. This technique can be used when the guest compound is in liquid form, and requires an auxiliary liquid component which is miscible with the guest compound, and which itself will not participate as a guest species. Initially, a dispersion of ice in the auxiliary liquid is made. The guest species is then added gradually while the refractive index (or some other suitable parameter) is monitored. Once a certain amount of the guest species has been added, the refractive index will remain constant while the additional guest species is consumed in clathrate formation. When all of the ice has been converted, the refractive index will again change as more guest species is added. From the known quantity

of ice and the known quantity of guest species consumed, the composition can be determined. Although this technique has not been used to determine hydrate compositions, it could be particularly useful for the study of the low-temperature, 3-phase equilibrium gas-hydrate-ice which is of interest here. Also it could be used to determine composition variation with temperature. Both of these might be of interest in any further study of the methanol clathrate.

In the present study, the objective was to determine the composition of the solid phase (i.e., solid gelant particles) of a methane/water gel and a methane/methanol gel. As the composition for the methane hydrate (at 273 K) is known with a reasonable degree of accuracy, comparison of the solid phase composition for a methane/water gel would indicate whether the crystalline particles are indeed clathrates. Further if the composition for the solid-gelant particles in a methane/methanol gel could be determined, this would provide further evidence for the clathrate formation theory and aid in determining the clathrate structure.

Initially, this requires the separation of the solid particles from the liquid medium. As the liquid methane is vaporized from the gel, the initial response will be elastic, i.e. the particle structure will contract. Eventually the particles will become so closely packed together that the gel will be quite rigid, behaving as a porous solid. To remove the remaining liquid methane requires an increase in temperature and/or a decrease in pressure. A typical adsorption/desorption isotherm for a porous solid is shown in Figure 3-19. Here the driving force for

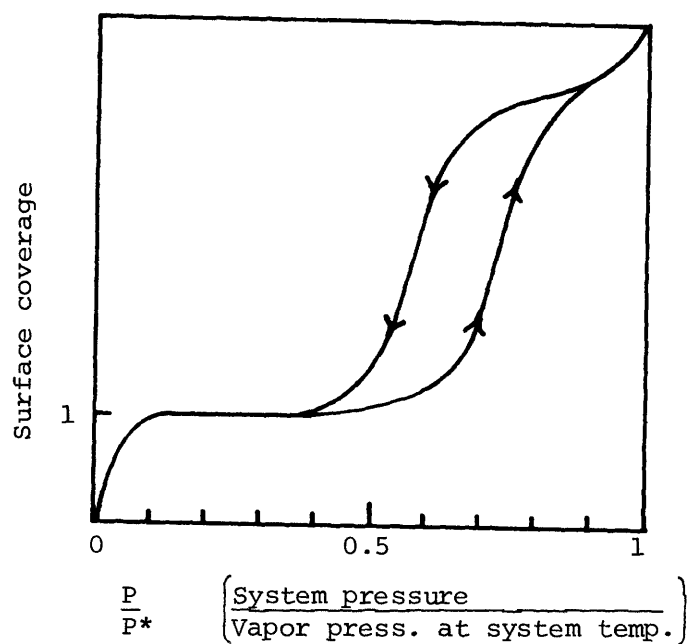


Figure 3-19 Typical Adsorption/Desorption Isotherm for a Porous Solid

desorption is the ratio p/p^* where p is the pressure of the vapor under operating conditions and p^* is the liquid vapor pressure at the temperature of the experiment. For porous solids, a hysteresis loop is often observed in the region $0.3 \leq p/p^* \leq 1$. This may be due to bottle-neck shaped pores which desorb based on the neck diameter but adsorb based on the internal diameter. Below 0.3, the Laplace equation gives an equivalent pore size of ≤ 10 A. This low value is equivalent to molecular dimensions and can no longer be considered capillary condensation, i.e., at most, multilayer adsorption can occur. For lyophobic gels which behave elastically, the capillary condensation region may also show an irreversibility. Here the capillaries may shrink upon desorption, but not re-expand during adsorption. In the present case, however, we are only concerned with desorption and the conditions necessary to desorb as much of the residual liquid methane as possible, while not imposing severe enough conditions to cause the clathrate to decompose to ice. For the water/methane gel, the sample was maintained at 163 K and 0.33 bar. These conditions are well within the clathrate stable region (See Chapter 2) and also give a favorable p/p^* of 0.015. This is much less than 0.3, and thus outside of the region of possible pore condensation effects. In general, the region of 0.1 to 0.3 represents monolayer surface coverage, but the present operating conditions are also well below this range, thus suggesting only fractional surface coverage. To better estimate the amount of residual adsorption, the results from a previous ice-nitrogen adsorption study were used (Adamson et al., 1967). At a

pressure ratio of 0.015 they found that fractional surface coverage occurred, and the fraction ranged from 0.005 to 0.5 (the lower value referred to so-called annealed ice samples while the higher referred to unannealed). The difference between these two values is considerable, and is not clearly explained, but, no doubt, is due to their temperature-pressure cycling into and out of the range of stability for the nitrogen clathrate. For the present case, however, the higher value will be used for estimating the maximum possible error due to adsorption.

Once the gelant particles had been isolated, they were allowed to decompose while the escaping methane vapor was collected and measured. Therefore, it was particularly important to remove initially as much of the residual methane as possible. If the residual amount is significant compared to the amount enclathrated, a composition analysis will be impossible. For the present gels, the particles are assumed to be spherical and approximately 100 Å in radius (dimensions based on rheological data--see Chapter 4). Therefore, the number of enclathrated methane molecules per particle would be 2×10^4 while the number of adsorbed molecules would range from 4.1×10^3 (fractional surface coverage = 0.5) to 41 (coverage = 0.005). This method will thus have a maximum possible error of 20 percent, methane being in excess. In the present case of an elastic contracting gel structure, one might also consider the possibility of completely entrapping a pocket of liquid methane. However, the present temperature condition is within a few degrees of the estimated superheat limit (169 K), and the numerous nucleation sites

present would certainly insure that no residual liquid remained.

During the desorption step in this experimental procedure, there was a decreasing rate of vapor release, and ultimately a decision had to be made as to when equilibrium had been established. In general, adsorption-desorption measurements require very little time (a few minutes maximum) to reach equilibrium if the solid is non-porous. Evaporation and condensation are thus quite rapid. In a porous solid, however, the adsorption-desorption process may be controlled by the rate of diffusion. The present experiments required ≈ 2 hours, but the equilibrium point appeared to be quite distinct (pressure increase < 1 mm Hg/hr which is equivalent to a vapor generation rate of < 1 cc/hr (273 K, 1 bar)). To give further evidence that pore diffusion was not a problem at this point, several calculations were made (Appendix P). From this low rate of vapor generation, the ratio of pore cross-sectional area divided by pore length was calculated. Maximum pore volumes and multilayer adsorption were then estimated using this ratio, and, in all cases the amount of methane which could remain entrapped at this presumed equilibrium point was negligible.

Two runs were made on water/methane gel samples yielding compositions of $\text{CH}_4 \cdot 6.7 \pm 0.5 \text{H}_2\text{O}$ and $\text{CH}_4 \cdot 5.9 \pm 0.5 \text{H}_2\text{O}$. The accuracies reported here are the maximum experimental errors. If a 20% error (methane in excess) occurred due to adsorption, the composition would then be $\text{CH}_4 \cdot 7.4 \text{H}_2\text{O}$ to $\text{CH}_4 \cdot 8.4 \text{H}_2\text{O}$. For both cases, the results are within the expected composition range for the clathrate, and thus sub-

stantiate the clathrate theory.

Several attempts were made to analyze the solid phase of a methane/methanol gel. This technique, however, was not suitable as the clathrate decomposition point was too close to the methane boiling point. When the sample was brought up to 133K at 250 mm Hg, a cycling effect occurred when the sample was isolated. The temperature would rise to 141 K accompanied by a decrease in pressure of 20 mm Hg, after which the reverse effect would occur. The explanation for this behavior is not clear, but a decrease in pressure would indicate either a conversion of pure solid to clathrate or a surface adsorption. It is unlikely, however, that it represents adsorption, as this would require the gel to have been subjected to a lower pressure prior to this point, which was not the case. Thus it seems likely that there was some pure solid present which may have been converting to clathrate, but was not detectable until gas desorption almost ceased. Once the pressure had decreased significantly, desorption and/or conversion of clathrate to pure solid occurred. Although some pure solid may have been present initially, it is likely that the amount was small (less than 10 percent), as the x-ray diffraction results did not indicate that a mixture of pure solid and clathrate was present in the gels.

Even though the methanol clathrate composition could not be determined by this technique, the previous evidence indicates that such a compound does exist and is important in the formation of LNG/methanol gels. For an accurate determination of its composition, the technique

which uses an auxiliary liquid (discussed earlier in this section) would probably be the most appropriate. The success of this study, however, is quite evident as the solid phase composition of the methane-water gel was in good agreement with the previously reported experimental values for the methane hydrate. Along with the results of the x-ray diffraction and the microscope studies, the evidence mutually supports the crystalline-clathrate nature of the gelant particles.

CHAPTER 4 - RHEOLOGY OF LNG GELS

4.1 General Rheological Behavior of Gels

The most important characteristic which distinguishes a gel from other fluids is its ability to resist flow below some minimum shear stress. This type of non-Newtonian behavior may be described by fairly simple models if the behavior is time independent. Two such models are the Bingham plastic and pseudoplastic with a yield stress (Figure 4-1). The Bingham plastic can be completely described by two constants, a plastic viscosity, η_p , and a yield stress, τ_y .

$$\tau = \tau_y + \eta_p (dv/dx) \quad (4-1)$$

where dv/dx = rate of shear

τ = shear stress

For applied stresses below τ_y , the rate of shear, dv/dx , equals zero. Pseudoplasticity is characterized by a shear rate which increases at a faster rate than does the corresponding shear stress. It is often called shear-thinning as its apparent viscosity, $\eta_{app} = \tau/(dv/dx)$, decreases with increasing rates of shear. If the substance also has a yield stress, three constants are necessary to represent such behavior, the simplest model being a power law.

$$\tau = \tau_y + \eta_p (dv/dx)^a \quad (4-2)$$

where a = constant less than 1

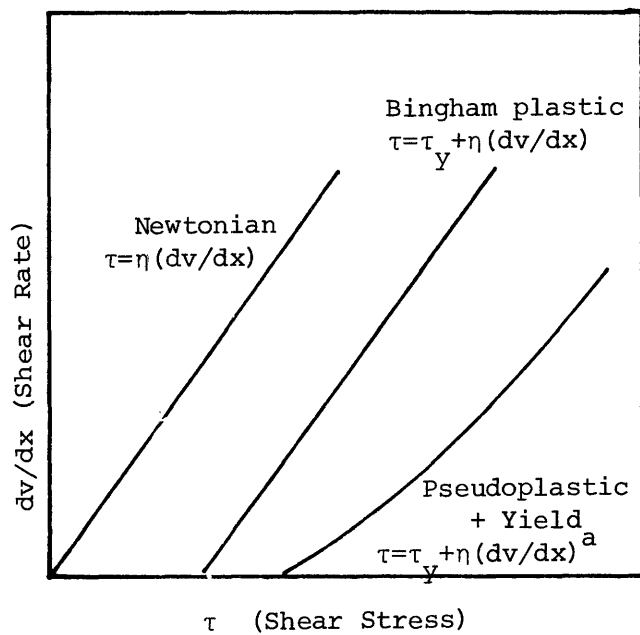


Figure 4-1 Models for Time Independent Flow Behavior

For many gels, these simple models rarely provide a sufficient description of the rheological behavior. In almost all cases there will be a time-dependency effect. The models, however, can be used to represent the steady-state behavior (Figure 4-2) which is almost always pseudoplastic at moderate to low shear rates (1 to 100 sec^{-1}) and Bingham plastic at high rates ($> 1000 \text{ sec}^{-1}$).

The time-dependency effect attributed to gels is thixotropy and is most appropriately defined as a comparatively slow isothermal relaxation, under constant rate of shear or constant shear stress, toward a steady-state value of apparent viscosity. In general, this effect occurs in materials exhibiting a yield stress and/or pseudoplasticity. Many other definitions have been proposed for thixotropy, the most common one being a time dependent, reversible and isothermal decrease in viscosity under steady-shear flow. The opposite effect, an increase in viscosity, has been referred to as "rheopectic". However, according to these common definitions, gels (as well as other time dependent materials) cannot be singly classified as either thixotropic or rheopectic due to a history dependence effect.

The time-dependent rheological behavior of gels has been studied by a number of investigators and distinctive patterns noted. If a gel is initially at rest (and has been for a sufficient length of time), an instantaneous application of some constant shear rate will result in a stress versus time curve similar to those obtained by Jachimiak et al. (1974) (Figure 4-3). Here two basic types of responses are possible, i.e., a maximum stress does or does not appear. Both

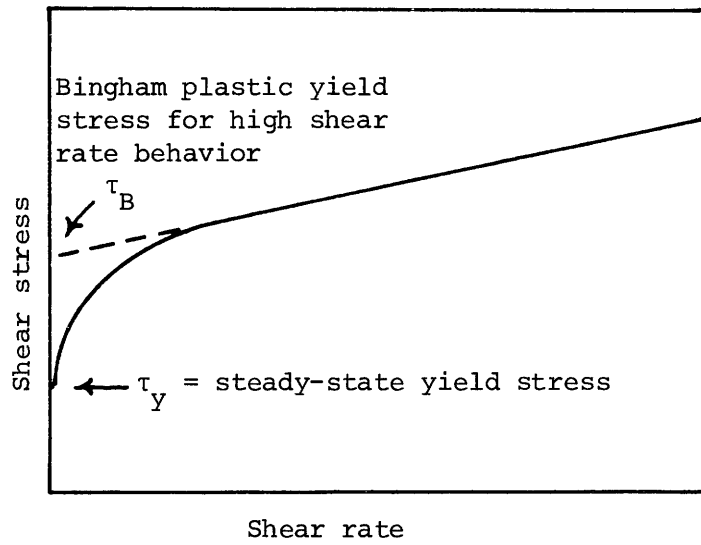


Figure 4-2 Typical steady-state rheological behavior for gels.

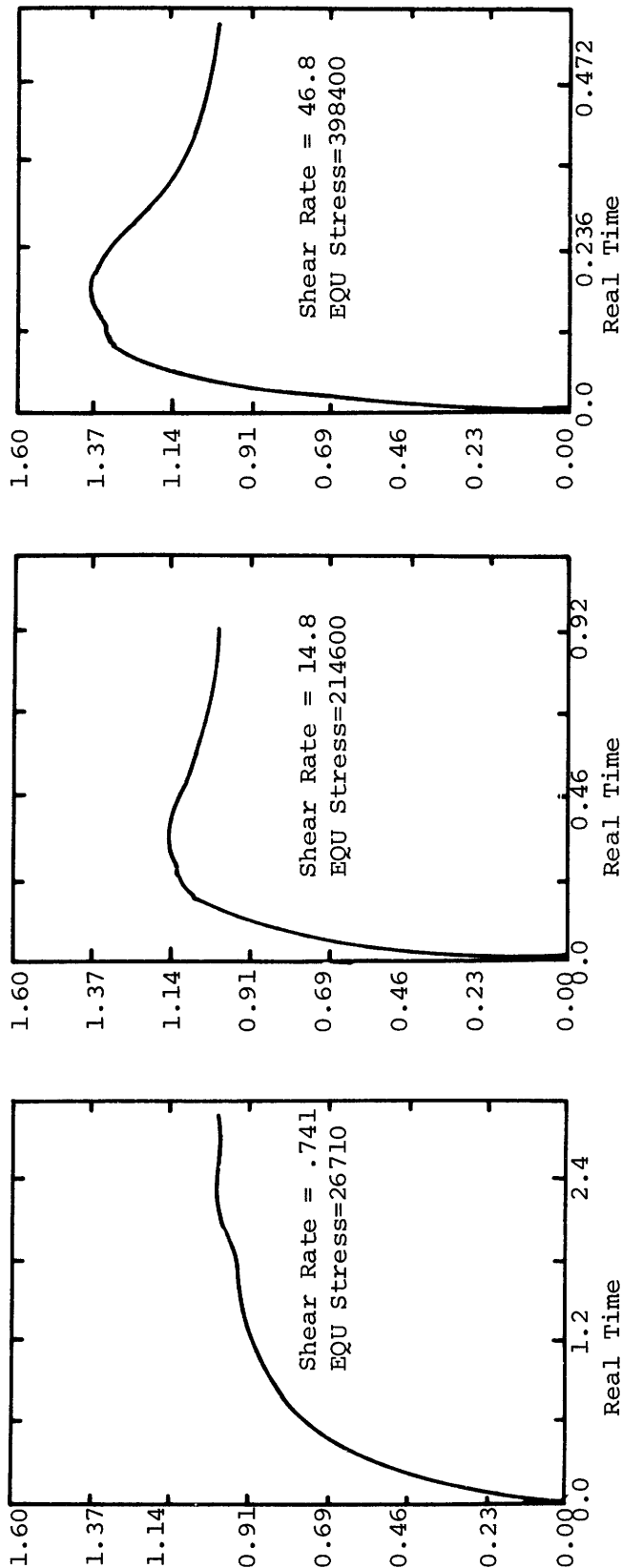


Figure 4-3 Shear stress response for an applied constant rate of shear. Data shown are from Jachimiak et al. (1974) for a solution of polymethylmethacrylate in diethylphthalate.

types of shear stress curves begin with a steep elastic-type response. If the shear rate is low, the steep portion will be followed by a distinct slope change into a somewhat slowly decaying exponential. At higher shear rates the initial elastic-type response shows comparatively little slope change until the peak is reached. A criterion for the onset of this peaking response will be discussed in a subsequent section. If the gel is not initially at rest, but at some other steady-state condition (such as with an applied shear rate which has reached a steady state response in shear stress), and is subjected to an instantaneous change to another constant shear rate, the response will be an initial rapid decay followed by a more slowly decaying portion as was observed by Michaels and Bolger (1962) (Figure 4-4). In this case no peaking occurs, and the change is always in the direction of the new steady-state value. Thus, the previous history of the sample determines whether the time dependency observed is a decreasing or increasing viscosity. If a sequence of increasing shear rate is followed by a decreasing shear rate, the resulting rheogram will have a hysteresis loop as in Figure 4-5. (A clearly distinguishable rheopectic behavior is shown in Figure 4-6). Again, a peak will occur in the shear stress curve if the sample is initially at rest. This behavior is typical of materials with a yield stress. Such materials at rest, provided they have been so for a sufficient length of time, will require an applied shear stress greater than the steady state yield value to initiate flow. This shear stress is often referred to as a static yield stress. Once flow has begun the system will

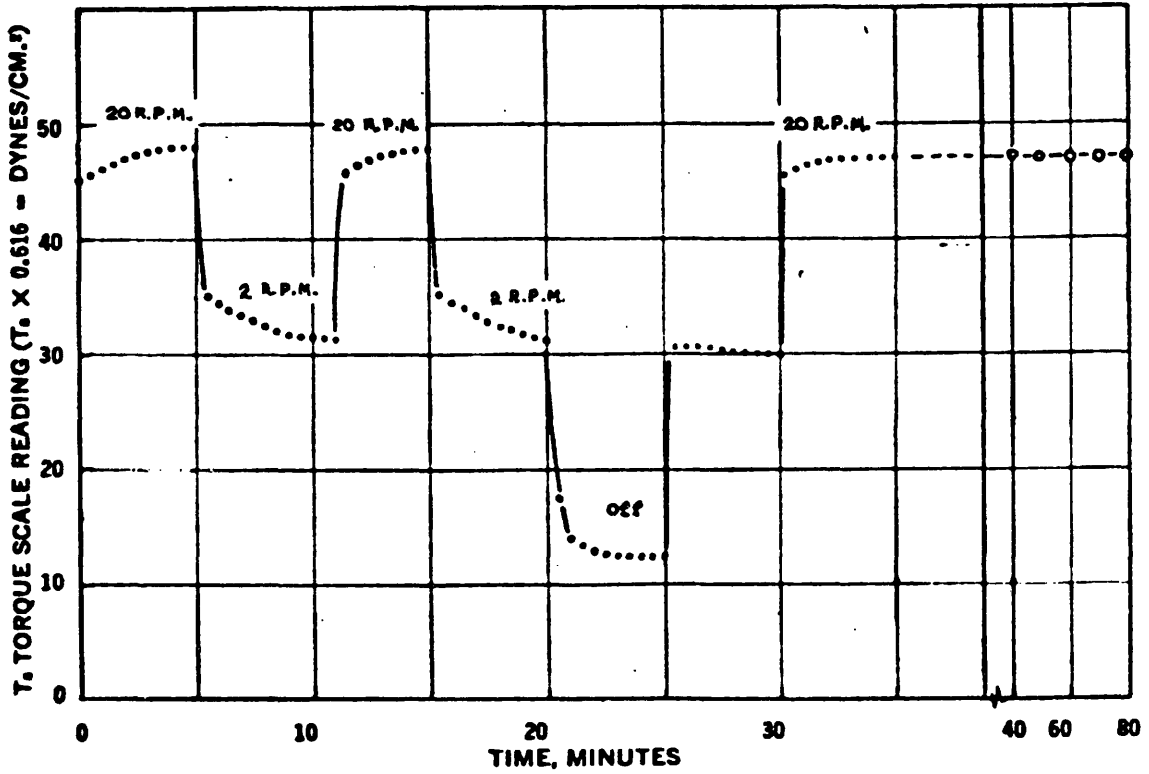


Figure 4-4 Shear stress behavior for varying constant shear rates. Experimental results shown are from Michaels and Bolger (1962).

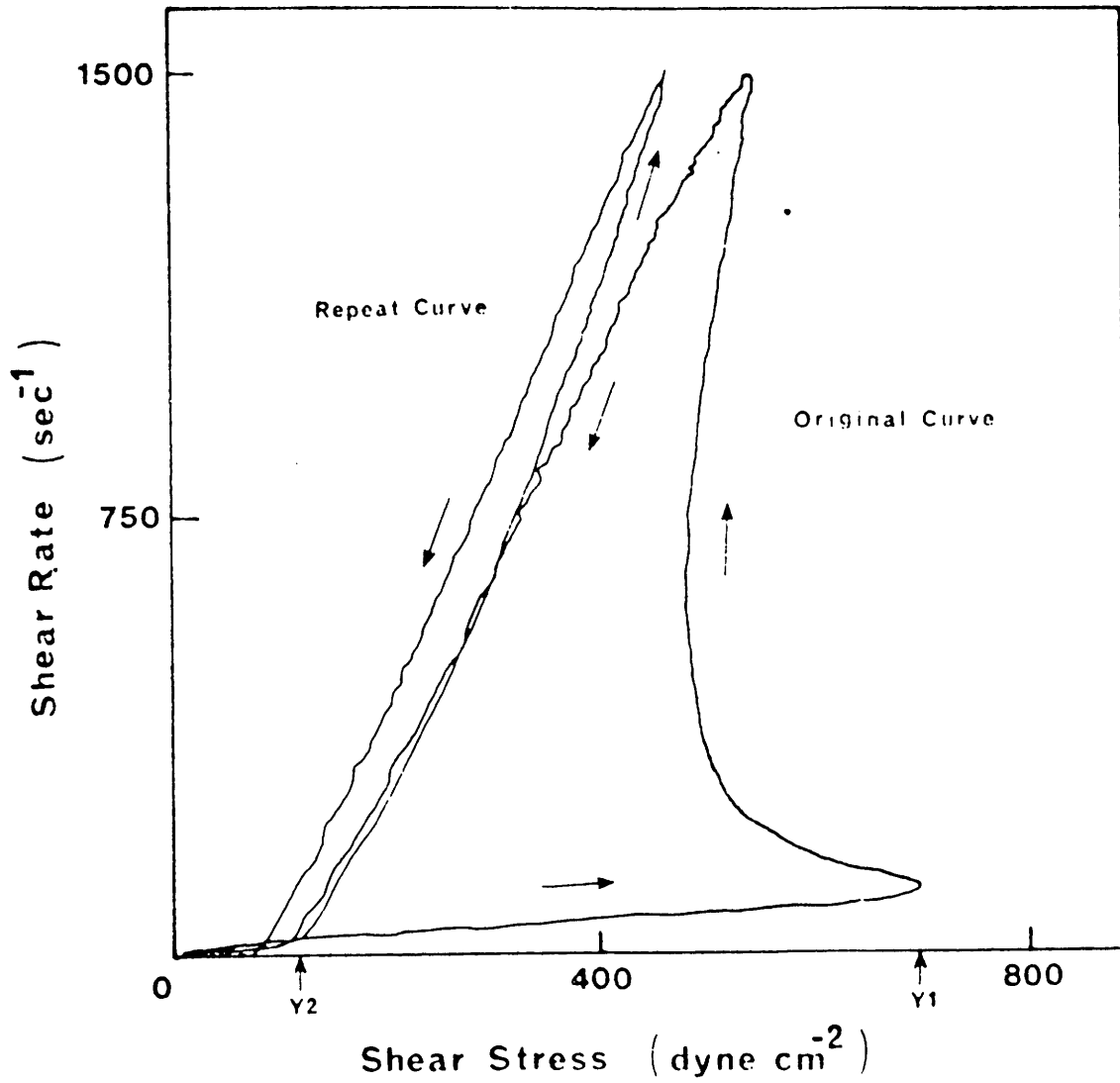


Figure 4-5 Thixotropic Behavior. Shown is a Ferranti-Shirley rheogram for pumpable shortening from Davis (1973).

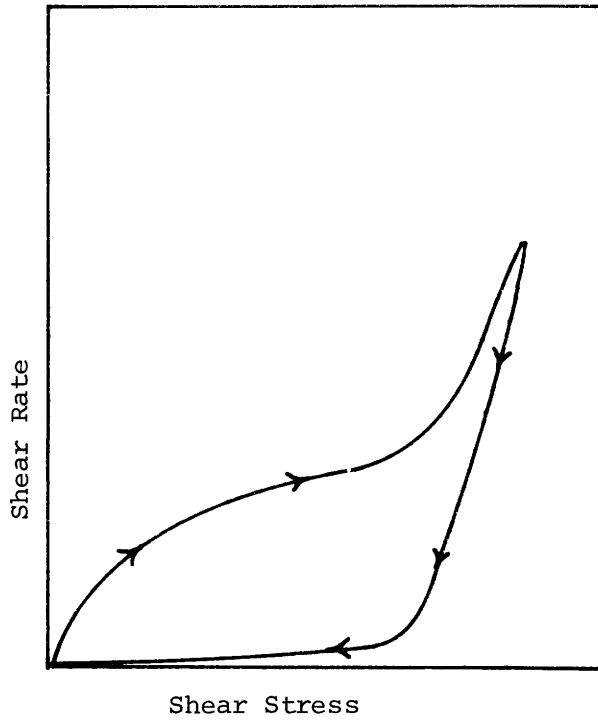


Figure 4-6 Typical rheogram for a rheopectic fluid.

approach its steady-state viscosity value. The observed peak value has been suggested to correspond to the static yield stress, but data obtained for varying shear rates show an increase in peak value with an increase in shear rate. Therefore, such rheograms cannot be expected to provide reliable values for static yield. This behavior also necessitates the definition of a rate of recovery, the time for the gel structure to return to its original static strength after having been subjected to flow. The present LNG gels are similar to other lyophobic gels, such as those formed with Cab-O-Sil in non-polar liquids, and their time for ≈ 90 percent recovery is typically about five minutes. (Lippe, 1976)

The simplest rheological model which includes a time dependency effect is the Maxwell model (modified to include a yield stress) which requires a single relaxation constant, $\lambda = (\eta_p/G)$

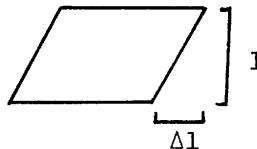
$$\tau + (\eta_p/G) (\delta\tau/\delta t) = \tau_y + \eta_p (d\gamma/dx) \quad (4-3)$$

where $G =$ linear elasticity

Below the yield stress the gel will behave as a Hookean elastic solid.

$$\tau = G\gamma$$

where $\gamma =$ shear $\Delta l/l$



According to this model, application of a steady rate of shear to a gel will give an initial elastic response until the stress builds

to its yield value. Above the yield point the response will be an exponential relaxing to the steady state value $\tau = \tau_y + \eta_p (dv/dx)$. This, of course, cannot account for the occurrence of peaks unless a distinction is made between the yield value for elastic response and the yield value for the steady-state behavior. If the gel is initially above the yield value, an instantaneous application of a constant shear rate will be an exponential. Such a change, however, can never be instantaneous, and the stress behavior during the rate change will be a steep elastic type response, again followed by the slowly decaying exponential. Despite the response similarity, a comparison with the data reported by Mercer and Weymann (1974) and Michaels and Bolger (1962) indicate that a steep, fast relaxation still occurs within the constant shear rate region which cannot be accounted for by this model.

Various other experiments are possible for assessing time dependency effects. Creep tests in which an instantaneous load (shear stress) is applied to the sample yield shear versus time plots similar to that in Figure 4-7. The figure also shows creep relaxation, the shear behavior when the stress is released, and the sample recovers from the deformation. Similarly the stress relaxation of a sample is measured by suddenly shearing the sample to a given deformation and recording stress as a function of time. Although such measurements can provide useful information about the sample, individually they cannot be used to provide a complete rheological description. For example, Davis (1970) performed creep tests on several gel samples,

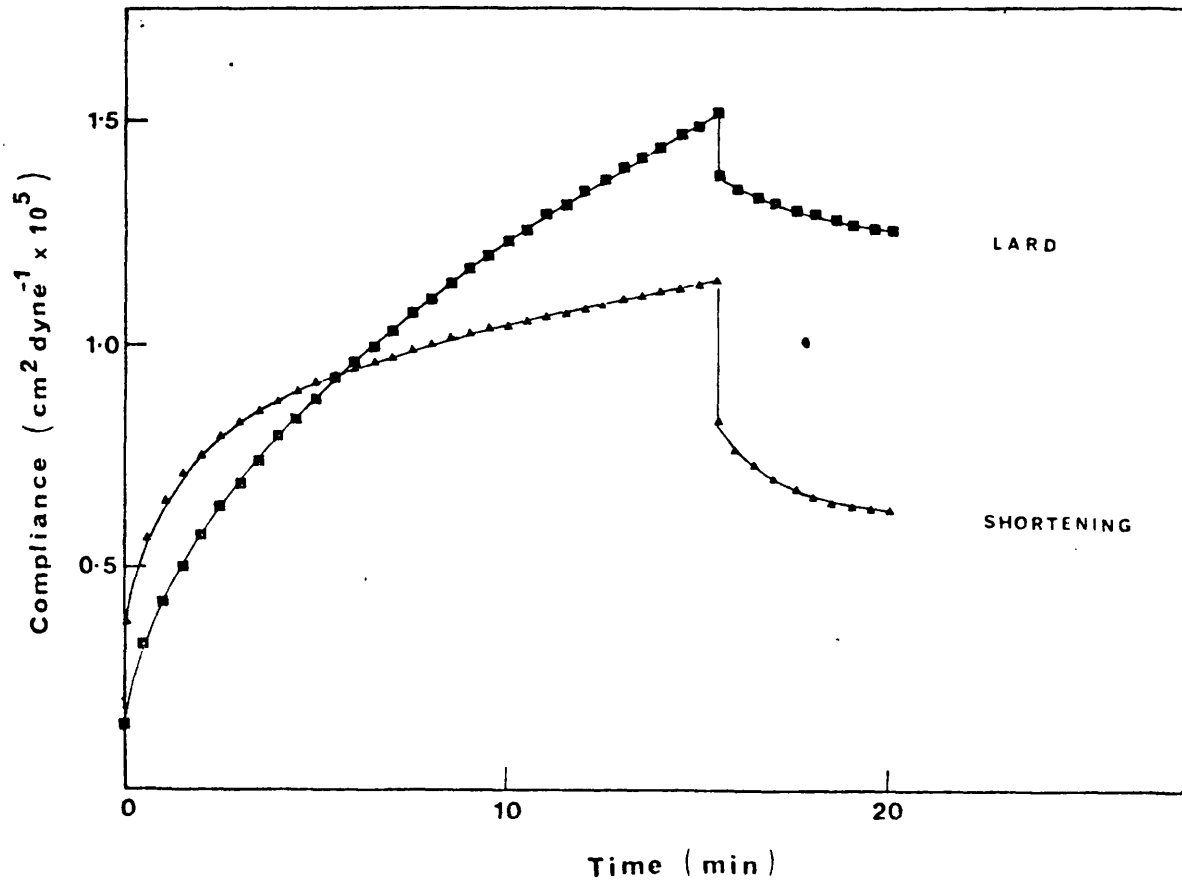


Figure 4-7 Creep curves for lard and shortening (Davis, 1973). Compliance = γ/τ .

and was able to fit the resulting data to a series of one or more Kelvin units plus a Maxwell unit (see Table 4-1), thus obtaining a spectrum of relaxation times. Such a rheological model does not account for the yield stress, i.e. it indicates that flow will occur at any applied stress. Its applicability to other flow circumstances is therefore questionable. If the observed responses for creep and creep relaxation are compared with the modified Maxwell model (i.e. with yield stress), the slow transient from elastic to viscous behavior cannot be accounted for.


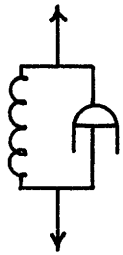
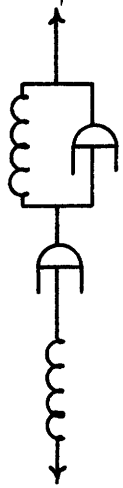
A further extension of the rheological equation has been proposed by Oldroyd (1959) and adds a second relaxation time. The relation is presented here with a yield stress.

$$\tau - \tau_y + \lambda_1 (d\tau/dt) = \eta_p [dv/dx + \lambda_2 \frac{\partial}{\partial t} (\frac{dv}{dx})] \quad (4-4)$$

where λ_1, λ_2 = relaxation times

This expression seems to be the most generally applicable to gels, but still does not account for the steep elastic transitions between steady-state rates of shear. Possibly this is similar to a yield type criterion and the response must be separated. At steady state the above equation approaches that for a Bingham plastic, as does the modified Maxwell model. Also for constant shear rate the equation reduces to the modified Maxwell model. If the steady state behavior is pseudoplastic, η_p in equations 4-3 and 4-4 will not be a constant but a function of shear rate.

Table 4-1 Mechanical Models for Viscoelastic Fluids

	Maxwell (series)	Kelvin (Parallel)	Burgers (Series and Parallel)
			
Shear Stress Relation	$\tau + \frac{\eta}{G} \frac{d\tau}{dt} = \eta \frac{d\gamma}{dt}$	$\tau = G\gamma + \eta \frac{d\gamma}{dt}$	$\left(1 + \frac{G_2 + \frac{\eta_2}{G_1}}{\eta_1}\right) \tau + \frac{\eta_2}{G_1} \frac{d\tau}{dt} + \frac{G_2}{\eta_1} \int \tau dt = G_2 \gamma + \eta_2 \frac{d\gamma}{dt}$
Response ($\tau = A \sin(\omega t + \phi)$) to sinusoidal shear	A	$\eta \omega \gamma_0 / \sin \phi$	$\frac{\eta_1}{\sin \phi} / (1 + \omega^2 \eta_1^2 / G_1^2) + \eta_2$
ϕ	$\arctan (1/\omega \tau)$	$\arctan (\omega \tau)$	$\arctan \frac{A}{\frac{\eta_1^2/G_1}{1 + \omega^2 \eta_1^2/G_1^2} + \omega}$

In general, the steady-state rheological behavior of gels is reproducible, but there are certain effects which may alter this. The steady-state values, particularly at low shear rates are strongly dependent on the original degree of dispersion (i.e. whether the gelant particles are uniformly dispersed throughout the liquid or partially compacted into aggregates which are loosely flocculated to form a less rigid structure). If this original degree of dispersion is altered either due to aging or by being subjected to a high shear rate, the steady state curve may also be changed.

4.2 Structural Model of Rheological Behavior

The various rheological patterns just discussed have been satisfactorily explained based on present knowledge of the structure of gels. Lyophobic gels, such as LNG gels, have been described (see Chapter 2) as a network of particles linked together by van der Waals forces, hydrogen bonding, and other forces such as electrostatic and polymeric linkages when applicable. Types of interparticle links are often classified as primary and secondary. Originally these two terms referred to primary and secondary minima in the interaction potential energy curve for two approaching particles. A secondary minimum, if it occurs, would be a second dip in the potential energy curve at a separation distance of 100 to 1000 Å. Some colloid scientists (Efremov and Us'yarov, 1976) believe that the existence of a

secondary minimum is necessary to obtain a thixotropic gel with the rheological behavior patterns just described, their reasoning being that only a secondary linkage would be weak enough to break down under shear yet reversible on setting. Such secondary minima, however, occur only in electrical double layer systems and in some cases where polymers are adsorbed onto the particle surface. There is evidence, however, that the linkages are generally much stronger than would be expected for secondary minima in systems where an electrical double layer exists. Hunter and Nicol (1968) suggested that these secondary minima are separated from the primary minimum by such small barriers that it is unlikely that such a barrier would be sufficient to prevent aggregation at the primary minimum under high shear rate conditions. As further evidence, Nicol and Hunter varied the electrostatic repulsion energy (by varying the electrolyte concentration) and observed no discontinuity in the energy of interaction of the particles as based on the observed yield stress value. Also, in the present case, there is thought to be no secondary minimum. A distinction between two types of bonds, however, can still be made, reversible and irreversible. Any linkage which has an energy of attraction which is not too large (≤ 100 kT) may be reversible under shearing conditions. In many colloid systems the primary minimum is thought to occur at a separation distance of 10 \AA which represents the separation by two adsorbed liquid layers. Such linkages are likely to be reversible unless the van der Waals attraction is unusually great. For the present LNG gels, the rheological data indicated that the particle radius

is about 150 Å. If a 10 Å liquid layer were to separate two particles, their attractive energy would be just slightly greater than kT (i.e. Brownian motion and free convection may be sufficient to inhibit flocculation), which suggests that the two particles must be in contact (with possible hydrogen bonding) if they are to stick together. The calculated attractive energy for such a linkage is still less than $100kT$, and thus may constitute a reversible bond under shearing conditions. Irreversible linkages will occur when two particles coalesce.

A gel network is likely to consist of a distribution of both primary and secondary linkages, and the structure may vary from a high degree of dispersion with chains throughout, to one which has compact particle aggregates (with primary and possibly secondary linkages) which are loosely linked together (Figure 4-8). When shear is applied to the gel structure, the linkages will be stretched and eventually the weakest points (i.e. the weakest bonds and the fewest bonds per unit area) will rupture. Once a sufficient number of bonds have been broken, the structure will have been fragmented and flow will occur. For any given shear rate (or shear stress) there is thought to be a steady state balance between the rate of flocculation of these aggregates and the rate of breakage of links due to shear. Flocculation will occur due to Brownian motion, but will also be enhanced by shear as the collision rate will increase. On the other hand, as shear rate increases, the particles/aggregates will be more energetic and resist sticking, and an increased hydrodynamic force will

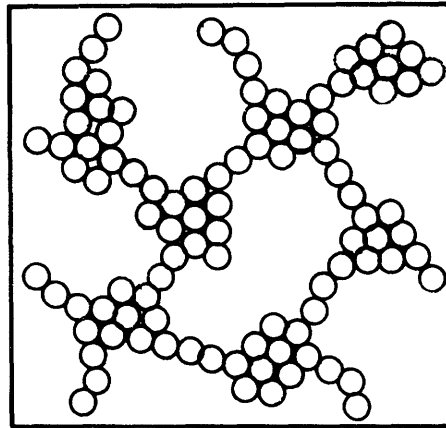


Figure 4-8 Compact particle aggregates with loose chain links--represents poor dispersion and a relatively weak network.

be present to break down the flocs which do form. At high shear rates the structure will be broken down into very small fragments, either small aggregates or individual particles; while at low shear rates the fragments will be quite large. Experimental evidence of Reich and Vold (1959) and Mason (1948) on the effect of agitation on aggregate size support this kinetic picture.

This structural model for the rheological behavior is widely accepted, but due to its complexity, the derivation of the corresponding rheological relations requires a number of simplifying assumptions. Here, the steady-state behavior at moderate and high shear rates has been the most extensively treated, and due to the variety of assumptions made, a number of different relations have been proposed. However, practically all of these relations are phenomenological, describing the basic flow behavior but requiring an empirical fit to determine the constants. A list of some of these proposed relations is given in Table 4-2, along with the assumptions made in each derivation. It is not possible to assess whether one of these expressions is more appropriate than another as each has been successful in fitting data for certain colloidal suspensions.

A few attempts have been made to derive a rheological expression using only known parameters such as particle size, energy of interaction for two particles, volume concentration, etc. Most of this work has dealt with the region of higher shear rate where the behavior closely approximates a Bingham plastic. This region is certainly the easiest to define as it is thought to consist of a highly fragmented

Table 4-2 Proposed Relations for
Pseudoplastic Behavior

Model	Gillespie (1960)	Cross (1965)	Casson (1959)
Assumptions	Detailed model of link formation and breakage	Chain structure with macro-molecular chain-length dependence used for viscosity	rod-like aggregates
Expression*	$\tau = S + \frac{C_1 S + C_2 S^2}{C_3 (C_4 + S)^2}$	$\tau = \eta_{\infty} S + \frac{(\eta_0 - \eta_{\infty})}{\alpha S^{1/3}}$	$\tau^{1/2} = \tau_y^{1/2} + \eta_p^{1/2} S^{1/2}$

*where S = rate of shear

C₁, C₂, C₃, C₄, α = empirical constants

structure, the basic flow unit being either a primary particle or a small aggregate. The energy dissipation in the flow process is divided into two parts; that due to the flow of fluid around the basic flow units, plus an additional energy due to the attractive interactions between particles, both within and between the flow units. In spite of this simplistic picture, several models are possible, each yielding a different relation. Firth and Hunter (1976) postulated three possible models: 1) single particle model; 2) hard floc model; and 3) elastic floc model. The single particle model assumes that the basic flow unit at high shear rates is the individual particle. The particle linkages must therefore all be secondary bonds. The hard floc model assumes that the flow unit is a spherical aggregate of primary bonded particles. The resulting collisions and separations are hard and inelastic with no energy dissipation within the floc during flow process. The elastic floc assumes that the hydrodynamic force, which ultimately causes rupture of the floc-floc bonds, is transmitted through all of the particle-particle interactions within each floc. Each successive bond is stretched to some extent until finally the floc-floc bond breaks. The floc will then snap back releasing energy.

Firth and Hunter derived expressions for the Bingham yield value, τ_B , of the high shear region (Figure 4-2) based on each of the three models.

Single particle

$$\tau_B = \frac{A\phi_p^2}{8\pi^2 r^2 D} \quad (4-5)$$

Hard floc

$$\tau_B = \frac{Ar\phi_F^2}{8\pi^2 a^3 D} \quad (4-6)$$

Elastic floc

$$\tau_B = \frac{3\phi_F^2 A}{2\pi^2 r^2 D} \quad (4-7)$$

where A = Hamaker constant or Lifshitz-Hamaker function (see Chapter 2)

r = particle radius

a = aggregate radius

D = separation distance between particles

ϕ_F = volume fraction of flocs

ϕ_p = volume fraction of the solid particles

To obtain these relations, they considered only van der Waals attraction between the particles. When electrostatic repulsion is present, the attraction energy will be lower. Also, when particles interact at such a small separation distance that hydrogen bonds form, this must also be included. (Further discussion will be given later in this section.)

To determine which, if any, of these expressions adequately represents observed behavior, Firth and Hunter (1976) used experimental data for various coagulated suspensions, including titania, kaolinite, latex, and oil and water emulsions. Experimentally

measured values of particle radius and calculated values of the Hamaker constant were used. For the single particle model, a separation distance could be calculated directly and then used to determine the maximum force, $F_{\max} = Ar/(12D^2)$, which must be overcome to separate two particles. This maximum force was then compared to the available hydrodynamic force as given by Goren (1971) for Couette flow.

$$F_H = 6.12\pi\eta_f a^2 S \quad (4-8)$$

where F_H = Hydrodynamic force

a = radius of basic flow unit

S = rate of shear

η_f = viscosity of surrounding liquid

This comparison showed large discrepancies, F_{\max} being larger than F_H by a factor of $\approx 10^6$, suggesting that even at high shear rates, the basic flow unit is an aggregate (floc) rather than a single particle.

To test the hard and elastic floc models, values of ϕ_F and "a" were necessary. Here Firth and Hunter assumed cubic close packing within the aggregate to obtain the relation $\phi_F = 1.28\phi_P$. For "a", several different values, thought to be the most realistic, were used in the calculations. When the resulting maximum interaction force was determined and compared to the available hydrodynamic forces, large discrepancies (F_{\max} was approximately three orders of magnitude larger than F_H) also existed for the hard floc model. The elastic model, on the other hand, gave quite realistic values for D (this generally ranged from 1 to 10 A), and subsequent estimates of F_{\max}

were in agreement with hydrodynamic force estimates (these ranged from 10^{-5} to 10^{-1} dynes).

The contribution to shear stress due to the viscous flow of the medium around the colloidal flow units can be calculated from the Einstein relation for non-interacting spheres.

$$\eta_p = \eta_f (1. + 2.5\phi_F) S \quad (4-9)$$

where η_f = fluid viscosity

Extensions and modifications of this relation have been made (Thomas, 1965; Manley and Mason, 1954; Krieger, 1972) but the change due to the additional terms is negligible for the volume fractions considered in this study (i.e. $\leq 10\%$).

Combining the two energy dissipation processes results in a Bingham plastic relation for shear stress.

$$\begin{aligned} \tau &= \tau_B + \eta_p S \\ &= \frac{3\phi_F^2 A}{2\pi^2 r^2 D} + \eta_f (1. + 2.5\phi_F) (dv/dx) \end{aligned} \quad (4-10)$$

Using high shear rate data for the same colloidal suspensions mentioned previously, Firth and Hunter obtained values for ϕ_F/ϕ_p based on the viscous flow term. For those suspensions with the largest particles ($\geq 1\mu\text{m}$) and largest volume fraction ($\phi_p \geq .1$) the value of ϕ_F/ϕ_p was approximately equal to the assumed value of 1.28. However, the value was slightly higher (2 to 4) for those suspensions of smaller

particles (2×10^{-5} cm to 7×10^{-6} cm) and lower ϕ_p (0.035 to 0.07). If these new values for ϕ_F/ϕ_p are then used in the expression for τ_B , the resulting values of D , F_{\max} , etc. change slightly but are still quite reasonable for almost all of the suspensions considered. Thus, the elastic floc model seems to give a good representation of the data presented by Firth and Hunter (1976). However, further studies by Firth (1976) have shown that the relation is not completely correct, as variation of different parameters indicated slightly different proportionalities. The floc volume fraction, ϕ_F , was found to be proportional to ϕ_p/r . If this is true, then the elastic floc expression gives $\tau_B \propto 1/r^4$ which differs significantly from the observed proportionality of $1/r$. To determine the functionality for the interaction potential, Firth varied the zeta potential (defined as the potential at the plane of shear, ξ , by varying the electrolyte concentration. Here he found a linear relation between τ_B and ξ^2 , suggesting that τ_B is proportional to either the total interaction energy (i.e. $\propto 1/D$) or the total interaction force ($\propto 1/D^2$). Based on dimensional reasoning, an attractive force proportionality is expected.

$$\tau_B \propto \frac{A\phi_p^2}{D^2 r} \quad (4-11)$$

If the data previously used by Firth and Hunter are applied to this expression, the constant of proportionality ranges from 10^{-3} to 10^{-5} . This relation, however, is very sensitive to changes in the particle-particle separation distance, a parameter which cannot be measured. Thus the wide range in the proportionality constant may be due at

least partially to inaccuracies in D.

As mentioned previously, if hydrogen bonding between particles occurs, this bond energy must be included in the Bingham yield stress expression. For the present LNG gels, if the particles are less than ≈ 200 A in radius, the hydrogen bond linkages will be the major attractive force. Based on the proportionality given in equation 4-11, a similar expression can be derived for the hydrogen bonding case (Appendix Q).

$$\tau_B \propto \frac{n (E_{HY}) \phi_P^2}{Dr^2} \quad (4-12)$$

where n = number of hydrogen bonds formed
between two particles

E_{HY} = hydrogen bond energy,
 3.5×10^{-13} ergs

The constant of proportionality for this expression ranges from 10^{-2} to 10^{-4} .

For describing flow behavior at low and moderate shear rates, Michaels and Bolger (1962) have developed the most complete model. They postulated that the gel structure was composed of rigid primary flocs which were loosely clustered into aggregates. Again the total energy dissipation was separated into parts, but three components were used: 1) a viscous energy term, as defined by the Einstein relation; 2) a creep energy term representing the energy used to break network bonds; and 3) a network energy term which represents the energy dissipated when aggregates are stretched and a floc-floc

bond breaks allowing the aggregate to snap back into a relaxed state.

(4-13)

$$\tau - \tau_N = A_2 (d_F/d_A) \phi_F^2 + \eta_f S (1. + 2.5 C_{AF} \phi_F)$$

$$\text{and } A_2 = \frac{5\pi C_{AF}^2 A}{8(C_{AF} - 1) 2\pi^2 D d_F^2}$$

$$\tau_N = F(S) (H_F/d_F^2) (\phi_F - \phi_{FO})^3$$

where $C_{AF} = \phi_A/\phi_F$

H_F = attractive force between flocs

d_F = diameter of floc

d_A = diameter of aggregate

$F(S)$ = orientation function which is dependent on shear rate

ϕ_{FO} = minimum floc volume fraction for gelation

The first term on the right hand side of equation 4-13 represents the creep energy term. At low shear rates d_F/d_A is a function of shear rate, while at high shear rates this ratio will be unity and the term will represent the Bingham yield stress. However, this expression was derived assuming the basic flow unit as a rigid inelastic floc. Although this term can be corrected to include floc elasticity, it is not certain whether it has already been accounted for in the network energy term or, in fact, which of the two terms should include this effect. The network yield strength term, τ_N , was not rigorously derived, but instead was based on the following assumed proportionality:

$$\tau_N \propto H\phi_A^3/d_A^2 \quad (4-14)$$

where H = interaggregate bonding force

d_A = mean aggregate diameter

ϕ_A = volume fraction of aggregates

Michaels and Bolger accredited this proportionality to Kaiser (1961), indicating that it represented the crushing strength of aggregates of colloidal particles. However, Kaiser actually proposed a slightly different relation. Also, it is not certain whether crushing strength is applicable to the present case of shear stress and structure breakdown.

Michaels and Bolger further defined the steady-state yield stress for zero shear rate as

$$\tau_Y = \lim_{D \rightarrow 0} \tau_N = F(0) (H_F/d_F^2) (\phi_F - \phi_{FO})^3 \quad (4-15)$$

This steady-state yield stress, however, has been studied by previous investigators (Norton et al., 1944; Thomas, 1961) and found to be proportional to ϕ_p^3/d_p^2 . One would also expect the yield stress to be a function of the interparticle bonding force (or energy), with an increasing bond strength producing a greater yield stress. If the yield stress is directly proportional to the interparticle attraction, the following expression results.

$$\tau_Y \propto A\phi_p^3/(Dr^2) \quad (4-16)$$

Although the bond strength could, in fact, be raised to some integer power greater than one, the best fit, based on available data, results

with this direct proportionality and a proportionality constant ranging from 5 to 30. This expression can also be modified to represent hydrogen bonding rather than van der Waals attraction.

$$\tau_y \propto n(E_{HY}) \phi_p^3 / r^3 \quad (4-17)$$

The proportionality constant for this relation ranges from 50 to 250. In the present study only low shear rate data were obtained for the LNG gels. Although it would be desirable to use these data to predict rheological behavior at moderate and high shear rates, the available models are only adequate for obtaining order of magnitude estimates. However, this will be satisfactory for the present application of LNG gels.

4.3 Time Dependency

The thixotropic behavior discussed in the previous section has been adequately characterized experimentally, yet theoretically is much less advanced compared with the steady-state behavior. For the case of a gel initially at rest which is instantaneously subjected to a steady shear rate, the resulting transient stress behavior has been discussed by Papenhuijzen (1972) and Jachimiak et al. (1975). Papenhuijzen suggested that this transient response was directly related to a bond breakage time effect. The medium needs sufficient time to fill the widening gap between the particles as a bond breaks, and vice versa to drain out if a new bond is formed. He further derived an expression for this effect; however, it required

a term dependent on time and shear rate, but of unknown functionality. His data also indicated no simple functionality for the term.

Although Papenhuijzen was unable to predict theoretically the observed transient responses, this time dependency effect does provide a qualitative explanation for the observed behavior. All of the data reported by Papenhuijzen showed a peak in the stress response (Figure 4-9). This could be attributed to an insufficient amount of time for the "steady-state" number of bonds to break. Initially the structure will be stretched until the force is sufficient to break network bonds. At this point, the process of bond breaking will begin, but the point at which bond breakage is noticeable will not occur until some point of greater shear is reached. This critical deformation was found to increase with increasing rate of shear, and the corresponding time to reach this point increased with decreasing rate of shear. A noteworthy effect was the increasing peak values with increasing shear rate. Also, the shear stress corresponding to a given shear was observed to increase with increasing rate of shear. The data of Jachimiak and coworkers (1975) show similar effects, but further indicate that at low enough shear rates a peak will not occur. They give the following criterion for the occurrence of a peak response.

$$S/k_{\tau} \geq 1$$

where $k_{\tau} = 1/\lambda_1$ (Eqn. 4-4); relaxation constant for steady shear rate transient response

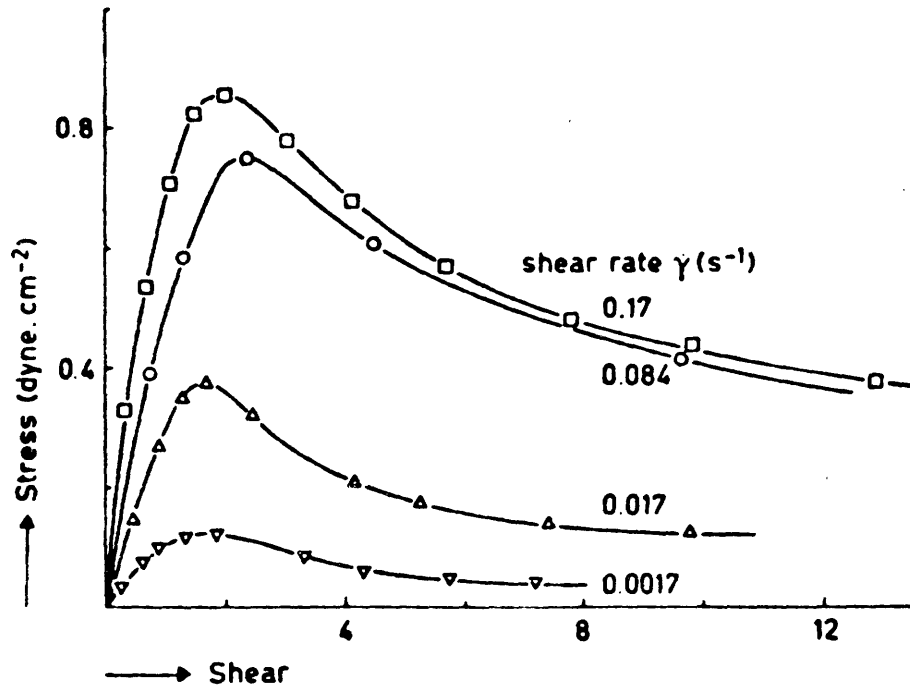


Figure 4-9 Transient response for an applied constant rate of shear. Experimental data for a water/oil emulsion (Papenhuijzen, 1972).

They further correlated their data to a combined kinetic expression and Oldroyd's viscoelastic relation without a yield stress. Their kinetic expression was as follows.

$$-d(CF_T)dt = k_1(\tau)^{P1}(F_T C)^m - k_2(\tau)^{P2}((1 - F_T)C)^n \quad (4-19)$$

where F_T = fraction of the network structure unchanged

C = concentration

k = rate constant

P = constant representing susceptibility to stress

m, n = reaction order

Both steady-state and transient data were necessary to determine the constants for this expression, and no further correlation was made between these constants and known parameters such as particle size, concentration, etc. The model, however, did provide a satisfactory fit for their data.

Thixotropic effects also occur in constant shear rate tests when the gel is not initially at rest. For the case in which the gel is at some steady state value and is instantaneously subjected to another constant shear rate, the time dependence behavior has been shown to be an initial rapid relaxation followed by a slower relaxation. Mercer and Weymann (1974) were able to fit satisfactorily such thixotropic data for bentonite-water suspensions to the following double exponential. (Figure 4-10)

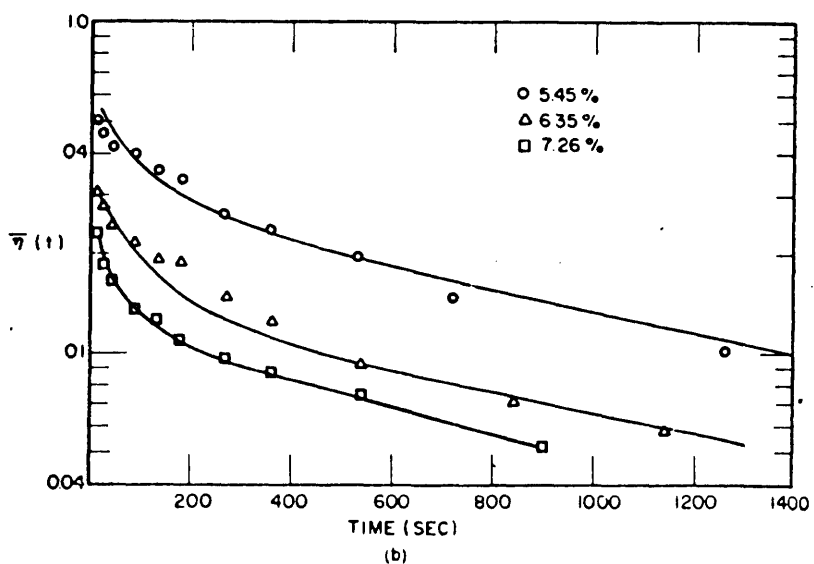
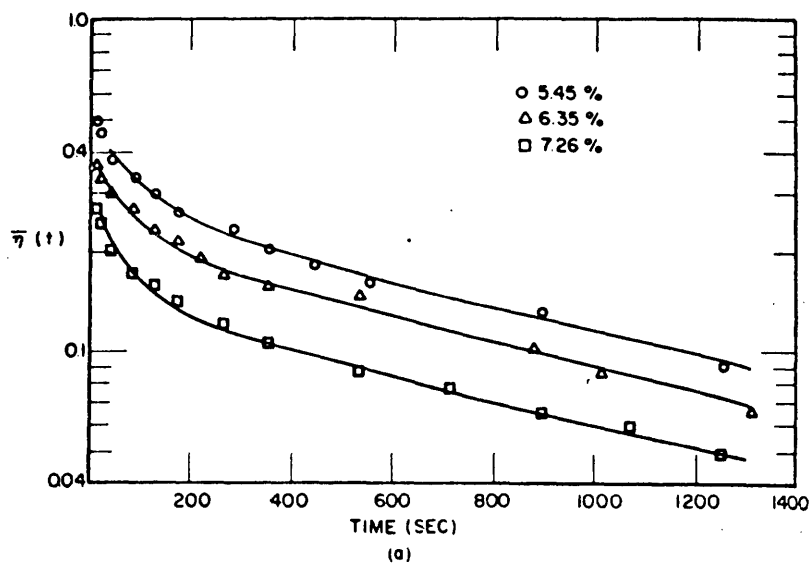


Figure 4-10 Reduced viscosity $\bar{\eta}(t) = \{\eta(t) - \eta_f\} / (\eta_i - \eta_f)$.

The solid lines represent the best fit of Equation 4-20 to the experimental data. At $t=0$ the steady-state shear rate is changed from (a) 193.5 s^{-1} to 64.5 s^{-1} ; (b) 39.8 s^{-1} to 64.5 s^{-1} . The dispersions are bentonite in water, and concentrations are by weight percent.

$$\bar{\eta}(t) = (1 - \epsilon) \exp(-(t/\lambda_1)^4) + \epsilon \exp(-t/\lambda_2) \quad (4-20)$$

where $\bar{\eta}(t)$ = normalized viscosity
 $(\eta_{\text{app}}(t) - \eta_f)/(\eta_i - \eta_f)$

η_i = initial steady state value
for viscosity

η_f = final steady state value
for viscosity

At present there is no theory which yields such an analytical solution. Mercer and Weymann did, however, develop a kinetic theory model which required a computer solution to a set of simultaneous rate expressions. In deriving these equations, several assumptions were made. First, collisions were assumed to be dependent on shear rate, i.e. Brownian motion was neglected. This will be true for large aggregates. For very small individual particles, however, Brownian motion will control the collision rate. Second, thixotropy was assumed to be controlled by the rate of change of the number densities, n_i , and only collisions between singlets and aggregates would take part in the adjustment of this aggregate size distribution. Third, at steady state this aggregate size distribution was assumed to follow Mooney's (1951) expression.

$$\eta = \eta_{\infty} \exp(2.5\phi/(1 - \Lambda\phi))$$

$$\text{where } \phi = \sum_{i=1}^{i_m} \eta_i V_i$$

i_m = maximum no. of particles which
can be combined in a stable
aggregate

Λ = crowding parameter

n_i = number density of aggregates
of size i particles

V_i = volume of an i particle aggregate

ϕ = total volume fraction of aggregates

In deriving the rate expressions, the rate of structure breakdown was assumed to be first order and the rate of recovery second order (similar to coagulation theory). This is a common assumption and was used in the derivation of several of the steady-state expressions. The computer solution to these equations proved to be a poor fit for their data. In general, the theoretical initial decay was not rapid enough.

Another type of transient response, creep relaxation, was kinetically modelled by Ruckenstein and Mewis, but no comparison with experimental data was made.

Thus, from the available literature it was found that all of the proposed models were quite complex and could only be handled using computer techniques. Yet, in many cases the observed rheological behavior was fairly simple to describe. Most of these models have, however, ignored the yield stress and the associated elasticity of the aggregates. Gels, initially at rest have clearly shown an initial elastic response prior to any network bond breakage and reformation. The transients between steady shear rates also show an initial elastic type response, indicating a sudden relaxation or stretching

of the aggregates before further bond breakage and reformation can occur. It may therefore be more reasonable to divide it into two separate responses, an initial elastic one followed by an exponential decay. This fits the data of Mercer and Weymann and Jachimiak (the peakless curve) quite well.

4.4 LNG Gel Rheology

In the present study an oscillating viscometer was used to measure the shear stress response of LNG gels under an applied rate of shear. This particular instrument (see Chapter 6 for detailed description) was selected primarily because of its ease of modification to operate under cryogenic temperatures, and because it would allow one to measure the elastic as well as the viscous properties of the gels. The oscillatory shear rate technique also has another advantage, as there is less chance for slip planes to occur (often at a wall). For viscometric measurements, the cone and plate and capillary viscometers have been the most successful in avoiding slippage under an applied steady shear rate, but no viscometer of either type was available which could be readily adapted to cryogenic temperatures. (The general gel behavior and results from previous studies which were discussed in Section 4.1 were presumably for conditions under which no slippage occurred.) In general, this slippage effect (i.e. the wall shear stress which will occur at any given rate of shear) cannot be predicted, and the results from one

particular flow situation cannot be applied directly to a different flow situation. For the present application of LNG gels to industrial scale use, the maximum (no slippage case) shear stress values are desired, as these can then be used for future estimates of the increased power requirements necessary for pumping the gels. To assess the possible safety benefit due to gelation, the most important rheological parameters will be the steady-state yield stress (also obtainable from the maximum shear stress vs. shear rate curve) and the static yield stress (these were measured using another technique which is discussed in Section 4.3.2). The present oscillating viscometer was suitable for measuring the desired rheological parameters. It avoided the slippage problem by limiting the maximum shear applied to the gel while allowing a variation in rate of shear by changing the frequency of the oscillation. However, the maximum shear was fairly low (0.15) and the resulting shear stress responses appeared to be transient viscoelastic effects. Previous investigators have interpreted such behavior in several different ways and these will be discussed in more detail after a brief description of general oscillatory behavior. The shear stress behavior will then be discussed on a microscopic level and a slightly different method of data analysis will be suggested with results presented for the present LNG gels.

4.4.1 Oscillatory Behavior

For a fluid sandwiched between two parallel flat plates and subjected to a sinusoidal variation of shear (Figure 4-11), the shear stress response will be a waveform of the same period as the input sine wave. If the fluid behaves as one of the two ideal systems, Newtonian liquid ($\tau = \eta(dv/dx)$) or Hookean solid ($\tau = G\gamma$), the output waveform will also be a simple sine wave with an appropriate phase shift (Figure 4-12). For viscoelastic fluids which combine elastic and viscous properties, sinusoidal oscillation is a particularly useful technique, as information can be obtained about both properties. As an example, if the rheological behavior of a particular viscoelastic fluid can be described by a linear combination of the two terms, i.e. $\tau = G\gamma + \eta(dv/dx)$ the response to an applied sinusoidal shear will also be a sine wave with a phase shift between zero and $\pi/2$ radians.

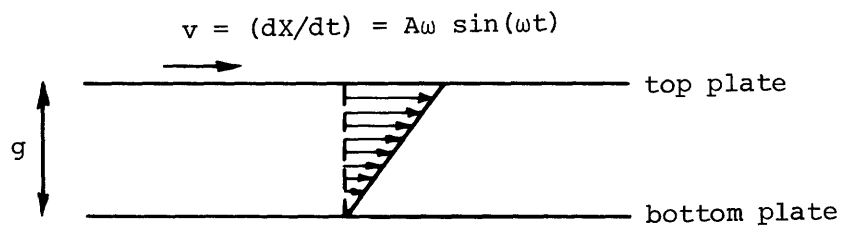
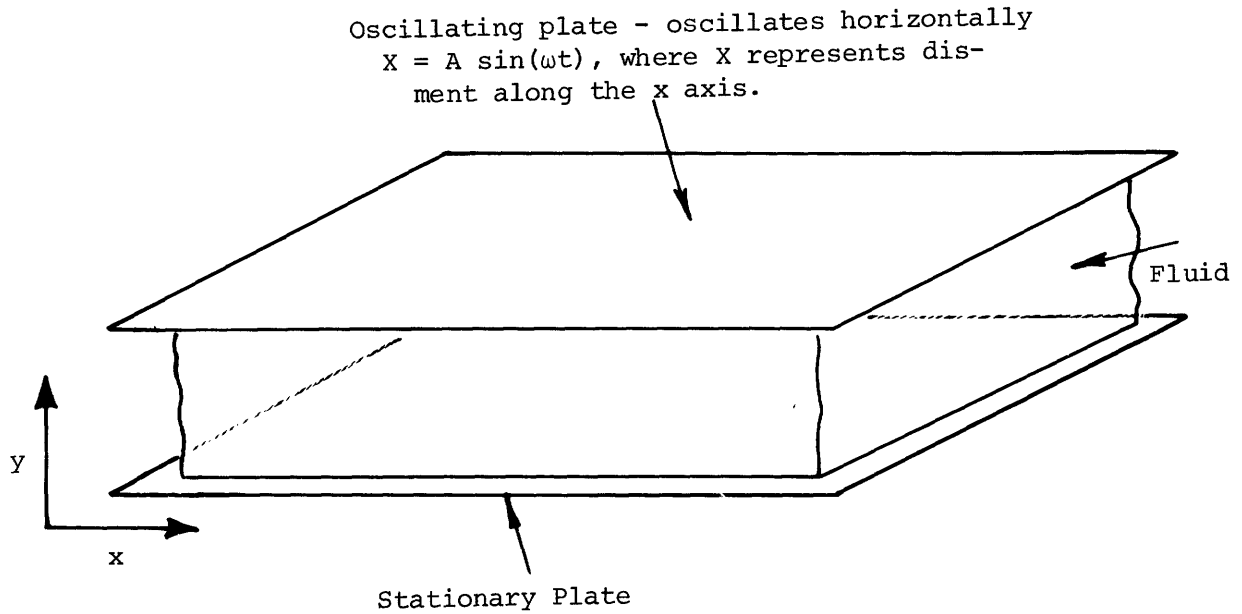
$$\begin{aligned}\tau &= G\gamma_0 \sin(\omega t) + \eta\omega\gamma_0 \cos(\omega t) & (4-22) \\ &= A \sin(\omega t + \phi)\end{aligned}$$

$$\text{where } A = \eta\omega\gamma_0 / \sin(\phi)$$

$$\phi = \arctan(\eta\omega/G)$$

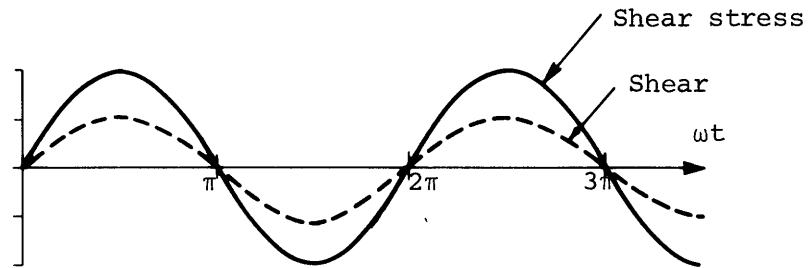
This model is equivalent to the Kelvin mechanical model of a spring and dashpot in parallel (Table 4-1).

Commonly used viscoelastic models include the Kelvin model,

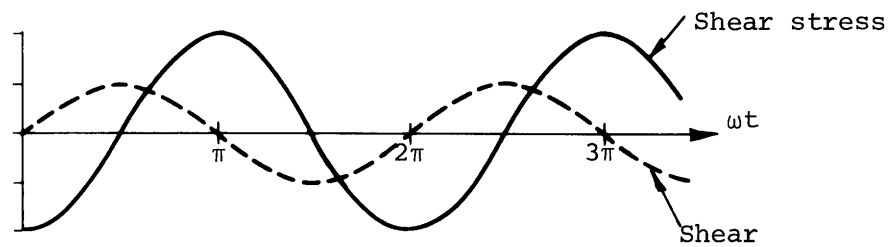


The shear rate, dv/dx , will be constant across the gap if the fluid is Newtonian or Bingham plastic, i.e. $(dv/dx) = (1/g)A\omega \sin(\omega t) = \gamma_0 \omega \sin(\omega t)$

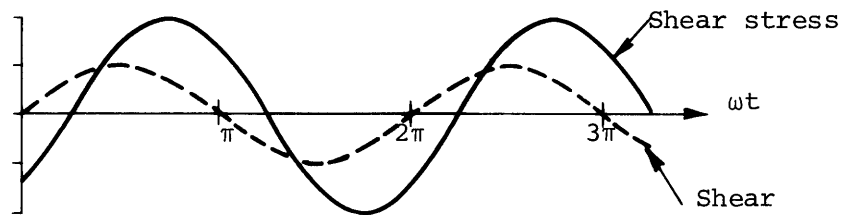
Figure 4-11 Oscillating Parallel Plates



Elastic response
(Hookean elastic)



Viscous response
(Newtonian)



Viscoelastic (Parallel combination of Newtonian element and Hookean element, Kelvin model)

Figure 4-12 Typical Shear Stress Responses for a Sinusoidal Shear Input

the Maxwell model, the Burger model (also shown in Table 4-1), and series and parallel combinations of these. All of these models are representations of linear viscoelastic fluids, such substances being defined as those in which the stress-strain ratio, although a function of time, is independent of stress. Also, the shear stress response for any linear viscoelastic fluid subjected to sinusoidal shear will be a sine wave with a phase shift.

If a yield stress is added to any of these models, nonlinear viscoelasticity will result. A simple Bingham plastic would be expected to behave as shown in Figure 4-13. The addition of a time-dependency effect as observed in actual gels, will add another degree of complexity to the observed output and its interpretation. In the case of the present LNG gels (and Cabosil gels which were run as ambient temperature test cases) the behavior under sinusoidal shear depended on the amplitude and the frequency of the oscillation. (Figure 4-14) (Although the present viscometer was cylindrical rather than flat plate, the dimensions were such that the approximation to parallel plates was good to within 10 percent when the measured shear stress was $\approx 1.25\tau_y$, Van Wazer et al., 1963). Starting with the sample at rest, if a sine oscillation at low frequency ($\leq .5$ Hz) and low amplitude (≤ 0.01 shear) was applied, the behavior was elastic, and variation of the amplitude showed a linear correlation of shear stress with shear, i.e. Hookean elastic. At low frequencies and higher amplitudes (up to $\gamma = 0.15$, the maximum shear attainable on the present instrument), a distinctive non-linear

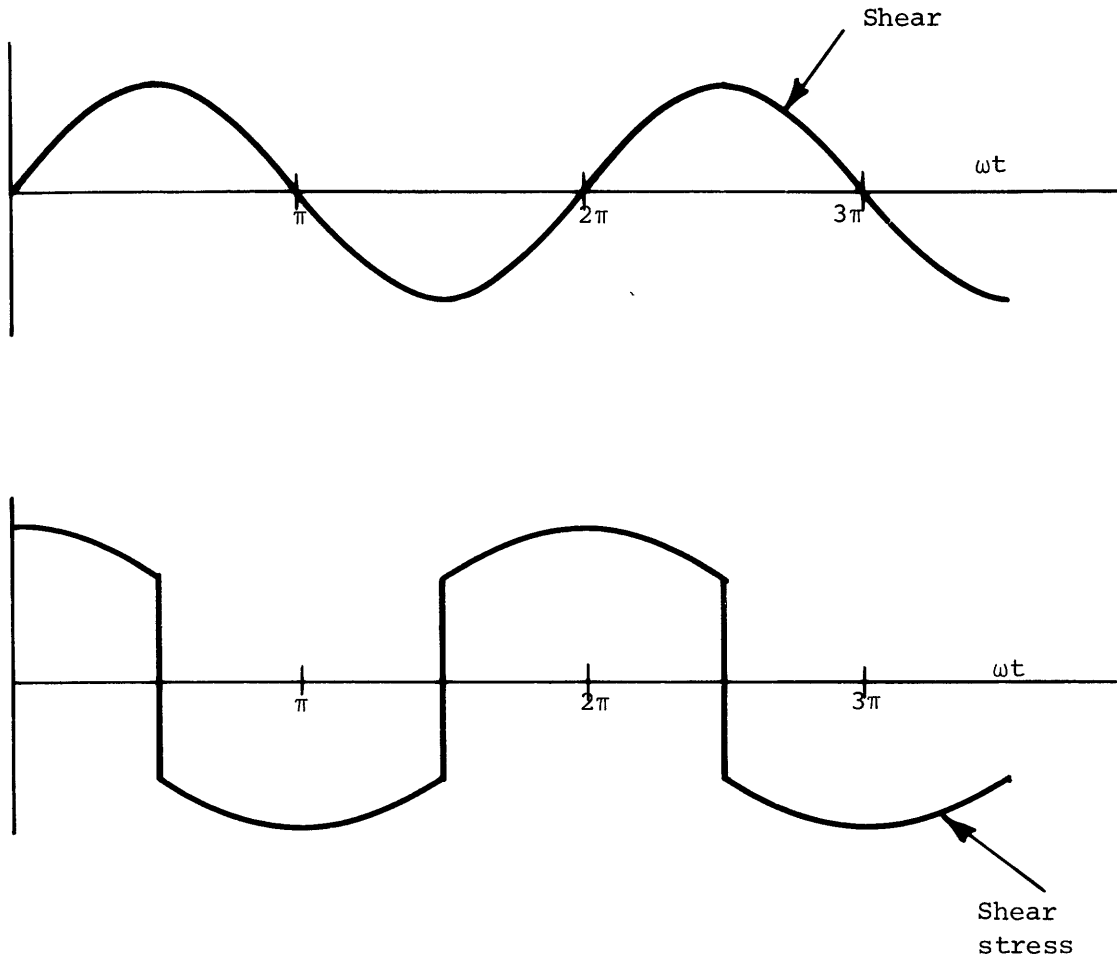
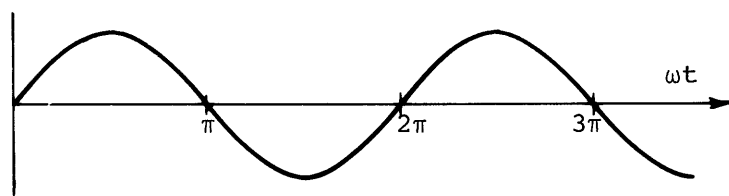
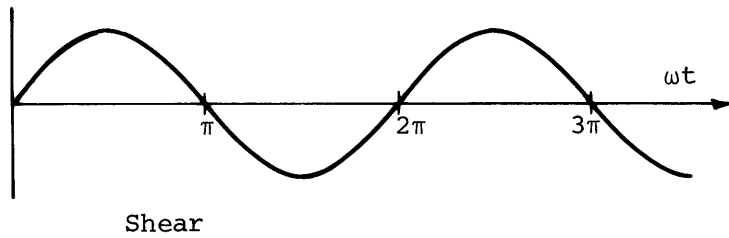
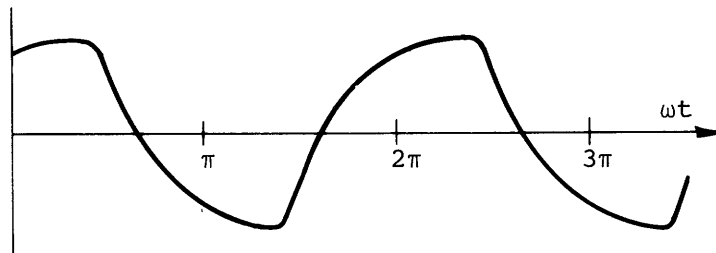


Figure 4-13 Shear Stress Response for a Bingham Plastic Subjected to a Sinusoidal Shear Oscillation



Shear Stress
Elastic response at low frequency-low
amplitude shear and at high frequency-
all amplitudes shear



Shear Stress
Non-linear viscoelastic response at
low frequency-high amplitude shear

Figure 4-14 Shear Stress Response for LNG Gels and Cab-O-Sil Gels Under an Applied Sinusoidal Shear

viscoelastic response was observed. At higher frequencies and maximum amplitude, the response was again elastic with the same elastic modulus as shown at the low frequencies.

The low frequency-low amplitude elastic response is representative of the static structure (assuming the sample was initially at rest). Such behavior has been studied by a number of investigators and has been shown to be Hookean elastic (Elliott and Ganz, 1975; Payne and Whittaker, 1970). As the amplitude is increased, a non-linear viscoelastic response will be observed indicating that the yield value has been exceeded and network bonds have been broken. Subsequent low amplitude oscillations often display non-linearity at lower amplitudes suggesting that the structure has not been completely rebuilt to its static value. However, despite this similarity to yield stress differences, the static yield stress (as measured using another technique) was never reached under the present oscillatory conditions. This was, no doubt, due to the type of viscometric technique which was used, i.e. a shear rate was applied to the gel and the shear stress response was measured. Under these conditions, particularly at low rates of shear, bonds will break long before the static yield stress is reached. In fact, the structure will begin to rupture below the steady-state shear stress and approach this value asymptotically (previously discussed in Sections 4.1 and 4.2). Non-linear viscoelastic behavior similar to that observed in the present study has been reported by a number of previous investigators, but the interpretation and method of analysis have been quite

varied. Also, none of these studies has shown a direct correlation of their data with steady state shear rate data.

Elliott and Ganz (1970, 1974) used a Weissenberg Rheogoniometer (oscillating cone and plate) to study Carboxymethylcellulose gels, ointments, and common foodstuffs including butter, margarine, cheese spread, etc. All of these exhibited non-linear viscoelasticity with somewhat similar shear stress response to those observed in the present study. In some cases they reported responses approximating square waves. For analysis, they suggested a "modified Bingham body" model (equivalent to the Maxwell plus yield stress previously discussed; see Figure 4-15), allowing the friction element to have both a static and dynamic yield value associated with it. Elliott and Green (1972) elaborated on this model, obtaining solutions for the two separate regions--below and above the yield value.

$$\tau - \tau_y = G\gamma_0 \left(\frac{\omega\beta\cos(\omega t - \epsilon)}{1 + \omega^2\beta^2} + \frac{\omega^2\beta^2\sin(\omega t - \epsilon)}{1 + \omega^2\beta^2} \right) + Ke^{-t/\beta} \quad (4-23)$$

where $\beta = \eta/G$

$\epsilon =$ phase shift (see Figure 4-15)

This expression defines the behavior above the yield stress. Below the yield stress, the behavior would be Hookean elastic. Using the boundary conditions at B ($\tau - \tau_y = 0$, $t = 0$) and C ($\gamma = \gamma_c$ at t_c), they obtained an expression for ϵ which they solved by computer for various conditions. Their model predicted several possible variations including an almost sinusoidal form (Figure 4-16). This is probably

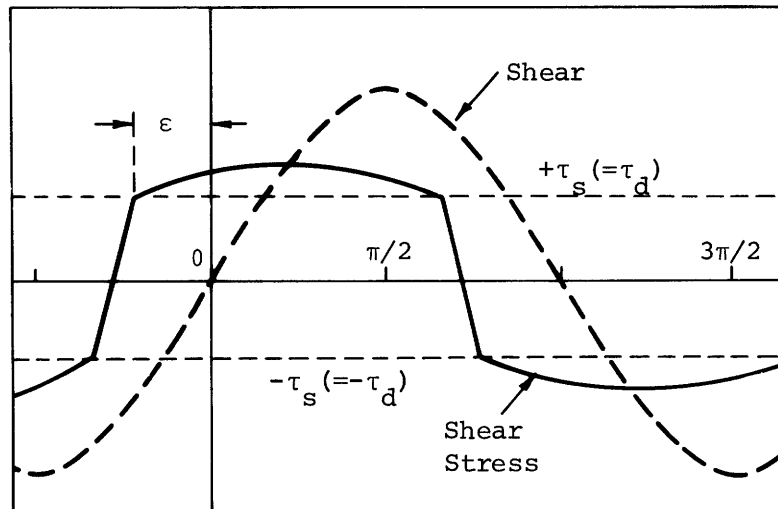
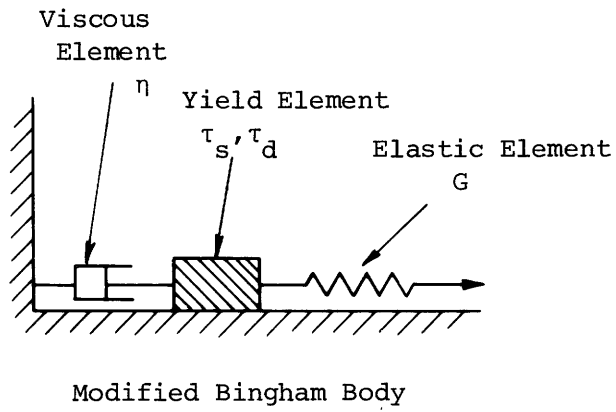


Figure 4-15 Shear Stress Response for a Bingham Body With Zero Relaxation Time and Single Yield Stress (i.e. dynamic yield stress equals static yield stress).

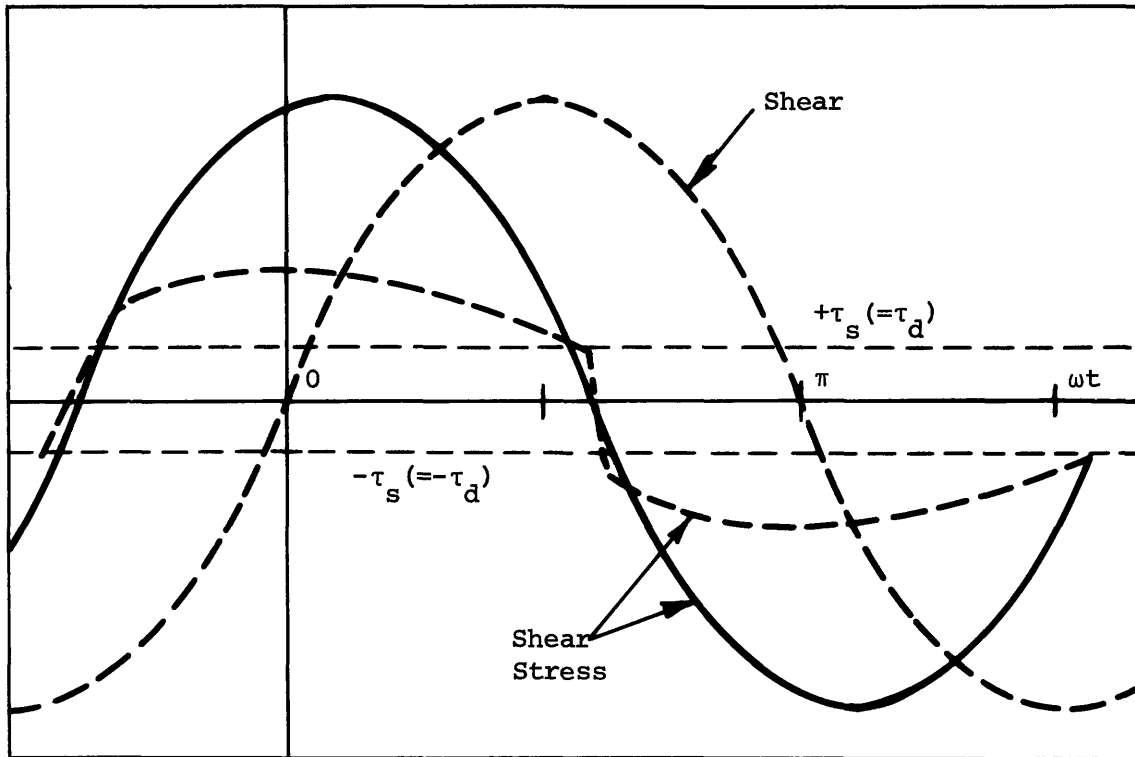


Figure 4-16 Shear Stress Behavior for Modified Bingham Body. The curves were generated numerically by computer (Elliott and Green, 1972).

the most appropriate of the models presented in the literature as it accounts for the yield stress, including the possibility of a yield stress peak response by allowing for both a static and dynamic yield stress. This model, however, neglects the transient response due to a changing shear (the $\lambda_2(d^2\gamma/dt^2)$ term in Oldroyd's relation), and under oscillatory shear this could be an important term, shifting the sinewave maximum. Also, this model assumed that the relation for behavior above the dynamic yield stress, τ_d , will define the behavior until the shear stress again returns to τ_d , at which point an elastic behavior will appear. Observed behavior in the present study as well as in some of their own studies (Elliott and Ganz, 1970) suggest that this is not always true. Stress responses have consistently shown a return to elastic behavior at approximately the peak shear or point of zero shear rate. Certainly if the cycle is long compared to the relaxation time the stress response will have reached steady state and would be decreasing down to τ_d as γ approaches γ_0 . On the other hand, if the behavior is still transient, τ_d would not be reached until a later time in the cycle. This particular point is not, however, critical to the analysis, as one can use only data prior to this point to fit the model and obtain the necessary parameters. This behavior is interesting from a structural standpoint. As the shear stress does not suddenly dip to τ_d indicates that the network can support a larger shear stress, as is commonly known from its larger static yield value. The almost instantaneous return to an elastic response at this point also suggests that flocculation is

quite rapid (momentum may enhance this rate which is usually due to Brownian motion alone). This would also indicate that particles/aggregates are stuck to the viscometer walls. During flow, all of the aggregates, including the loose structure fragments, are stretched, and at the point of zero shear, flocculation of the loose aggregates with those stuck to the walls apparently occurs more rapidly than stress relaxation within the aggregates. A similar effect was noticed when a step function was used for the applied shear. If the amplitude was low enough such that no bonds were broken, the response was representative of the structure elasticity, i.e. it rapidly approached a constant value equivalent to $G\gamma$. If particles were not attached to the walls, the shear stress would represent a viscous layer near the wall and would therefore, be expected to relax to zero shear stress. Also, if a high amplitude step function was used, structural bonds apparently broke, as the stress response displayed a peak and relaxed to some residual shear stress. This too indicates that the network rebuilds at a faster rate than that of the relaxation of the stretched flocs. Although the step function was not used in all of the present gel measurements, for those cases which included this input function, the results indicated that the observed residual stress was approximately equal to the steady state yield stress (extrapolated from steady-state shear stress vs. data which will be discussed later in this section).

Use of the modified Maxwell model (as proposed by Elliott and Ganz) may be straightforward in cases where the response is approx-

imately a square wave (although such response may have been due to slip planes). However, in cases where the response is a distorted somewhat flattened sine wave, the yield transition point is often not well defined on the output. This makes curve fitting and parameter determinations more complex. Also, if one is going to fit such data to a model which includes a transient stress response, it might be best to include also the shear-rate transient term, i.e., use the modified Oldroyd relation.

Payne and Whittaker (1970) obtained non-linear viscoelastic responses for concentrated clay-water mixtures. Their results were in the form of Lissajous figures where a sinusoidal response appears as either a line or an ellipse. At low amplitudes the stress response was linear, and thus elastic. At higher amplitudes, a hysteresis-type loop developed (Figure 4-17). They defined a dynamic modulus as the total stress amplitude divided by the total strain amplitude, and then used a normalization technique to relate this dynamic modulus to the strainwork (defined as double-stress amplitude times double-strain amplitude). No attempt, however, was made to obtain a value for viscosity, and no rheological model was presented. Also, as the concentrations used were quite high, a dilatancy effect could have occurred. This effect is defined as a steady state response in which the shear stress increases at a faster rate than does the corresponding shear rate, i.e., shear-thickening. Such behavior is also a particle interaction effect, but in this case is due to the close packing of the particles. At increasing applied shear stress,

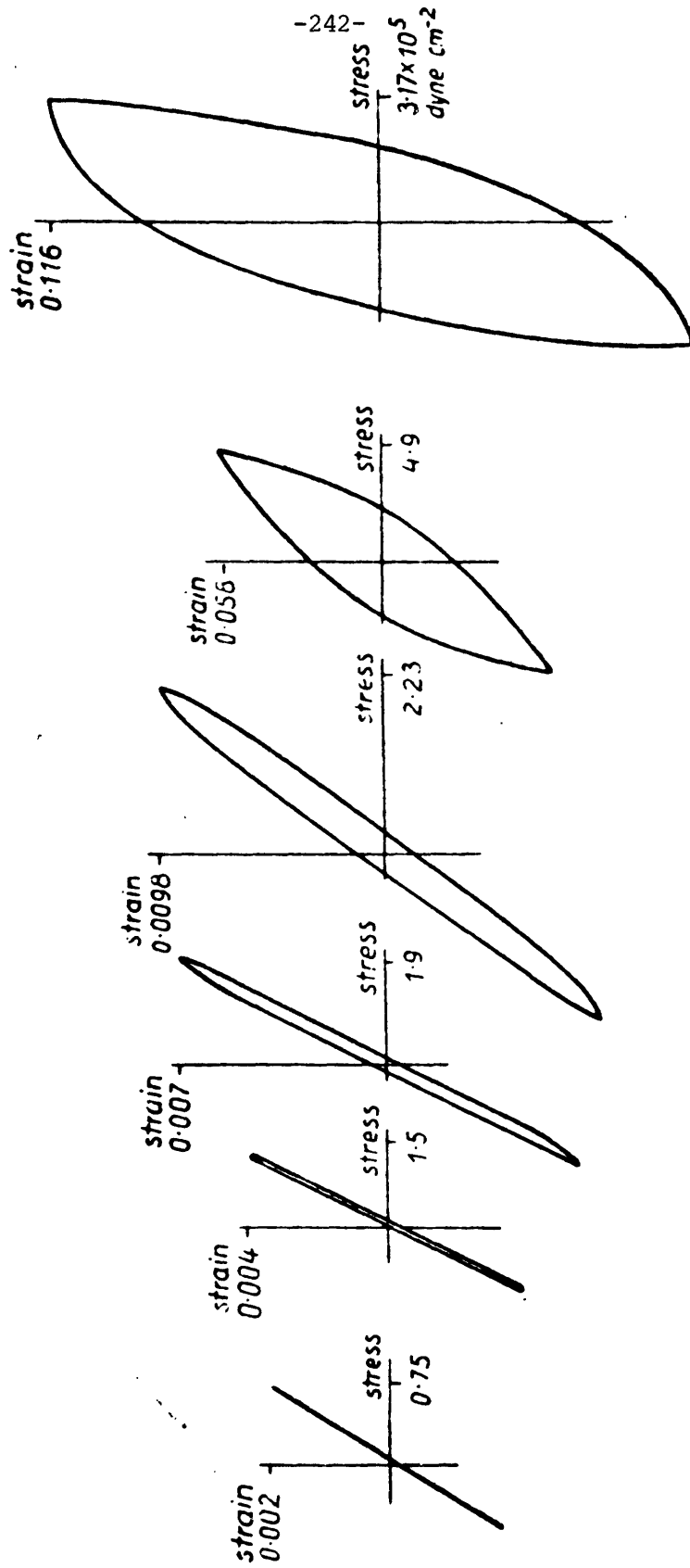


Figure 4-17 Sequence of hysteresis loops from low to high stress levels for 100 parts bentonite, 80 parts by weight of water (Payne and Whittaker, 1970)

the particles are forced together and require more time to move past each other. In many cases, a volume expansion also occurs, as there is not enough fluid to fill the gaps which form as the particles move past each other. In high concentration gels and pastes, the behavior is generally plastic or pseudoplastic at low shear rates (as the particle attractive forces dominate) and does not become dilatant until moderate to high shear rates. The single low frequency, 0.1 Hz, used by Payne and Whittaker, was no doubt low enough to be in the range of plastic or pseudoplastic behavior, thus accounting for the similarity in responses between their clay systems and the present LNG gels. They also had problems with the occurrence of slip planes at high amplitudes which could have been responsible for the plateau regions.

Astbury and Moore (1970) also studied high concentration clay systems, obtaining similar hysteresis-type loops. They suggested analyzing the curves as a Fourier series

$$\tau(t) = \sum_n A_n \sin(n\omega t + \delta_n) \quad n=1,2,3\dots$$

$$\text{or} = \tau_0 \sin(\omega t + \delta(t))$$

where $\delta(t)$ is no longer constant, but varies around the cycle. Here they propose a model which contains a given number of elastic elements, n_e , which obey $g_1 x = F$, and viscous elements, n_v , which follow $g_2 \dot{x} = F$, the sum of these two components, N , remaining constant. The elastic elements will sustain the same force while the viscous elements will sustain the same displacement (equal to the total displace-

ment of the elastic elements) that is

$$F = (g_1/n_e)x + n_v g_2 \frac{dx}{dt} \quad (4-25)$$

The major assumptions in their derivation are 1) as elastic strain energy builds up, the elastic elements convert to viscous elements and 2) the change in n_e is proportional to both δU (change in elastic strain energy) and to n_e . Their result is in the form of a phase modulation system.

$$\tau(t) = \epsilon_0 (P\omega t) \sin \omega t + Q(\omega t) \cos \omega t \quad (4-26)$$

$$\text{where } P(\omega t) = K_1 / (1 - \lambda \sin^2 \omega t)$$

$$Q(\omega t) = K_2 (1 + \lambda c_0 \sin^2 \omega t / (1 - c_0))$$

The values for these constants can be easily obtained using the stress responses at zero and peak ($\pi/2$ radians) shear. In fact, Astbury and Moore were quite successful with this proposed relation. For each of their Lissajous figures, the two necessary data points were used to determine the constants for equation 4-26, and the resulting theoretical curves, in all cases, were almost precisely equal to those experimentally observed. As a rheological model, however, their relation does not seem adequate. Written in terms of shear, shear rate, etc.,

$$\tau = \frac{g_1 \dot{\gamma}}{\left(1 - \frac{g_1 \dot{\gamma}^2}{2n_0 U_c}\right)} + \left[N - n_0 \left(1 - \frac{g_1 \dot{\gamma}^2}{2n_0 U_c}\right) \right] g_2 \dot{\gamma} \quad (4-27)$$

where $\eta_0 = C_0 N$ and C_0 is an initial concentration factor

U_c = an intrinsic energy level which governs the breakdown process

For steady shear rate this relation predicts an ever-increasing shear stress with time.

Komatsu and Mitsui (1973) studied the nonlinear properties of selected commercial cosmetic creams (semisolid emulsions) using a Weissenberg rheogoniometer. They correlated their results using an expression based on the general theory of continuum mechanics.

$$\begin{aligned} \tau(t) = & (G'_{11} \gamma_0 + G'_{13} \gamma_0^3) \sin \omega t + (G'_{11} \gamma_0 + G''_{13} \gamma_0^3) \cos \omega t \\ & - G'_{33} \gamma_0^3 \sin 3\omega t - G''_{33} \gamma_0^3 \cos 3\omega t \end{aligned} \quad (4-28)$$

This is a Fourier series of odd harmonics. Calculations of the coefficients were done by computer, and their sample result indicated that the use of just the first and third harmonic did not provide an adequate fit for the observed curves. They studied two undefined commercial creams, one of which consistently gave square wave responses with a very slight (but pointed) overshoot with each change in direction, the other which gave peaked responses at high shear amplitude similar to those predicted by the "modified Bingham model" of Elliott and Ganz. At low shear amplitude, the non-linear response was quite similar to those observed in the present study. They also superimposed a constant shear rate on a sinusoidal shear strain and suggested that the observed responses were indicative of a yield stress

(which they referred to as dynamic yield stress). Further, they mentioned that the Casson equation would give a response $(\tau^{1/2} = k_0 + k_1 \dot{\gamma}^{1/2})$ similar to several of their experiential results. However, no correlation of their data was attempted and not enough quantitative information was reported for any further analysis of their results. In other studies of polymeric latex particles dispersed in polymer solutions (Matsumoto, et al., 1973; Onogi, et al., 1970), a slightly different type of skewed curve was obtained (Figure 4-18). They used similar Fourier series type correlations to analyze their results with no further explanation of the unusual behavior. Similar curves were occasionally observed in the present study, but they were generally assumed to be due to slip planes. In the latex studies, however, the dispersion medium was also viscoelastic and possibly their results were due to superimposed structure and fluid viscoelasticity.

Although gels are distinctly viscoelastic, the study of their rheological properties using sinusoidal oscillation has not been straight-forward, as indicated by the variety of past interpretations. The non-linear behavioral pattern observed in the present study, however, is quite similar to the transient responses for steady shear rate. In fact, the actual shear oscillation was quite linear over much of the region around the inflection point (Figure 4-19) and the oscillation was therefore similar to one alternating between two steady shear rates. Such alternating shear rate oscillation can be precisely represented by a sawtooth function which is an available input waveform on the present viscometer. Thus, sample tests were

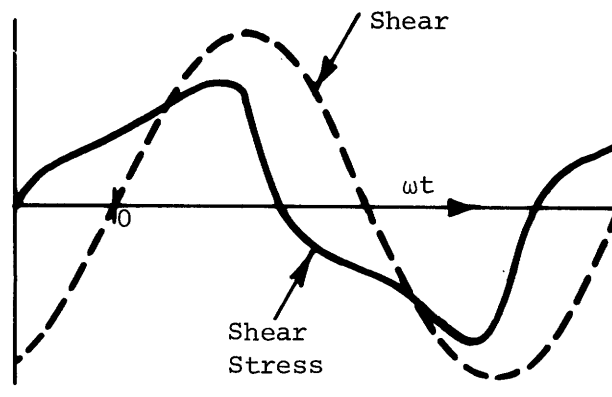


Figure 4-18 Shear stress response for disperse systems of polystyrene solution and styrene-divinyl benzene copolymer particles (Matsumoto et al., 1973).

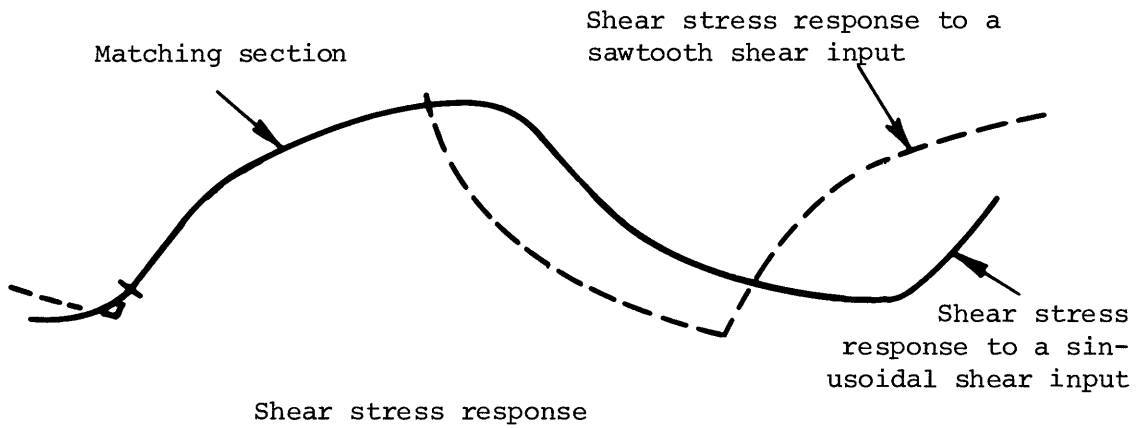
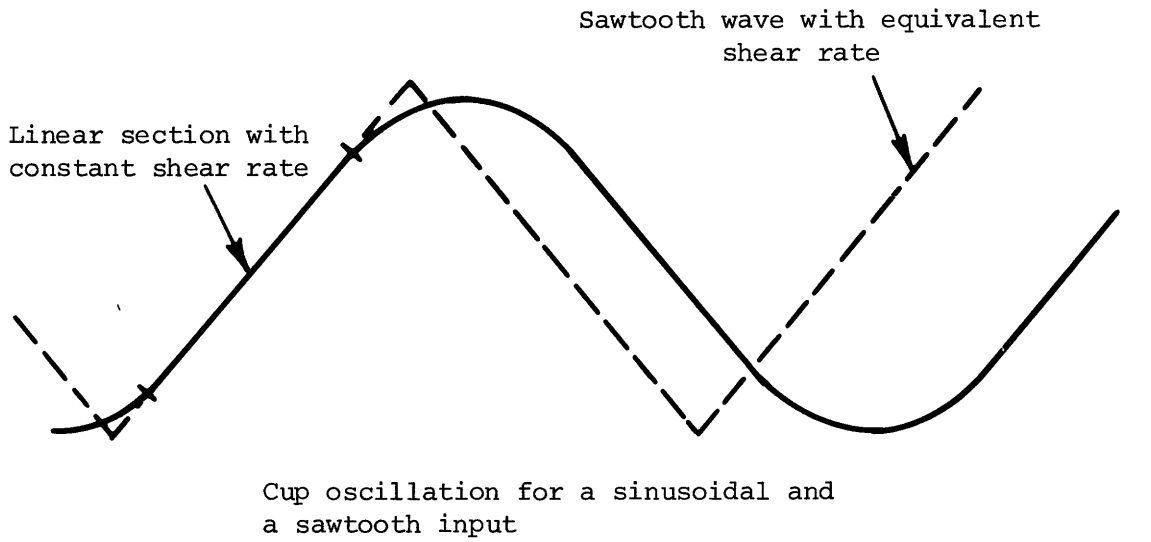


Figure 4-19 Comparison of responses for the constant shear rate portion of a sinusoidal input and an equivalent shear rate sawtooth input.

run with this sawtooth input to ascertain whether the transient response observed during the linear portion of the sinewave was the same as that under an equivalent alternating steady shear rate. The results did, indeed, show a match between the two transient responses, suggesting the shear stress had no complex history dependence and that the gel rheological behavior could probably be defined with a relation no more complex than the modified Oldroyd expression. This also indicated that either a sawtooth or sinewave could be used to obtain transient shear stress data for steady shear rates. (Although a sawtooth function might appear to be more appropriate, the electronic feedback loop in the present viscometer often distorted the shear waveform when highly rigid gels were being measured. In this case, the resulting linear regions for the two waveforms were approximately equal, and there was no advantage to using one waveform over the other.) In the earlier discussion on the interpretation of such transient stress data, it was mentioned that the slowly decaying portion closely approximated an exponential which asymptotically approached the steady-state shear stress. This was also assumed to be true for the present LNG gels, and shear stress analysis for a sinusoidal shear at low frequencies and high amplitude (i.e. the conditions which produce a nonlinear viscoelastic response) was done as follows. Only the linear portion of the shear oscillation was considered, and the shear-stress response in this region always included an initial steep elastic portion followed by a smooth transition into a more slowly decaying response. The transition was generally quite rapid and easily

distinguished from the desired region of slow relaxation. The slowly decaying response was then fitted to an exponential, and the value of this function at infinite time was assumed to be the desired steady-state shear stress. Varying the frequency was then used to obtain the desired steady-state shear stress versus shear rate curve. The steep portion of the shear stress response was used to measure an elasticity for the gel structure. Sample tests showed that this elasticity ratio (Δ shear stress / Δ shear) was about 25 percent lower than that measured for the low frequency-low amplitude sine oscillations, indicating that the structure did not completely rebuild at each direction change. However the value obtained using the non-linear viscoelastic response is certainly a reasonable estimate for the structure elasticity.

As sinusoidal oscillation allows the structure to rebuild with each change in direction, a yield stress is continually present (but alternates direction). As discussed in Section 4.2, when a gel, initially at rest, is subjected to a constant shear rate, the transient response may exhibit a peak. Thus, it is possible that a peak might occur in the present transient shear stress measurements. However, Jachimiak, et al. (1974) have given a criterion for this peaking, i.e. when $\dot{\gamma}/k_T \leq 1$ no peak will occur. To predict whether a peak will occur under the present conditions, one must, apriori, know the relaxation constant, k_T , or assume that the conditions are within the limit and obtain k_T by fitting an exponential to the curve. There are several qualitative reasons to believe that the present

systems will not peak in the frequency range being considered (≤ 0.5 Hz.). Examples of transient data (Papenhuijzen, 1972 and Jackimiak, et al., 1974) show two important characteristics of those curves which peak. First, the ascent is steep with little change in slope until the peak is approached. Second, when transient responses for different shear rates are compared, the observed shear stress for a given shear increases with increasing rate (Figures 4-3 and 4-9). Neither of these characteristics fit the present case. Also if the structure is partially broken, the transients are less likely to peak, as Michaels and Bolger (1962) did not observe peaks when shifting from one constant shear rate to another. When the slowly decaying portions of the shear stress responses were fitted to exponential functions, the resulting relaxation times did indeed yield $\dot{\gamma}/k_t$ ratios less than 1, further confirming that no peak is expected.

The shear stress versus shear rate results for the LNG gels using the proposed method of data analysis are presented in Figure 4-20. Several different parameters have been varied, including the gelant, final gelant concentration, natural gas composition, and gelant concentration in the initial vapor mixture. In all cases the gel behaved as a Bingham plastic at these low frequencies (i.e. low shear rates). Also, the data used in the analyses adequately fit exponential curves, indicating that a single stress relaxation time, as in the Maxwell model and Oldroyd's model is sufficient to describe this slowly decaying region. This Bingham plastic behavior is not unexpected, as shear stress/shear rate data from other investigations

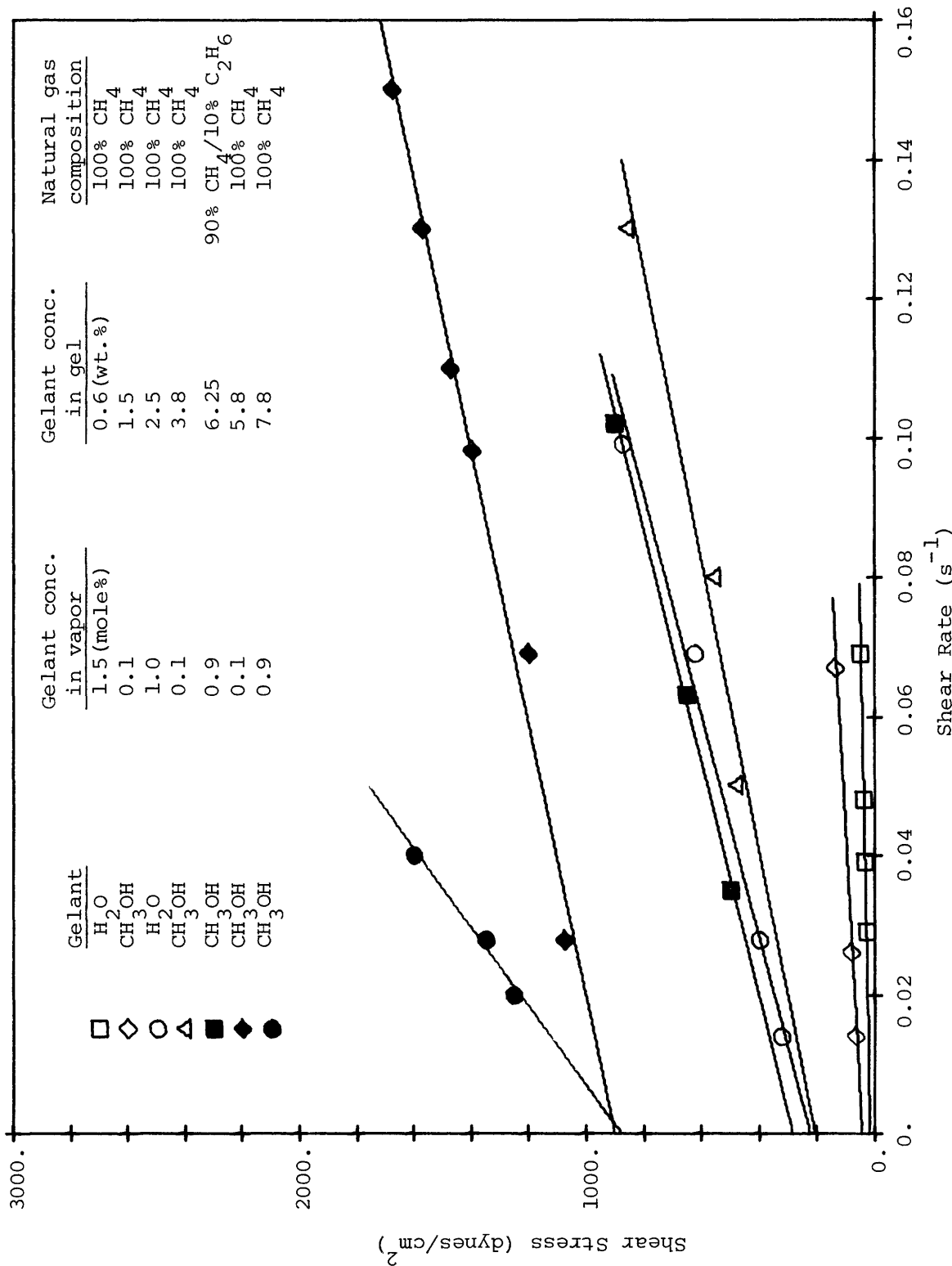


Figure 4-20 Rheological behavior of LNG gels.

have indicated that this may occur (Michaels and Bolger, 1962; Bantoft, 1959). These Bingham plastic curves were extrapolated to zero shear rate to obtain the steady-state yield stress values. These are tabulated in Table 4-2 along with the viscosity coefficient, structure elasticity, static yield stress (the technique for measuring this quantity is discussed in the next section), and relaxation constant. The viscosity coefficient represents the slope of the shear stress/shear rate line. The structure elasticity was determined from the steep elastic shear stress response as mentioned previously, and the relaxation constant was the average value for the range of shear rates considered. In general, this relaxation time was fairly constant (within the accuracy of its determination and reproducibility), although for some of the dilute gels there was a noticeable increase with increasing frequency. The modified Maxwell model indicates that this time constant may be equal to G/η_p . However, this was not found to be true.

Although the oscillating viscometer could only be used to obtain viscosities at low shear rates, the behavior at higher shear rates can be estimated using the relations previously discussed. First, the values for the steady-state yield stress were used to determine the particle size, and, for all of the LNG gels, the particle radius ranged from 100 to 200 A. The results for the methanol gels clearly showed that changing the gelant concentration in the initial vapor mixture (i.e. the gas mixture from which the gelant was condensed) affected the final gel rigidity. Lower gelant concentrations in the

Table 4-3

Elastic and Viscous Properties of LNG Gels

<u>Gel</u>	<u>Yield Stress</u>		<u>Viscosity</u> <u>coeff.</u>	<u>Elasticity</u> <u>(dynes/cm²)</u>	<u>Relax.</u> <u>(1/λ₁)</u>
	<u>Steady-State</u> <u>(dynes/cm²)</u>	<u>Static</u> <u>(dynes/cm²)</u>			
1 □	15	60	500	200	0.13
2 ○	235	1050	5000	2000	0.23
3 ■	290	1425	5833	10,000	0.17
4 ●	900	3600	20,000	40,000	0.21
5 ◇	800	3300	5833	20,000	0.09
6 △	230	1050	6250	3500	0.05
7 ◆	45	225	1333	1200	0.06

Symbols refer to graph on previous page.

vapor produced higher yield stress gels (for the same final gel composition) suggesting that smaller particles were formed. However, for the observed variation in yield stress with vapor gelant concentration, the estimated difference in radius was only 30 percent. Although the water gels did not show a similar variation in yield stress, this may have been due to the small concentration range studied. The gelant concentration in the vapor mixture was only varied by a factor of two, whereas it was varied by a factor of 9 in the methanol gels.

To estimate τ_B for the various LNG gels, Equation 4-12 was used with the following conditions: proportionality constant = 10^{-1} , $D = 1A$, $r = 100A$, $n = 2$ to 3 . The resulting values were all quite reasonable as τ_B was always greater than τ_y by a factor ranging from 2 to 10. The viscosity coefficient for this high shear rate Bingham plastic range can be estimated using Equation 4-9 and an assumed value of 4 for ϕ_{FP} . However, this viscosity term proved to be negligible for all of the LNG gels considered here. Thus, the shear stress will be approximately constant for high shear rates. At moderate shear rates, the behavior will be pseudoplastic, but not enough information is known to adequately describe this region.

Thus, a fairly new oscillating shear technique has been used in the present study. The resulting shear stress behavior has been discussed and interpreted in light of what is presently known about gel rheological behavior, and steady state shear stresses were obtained for the low shear rate region. Although this technique was adequate

for the present application of LNG gels, future application to other gels, where very precise measurements are desired, should include viscometer modifications and further confirmation of this method of analysis using steady shear rate data. A higher maximum shear (but not so high that slippage occurs) would be desirable as the steady-state value could then be more closely approached. Although the maximum shear can be modified by decreasing the gap width between the cup and the bob, there are limitations due to particle size. Thomas (1961) observed that in capillary viscometer measurements, a tube diameter greater than 400 times the particle diameter was necessary to avoid wall effects. In spite of the drawbacks associated with this viscometer, the oscillating shear technique provides data on both the viscous and elastic properties of gels and appears to be a promising technique for future gel rheology studies.

4.4.2 Static Yield Stress

A useful technique for estimating the static yield value is the measurement of the height of the gel remaining on a suspended disk which has been submerged in the gel and gradually withdrawn. This gel height is indicative of the structure strength of the gel, i.e. the structure is strong enough to resist the hydrostatic forces present. To determine what the actual correlation was between yield stress and gel peak height, several Cabosil gels were made and analyzed using a Stormer

viscometer. This instrument has a Couette (coaxial cylinder) geometry and operates by applying a constant torque to the bob. When the torque (i.e. applied shear stress) is less than the static yield, the bob will not rotate (although it may move slightly due to gel elasticity). As the torque is increased, eventually the gel structure will fragment and flow will occur. Thus, this is a particularly useful technique for measuring the static yield value for a gel. The results from the study on Cabosil gels (Table 4-4) showed that the static yield stress was equal to 0.25 to 0.35 ρgh where h equals the peak height, g equals the acceleration due to gravity, and ρ equals the gel density. This functionality of τ_s with ρgh is not unexpected as the gel structure is opposing the hydrostatic force. The coefficient is also in close agreement with that derived for various piling geometries. (Appendix R) If the geometry is cylindrical, the maximum shear stress occurring in the pile would be $\frac{1}{2}\rho gh$. On the other hand, if the pile were hemispherical, the maximum shear stress would be $\approx 0.35 \rho gh$. The geometries actually observed were slightly flattened hemispheres and thus would be expected to lie somewhere in between these two values. Thus, the experimental results were close to those predicted, suggesting that this is a useful technique for determining an approximate value for the static yield stress. Based on experimental results, the best correlation is $\tau_s = 1/3 \rho gh$.

To determine the static yield stresses for the different LNG gels, this gel height measurement was primarily used (Figure 4-21). However, for further confirmation, one of the gels was also tested

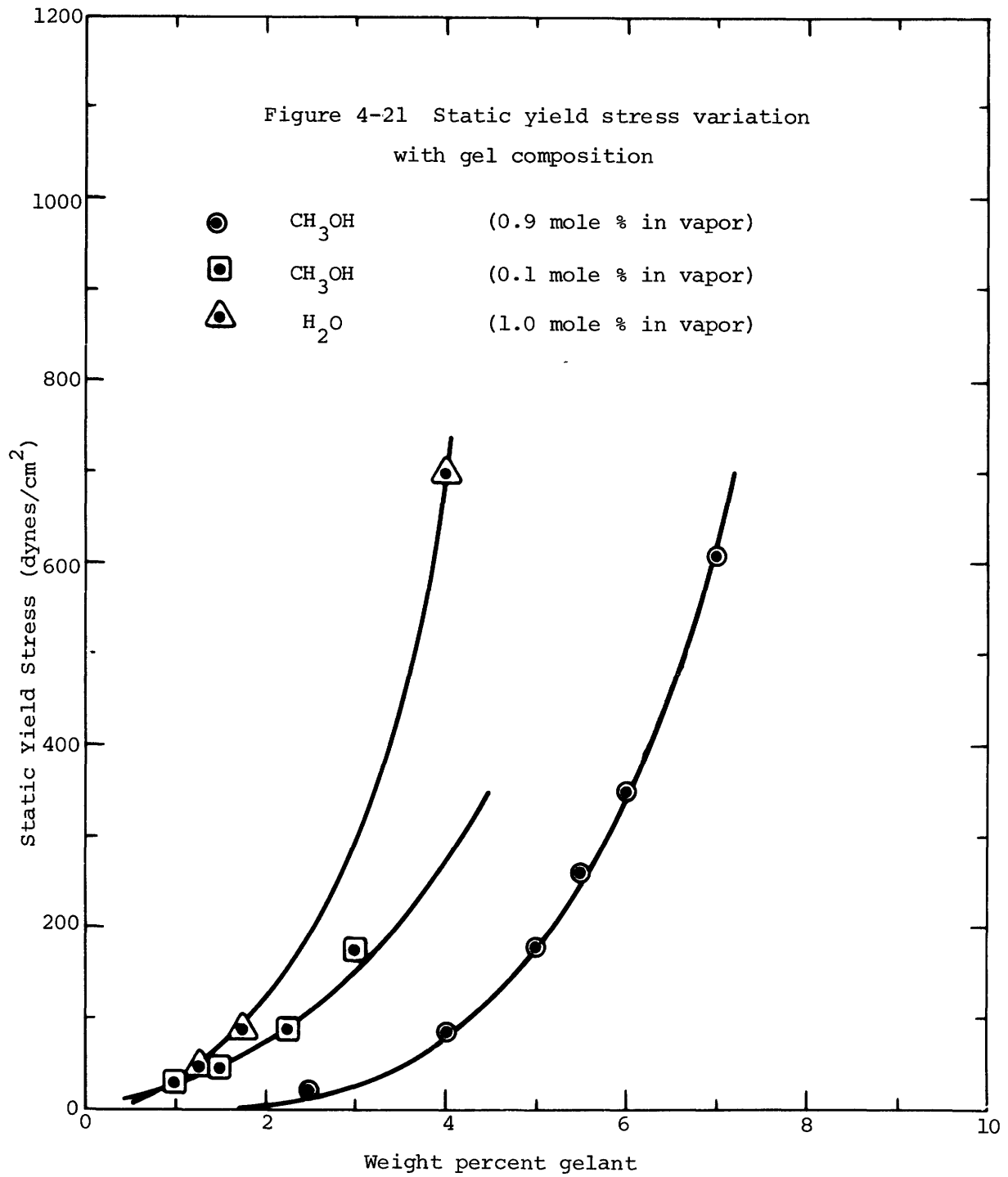


Table 4-4 Static Yield Stress for Cabosil Gel

<u>Solvent</u>	<u>Cab-O-Sil Concentration (Vol %)</u>	<u>Static Yield (dynes/cm²)</u>	<u>Peak Height (cm)</u>	<u>$\frac{1}{3} \rho gh$</u>
Ethylene Dichloride	5.0	97	0.24	106
	6.5	244	0.64	282
	7.0	1170	> 2.54	1120
Methanol	8.	59	0.32	84
	8.2	136	0.64	167
	9.	234	0.8	200

using a Brookfield viscometer. (This instrument is described in Chapter 6.) Although difficulties due to the occurrence of slippage planes can arise using this technique, the results were in fair agreement with the gel height measurements (see Table 4-5). Comparison of the static and steady-state yield stress values indicated that the static yield stress was approximately four times greater than the steady-state yield stress for the present gels.

Table 4-5 Static Yield Stress for Liquid
Methane-Methanol Gels

<u>Conc. (wt %)</u>	<u>Static yield stress measured using Brookfield viscometer</u>	<u>Static yield stress peak height esti- mation ($1/3 \rho gh$)</u>
1.0	250	261
5.5	636	550
9.0	1844	> 700

CHAPTER 5 - VAPORIZATION OF LNG GELS ON WATER

5.1 General Boiling Behavior

The boiling of liquids on solid surfaces has been well characterized both qualitatively and quantitatively, and two distinct stable boiling regimes have been shown to occur (Figure 5-1). When the temperature difference between the hot solid surface and the bulk liquid (ΔT) is small, nucleate boiling results. This is characterized by bubble formation and growth at specific nucleation sites on the solid surface. Thus, the surface properties of the solid play an important role in determining the resulting behavior. As the temperature difference increases, smaller and smaller surface disparities can act as nucleation sites. Eventually the active bubble initiation sites become very closely packed together, and a thin film of vapor forms between the boiling liquid and the solid. A simultaneous drop in heat flux occurs, thus initiating film boiling. As the temperature difference is further increased, the film thickness will increase slightly, but by a factor less than that for the increase in ΔT . This results in an increasing heat flux with increasing ΔT . In the film boiling region, the surface properties of the solid are much less important, the controlling factor being the vapor film limitation on heat transfer. In general, there is a range of ΔT 's which separate the nucleate and film boiling regions, and this regime is referred to as unstable transition boiling. Due to the transient nature of such boiling

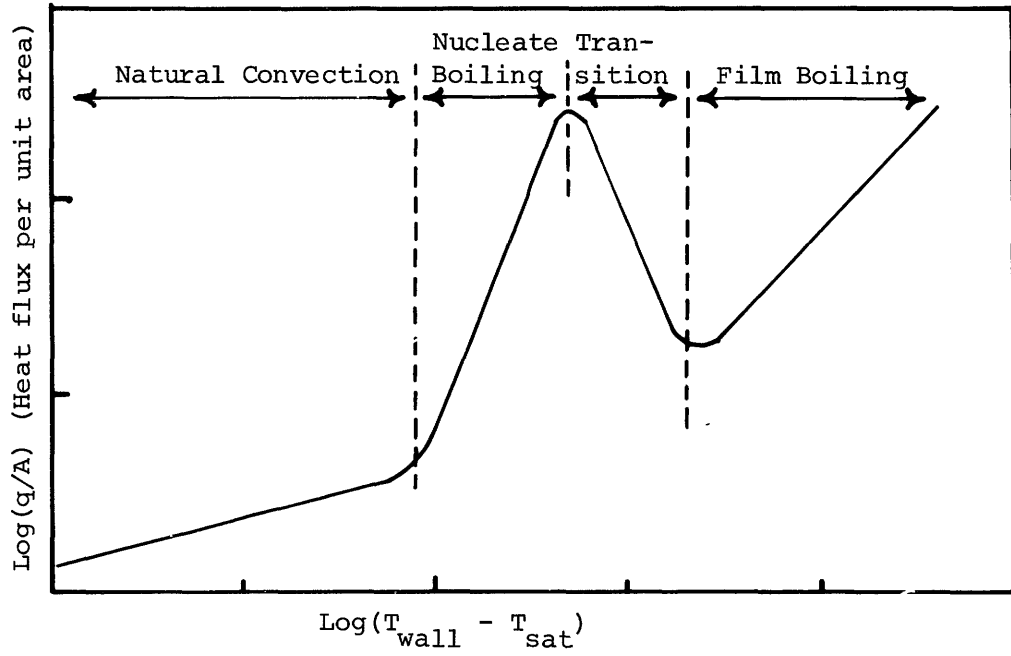


Figure 5-1 Characteristic Boiling Curve
 T_{sat} is the temperature of the saturated fluid.

behavior, experimental values of heat flux versus ΔT for this region have not been obtained.

In this study the liquids of interest are liquid methane and LNG (methane plus small quantities of ethane and propane), and some data are, in fact, available on the steady-state boiling behavior of these cryogenics. Colver and coworkers (Brown and Colver, 1968; Science et al., 1967) experimentally determined the film and nucleate boiling curves for these liquids boiling on a gold-plated cylindrical heating element. These are shown in Figure 5-2 and will be referred to in later discussions.

The boiling of a liquid on top of another immiscible liquid has not been as well characterized experimentally, but a few steady-state experiments have been performed with a liquid boiling on top of mercury. (Navokovic and Stefanovic, 1964; Gordon et al., 1961; Viskanta and Lottes, 1962). In general, it was found that surface contamination and adsorbed gases had a significant effect on the observed heat fluxes in the range appropriate for nucleate boiling. Such contamination apparently lowered the liquid superheating required for vapor nucleation. If the interface could be kept perfectly clean, one might expect convective heat transfer with no bubble formation until the liquid superheat became large enough to produce homogeneous nucleation. Interfacial turbulence was also found to affect heat transfer rates, an increased heat flux resulting from increased agitation.

Several studies have been made on the transient boiling of a

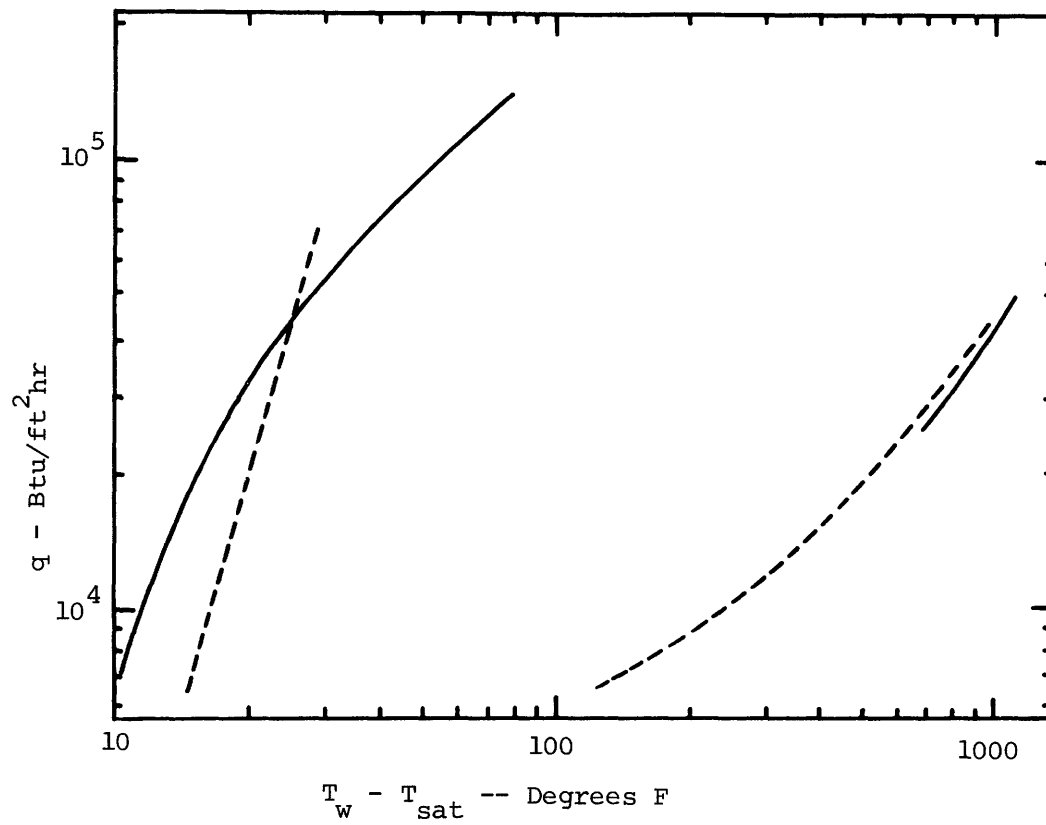
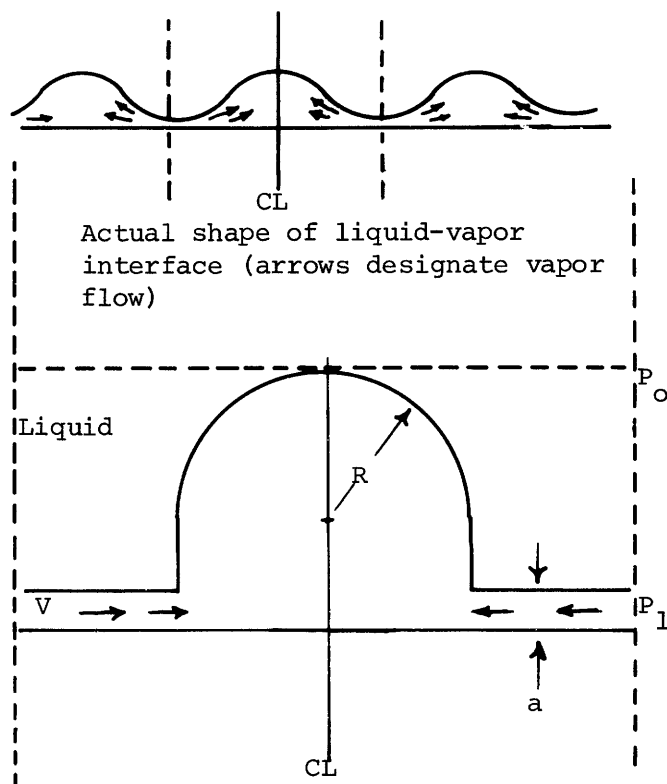


Figure 5-2 Boiling curves for Methane (dashed lines) and LNG (solid lines). From Sciance et al. (1967) and Brown and Colver (1968).

cryogen on water (Burgess et al., 1970; Boyle and Kneebone, 1973; Nakanishi and Reid, 1971; Drake et al., 1975). In these studies, various cryogens (liquid nitrogen, liquid methane, liquid ethane, and LNG) were spilled onto a confined region of water. In all of these investigations except that of Boyle and Kneebone, the quantities spilled were sufficient to give complete coverage of the water surface and ranged in initial cryogen height of 0.8 cm to 6 cm. The vaporization rates were measured by recording mass as a function of time. In this type of experiment, the temperature at the water surface may change with time and ice may form, thus the appropriate temperature difference (ΔT) and surface features will be transient. It is also possible that the vapors coming off may be substantially superheated if film boiling occurs. Bubble formation in film boiling proceeds by a wave motion with an influx of partially warmed vapor from the thin film region in toward the crest of the forming bubble (Figure 5-3). This allows the vapor in the departing bubble to be at a temperature above the saturation temperature. In nucleate boiling, on the other hand, little or no superheating of the vapor has been observed (van Stralen, 1966) when the boiling occurs on a solid surface. For the nucleate boiling of a cryogen, the interface temperature must be fairly low, thus requiring ice formation in the present case. This ice will provide nucleation sites for bubble formation, and the resulting nucleate boiling behavior should, therefore, be similar to that observed using other solid heat sources, i. e. little or no vapor superheat should be observed. Drake et al. were the first to measure



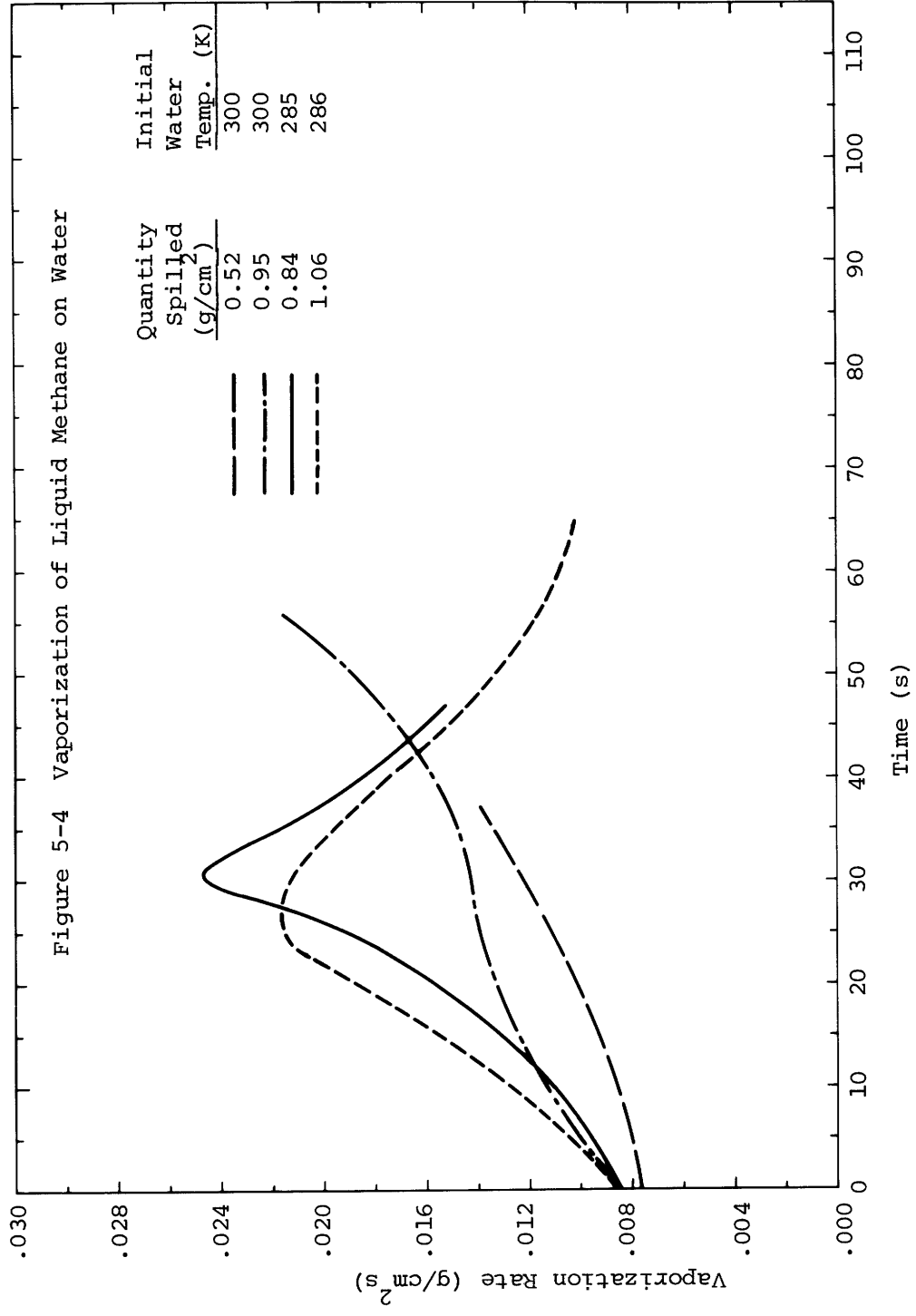
Physical model of film boiling
from a horizontal surface

Figure 5-3 Film Boiling Model Used
by Berenson (1961)

the temperature of the escaping vapor during cryogen boil-off. In the case of liquid nitrogen boiling on water, they found the vapor to be substantially superheated and showed that this sensible heat effect must be included with the mass boil-off rate to obtain the actual heat fluxes. Liquid methane, liquid ethane, and LNG, on the other hand, showed little or no superheating of the boil-off vapors suggesting a nucleate boiling mechanism.

5.2 Characteristics of Liquid Methane and LNG Boiling on Water

The primary objective of this study was to determine whether gelling LNG significantly affected the boil-off rate. Initially, confined spills of liquid methane (>99% pure) and LNG were made to compare with the results of previous studies. The apparatus and procedure are discussed in Chapter 6, and the results are shown in Figure 5-4. These boil-off curves are quite distinctive, showing an initial increase in boil-off rate. If the initial quantity spilled was sufficiently large, the boil-off rate would peak and then continue to decrease. The end points for these curves represent a residual cryogen height of ≈ 0.2 cm as this is the point when surface tension causes pool breakup and thus incomplete surface coverage. Such behavior was also observed in the previous investigations and seems to be typical for the boiling of LNG and liquid methane on water under a wide range of conditions. The measured boil-off rates (Figure 5-4) were higher than those reported by Drake et al., but



were similar to those obtained by Burgess et al. Some variation, however, is not uncommon, and Drake et al. observed that even small amounts of heavier components (≥ 1 percent) caused a significant increase in the observed boil-off rates. The higher values here may also be representative of increased turbulence at the interface. In this study the cryogen was spilled directly onto the water surface, whereas Drake et al. poured the cryogen onto a distributor which caused the liquid to flow smoothly onto the water surface. Such a technique was inappropriate for studying gel boil-off as the gels would tend to stick to the distributor. Also the impact and resulting turbulence from a free spill may be more representative of what would occur in a major accidental spill, such as from a ruptured LNG tanker.

Drake et al. reported that there was no significant effect of initial water temperature (for the range 9.9 to 52.7 C) and quantity spilled (range 0.33 to 1.01 gm/cm² or 0.79 to 2.4 cm initial height) on the resulting boil-off rates. However, Burgess et al. studied larger quantities (1.13, 1.7, and 2.55 gm/cm²) and did observe a variation in boil-off rate for the different quantities spilled. In the present study, a slight effect on boil-off rate was noticed when these factors were varied. However, the observed effects were insignificant compared to the variation in boil-off rate which occurs due to slight changes in composition.

The increasing boil-off rate which is characteristic of both liquid methane and LNG vaporizing on a confined water surface is thought to represent a transition between film boiling and nucleate

boiling. The fact that it is gradual indicates a fractional shift of the interface to nucleate boiling, i.e. ice patches form and grow at certain preferential locations until there is complete surface coverage. Such ice formation was, in fact, observed in all the liquid methane and LNG spills. However, a disadvantage of the confined water surface is its susceptibility to ice crust formation and growth at the container walls. In unconfined spills, a few residual ice patches have been noticed once the LNG has boiled away, but no substantial ice crusts have ever been observed. In fact, Boyle and Kneebone (1973) performed unconfined spill studies by pumping LNG at a steady rate onto a pond and measuring the steady-state pool diameter. In almost all of their tests, they observed a low boil-off rate per unit area suggesting film boiling. Burgess et al. (1970), on the other hand, performed instantaneous-type spills (i.e., a given quantity was dumped from a barrel onto the water surface) and found that their results indicated that a much higher heat flux occurred, typical of the confined spills. If such high heat fluxes do occur in unconfined spills, this suggests that numerous ice patches actually form during the spreading and boil-off process, but which melt quite rapidly once the cryogen is completely vaporized.

For the present confined spill tests, a comparison can be made between the transient heat flux values and the previously reported steady-state boiling curves for LNG and liquid methane on a solid surface. The recorded initial heat fluxes were similar to the minimum steady-state film boiling heat fluxes reported for liquid methane and

LNG (Brown and Colver, 1968; Sciance et al., 1967) (See Figure 5-2). The recorded peak values, however, were significantly lower than the previously reported peak steady state values for nucleate boiling. This indicates that once an ice patch forms, the surface temperature drops fairly rapidly causing further transients in the observed boil-off rates.

In the case of liquid methane, the initial temperature difference ($T_{\text{water}} - T_{\text{CH}_4}$) was well within the film boiling region. The observed shift to nucleate boiling therefore suggests that conduction and convection in the water phase could not maintain the necessary heat flux without a substantial drop in the water surface temperature, and subsequent ice formation (i.e., q_{CH_4} (for $\Delta T = T_{\text{ice}} - T_{\text{CH}_4}$) $>$ $q_{\text{H}_2\text{O}}$ (conduction and convection)). This limits further heat transfer to conduction. The steady-state boiling curves for LNG indicate a much higher minimum temperature difference (compared with liquid methane) for film boiling. Although this value was expected to be higher, it is significantly higher than would be predicted from available expressions. Thus it is not certain whether the initial temperature difference in an LNG spill is representative of film boiling or transition boiling.

The addition of heavier components to liquid methane (thus forming LNG) will also cause heat flux transients due to composition variation during boil-off. In the case of LNG (a typical heavy composition) boiling on a solid surface, Brown and Colver (1968) (Figure 5-2) made steady-state measurements for both the film and

nucleate boiling regimes. Here they found an expanded nucleate boiling regime (as compared with pure liquid methane) with larger temperature differences often required for an equivalent heat flux. Also, the peak nucleate boiling flux was substantially increased, the minimum temperature for film boiling was shifted to a larger ΔT , and the film boiling heat fluxes were slightly lower for the same ΔT . The expanded nucleate boiling region, along with the higher peak heat flux are, no doubt, responsible for the observed transient boil-off behavior on water, i.e. the more rapid initial increase in boil-off rate (as compared with liquid methane) and the overall higher heat flux values.

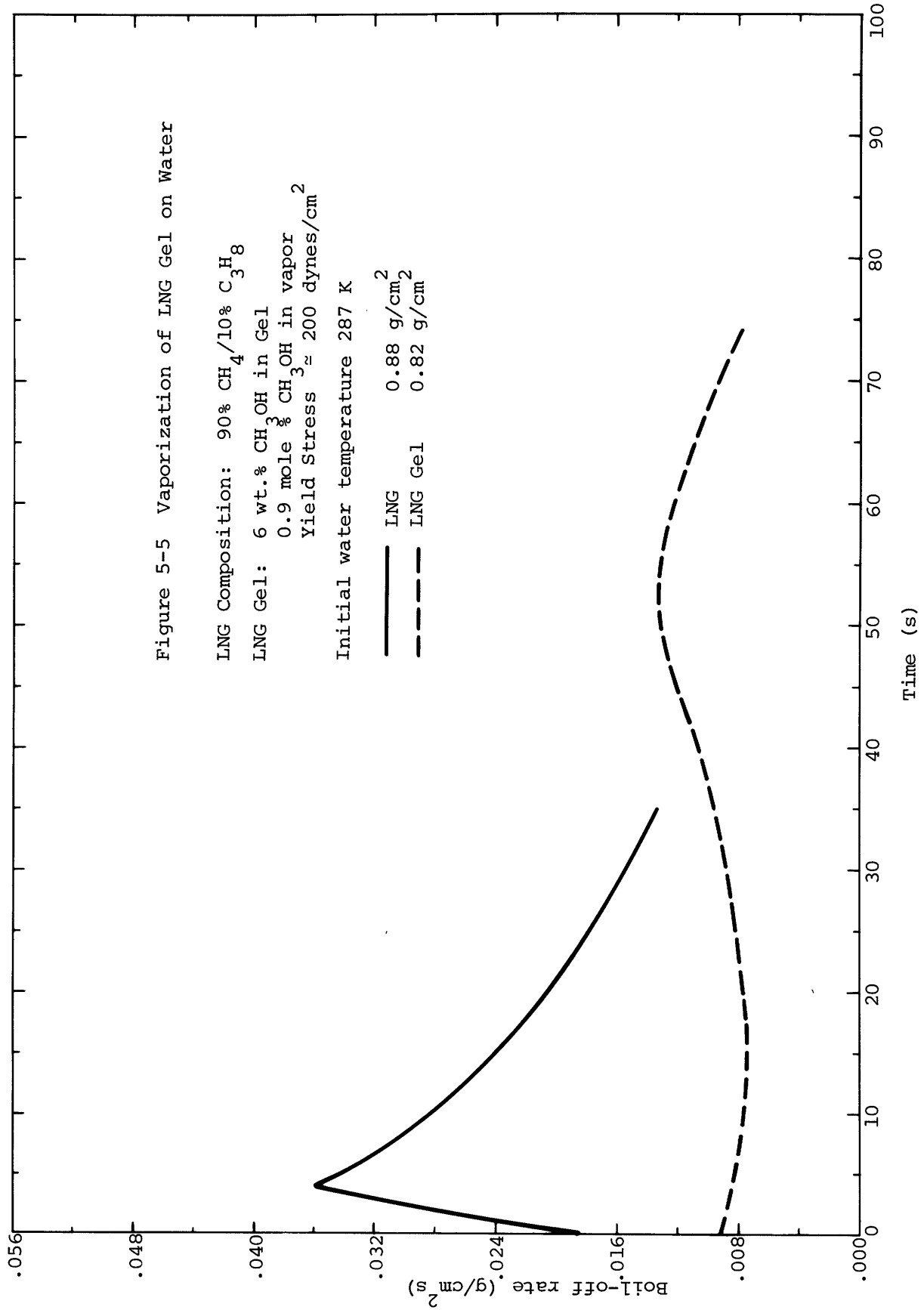
5.3 Boil-off Behavior of LNG Gels on Water

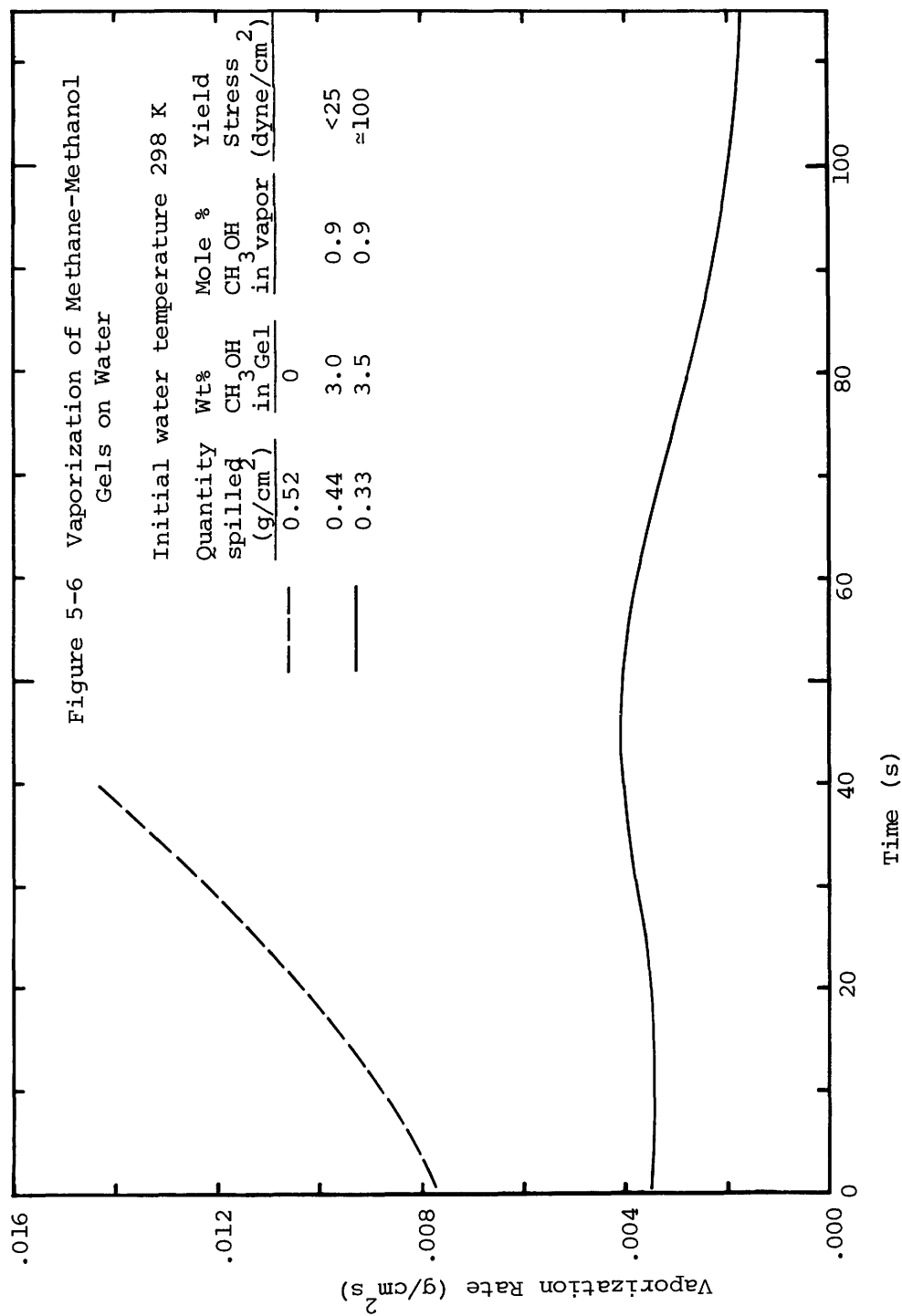
Although the vaporization rate of liquid methane and LNG on water is quite transient with a combination of both film and nucleate boiling, the boil-off rates for liquid methane- and LNG -methanol gels were low and fairly steady, indicating steady-state film boiling (Figures 5-5, 5-6, and 5-7; all original data for mass vs. time are given in Appendix S). Also, the boil-off vapor was observed to be superheated by as much as 30 to 70 K, lending further evidence to a film boiling mechanism. A further discussion of film boiling and the correlations available for this region will help to elucidate why film boiling behavior might be expected for these gels.

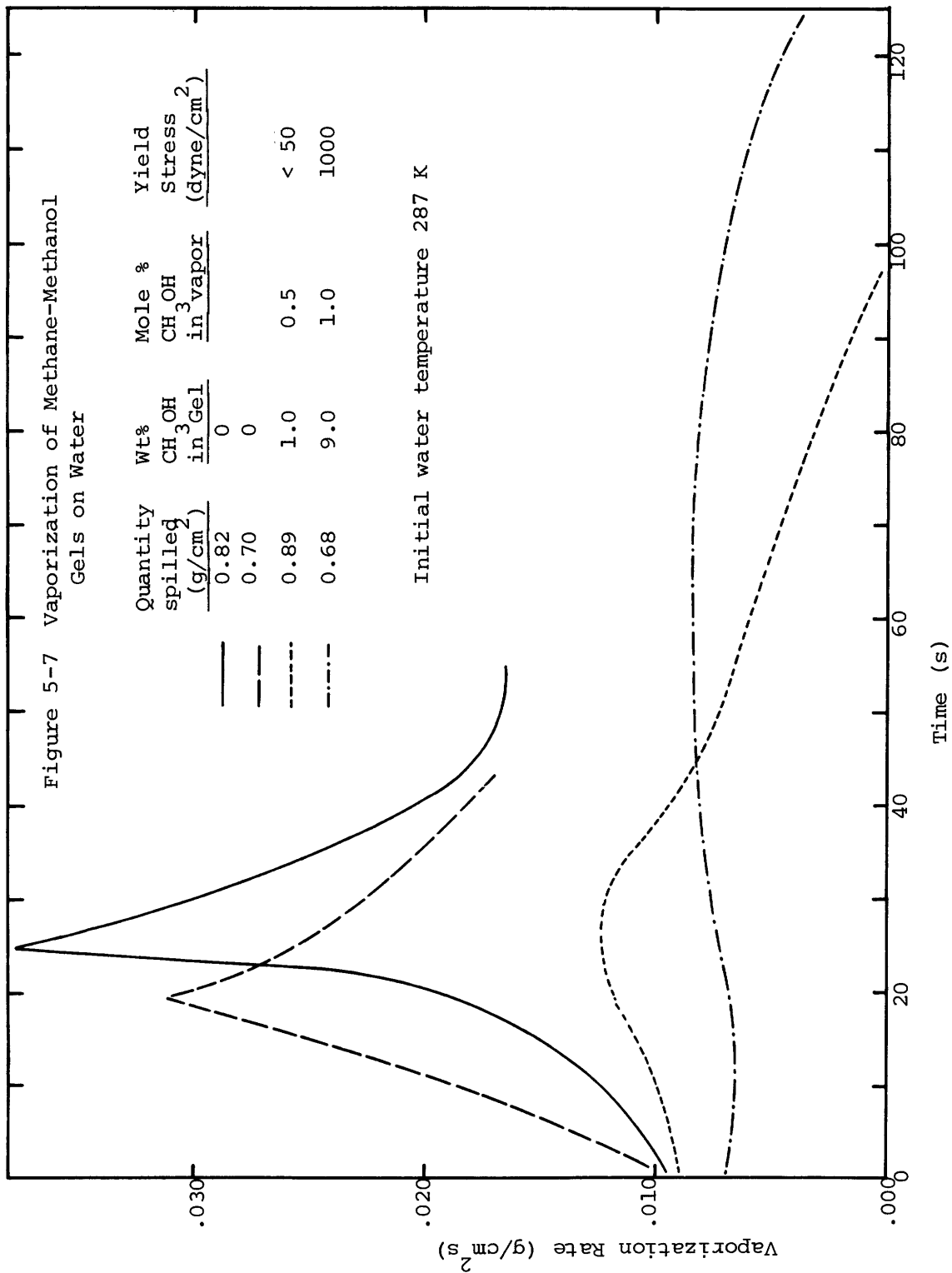
Figure 5-5 Vaporization of LNG Gel on Water

LNG Composition: 90% CH₄/10% C₃H₈
LNG Gel: 6 wt.% CH₃OH in Gel
0.9 mole % CH₃OH in vapor
Yield Stress ≈ 200 dynes/cm²
Initial water temperature 287 K

— LNG 0.88 g/cm²
- - - LNG Gel 0.82 g/cm²







The vaporization behavior of LNG and liquid methane on water suggested that the heat flux variation with ΔT (particularly for $\Delta T = T_{\text{ice}} - T_{\text{cryogen}}$) may be important in determining whether the cryogen will film boil. In the case of the methanol gels, it might be possible for the water to come into contact with gelant particles at the cryogen-vapor film-water interface and result in methanol being transferred to the water phase. This could lower the temperature for ice formation. However, it is not known whether such a phenomenon actually occurs, and if so, whether the methanol transfer is actually rapid enough to affect ice formation. Even if this phenomenon does occur, it is still important to know what effect viscosity and yield stress have on the film boiling curve, in particular to know that expected shifts will also be beneficial.

Berenson (1961) has theoretically derived a relation for film boiling heat flux as a function of ΔT . He further derived expressions for the minimum film boiling heat flux and the corresponding ΔT_{min} , and provided supporting experimental measurements. Here he analyzed the vapor-liquid interface with regard to a Taylor-Helmholtz hydrodynamic instability and, by making various assumptions, was able to derive the dominant wavelength, i.e. the wavelength of the fastest growing disturbance.

$$\lambda = 2\pi \{3\sigma/(g(\rho_L - \rho_V))\}^{\frac{1}{2}} \quad (5-1)$$

where σ = surface tension

g = acceleration of gravity

ρ_L = density of the boiling liquid

ρ_v = density of vapor

Within a given wavelength one would expect two bubbles to grow in an alternating fashion, and correlation with experimental data on bubble sizes (Berenson, 1961) did, in fact, indicate that the bubble diameter is slightly less than half a wavelength. Berenson reported that the best fit for the data was.

(5-2)

$$r = 2.35\{\sigma/[g(\rho_L - \rho_v)]\}^{1/2}$$

One of the assumptions made in deriving equation 5-1 was that the viscous effect was insignificant compared to the surface tension effect. For more viscous fluids, Bellman and Pennington (1948) have theoretically shown that an increase in viscosity will cause a shift to longer wavelengths (and therefore an increased bubble size).

The expression for the film boiling heat fluxes was further derived based on laminar flow of the vapor in the film. The flow was assumed to be directed radially inward toward the bubble, the pressure driving force being due to the curvature of the bubble and the difference in liquid height from the base to the crest of the forming bubble. (Figure 5-3) The vapor flux into this growing bubble was assumed to be equal to the amount vaporizing in the thin portion of the vapor film. The resulting expression was

$$\frac{q}{A} = 4.625 \left[\frac{k_{vf}^3 \Delta h_{p_{vf}} g(\rho_L - \rho_v)}{\mu_{vf} \lambda} \right]^{1/4} \Delta T^{3/4} \quad (5-3)$$

where q/A = heat flux per unit area

k_{vf} = thermal conductivity of
vapor film

ρ_{vf} = density of vapor film

Δh = change in enthalpy due to
vaporization and any sensi-
ble heat effect

μ_{vf} = vapor film viscosity

Thus for a given ΔT , q/A is proportional to $1/\lambda^{1/4}$ and a significant increase in viscosity would be expected to cause an observable decrease in heat flux for a given ΔT . The effect of a yield stress (if large enough) would be to cause the gel to behave as a vaporizing solid. Under such conditions, the vapor formed at the interface must flow to the outer edge to escape, and the pressure which supports this flow is due to the height of the gel at that point. The following expression can be derived for this case (Appendix T).

$$q/A = \frac{6R^2 k_{vf}^2 (\Delta T)^2}{\rho g^2 H \Delta h} \quad (5-4)$$

where H = maximum gel height

R = radius for heat transfer
area

To obtain values for the minimum film boiling heat flux and the corresponding ΔT_{\min} , the Taylor-Helmholtz instability analysis was again used. Here, Berenson assumed that the minimum heat flux corresponded to that flux necessary to sustain the growth rate for his predetermined disturbance (i.e. the disturbance with wavelength

as given in equation 5-1).

$$(q/A)_{\min} = .09\rho_{vF}\Delta h \left(\frac{g(\rho_L - \rho_v)}{\rho_L + \rho_v} \right)^{1/2} \left(\frac{\sigma}{g(\rho_L - \rho_v)} \right)^{1/4} \quad (5-5)$$

$$(\Delta T)_{\min} = .127 \frac{\rho_{vF}\Delta h}{k_{vF}} \left(\frac{g(\rho_L - \rho_v)}{\rho_L + \rho_v} \right)^{2/3} \left(\frac{\sigma}{g(\rho_L - \rho_v)} \right)^{1/2} \left(\frac{\mu_{vF}}{\rho_L - \rho_v} \right)^{1/3} \quad (5-6)$$

The experimental results reported by Berenson were in good agreement with the values predicted from these expressions. However, the agreement with the experimental values for liquid methane and LNG (Figure 5-2) is much less adequate. The functionality of $(\Delta T)_{\min}$ with surface tension may explain the observed shifts with composition. LNG is known to have a higher surface tension than its pure components, and has been observed to be as high as 40 dynes/cm compared with liquid methane at 10 dyne/cm (Booth et al., 1974). This, however, only accounts for a factor of 2 increase in $(\Delta T)_{\min}$ where as the reported shift was much higher. The reason for this is not known, possibly the film boiling region was not adequately measured and stable film boiling is possible at lower ΔT 's than reported.

The derivation of equations 5 and 6 also neglected the effect of viscosity, and yield stress. For a Taylor-Helmholtz instability, Bellman and Pennington (1948) have shown that the effect of viscosity is a shift to longer wavelengths (as mentioned previously) and a decrease

in the growth rate of the disturbance. These two effects, however, oppose each other $((q/A)_{\min} \propto \lambda^b$ and $\Delta T_{\min} \propto b(\lambda)^{5/4}$ where $b =$ growth rate), the greater wavelength producing a larger $(q/A)_{\min}$ and ΔT_{\min} while the slower growth rate produces a smaller q_{\min} and ΔT_{\min} . Thus both effects, either an increase or a decrease in q_{\min} and ΔT_{\min} , are possible and depends on whether the growth rate term or the wavelength term dominates. However, Bellman and Pennington's analysis does suggest growth rate dominance when the appropriate wavelength for surface tension controlled growth is large (>1 cm), and in the present case $\lambda=1.6$ cm for liquid methane. For high yield stress gels, bubble formation does not occur and the Taylor-Helmholtz instability analysis cannot be used. In such case there is probably some minimum film thickness necessary to avoid contact of the water with the gel.

5.4 Further Qualitative Aspects of Boiling LNG

Although LNG boils on water with a behavior similar to that of liquid methane, there are several interesting qualitative differences. LNG forms a substantial head of foam (>6 inches in the present study) while liquid methane shows little or no foaming tendency. The gels also did not foam, probably due to the wetting properties of the gelant (methanol) particles acting to break the foam. Also, the lower boil-off rate would reduce the head of foam observed. In the case of boiling LNG, photographs taken of the interface (Drake et al., 1975) showed a

mass of very small bubbles (diameter 1 to 3 mm) with a few large bubbles (diameter ≈ 1.3 cm). The boiling of liquid methane, on the other hand, showed only large bubbles similar to the large bubbles observed in LNG. These large bubbles are significantly larger than would be predicted for either film boiling (0.7 cm) or nucleate boiling (≈ 1 mm) of liquid methane, and thus probably represent coalesced bubbles. The higher surface tension of LNG could, however, produce such large bubbles if film boiling occurs. Nucleate boiling, on the other hand, is independent of surface tension, and is undoubtedly responsible for the formation of the very small bubbles.

The ability of a given mixture to foam is directly related to the rapidity at which coalescence occurs. Andrew (1960) and Marrucci (1969) have discussed the process of coalescence and suggested two possible surface tension effects which determine the frothing ability of mixtures. (Pure liquids do not froth, and foam formation is, in fact, most often associated with small concentrations of surfactants. However, in any mixture the component with the lower surface tension will behave essentially as a surfactant and will positively adsorb at the interface, i.e., the interfacial concentration will be higher than in the bulk.)

As two bubbles approach each other at a relatively small distance ($\approx 10^{-3}$ cm) a flattening of the surfaces begins to occur. As a consequence of this deformation (i.e. a difference in curvature of the vapor-liquid interface), the pressure in the liquid film between the two bubbles is greater than in the bulk. At very small film thicknesses ($\leq 1000\text{\AA}$) Marrucci suggests that van der Waals attraction between the two

gas bubbles will also cause an increase in the liquid film pressure.

(5-7)

$$P = \frac{2\sigma}{r} + \frac{A}{6\pi h^3}$$

where σ = surface tension of bulk liquid

r = radius of curvature of bubble
at point of contact with the
bulk liquid

A = Hamaker constant or Lifshitz-
Hamaker function

h = thickness of liquid film

This excess pressure causes liquid in the film to be pushed outside the film, which in turn tends to stretch the vapor-liquid interface increasing the radius of the planar separating film. If this rate of thinning is controlled only by the inertia of the fluid being pushed away from the film, the estimated time for thinning of the film down to 100 A (Marrucci, et al., 1968, suggest that this is a good estimate of the film thickness at rupture) is 10^{-4} to 10^{-3} sec. In frothing mixtures, the coalescence times are considerably larger than this ($\geq .1$ sec), and thus there must be some film elasticity which resists this thinning process. Andrew (1960) discussed two possible phenomena-- a dynamic rise in surface tension, and an equilibrium rise in surface tension. The former effect is a transient effect which occurs whenever a vapor-liquid interface is stretched. Bulk solution will be exposed at this newly formed surface and will thus have a higher surface tension than the surrounding vapor-liquid interface. This will tend to draw the film back

together. However, diffusion of the lower surface tension component to the new interface may be so rapid that the surface does not have time to heal itself. In fact, Marrucci, et al. (1968) have estimated the coalescence time based on this dynamic effect (neglecting inertial effects) and obtained values less than 10^{-5} sec. Therefore, dynamic surface tension is not the dominant effect in such frothing mixtures. The equilibrium surface tension effect was first proposed by Gibbs (1928) and refers to a change in surface tension due to a mass balance effect in the expanding liquid film. When a given mass undergoes a change in surface area, Δs , the equilibrium bulk concentration, c_i , and surface concentration, Γ_i , will also change, as a different distribution of each component is attained between the surface and the bulk. When $\left| \frac{\Delta \Gamma_i}{\Gamma_i} \right| \ll \left| \frac{\Delta s}{s} \right|$, this effect can be estimated as $\Delta c_i = -\Gamma_i (\Delta s/V)$, where V is the volume of the liquid film. Thus, for the component with the lowest surface tension, Γ_i will be positive and the net effect upon expansion of the liquid film will be to lower the concentration of this component, therefore increasing the surface tension. Marrucci then envisages that the film will continue to stretch until the resulting equilibrium surface tension balances the pressure difference ($h\Delta P = 2\Delta\sigma$), where h equals the film thickness and $\Delta\sigma$ represents the difference in surface tension between the liquid film and the bulk liquid. For this quasi-equilibrium point at which stretching of the film ceases, Marrucci derived the following expression.

$$(kh_o)^2 + 1/(h_o k) = crk^2/\sigma \quad (5-8)$$

$$\text{and } k = \left(\frac{12\pi\sigma}{A r} \right)^{1/3}$$

$$c = \left(\frac{2a_1}{RT} \right) \left(\frac{d\sigma}{da_1} \right) \left(\frac{d\sigma}{dc_1} \right) \left(\frac{1}{1 + (x_1v_1/x_2v_2)} \right)$$

where v_1, v_2 = molar volume of components 1 and 2 respectively

x_1, x_2 = molar fractions for components 1 and 2, respectively in the bulk liquid

a_1 = activity of compound 1

R = ideal gas law constant

T = absolute temperature

The curve for crk^2/σ versus kh has a minimum at $crk^2/\sigma = 1.89$, which suggests a difference in behavior for mixtures whose value of crk^2/σ is less than $\sqrt{2}$ and those with values greater than 2. In fact, Marrucci et al. (1968) have shown experimentally that for mixtures whose value is <2 , the coalescence process is quite rapid (i.e. the equilibrium surface tension never becomes large enough to balance the pressure difference).

The time necessary for thinning of the film down to this quasi-equilibrium point will be controlled by the inertial resistance as discussed previously. As this time is much smaller than observed coalescence times in frothing mixtures, the coalescence rate is therefore determined by the processes which cause further thinning down to rupture. Vrij (1966) has suggested that rupture occurs as a result of the growth of thickness fluctuations due to thermal motion. However, Marrucci suggests that the time value estimates from this theory are too large for the relatively rapid coalescence process (.1 to 10 sec)

which he is considering. For such cases, Marrucci suggests that further thinning occurs due to a diffusion process. Due to the lower concentration of the lower surface tension component in the liquid film as compared to the bulk, diffusion will tend to restore this liquid film concentration to its original bulk value. This in turn will decrease the surface tension causing further stretching of the film until rupture occurs. Marrucci has also derived expressions describing this process and found that the coalescence time increased with increasing crk^2/σ . Although no experimental data were given, he suggests that the available data are in good agreement with the proposed mechanism. Thus the value of crk^2/σ (in particular $|d\sigma/dc|$) determines whether a mixture is likely to foam or not. For an LNG mixture of 90 percent CH_4 and ten percent C_2H_6 , the value of crk^2/σ is estimated to be approximately 10 (Appendix U) indicating that frothing might be expected.

The above explanation for foam formation assumed thermal equilibrium and the absence of mass transfer effects due to boiling. Both of these effects, however, may be important in the present application to a boiling cryogenic mixture, and a further discussion of nucleate boiling will indicate the transient effects which may occur.

Van Stralen (1966, 1967, and van Stralen et al., 1974) has discussed the mechanism of nucleate boiling on a solid surface and has shown that bubble growth and the resulting bubble sizes are independent of surface tension. Initially the liquid will be in contact with the solid, and heat transfer will cause a thin layer of liquid to superheat. Eventually the superheat will be sufficient to cause

a vapor nuclei to form on some surface disparity, and in so doing, will push away a thin superheated layer. This layer will form part of the bubble interface being located either at the bubble dome or sides and will provide an available source of vapor for the growing bubble. There will also be a superheated microlayer at the base of the bubble which, by evaporation, will induce further bubble growth. In the case of mixtures, this growth rate may be limited by the rate of diffusion of the more volatile component to the interface, and in such cases smaller bubbles are formed at a higher frequency. Larger values of peak nucleate boiling heat fluxes are also associated with this phenomena and apparently result from an increased contact time between the liquid and the solid. For boiling LNG (i.e. the addition of heavier components to liquid methane) no conclusions can be made regarding bubble size, as the initial methane bubble size is not known due to immediate coalescence. However, the observed peak nucleate boiling heat fluxes are substantially higher for LNG as compared with liquid methane, indicating that a mass diffusion effect is probably occurring. If mass diffusion is restrictive, surface tension transients may also occur. At the interface, the more volatile component will be at a lower concentration compared to the bulk, as it is preferentially vaporizing. This will tend to raise the surface tension. (Although LCH_4 and LC_2H_6 have similar surface tensions at their respective boiling points, the surface tension of LC_2H_6 at the boiling point of LCH_4 is much higher, and thus causes the mixture to have a higher surface tension. The addition of LC_3H_8 behaves similarly.) On the other hand, the interface will also be at a slightly higher temper-

ature than the bulk, which has the opposite effect of decreasing the surface tension, although this decrease will be less than the increase corresponding to the concentration variation. Once the available superheat layer is evaporated, the more volatile component (lower surface tension component) can diffuse to the surface and establish the equilibrium surface tension for the bulk composition. This is expected to take no more than a millisecond, as surface tension transients for larger molecules at much lower concentrations require no more than a few milliseconds to reach equilibrium (Netzel et al., 1964). According to van Stralen, bubble growth at the solid surface prior to departure lasts approximately a few milliseconds and essentially no superheated layer remains at the bubble interface at departure. (Some slow growth due to a slight superheating of the bulk liquid, however, will still occur after departure.) Thus, if the bubble spacing is not too close, the bulk equilibrium surface tension may be able to establish itself before two bubbles become close enough to begin the process of coalescence. However, at peak nucleate boiling fluxes the spacing is expected to be as close as possible, and one should, therefore consider two bubbles growing side by side. In this case, it is particularly important to know the exact position and extent of the superheated microlayer which has been pushed away from the solid surface during the vapor nuclei formation. Experimental data on this is not, however, available. Therefore, the bubble sides may or may not be superheated with transient diffusion and surface tension effects. If transient surface tension effects do occur (i.e. a higher surface tension or a lower surface tension due to depletion of

the more volatile component) but vary across the interface, the areas of lower surface tension will tend to expand and the higher tension regions to contract. If the bubbles are close enough together such transient effects may influence the coalescence process. In this case, a higher surface tension at the side walls may resist expansion into a neighboring bubble.

Hovestreijsdt (1963) has proposed an alternative explanation based on surface tension gradients. For boiling mixtures, he suggests that the liquid microlayer at the base of the bubble and the liquid layer separating two bubbles are depleted in the more volatile component due to its preferential vaporization. If the more volatile component has the lower surface tension (referred to as a positive mixture) this will result in a greater equilibrium surface tension at these points of depletion. The higher surface tension at the base will presumably pinch off the bubble at a smaller diameter, while the higher surface tension at the bubble sides will draw liquid in between the two bubbles (i.e. resist coalescence) as they approach each other during formation and growth. This greater surface tension at the side interfaces is also presumed to keep the bubbles from coalescing as they rise through the liquid, although the explanation for this is not clear.

For negative mixtures (where the more volatile component has the higher surface tension) he suggests that these effects are reversed and foaming does not occur, but the reported evidence is not conclusive. For positive mixtures, the suggested higher surface tension is a transient rather than an equilibrium effect and has been observed photographically to decrease the area of the bubble base. However, van Stralen has

given evidence that this effect does not control the final bubble size but rather a mass diffusion limitation is controlling. Also Hovestreijsdt's explanation fails to explain why the bubbles do not break through the top liquid surface. Once thermal and vapor-liquid equilibrium have been attained, the foaming criterion of Marrucci should be applicable. According to van Stralen such equilibrium is attained before bubble departure from the wall. Thus, if the bubbles can resist coalescence during formation the value of crk^2/σ for the mixture (for bubble coalescence this should be the initial composition in the liquid film, which may differ from the bulk; for surface breakthrough, this should be the bulk composition) should determine its frothing ability. If bubble coalescence occurs during formation, the larger bubbles will, in general, produce a less stable foam (i.e. reduce the head of foam), but will not alter its ability to form a foam. Thus, the differences in frothing ability for Hovestreijsdt's positive and negative mixtures may have been due to a variation in the value of $|d\sigma/dc|$ and/or a transient decrease in the bubble wall surface tension resulting in coalescence during bubble growth.

5.5 Conclusions on Gel Vaporization Behavior

Data for liquid methane/methanol gels were presented, and an analysis of the observed behavior was discussed. No reliable boil-off rate data, however, could be obtained for liquid methane/

water gels, as they stuck to the Dewar walls and would not readily pour. The gelant particles seemed to have a strong affinity for all solid surfaces, and in dilute gels, the particles would congregate and pack together at the Dewar walls, leaving a small puddle of liquid in the middle. Only this small portion of liquid would flow out of the Dewar, and it boiled essentially the same as liquid methane or LNG. If samples of the gel were spooned onto the surface, complete surface coverage did not result and reliable values could not be obtained for the boil-off rate per unit area. However, estimated values (i.e. based on an estimated surface area) indicate that the boil-off rates were similar to those found in the liquid methane/methanol gels.

In this study, the final gel compositions and the vapor mixture compositions during gel formation (see procedure discussion in Chapter 6) were varied to determine whether they might affect the resulting boil-off rate. The results indicated no significant effects due to variation of either of these parameters, and further showed no variation of boil-off rate with yield stress. This was somewhat unexpected as the increased viscosity would affect the film boiling heat fluxes. However, for low yield stress gels in which the viscosity controls the bubble size, the heat flux varies as $1/\lambda^{1/4}$. Thus a substantial increase in wavelength (bubble size) would be necessary to alter the heat flux noticeably. For high yield stress gels, the inertial effect will dominate. In this case, the depth of the vaporizing gel will have a significant effect on the observed boil-off rate. This effect was not studied in the present investigation as only small quantities of

the gels could be made with the present gelation apparatus. The results of this particular study were, however, quite favorable from an LNG safety point of view, as they indicated that even a fairly low yield stress methanol gel will give a factor of two to three reduction in boil-off rate.

It is also of interest to consider the possibility of a vapor explosion. These have been linked to liquid-liquid contact causing the cryogen to superheat until homogeneous nucleation occurs. In the case of gels the gelant particles may serve as nucleation sites and reduce the possibility of such large liquid superheats, thus reducing the possibility of an explosion.

CHAPTER 6 - EXPERIMENTAL EQUIPMENT AND PROCEDURES

6.1 Gelation Apparatus

The gels were made using an apparatus similar in design to that used in a previous study performed by Aerojet Liquid Rocket Company (Vander Wall, 1971). The design schematic is shown in Figure 6-1 and a photograph in Figure 6-2. Two separate lines were used. The first line carried methane gas which was then condensed to form an initial charge of approximately 500 cm^3 in the preparation vessel. In the second line, a natural gas/gelant mixture was produced and subsequently bubbled into the initial quantity of liquid methane to form the gelant particles. In the design of this apparatus, a major consideration was the materials of construction. Any part which would encounter cryogenic temperatures was constructed of copper, brass, aluminum, Pyrex, or a suitable stainless steel.

The technique for condensing the initial quantity of methane used liquid nitrogen at atmospheric pressure and its respective boiling point (70 K at 1 bar). Since the temperature of the liquid nitrogen is below the freezing point of methane (90 K), a heat exchanger configuration such as a coil submerged in the liquid nitrogen would freeze the methane and eventually clog the tube. However, for producing small quantities of liquid methane, such as used in this study, another straightforward laboratory technique was available. An extension of 0.635 cm ($\frac{1}{4}$ " OD) copper tubing provided the exit line for the methane gas. This tube was extended down into the preparation

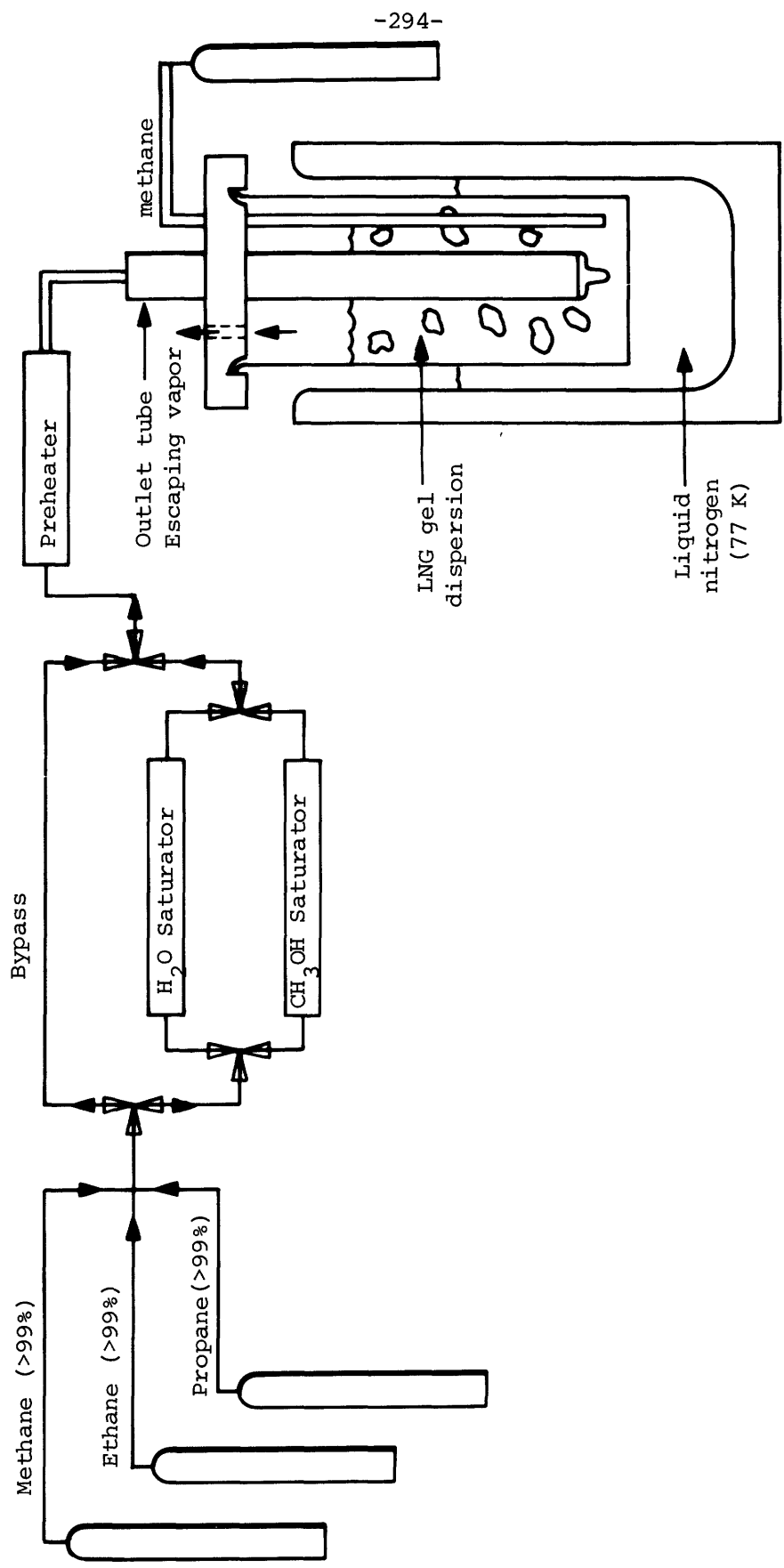


Figure 6-1 Gelation Apparatus

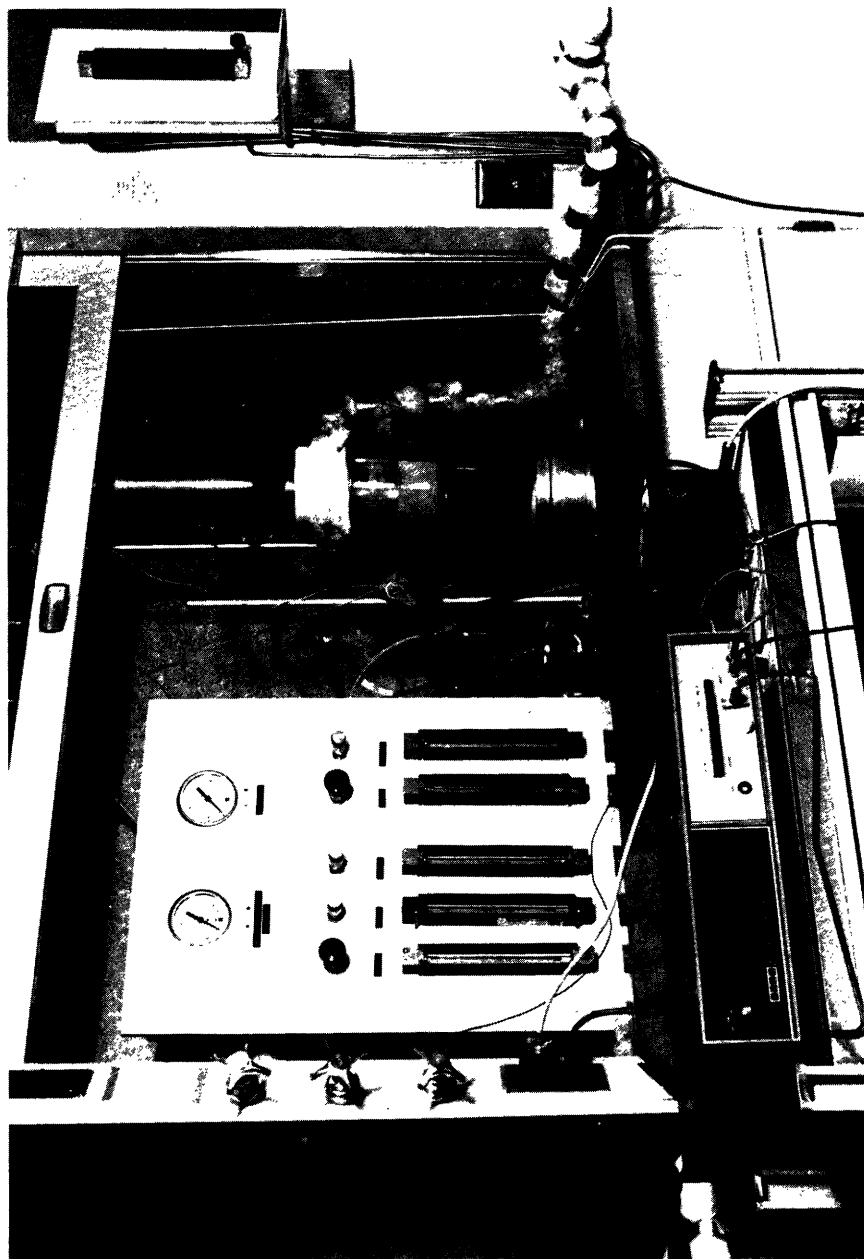


Figure 6-2 LNG Gelation Apparatus. Rotameters and valves on panel at left control flow rates for natural gas/gelant stream. Rotameter at far right controls flow of separate methane stream used for initial condensation. Outlet tube is suspended above the gel preparation vessel (Pyrex beaker inside unsilvered Dewar).

beaker and clamped such that the end was approximately 1 cm from the bottom surface of the beaker. This beaker was placed in a Dewar. After sufficient purging of the beaker with methane gas, the Dewar was filled with liquid nitrogen and the methane flow rate was set at approximately 9000 cm³/min. As it exited from the tube and contacted the liquid nitrogen-cooled surface, the methane cooled and condensed. Because the flow rate was quite high, agitation in the liquid was sufficient to avoid freezing of the liquid methane. Due to the small amount of surface area available for heat exchange, however, approximately 45 minutes was required to make the initial 500 cm³ of liquid methane.

The total flow rate for the natural gas/gelant vapor mixture was 113 cm²/s which is considerably less than that used in the Aerojet study (estimated from orifice size and pressure drop to be at least 250 cm³/s). However, initial runs using the higher flow rate indicated that sloshing was particularly severe, and that the liquid nitrogen could not provide sufficient cooling to maintain the gel level in the preparation vessel. To eliminate these difficulties, the flow rate of 113 cm³/s was selected and maintained constant for all of the gels prepared.

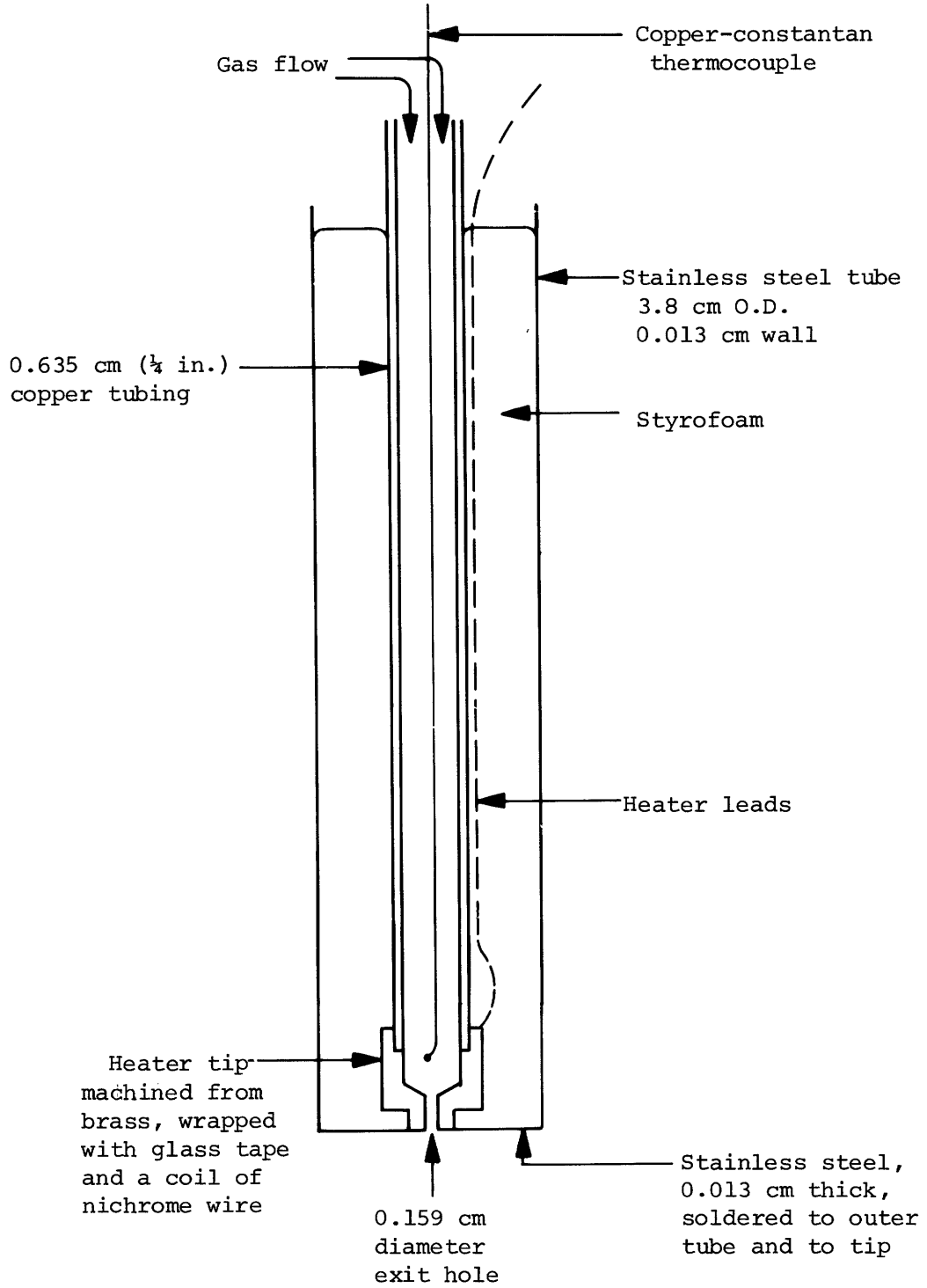
The selection of rotameters and valves was made to allow for natural gas mixtures ranging from the heavy composition of 80/15/5 mole percent methane/ethane/propane to pure methane. Each gas used had a guaranteed purity of > 99. percent. During each run, inlet gas samples were taken and analyzed using a gas chromatograph to confirm the natural gas composition. The selection of operating pressures

was made to insure critical flow through each valve and thus eliminate fluctuations in flow rate due to down-stream pressure fluctuations. Two-stage regulators were also used to minimize changes in the flow rate. This design resulted in flow rates stable to within ± 1 percent in all lines except the methanol saturator line. At the lowest flow rate used ($100 \text{ cm}^3/\text{min}$), rapid pulsing resulted with a deviation of ± 3 percent. At higher saturator-line flows, the rates used were all stable to ± 1 percent.

The addition of gelant vapor to the natural gas was accomplished by splitting the natural gas stream. One part was bubbled up through a packed column of the liquid gelant. The second portion became a bypass stream which acted to dilute the gelant when the two streams were subsequently mixed together. Either the water saturator or the methanol saturator line could be used, but not both at once. The saturators and copper tubing lines comprising this section were all submerged in a constant temperature water bath maintained constant during each run to ± 1 K, but from run to run ranged from 300 K to 306 K. The primary purpose of the constant temperature bath was to avoid substantial cooling of the liquid gelant in the saturator due to continued vaporization of the gelant. Saturator temperatures were measured with copper-constantan thermocouple probes (permanently situated within the liquid) and were found to be steady to within ± 0.3 K.

The natural gas/gelant vapor mixture entered the liquid methane (or LNG) via an outlet tube (Figure 6-3) with a single exit hole of

Figure 6-3 Outlet Tube



0.159 cm (1/16") diameter at the bottom. To avoid condensation and/or freezing of the gelant inside the outlet tube, the vapor stream was preheated with a glass-tape heater, and the outlet tube itself was insulated and heated at the exit port. The copper-constantan thermocouple was located approximately 1 cm from the exit hole, and during a methanol-gel run, the measured temperature was $348 \text{ K} \pm 2 \text{ K}$. During a water-gel run it was necessary to increase this temperature to $386 \text{ K} \pm 3 \text{ K}$ to avoid freezing of the gelant and plugging of the outlet tube.

The vapor mixture exited through the 0.159 cm hole, and due to its high velocity, it appeared as a downward jet approximately 2.5 cm in length and 0.6 cm in diameter. When the liquid methane (or LNG) was substantially subcooled, the majority of the exiting natural gas would condense, i.e. very little of the gas would break away from the jet and bubble up through the liquid. If the liquid, however, was not subcooled, the bubbling was considerable. During a run, it was desirable to maintain a constant liquid level in the preparation vessel. In the case of producing a liquid methane gel, this is equivalent to subcooling the liquid just enough to provide sufficient heat transfer to cool the exiting gas down to 113 K but not to condense any. In general, this cannot be accomplished--the system is too small for a liquid nitrogen level controller--two-phase flow which occurs when the solenoid valve opens would be sufficient to force liquid nitrogen out of the Dewar. The levels were therefore controlled manually. At the initiation of gelation, the dispersion

was dilute and behaved essentially as a liquid with heat transfer provided by both convection and conduction. At this point, the liquid methane level cycled between increasing and receding, but was maintained at about the 700 cm^3 level $\pm 50 \text{ cm}^3$. As gelation proceeded and the dispersion thickened, a semi-solid gel-like layer formed at the vessel surface, limiting heat transfer to conduction and requiring a higher liquid nitrogen level to keep the liquid methane level from receding. Also, as the gel thickened, the bubble size increased considerably. Initially the range was $\leq 1 \text{ cm}$ and increased to $\leq 2 \text{ cm}$.

The fact that some of the exiting methane was condensing during the gelation procedure may have affected the fraction of gelant captured by the liquid. Probably only those particles which reach the vapor-liquid interface (by diffusion and convection) will be retained (assuming particle wettability). To determine the actual gelant capture efficiency, mass balances were made on many of the experiments by collecting and volumetrically measuring the liquid residue remaining after vaporization of the natural gas and melting of the gelant crystals. The results showed a range of 10 percent to 70 percent of the total gelant being retained in the liquid, the water gels being particularly low, and thus more difficult to produce.

At high gelant vapor concentrations the gas which breaks the liquid surface appeared as a fog or smoke. A fog is defined as a dispersion of fine liquid droplets in a gas whereas a smoke is a dispersion of fine solid particles in a gas. It is not certain which is actually observed, but temperature considerations would lead one to

believe that it was a smoke. The appearance of this smoke does, however, indicate a loss of gelant.

The preparation beaker was isolated from the atmosphere by a snugly fitting styrofoam cover. A small outlet hole (0.6 cm dia) was made for the methane outflow which was continuous during the gelation process. As the gelant particle concentration increased, gel-like buildup occurred at all available surfaces--the beaker surface, the outlet tube surface, etc. Evidently the particle agglomerates attached themselves to the walls and flocculation of these with free agglomerates resulted in an increased particle concentration near these surface. The gelant particles formed in the water gels were particularly tenacious and some of the gelant loss indicated in the mass balances may have been due to the difficulty in final transfer of the gel to the Dewar.

The vapor mixture of natural gas and gelant was run for two to three hours depending on the gelant concentration in the mixture and the desired thickness of the gel. The lower concentrations required longer run times. Once the gelation procedure was complete, the fresh gel was transferred to a Dewar and used in subsequent analyses.

6.2 Solid Phase Analysis

To analyze the composition of the crystalline particles in the liquid methane gels, the apparatus as shown in Figure 6-4 was used. It consisted of a test tube for the gel sample with a Cajon glass fitting to connect it to the rest of the apparatus. A standard

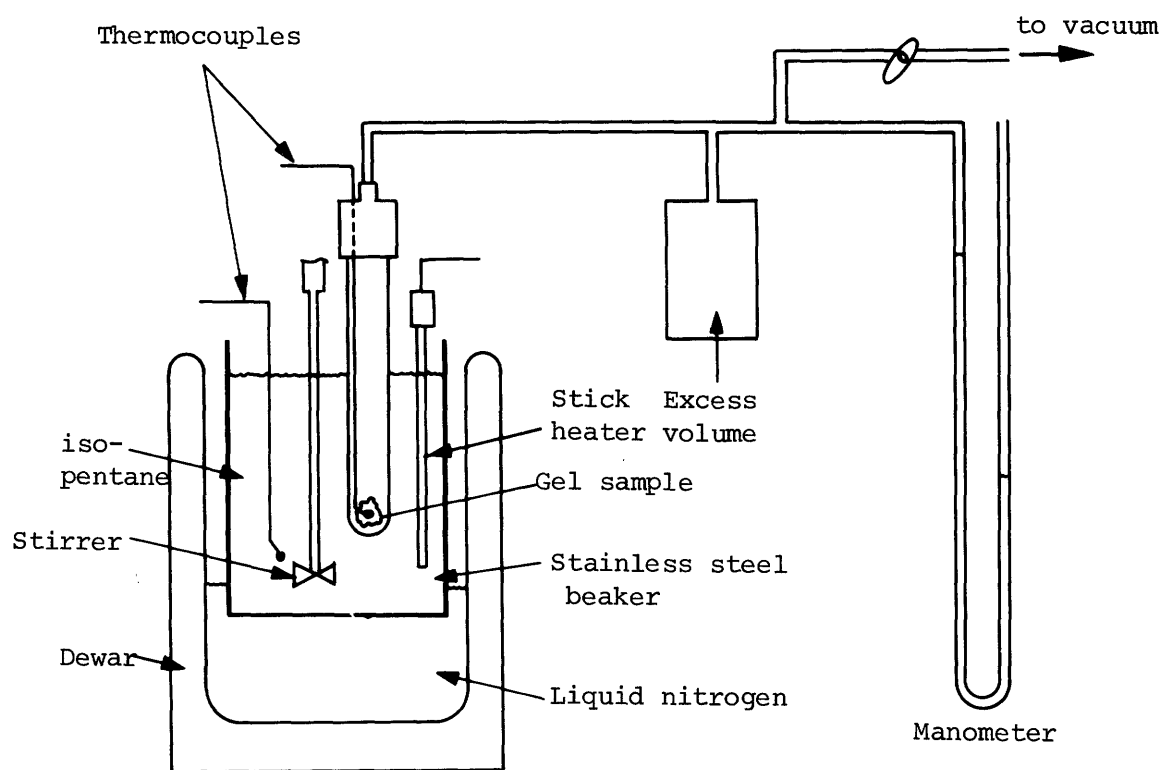


Figure 6-4 Apparatus for Solid Phase Composition Analysis

vacuum pump was used as only moderately low pressures were required. A mercury manometer and a flask for excess expansion volume composed the remainder of the glass section. A temperature-controlled cryogenic bath was necessary to maintain the sample below the clathrate decomposition point. This consisted of a bath of isopentane surrounded by a Dewar partially filled with liquid nitrogen. A temperature controller with a platinum resistance temperature sensor was connected to a stick heater (125 watts) and used to insure that the temperature did not get too low. Liquid nitrogen was added occasionally to maintain sufficient cooling throughout the run.

The general procedure was as follows: A liquid methane gel was made using a gelant concentration of 1 mole percent in the vapor stream. This high concentration was used to avoid a major effect from the contaminant frozen carbon dioxide. Carbon dioxide may also vaporize at a temperature at or above the point of clathrate decomposition. If this quantity were substantial compared to the gas which escaped from the decomposing clathrate crystals, erroneous compositions would be measured. To avoid this problem, the CP grade methane was always analyzed by gas chromatography before use in this analysis, and only those cylinders which gave CO₂ analyses of ≤ 50 ppm were used. This low carbon dioxide concentration plus the relatively high gelant concentration insured that CO₂ vaporization was negligible during the composition analysis.

A sample of the "thick" gel was placed in the the test tube, connected to the apparatus, and placed in the cryogenic temperature

bath. For the methanol gels, the bath was kept at $132\text{ K} \pm 5\text{ K}$ and for the water gels, $163\text{ K} \pm 5\text{ K}$. Once the major portion of the methane had vaporized from the sample, a slight vacuum was pulled on the sample (0.33 bar). The sample was maintained at these temperature and pressure conditions until the efflux of methane was $< 1\text{ cm}^3/\text{hr}$. At this point it was assumed that the residual liquid methane had been removed and, at most monolayer adsorption remained. The stopcock connection to the vacuum line was then closed and the temperature bath gradually warmed. In this way, the gas, if any, which escaped as the clathrate decomposed could be collected and measured using the known volume of the apparatus and the initial and final temperature and pressure conditions.

The volume of the apparatus was measured by filling all but the manometer section with water and taking weight measurements before and after. The volume of the manometer tube was estimated using the inner diameter of the glass tube. The temperature expansion effect due to warming of the gas inside of the test tube, was measured separately using ice or solid methanol as a standard respectively. Care was taken to insure that this effect was constant in all of the runs by using the same level of submersion in the cryogenic bath, making connecting lines of fairly small diameter, and allotting sufficient time for temperature equilibration before the apparatus was isolated and the composition measured by warming the sample. Copper-constantan thermocouples were used to measure the temperature of the bath, the gel sample, and the gas in the excess volume flask.

6.3 Powder X-ray Diffraction

The crystal structure of the solid phase of the gels was analyzed using a GE XRD4 x-ray diffractometer. The diffractometer was equipped with a proportional counter for detecting the diffracted x-ray beam, and the measured intensity was recorded on a strip chart recorder. Copper K α radiation (wavelength 1.542 Å) was used. To obtain cryogenic temperature control of the sample, a cold stage was necessary. Such a cryogenic stage had previously been designed and constructed in the Materials Science Department at MIT (Figure 6-5). It was constructed of copper because of its high thermal diffusivity. Liquid nitrogen flow provided the cooling. As there was no heating element in the design, temperature control was done manually, by initiation and shut-off of the liquid nitrogen flow based on the measurement of the copper-constantan thermocouple.

The general procedure for analyzing the gels was as follows. The stage was precooled with liquid nitrogen. During this time the glass cover was in place, and due to the small volume of air initially enclosed, frost formation was not a problem. (Had it been, the chamber could have been purged with helium.) A sample of the concentrated (almost solid) gel was placed on the stage. A large precooled stainless steel spatula was used to pack the sample into place, smoothing the top surface so that it was flush with the outer copper surface. (The glass cover was removed for this brief period of time and quickly set back in place after the sample was properly mounted.) Since methane was still vaporizing from the gel, frost formation on

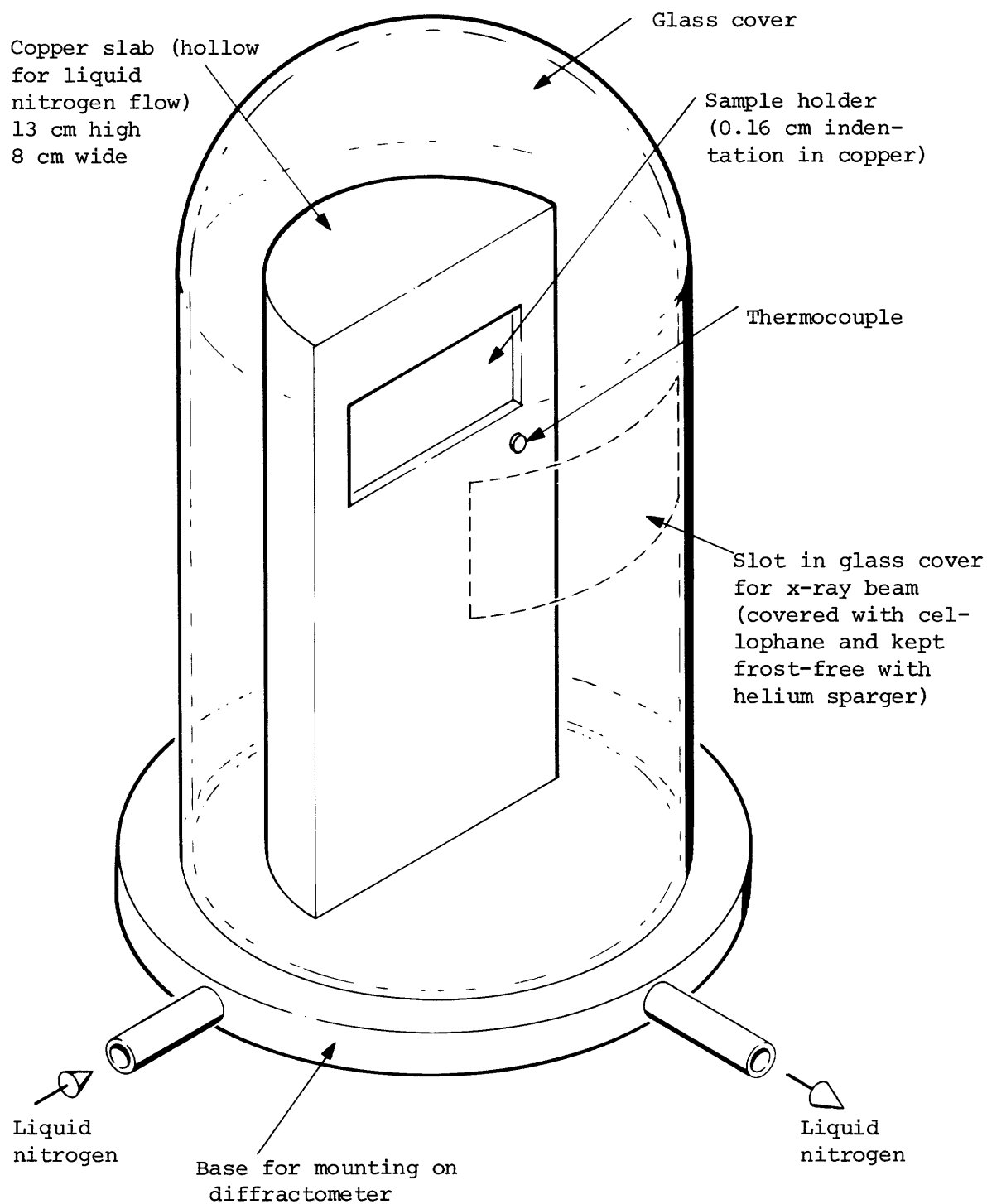


Figure 6-5 Cold Stage for X-ray Diffractometer

the surface of the gel sample was also not a problem. The convection away from the sample was either sufficient to insure that little condensation from the air reached the sample surface, or the frost which did collect was negligible and not detectable on the output. When the sample was in this gel-like state, the output often had a flat broad peak in the lower angle region indicating an amorphous state. Undoubtedly this was due to the methane entrapped in the gel structure. The liquid nitrogen flow was then halted, allowing the stage to warm, but always maintaining it below the decomposition temperature. As methane evaporated from the sample leaving only the solid crystalline particles, the diffraction angles ranging from 10° to 60° were then cycled through several times at a rate of $4^{\circ}/\text{min}$ until sharp peaks were obtained.

Standards such as ice and solid methanol were obtained by cooling the stage and spraying the liquid onto the sample indentation. The sample surface was then scraped and smoothed to make it flush with the outer copper surface. X-ray analysis proceeded, and sharp diffraction peaks were generally obtained indicating that this technique was satisfactory for forming small randomly oriented crystal grains.

Other clathrate compounds (nitrogen/water and carbon dioxide/water) were formed by continuously vaporizing a quantity of either methanol or water into an appropriate gas stream. The tube exit was projected toward the cryogenic stage such that the exiting gas would contact the cold surface and crystallize the gas and liquid into clathrate crystals which would then stick to the surface. This process was continued until a sufficiently thick layer of clathrate crystals

had been formed. X-ray diffraction analysis then proceeded.

6.4 Microscope Analysis

A Leitz incident light microscope was used to study the gelant particles. This microscope was equipped for bright-field, reflected-light illumination with a vertical illuminator Leitz model 563 018 which permitted aperture and field diaphragm adjustments. A long-working distance objective Leitz H 32x with a numerical aperture of 0.60 was used. This particular objective was corrected for 1.8 mm of quartz, as it was originally purchased for a different type of experiment. The distortion due to this was, however, negligible. A 10x Leitz periplanatic eyepiece was also used. The microscope was equipped for 8.2 cm by 10.8 cm Polaroid photomicroscopy.

The cold stage design is shown in Figure 6-6. It was machined out of aluminum and consisted of a sample holder with a surrounding temperature bath. The technique used was to fill both the sample and bath containers with a dilute dispersion of the gelant particles in liquid methane. A cover was placed over the sample and securely fastened with wing nut screws. This, however, was not a pressure-tight seal--the vaporizing methane was allowed to escape, but the seal was sufficient to avoid the back-flow of air into the chamber. As the liquid methane boiled away in the outer bath, the methane in the sample chamber would also boil off leaving a collection of particle agglomerates on the small Pyrex slide. The temperature of

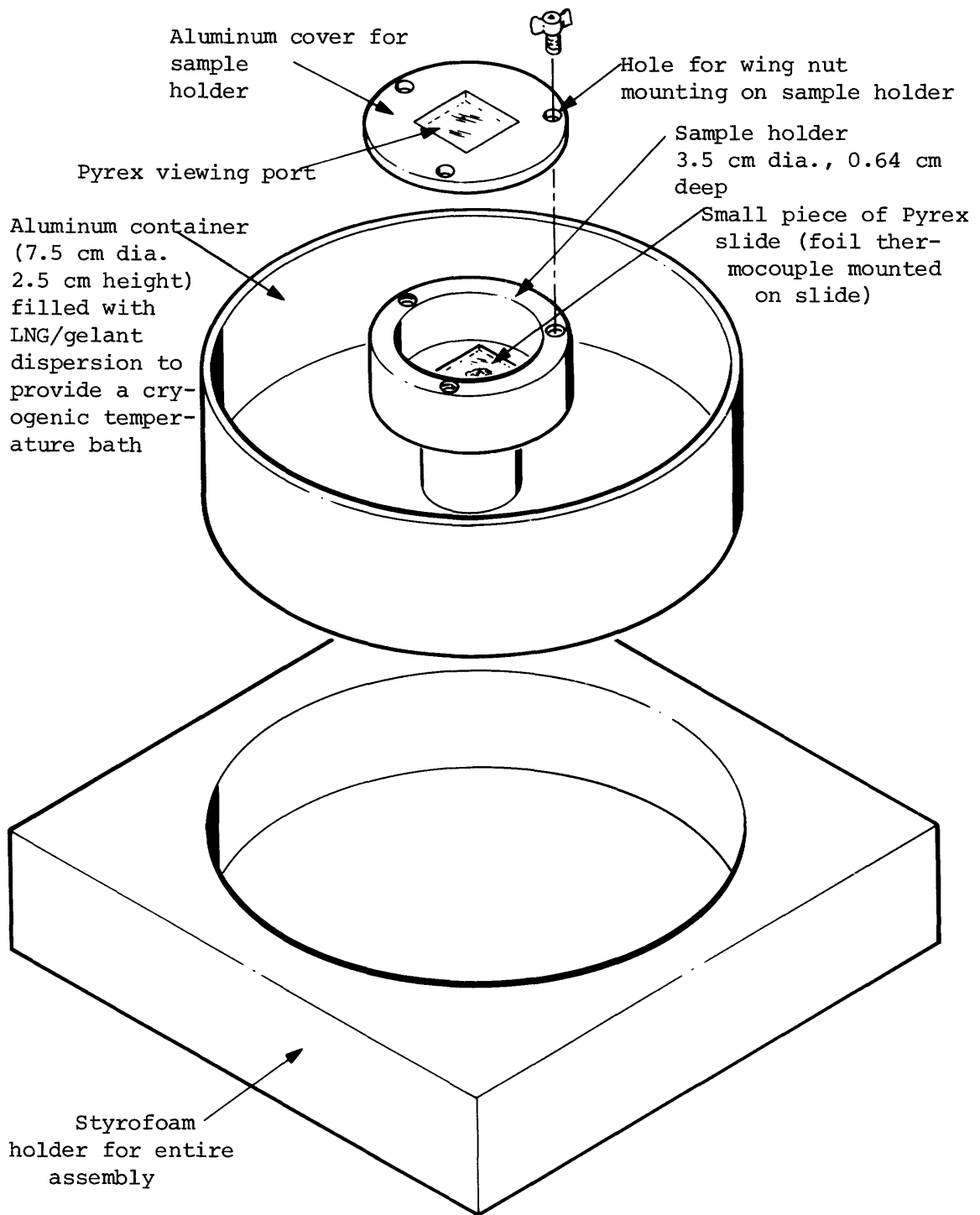


Figure 6-6 Microscope Cold Stage

these agglomerates would gradually rise at a rate of ~ 2 K/min until approximately 133 K was reached. At this point, the liquid methane in the surrounding bath had completely vaporized and the temperature rise became more rapid (5 K/min), but not so rapid that transitions could not be detected. Another liquid could be added to the bath container such as precooled liquid propane, which would then provide a much lower rate of temperature increase. However, there was no advantage to the use of this for the methanol gelant particles, as they decomposed close to 133 K.

This procedure was initially used for the study of liquid nitrogen-gelant dispersions in order to develop the cold stage technique and to become familiar with the observed transformations. When the liquid methane/gelant dispersions were eventually analyzed, it was necessary to use ultra-high purity methane to avoid residual liquid ethane surrounding the agglomerates. Once developed, this technique proved to be satisfactory for measuring the thermodynamic decomposition points for the clathrate crystals to within ± 5 K.

6.5 Boil-off Rate Apparatus

An insulated cylindrical container, which allowed for some visibility, was constructed using 4 layers of 0.0127 cm thick cellulose acetate separated with 1 mm thick styrofoam spacers. A plexiglass base was sealed to the inner sheet with silicone rubber cement. This container was partially filled with water and tared on a digital balance equipped with analog output. To record the weight versus time data

during a spill, a Nova 840 computer with a multirange real-time peripheral was used. Data points were recorded every second, 30 analog readings being averaged for each data point. The response time for the balance was less than a second, and the accuracy of the readings was within 1 percent.

To determine whether the escaping vapor was superheated, a 0.254 mm copper-constantan thermocouple was mounted on a frame which could be lowered into the container once the spill had been made. The multirange peripheral had millivolt ranges which were suitable for thermocouples. Thus temperature measurements could be recorded by the computer simultaneously with the weight measurements.

The circular cross-sectional area of the container was assumed to be the area of heat transfer. Certainly the presence of waves would increase this area, but similar wave formation is likely to occur whether a spill is confined or not, and the heat transfer rate obtained in these experiments would therefore still be applicable to a large unconfined spill.

The multilayered container was designed to avoid convection and frost formation on the container walls. However, it was still very difficult to observe the boiling behavior of the cryogen due to the condensation and cloud formation above the boiling liquid. The only major observation which could be made was that LNG (i.e. mixtures) tended to foam while liquid methane and all of the gels (including LNG gels) did not.

This apparatus was used to measure the boil-off rates for

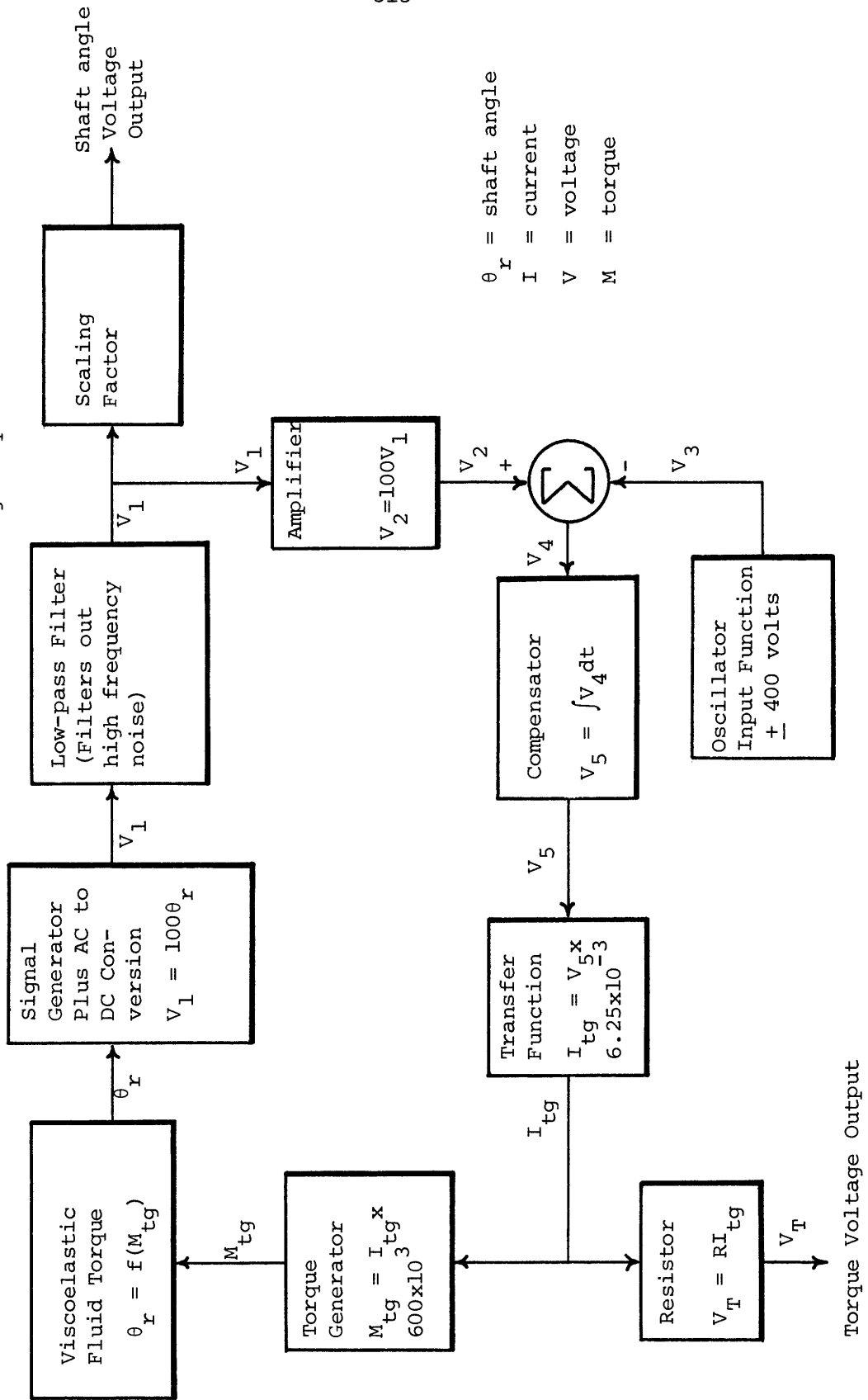
both LNG and LNG gels. As the rates were very sensitive to slight composition changes, each gel was compared with liquid methane or LNG of the same composition. Even when the C.P. grade of methane (> 99 percent pure) was gelled, liquid methane condensed from the same cylinder was used for comparison.

The sample was poured from a Dewar whenever possible. However, some of the gels were so thick that it was necessary to spoon them onto the water surface. This method of spilling splashes LNG (or gel) onto the container walls. Thus it was important to minimize the heat transfer resulting from contact with the container. For the thin liner of cellulose acetate, this effect was negligible.




6.6 Viscometer

An oscillating coaxial cylinder viscometer designed by P. J. Gilinson and C. R. Dauwalter of Draper Laboratory was used to study the rheological properties of the LNG gels. It consisted of an inner cylinder (bob) which was fixed to the viscometer frame, and an outer cylinder (cup) which was mounted on an essentially frictionless vertical shaft in a pressurized air bearing. The cup was caused to rotate in a slow oscillating motion by the injection of a controlled periodic signal into a torque balance feedback loop (Figure 6-7). The feedback control current necessary to bring about this oscillating motion was a direct measure of the fluid shear stress at the cup wall. This viscometer was capable of measuring torques ranging from 0.01 to 30,000 dyne-cm with an uncertainty of 0.001 dyne/cm.

Figure 6-7 Electronic Feedback Loop which Controls Cup Oscillation and Measures Resulting Torque



Torque Voltage Output

Four different waveforms could be generated with this input oscillator--sinusoid, sawtooth () , step () , and ramp () , at frequencies ranging from 0.01 Hz to > 10 Hz. However, at frequencies > 2 Hz, the torque current in the feedback loop was no longer linear with respect to the viscous torque, and thus accurate measurements could not be obtained. The maximum possible deflection was ± 15 milliradians, which, for the present cup and bob dimensions, corresponded to a maximum shear of ± 0.15 .

As the original viscometer was designed for operation at or near room temperature, several modifications were necessary to allow for operation and temperature control at cryogenic temperatures. A double cup (Figure 6-8) was made with a balsa wood base to insulate it from the air bearing and electronic parts. The inner cup contained the gel whose rheological properties were to be studied. The outer annular space was also filled with gel plus a small amount of liquid nitrogen to keep the inner cup wall at a temperature slightly below the gel boiling point. Although this temperature could not be continuously recorded during each run (a thermocouple could not be attached to the cup without affecting the torque measurements), an initial temperature study showed that a volume ratio of approximately 10 to 1, gel to liquid nitrogen, resulted in an outer surface (of the inner cup) temperature between 100 K and 110 K. The actual temperature was not critical as long as it was below the boiling point and above the freezing point of the LNG. The primary temperature control was maintained by the hollow bob. Cold nitrogen gas was produced by

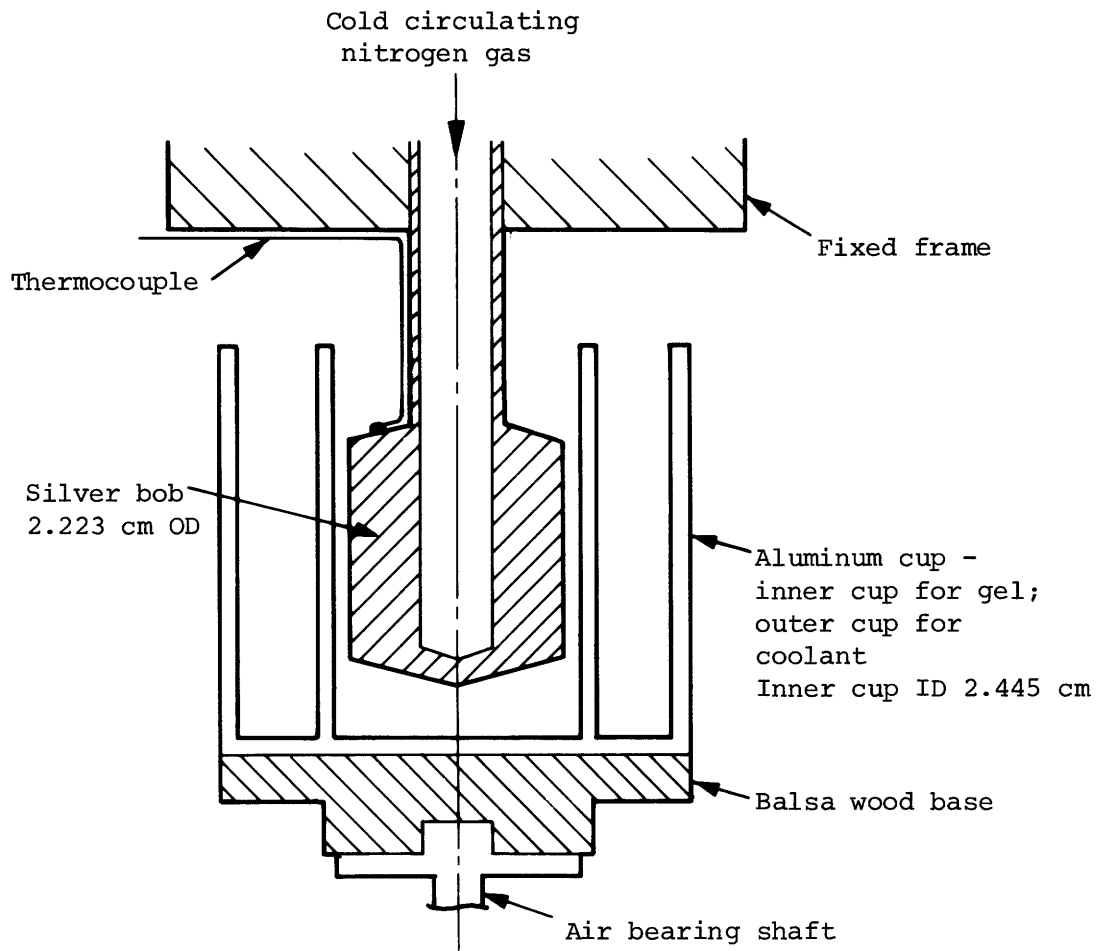


Figure 6-8 Cross-sectional View of Cup and Bob

appropriate heating of a stream of liquid nitrogen, and this was continuously circulated through the bob. A thin foil thermocouple was situated on the top outer surface of the bob, and its temperature reading was recorded continuously during each run. Although it would have been desirable to have the heating unit within the bob, the small bob dimensions precluded this possibility. Thus, the heating unit had to be placed along the nitrogen inlet line, which resulted in a lag time between heater voltage changes and bob temperature changes. In general, the temperature could not be maintained constant for any length of time, but could be recorded and kept within the desired temperature range. Fortunately, the observed viscosity change with temperature was negligible for the methanol gels. For the dilute water gels, however, there was a noticeable change, but the effect was no more than ± 20 percent difference in torque for the entire temperature range.

Due to the small gap width, it was not possible to place a thermocouple on the portion of the bob surface where the torque was actually being produced. However, a separate temperature study was made in which thermocouples were placed on the inner cup wall and the outer bob surface (in the small gap portion) as well as at the top of the bob. Both thermocouples on the bob surface continuously measured the same temperature within ± 2 K, and the wall temperature was generally a few degrees warmer than the bob but always within 5 K.

To avoid frost formation, the viscometer parts were enclosed in a plexiglass chamber which was continuously purged with helium (Figure 6-9).

-317-

Nitrogen gas

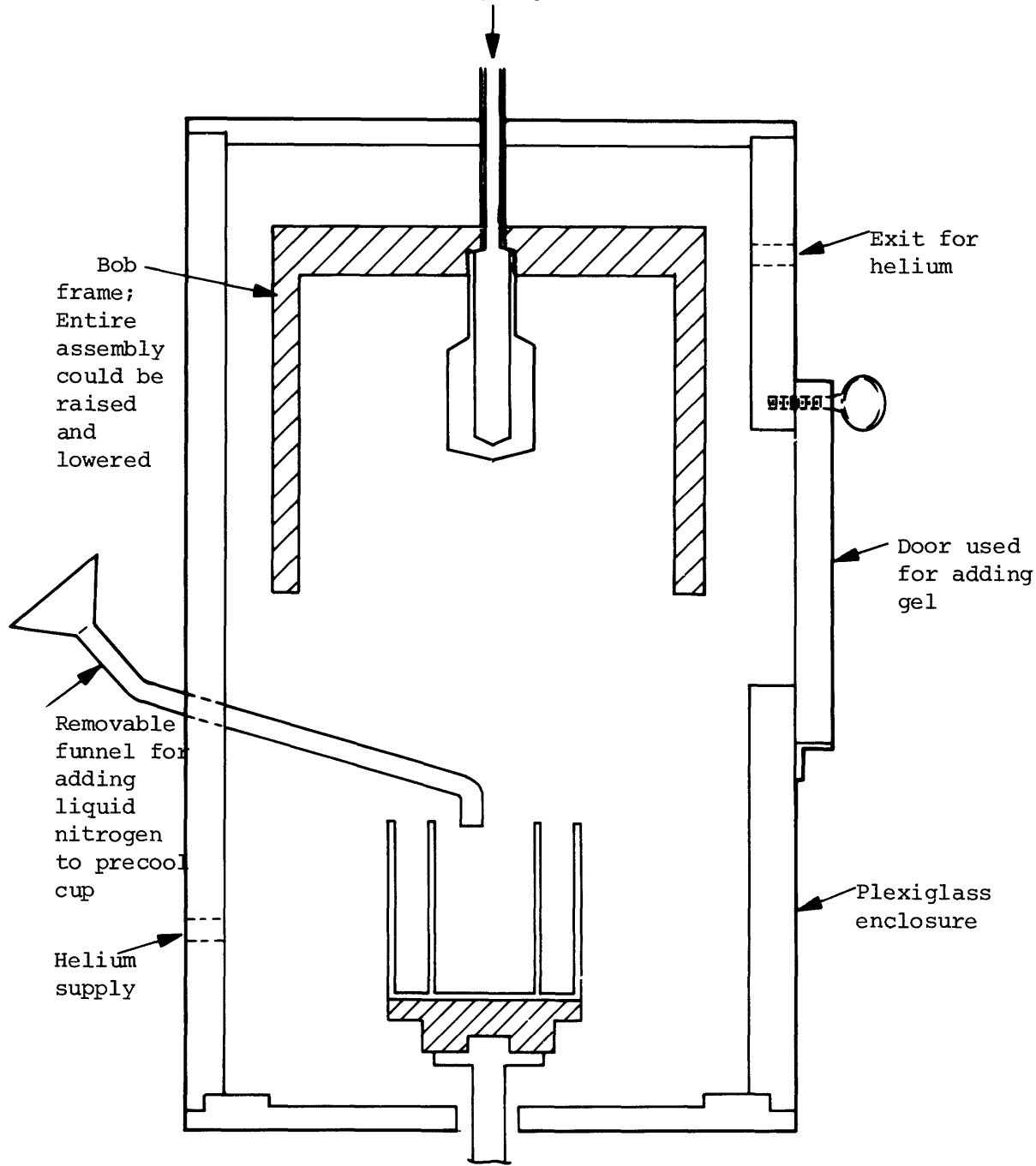


Figure 6-9 Cross-section of Viscometer Parts Inside Plexiglass Chamber

As all of the viscometer parts had to be precooled before the gel was added, provisions were made for raising and lowering the bob while being maintained at cryogenic temperatures. The cup was precooled by initially filling it with liquid nitrogen which subsequently boiled away as the cup cooled. Prior to the addition of the gel, the outer annular space was filled approximately 1/10 full with liquid nitrogen. The gel was then added using a long-handled dipper through a door in the Plexiglass chamber. (It would have been desirable to add the gel by means of a funnel; however, the gels were generally too thick to flow through such a small diameter tube.) The short amount of time that this doorway was open during the addition of the gel did not cause any problems with frost formation.

Once the cup had been filled with gel, the bob (having already been cooled to the desired temperature with circulating nitrogen gas) was lowered into place. As this process sheared the gel, its structure may have been partially destroyed, and a short resting period (1 to 2 minutes) was thus allowed for the structure to rebuild. This seemed to be adequate as the torque (shear stress) showed no noticeable increase with time when the cup was first caused to oscillate. As the liquid nitrogen/gel mixture in the outer annular space of the cup would boil off with time, there was a time limitation of approximately 10 minutes for any given run. However, a sufficient number of frequencies could be tested in this period of time, and for each run, both cup angle and torque were recorded as a function of time. Due to the non-linear viscoelasticity of the gels, the angle

oscillation did not always precisely follow the input function. However, at the very low frequencies, 0.02 to 0.1 Hz., the agreement was generally good. Thus it was important to record the cup angle oscillation as well as the torque. A few experiments were run with the sawtooth, ramp, and step function inputs, but, primarily the sinusoid was used with a frequency ranging from 0.02 to 2 Hz. However, at frequencies > 0.5 Hz, the torque response was completely elastic and viscosities could not be measured. This is discussed in detail in Chapter 4.

Initial experiments on the general rheological behavior of gels under oscillating conditions were made using Cab-O-Sil gels. These gels were produced by mixing powdered Cab-O-Sil with a non-polar liquid. This formed a lyophobic gel similar to LNG gel, but which could be produced and studied at room temperature. Silicone oil/Cab-O-Sil gels were used for the study of gel oscillatory behavior, but other liquids, diethylene chloride and methanol, were also gelled with Cab-O-Sil for an experimental study on static yield stress. Here it was desired to correlate the gel peak height (i.e. the maximum height that the gel structure could support) with static yield stress. As the yield stress was expected to be proportional to ρgh , the density of the liquid dispersion medium was varied as well as the gel rigidity. Yield stresses were measured using a Stormer viscometer. This viscometer was also a couette-type (coaxial cylinder) device, but operated by applying a constant torque to the bob and measuring the resulting speed of rotation. A

cup (radius = 1.6 cm and height = 5. cm) and bob (radius = 1.5 cm, length = 3.0 cm) were machined out of copper to be used with this viscometer.

Another instrument, a Brookfield Synchro-Lectric viscometer, was used to measure the static yield stress of some of the LNG gels. This device consisted of a spindle at the end of which was a small disk (1 cm in radius and 0.5 cm in height). This disk was submerged in the liquid to be studied. Although this instrument was constructed to allow the spindle to rotate at a constant speed while the torque was being measured by a calibrated spring, the yield stress measurement did not require this feature. The LNG gel yield stresses were measured as follows. Initially the spindle was precooled by submerging it in liquid nitrogen. The spindle was then submerged in the gel to be measured (a small Dewar was used to hold the gel), and the Dewar was slowly rotated coaxially about the spindle. Under such conditions the bob will rotate with the gel, and the measured spring torque will increase until the static yield value is reached. The gel will then begin to flow around the spindle, the torque decreasing to its steady state value. The peak value is, therefore, a measure of the static yield stress. However, difficulties can occur with this technique, as submersion of the spindle in the gel may leave a hole and create planes susceptible to slippage. In such cases the measured peak value will be lower than the static yield, and repeated experiments may be necessary to obtain the static yield stress.

6.7 Gel Concentration Measurements

To determine the gelant concentration of the gels used in both the viscosity and boil-off rate studies, a small styrofoam cup (capacity $\approx 25 \text{ cm}^3$ with 2.5 cm thick walls) was used. Weight measurements were made as follows. Initially a dry weight was measured. A sample of the gel was then added to the container, and a light cover of aluminum foil was placed over the container (this was included in the dry weight). Another weight measurement was made to determine the weight of the added gel. Subsequent measurements followed the weight decrease as the LNG vaporized from the gel. Eventually only the dry gelant particles remained, which, upon warming, melted and remained in the container. Although evaporation of the gelant may occur during this time, the rate is very slow (0.001 gm/min) and is easily distinguished from the fast rate of natural gas vaporization. Thus, the final weight measurement represents the dry weight plus the gelant, and can be used to determine the gelant concentration. A small amount of frost formation usually occurred on the aluminum cover during vaporization of the LNG. This was removed before the final weight measurement.

CHAPTER 7 - INDUSTRIAL SCALE APPLICATION OF LNG GELS

The primary incentive for this study was the possible use of gelled LNG as a safer form in which to transport natural gas. For oceanic transport, natural gas is presently converted to its liquid form (boiling point-110 K, 1 bar). This has a volumetric advantage over shipment in the gas form as the liquid density is 0.42 g/cm^3 while the gas is 0.02 g/cm^3 at 30 atms. Economic considerations have, therefore, shown that liquid transport in large insulated tankers is preferred to gas transport in thick-walled vessels. A concern associated with such cryogenic transport is the possibility of a tanker accident resulting in an LNG spill. With its low viscosity (.12 cp) and high volatility, LNG will readily flow out of a ruptured tank, spread and vaporize. As the cold, newly vaporized natural gas mixes with air, a vapor cloud forms above the spreading pool of LNG. This vapor cloud may travel considerable distance before there has been sufficient dilution to reduce the natural gas concentration below its lower flammability limit (5 mole % in air).

The possible magnitude of this safety hazard can be assessed by considering the extent of present and projected LNG transport along with the number and capacity of the tankers. Although the United States presently imports less than .1 percent of its natural gas (the U.S. is actually a net exporter of LNG as Alaskan exports to Japan exceed the Algerian imports to Massachusetts), the overall international trade is considerable. Japan imports about 80 percent of its natural gas and

Western Europe 5 percent. These annual imports total 450,000 cubic meters which is equivalent to approximately 12 shiploads according to current tanker capacities.

The magnitude of U.S. LNG importation is also likely to increase in the future as domestic production has been declining rapidly since it reached a peak in 1973. This sharp decline is likely to continue unless new sources are found and developed. Although there has been a new emphasis on U.S. energy autonomy in the last few years, a great deal of further research is necessary before feasible alternative sources of energy are available. In the case of natural gas, which is a particularly desirable fuel due to its clean burning and ease of distribution, such alternatives as coal or oil gasification are presently being investigated, but they are not yet economically feasible. Thus, LNG importation remains the most viable alternative for supplementing domestic supplies.

The magnitude of the hazard associated with any major LNG spill is directly related to the quantity spilled and thus dependent on tanker capacities. Thirty-five natural gas tankers with an average capacity of 46,000 cubic meters are now in operation. Fourty-one other tankers, with a mean capacity of 124,000 cubic meters, are either under construction or in the design stage. Plans are also being laid for vessels which will carry 165,000 cubic meters. These tankers generally consist of five or six separate storage tanks each with a capacity of 15,000 to 20,000 cubic meters. Although there are different basic designs (freestanding, membrane, and spherical) for inner tanks, the

primary container is made of welded metal and the tanks are separated from the ship's hull by greater than a meter thickness of insulation. Thus a collision must be quite severe (greater than that expected from either ramming or grounding) to result in a loss of cargo. Nevertheless, there is still much concern due to the large quantities being transported. It has been estimated that the spill from a single inner storage tank could result in flammable gas mixtures several miles from the spill site. Thus it is still desirable to reduce this hazard should a feasible means be available. In order to obtain such a safety benefit, one would like to significantly reduce any or all of the following rates: the spill rate, the spreading rate, and the rate of boil-off per unit area. The first two rates are affected primarily by the rheological properties of the fluid, and a gel would have two such desirable properties - a yield stress and a high viscosity. The high viscosity should reduce the rate of spreading while the yield stress will halt the spreading altogether once its height can be supported by the gel structure. Thus the investigation of the gel rheological properties was a particularly important part of this study. The results are discussed in detail in Chapter 4 and will be used in this chapter to assess the possible safety benefit.

The third factor, the rate of boil-off per unit area, was also investigated (Chapter 5) and, in confined spills, the LNG gels were found to boil at a rate which was 1/3 to 1/2 that of LNG.

To further determine the feasibility of industrial scale use of such LNG gels, other factors relating to the gel structure and stability

were also studied. Based on these results, possible industrial scale gelation procedures, as well as suspected problem areas associated with the use of such gels, will be discussed in the last section of this chapter.

7.1 Assessment of Safety Benefit

Estimating the maximum distance at which a flammable gas mixture can result after a major spill requires a detailed model of the spill. This includes the type of spill--whether it is instantaneous or continuous, how fast it spreads and the corresponding rate of heat transfer and vaporization per unit of contact area. Further, one must model the vapor cloud formation and dispersion with time. In general, the important quantity, the maximum travel distance for a flammable mixture can be related to the overall rate of vapor generation using the dispersion equation for a continuous line source.

(7-1)

$$c = \left(\frac{\dot{m}}{UL} \right) \left(\frac{2}{\sqrt{2\pi} \sigma_z} \right) \operatorname{erf} \left(\frac{L}{2\sqrt{2} \sigma_y} \right)$$

where c = lower flammability limit, mass/volume

\dot{m} = rate of vapor generation, mass/time

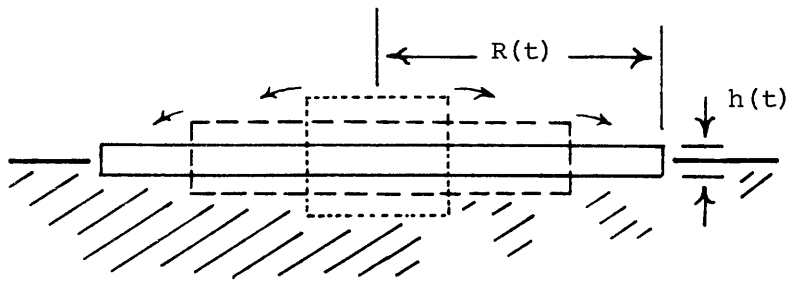
L = length of vapor source

U = wind velocity (a commonly used average value is 4.5 m/s, for a neutral weather condition)

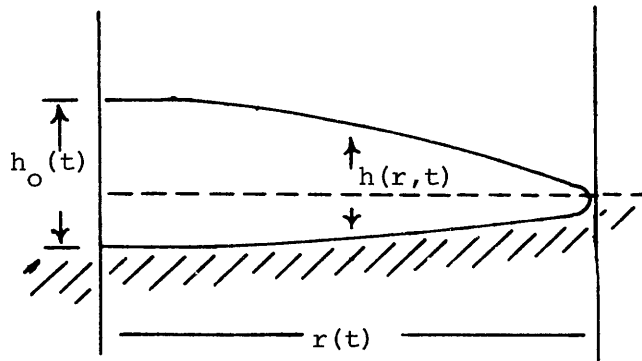
σ_z, σ_y = variance of Gaussian concentration profile resulting from vertical and lateral diffusion respectively (generalized correlation given in Appendix V).

Although the vaporizing pool could be better approximated by a continuous area source, a closed analytical solution cannot be obtained for such a case. A reasonable approximation, however, can be made by using the relation for a line source with the characteristic length being the pool diameter. It is evident that the maximum distance is directly related to the maximum rate of vapor generation, and this, in turn is generally estimated using the maximum pool diameter and an appropriate average boil-off rate. In confined spill tests, the boil-off rate for LNG showed an initial increase with time characteristic of a shift from film to nucleate boiling. For large spills (large initial cryogen heights) the boil-off rate peaked and then continued to decrease until complete evaporation. These boil-off rates were also very sensitive to composition. Such transient effects have not been precisely characterized for unconfined spills, and the most appropriate solution has, therefore, been to use a constant average boil-off rate.

The most important parameter will, therefore, be the maximum pool size which, in turn, is dependent on the rate of spread. The spreading behavior of one fluid on another has been considered by several investigators. In all cases the spill is assumed to be instantaneous and the flow behavior to be as shown in Figure 7-1. The rate of spread varies with time and spill size, but in general, the spreading behavior can be separated into three distinct regimes. The



Physical model for radial spreading in the gravity-inertial regime



Physical model for radial spreading in the gravity-viscous regime

Figure 7-1 Physical Models for the Spreading of One Fluid on Another.

initial regime is gravity-inertia spreading where the hydrostatic head is balanced with the acceleration of the fluid mass. Not accounting for any loss of fluid by boil-off, the relation for a radially spreading pool of liquid on water is (Fannelop and Waldman, 1972).

(7-2)

$$r = 1.14 (GV)^{1/4} t^{1/2}$$

where r = pool radius

G = effective gravity $g(1-\rho_L/\rho_W)$

V = spill volume

t = time

ρ_L = density of spreading liquid

ρ_W = density of water

g = acceleration due to gravity

Raj and Kalelkar (1973) have included a constant boil-off rate and arrived at the following expression.

(7-3)

$$r = V^{1/3} \left[1.3 \left(\frac{G}{V^{1/3}} \right)^{1/2} t + \frac{.442 q}{\sqrt{\frac{V}{G^3}} \lambda \rho_L V^{1/6} G^{1/2}} t^3 \right]^{1/2}$$

where q = heat flux to the boiling liquid

λ = heat of vaporization of the liquid at its normal boiling point

The second flow regime is referred to as gravity-viscous. Here the viscous effects are assumed to be much greater than the inertial resistance. The flow behavior expression for this regime is dependent

on the viscosity of the spreading volatile liquid. For the case of $(\mu_L/\mu_w) \ll 1$, as in LNG, and neglecting boil-off, the following expression has been derived (Raj and Kalelkar, 1973).

$$r = .8412 \left(\frac{GV^3}{\nu_L} \right)^{1/8} t^{1/8} \quad (7-4)$$

where ν_L = kinematic viscosity of the spreading liquid

The critical time for changeover from the gravity-inertial to the gravity-viscous regime is given as

$$t_c = .4446 \left(\frac{V}{G\nu_L} \right)^{1/3} \quad (7-5)$$

For $(\mu_L/\mu_w) \ll 1$, and also neglecting boil-off, the expression is

$$r = 0.98 \left(\frac{G^2V^4}{\nu_w} \right)^{1/12} t^{1/4} \quad (7-6)$$

where ν_w = kinematic viscosity of water

$$t_c = .546 \left(\frac{V}{G\nu_w} \right)^{1/3} \quad (7-7)$$

Raj and Kalelkar also derived an expression for the gravity-viscous spread of LNG on water which includes boil-off.

$$r = r_c (\tau/\tau_c)^{1/4}$$

$$\text{and } r_c = 1.3 \left(\frac{V^{1/3}}{G} \right)^{1/2} t_c + \frac{.442 q}{\lambda G \rho_L V^{1/3}} t_c^3 \quad (7-8)$$

$$\tau_c = t_c / (V^{1/3} G)^{1/2}$$

$$\tau_c^{1/2} = \Gamma_w \frac{(1. - 2.04 \tau_c^2 \Delta + .347 \tau_c^4 \Delta^2)}{\pi (1.3 \tau_c + .442 \tau_c^3 \Delta)} \quad (7-9)$$

$$\text{where } \Delta = \frac{q}{\lambda \rho_L (V^{1/3}/G)^{1/2}}$$

$$\tau = \frac{t}{\sqrt{V^{1/3} G}} \quad \Gamma_w = \frac{(VG)^{1/4}}{v_w^{1/2}}$$

These relations suggest that there is no advantage to having a fluid more viscous than water. However, intuitively, one would expect otherwise, and the problem with these expressions may be in the assumptions used in deriving them. In the case of a high viscosity fluid, it was assumed that the vertical velocity gradient was extremely small (i.e. the fluid moves as a homogeneous slab), and thus the viscosity term for the spreading fluid could be neglected in the Navier-Stokes equation. The viscous boundary layer in the water phase, therefore, provided the viscous retarding force in the gravity-viscous regime. An order of magnitude analysis (see Appendix W) indicates that this assumption is correct as long as

$$\frac{\Delta U}{U} \ll \frac{.001 v^{1/2}}{\mu_L t^{3/2}} \quad (7-10)$$

U = the velocity of the leading edge

ΔU = the vertical change in velocity across the fluid slab

Although an experimental study of spreading oil slicks was done by Hoult and Suchon, 1970, no measure of velocity gradients was made, and the overall viscosity variation was not significant enough to adequately determine whether these expressions were correct.

For the case of a low viscosity fluid, the fluid was assumed to spread on a solid or no-slip surface as $\mu_w \gg \mu_L$. This would be appropriate in the case where LNG is in direct contact with the water and thus in nucleate boiling. However, LNG may begin in film boiling (see Chapter 5) and a more conservative model might be a free-slip boundary condition with LNG spreading on a thin film of vapor. Another consideration is the water inertia effect. For large spills such an inertia effect might be important, and the spreading behavior might better be thought of as the liquid or gel spreading on itself (at water level) rather than on a thin gas film. In this case, the spread of LNG could be approximated using a free-slip boundary while the gel would be closer to a no-slip boundary condition.

Previous experiments on instantaneous LNG spills have been limited to small quantities. Boyle and Kneebone spilled 21, 42, and 84 lb quantities and reported average spread rates (increase in diameter) of 4 to 4.5 ft/s (1.2 to 1.4 m/s) for the two smallest spills and 2.5 ft/sec for the 84 lb spill. These spreading rates are similar to those predicted using Equation 7-3. Burgess et al. (1970) also studied the spreading and boil-off behavior of LNG but used a slightly larger quantity, 50 gal. They reported an approximately linear rate of spread of 2.5 ft/s. Although the predicted rate is

not constant, the predicted average rate is approximately equal to that observed.

In spite of the fair agreement between these small-scale spills and the analytical model, no large-scale instantaneous spills have been made, and thus it is not certain whether the expressions will predict accurate spreading rates under these conditions. Also, the present equations do not seem adequate for predicting the spreading behavior of LNG gel due to the questionable assumptions made. To determine whether gelation would significantly affect the spreading rate, a numerical technique was used. This particular numerical method was developed by Amsden and Harlow (1970) and is referred to as the SMAC method. A brief description of the numerical procedure is given in Appendix X. Except for modifications associated with computer compatibility (an IBM 370 was used in this study), the computer program used here was the same as that written by Amsden and Harlow. Although this program was not designed to handle two different fluids simultaneously, nor to allow for any loss of fluid by boil-off, the effect of gelation could still be adequately demonstrated using the simple case of a breaking dam. As the Navier-Stokes equations pertain only to Newtonian fluids, the gel was modeled as a highly viscous Newtonian fluid. The maximum shear rate observed in the LNG spill case (see Figure 7-2) was approximately 1 sec^{-1} . If a gel with a steady-state yield stress of 500 dynes/cm^2 were sheared at this rate, it would have an apparent viscosity of ≥ 500 poise. Thus a value of 500 poise was selected to represent the gels.

Several cases were considered for the breaking dam model. Both

a free-slip (shear stress equals zero) and a no-slip (velocity equals zero) surface were used, and both LNG and LNG gel were analyzed. The results for these different numerical cases are shown in Figures 7-2, 7-3, 7-4, and 7-5. The leading edge distances are tabulated versus time and compared with the analytically predicted values in Table 7-1. For LNG, the spreading rate was considerably faster than that predicted. This is no doubt due to actual fluid mass behavior. Much of the fluid remains as if suspended at its initial height while a small portion of the fluid is accelerated outward at the base. This is quite different from the assumed physical model. The spreading behavior of the LNG gel for the free-slip boundary condition showed a decreased rate of spread, approximately 2/3 that of LNG (both free-slip and no-slip were similar for LNG). On the other hand, the spreading rate of the gel under a no-slip boundary condition was considerably less (approximately 1/8 that of LNG), and was in good agreement with that predicted from the analytical expression for one-dimensional spreading in rectangular coordinates (Table 7-2). The spreading behavior of LNG gel in an actual spill on water is likely to be somewhere in between these two rates. Thus it is difficult to accurately assess the safety benefit. If LNG is assumed to spread at a constant rate of 0.8 m/s and LNG gel is assumed to spread at 0.3 m/s, the behavior for a spill of 10^7 kg would be as shown in Figure 7-6. If the gel did not possess a yield stress it would spread to a maximum pool radius of 375 m (as compared with 410 m. for LNG). However, the fact that it has a yield stress indicates that for pool heights

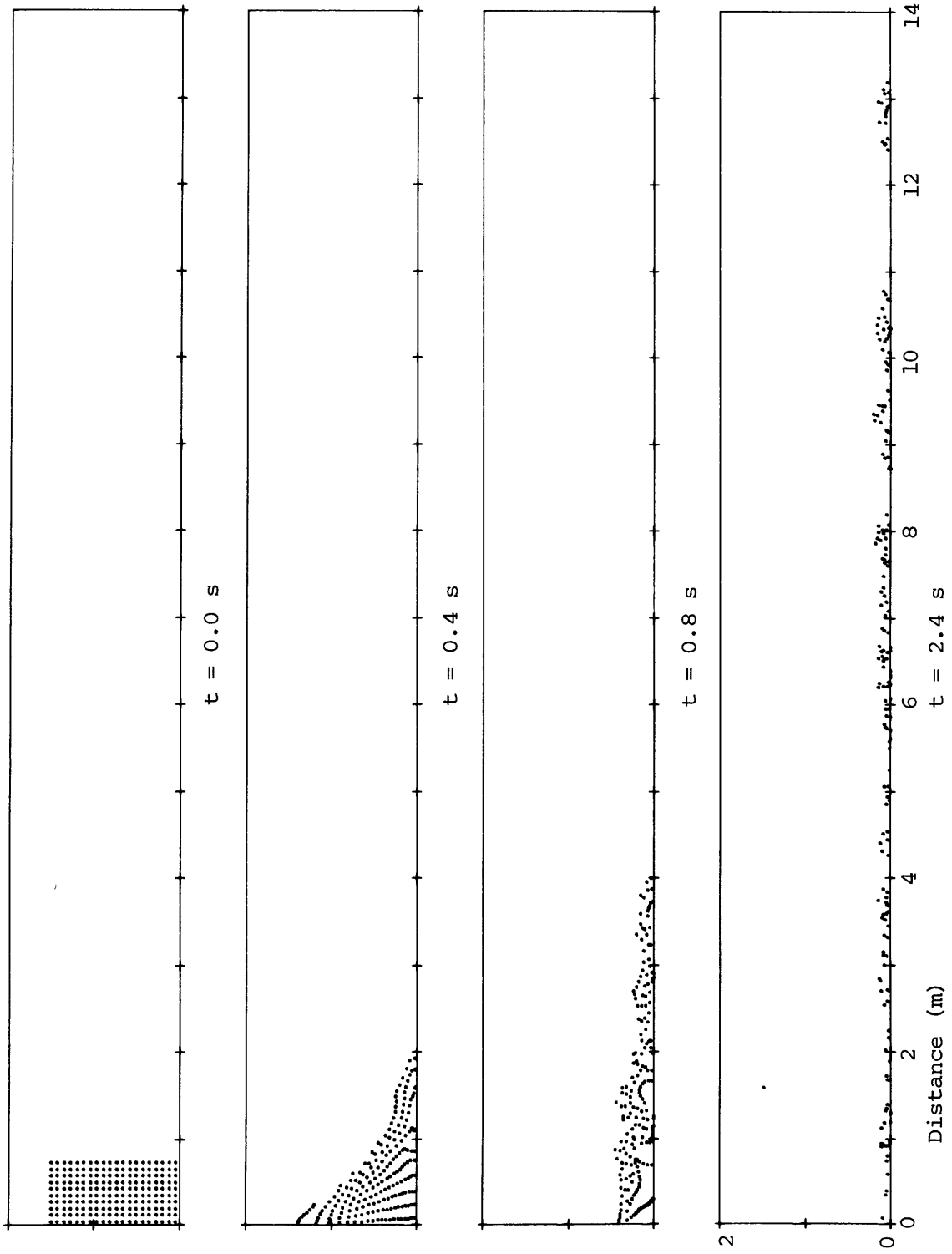


Figure 7-2 Numerical results for breaking-dam model using LNG and a free-slip boundary condition

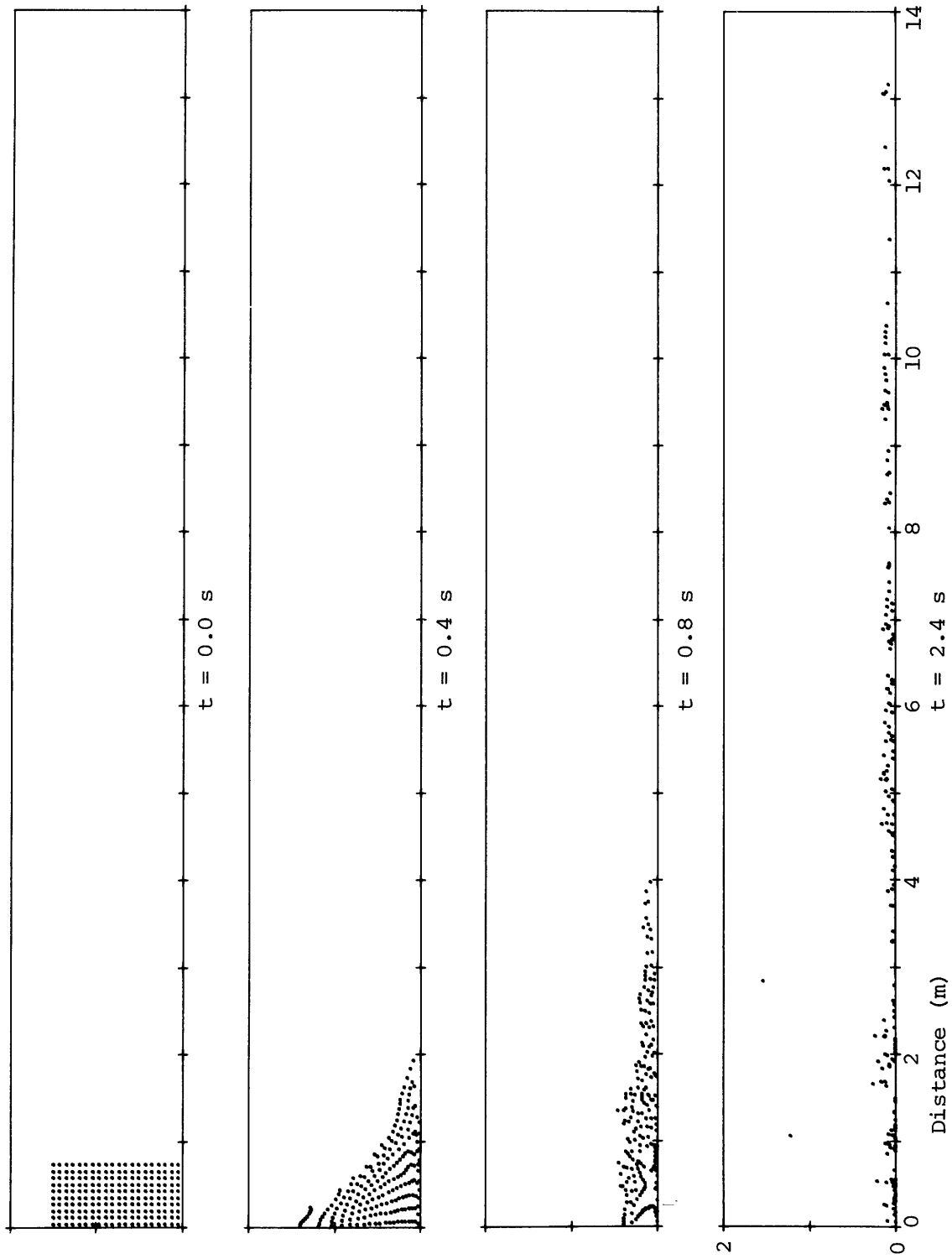


Figure 7-3 Numerical results for breaking-dam model using LNG and a no-slip boundary condition

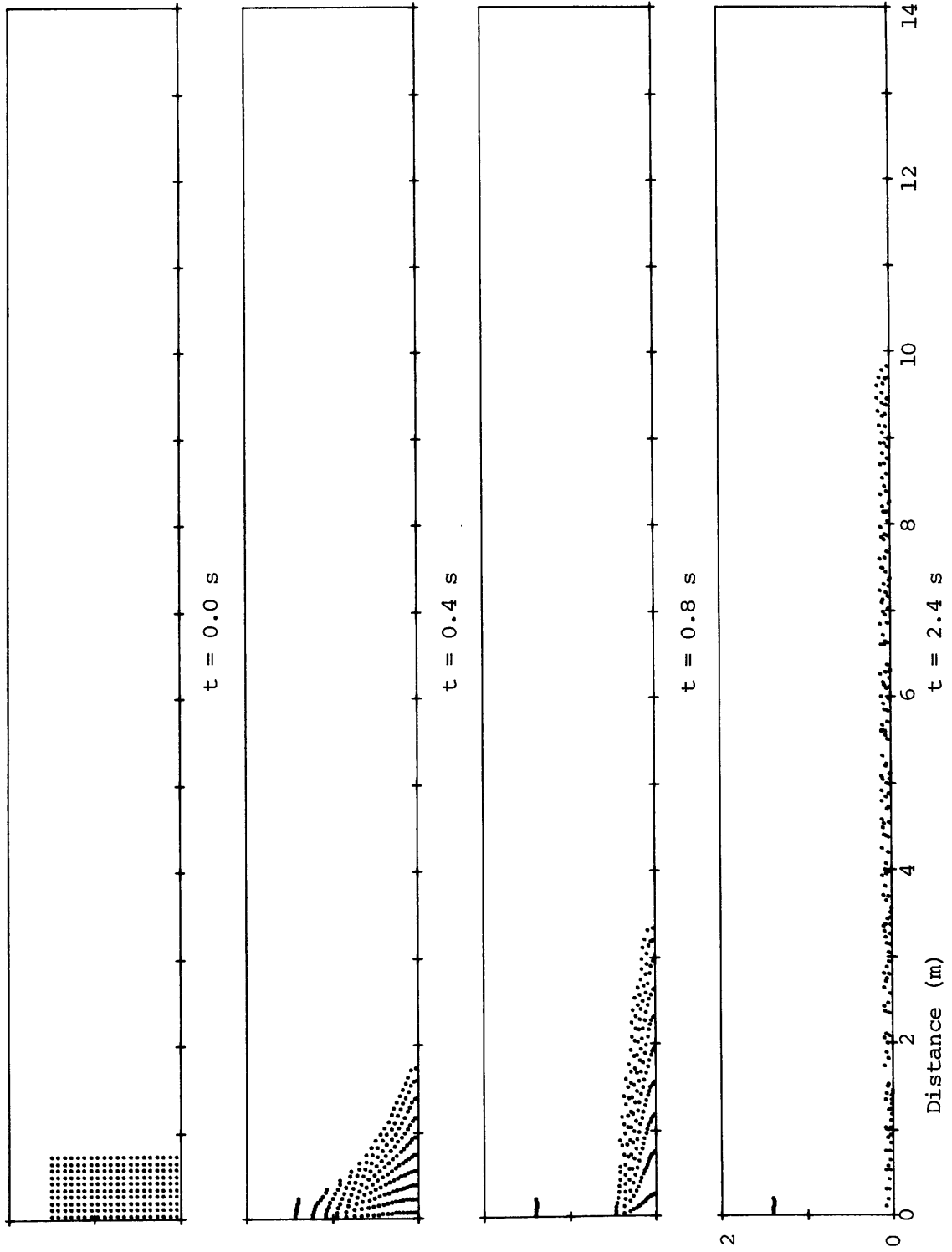


Figure 7-4 Numerical results for breaking-dam model using LNG gel and a free-slip boundary condition

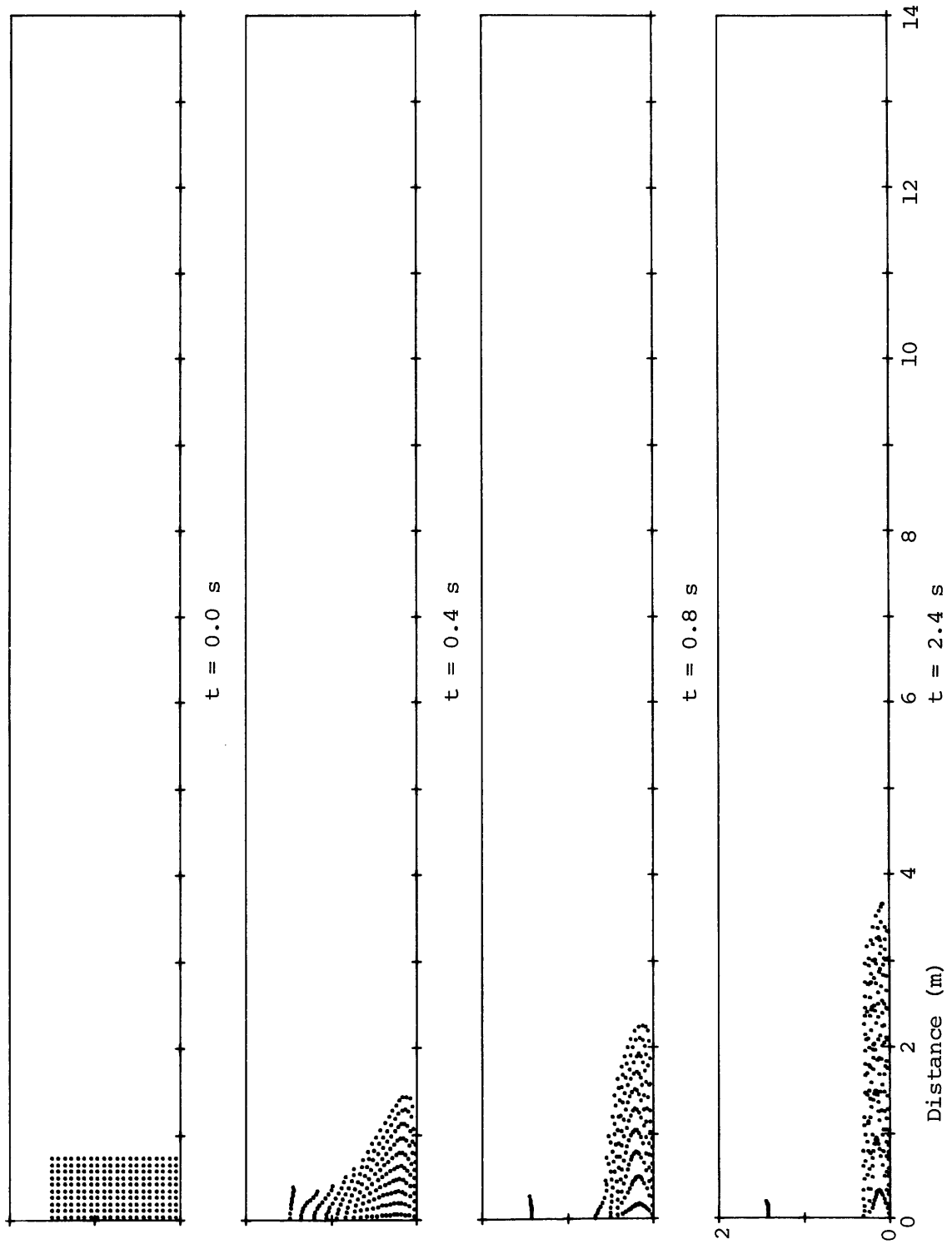


Figure 7-5 Numerical results for breaking-dam model using LNG gel and a no-slip boundary condition

Table 7-1 Spread Distances for Breaking Dam

Time	LNG Free-Slip	LNG Gel Free-Slip	LNG No-Slip	LNG Gel No-Slip	LNG* Analytical	LNG Gel** Analytical
<u>(sec)</u>	<u>(m)</u>	<u>(m)</u>	<u>(m)</u>	<u>(m)</u>	<u>(m)</u>	<u>(m)</u>
0.4	0.6	0.5	0.6	0.2	1.4	1.4
0.8	2.6	2.0	2.6	0.9	2.1	1.9
1.2	4.9	3.7	4.9	1.5	2.8	2.0
1.6	7.2	5.2	7.2	2.0	3.4	2.2
2.0	9.4	6.9	9.4	2.1	4.0	2.3
2.4	11.7	8.4	11.7	2.3	4.4	2.3
2.8	>14.	10.1	>14.	2.4	4.9	2.4
3.2		11.6		2.6	5.4	2.5
3.6		13.1		2.6	5.9	2.5
4.0				2.6	6.3	2.6
4.4				2.7		2.7

* The analytical expression for rectangular coordinates and one-dimensional spreading is $x = 1.39 (GA)^{1/3} t^{2/3}$ where x equals leading edge distance from initial dam edge and A equals half of the spill cross-sectional area (i.e. one-half of the spill volume per unit width of channel).

**The analytical expression for one-dimensional gravity-viscous spreading with a no-slip boundary condition is
$$x = 1.132 \left(\frac{GA^3}{\nu_L} \right)^{1/5} t^{1/5}$$

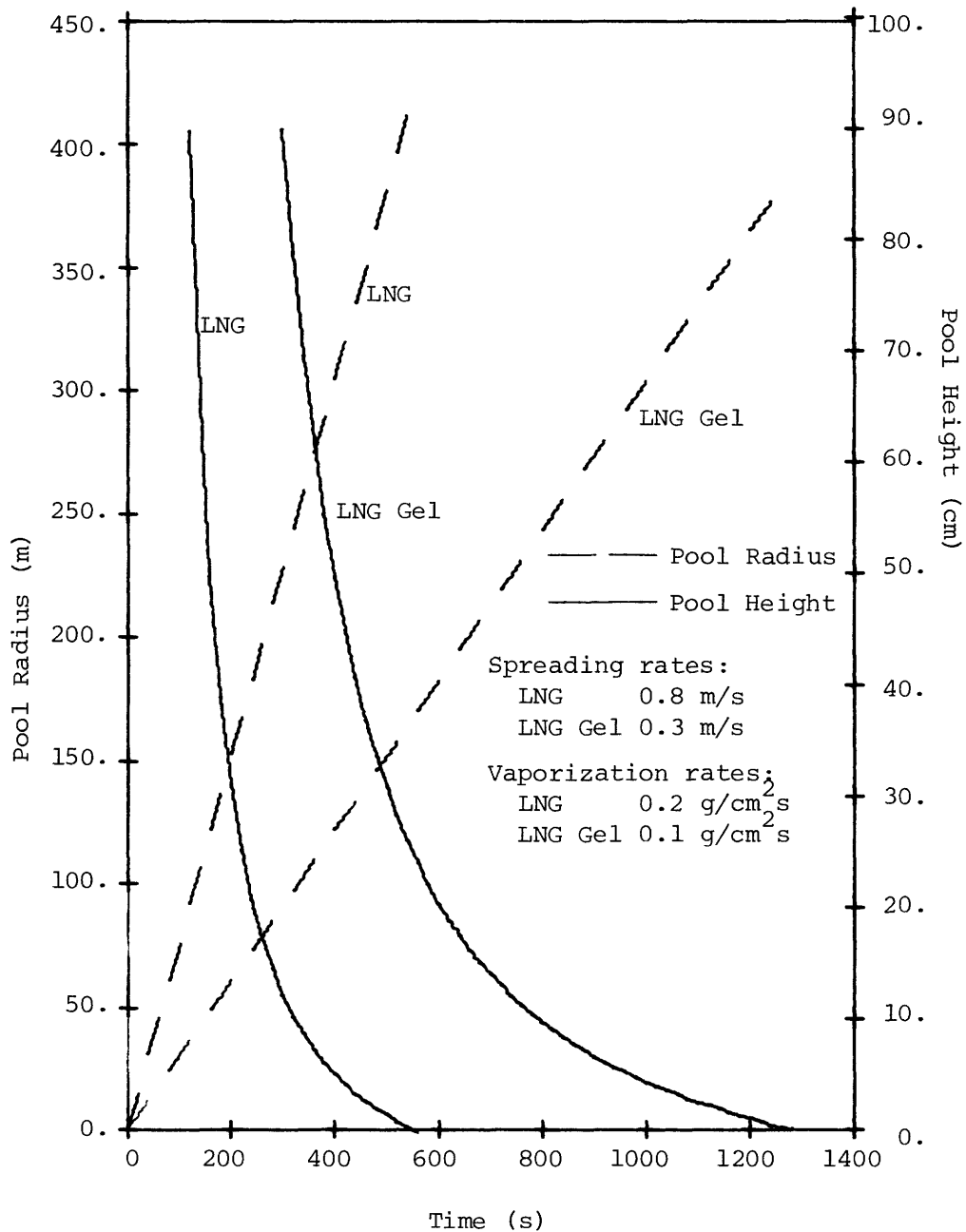


Figure 7-6 Spreading and Vaporization of 10^7 kg LNG and LNG Gel

less than some critical value, the gel will no longer spread (i.e. the gelant particle interactions are strong enough to oppose the hydrostatic head). This has been discussed in Chapter 4 with respect to gel buildup on a suspended disk and has been correlated with static yield stress. In a flow situation the steady-state yield stress is probably more appropriate and this is approximately 1/4 of the static yield value. The corresponding height is $h \approx 3\tau_y/\rho g$. For a gel with an initial steady-state yield value of 500 dynes/cm^2 (this corresponds to $\approx 5 \text{ wt } \% \text{ H}_2\text{O}$ or $7.5 \text{ to } 10 \text{ wt } \% \text{ CH}_3\text{OH}$ for the gels produced in this study), $h \approx 3.5 \text{ cm}$. This height would correspond to that above the water level, i.e. due to water buoyancy, the equivalent height would be 5 cm . During boil-off, the concentration will change and the yield stress will increase. When 20 percent of the methane has vaporized the yield stress will have doubled, and when 40 percent of the methane has boiled off the yield stress will be approximately five times its original value, as yield stress is approximately proportional to the concentration cubed. If this is taken into account, the gel spreading will cease when the pool radius reaches $\approx 230 \text{ m}$. This results in a reduction in maximum vapor generation rate by a factor of ≈ 5 , as compared to LNG. This, in turn, results, in a reduced maximum distance for flammable mixtures by a factor of approximately 5. If equations 7-3 and 7-8 are used with the viscosities of LNG and LNG gel, the spreading and boil-off rates for the gels (as compared to LNG) is even more reduced (a factor of 10 for the maximum distance). However, this has assumed a no-slip

boundary condition for the gel and probably over-estimates the gel viscosity effect. However, the numerical results clearly show that there will be a reduced spreading rate due to gelation (i.e. the transition to a gravity-viscous regime occurs very rapidly before a significant amount of spreading has occurred and the subsequent gravity-viscous flow is controlled by the viscosity of the gel), and a realistic estimate suggests that the maximum distance can be reduced by a factor of 5 if LNG is appropriately gelled to give a steady-state yield stress of 500 dynes/cm².

7.2 Spill Behavior

Although the analytical spreading models discussed in the previous section were all based on instantaneous spillage, a major spill may closer approximate a continuous spill. In fact, if the rupture is small enough in diameter, the spill rate will be the controlling factor (i.e. the maximum boil-off rate will be equivalent to the spill rate). The size of a single inner transport tank is quite large and any rupture is likely to be small in comparison. In such a case, flow from the tank can be described using the relation for orifice flow.

$$v = V/A = C\sqrt{2gH}$$

where v = discharge velocity
 V = volumetric discharge rate
 A = cross-sectional area of orifice
 g = acceleration due to gravity

H = head of liquid above orifice

C = coefficient of discharge (≈ 1)

According to this expression, viscosity does not affect the flow rate. However, it was expected that if the fluid possessed a high enough viscosity that the flow rate would actually be reduced. An attempt was made to model the draining of LNG gel from a storage tank using the previously-mentioned numerical technique. However, a satisfactory solution could not be obtained due to numerical instabilities and excessive computer time requirements.

7.3 The Gelation Process

The gelation procedure used in this study has been thought of as a laboratory process only. It is clearly not energy efficient, as it requires preheating the gas to keep the gelant vaporized prior to contact with the LNG. Once in contact with the LNG, the heat transfer necessary for cooling the mixture and freezing the gelant causes vaporization and loss of natural gas. For every 500 cm³ of gel produced, ≈ 1500 cm³ of LNG was boiled away. Thus an alternative gelatin process is needed for industrial scale use.

One possible industrial scale procedure is vapor phase addition of the gelant to the natural gas prior to its liquefaction. Formation of the gelant particles would then occur on stream. However, this

process has several drawbacks. In base-load liquefaction cycles, the inlet natural gas is at a pressure of approximately 150 psi. (In peak-shaving plants, a much higher pressure, ≈ 750 psi, is used.) At 150 psi the ideal gas law indicates that no more than 0.2 percent H_2O or 1.4 percent CH_3OH vapor could be introduced into this stream. Gas nonidealities would increase this value but not appreciably. Subsequent liquefaction involves cooling and condensing the natural gas in a heat exchanger (the coolant side being part of a suitable refrigeration cycle). If a gel is to be produced under these conditions, the cooling rate will be a critical factor in determining the final particle size. Typical liquefaction conditions cool the natural gas at a rate of 50 to 100 K/s, which may be too slow to achieve small enough particles. In the present laboratory process the cooling rate was much more rapid, ≥ 100 K in 10^{-4} sec, and the resulting particle radius was estimated (from the rheological data) to be ≈ 150 A. However, the vapor phase residency time and/or a low probability of coalescence may have actually controlled the final size, as nucleation and particle growth calculations suggested that larger particles were possible. Whatever the controlling factor may have been, an important consideration is the fact that even under these laboratory conditions a moderately thick gel required a gelant concentration (in the final gel) greater than the concentration used in the vapor mixture from which the gelant particles were formed. Thus, if one were to start with a 1 mole % gelant vapor mixture and condense it in such a way as to produce 100 A radius particles, one would obtain a dilute

gel (≤ 50 dynes/cm²). If a more concentrated, thicker gel were desired, either methane would have to be vaporized from the gel or an alternative method of producing and adding the dry gelant particles would be necessary. On the other hand, if one could condense this 1 percent gelant vapor mixture in such a way as to produce ≤ 50 A radius particles, the gel could, theoretically, be produced directly. This might be feasible with a supersonic jet, as Stein and Wegener (1967) obtained H₂O particles in this size range when air containing ≤ 1.5 mole percent of H₂O was rapidly expanded using a supersonic jet. However, this requires that the particles be well-dispersed, and that they not coalesce. Brownian motion of such small particles is sufficient to overcome ordinary van der Waals forces for particle separations ≥ 4 A (the diameter of a methane molecule). Thus, if two such particles stick together, they are undoubtedly in contact with hydrogen bond linkages. Once such linkages have formed, coalescence may be possible, the rate of which will be dependent on the particle size and the gelant solubility in the surrounding phase. The smaller the particles are, the greater will be the rate of coalescence, but estimates for the magnitude of this rate are not available.

The crystal structure analysis, composition analysis, and microscopic observation of the gelant particles indicated that the particles were crystalline clathrates. Therefore, an alternative approach might be to form the desired clathrates as large crystals and subsequently grind them to obtain fine particles. The dry particles (or alternatively a highly-concentrated gel) could then be added to the LNG using some suitable mixing procedure. Grinding techniques,

however, cannot produce particles less than $\approx 1 \mu\text{m}$ in size. This size would require a concentration of 80 wt. percent (63 volume percent) to obtain a yield stress of 500 dynes/cm^2 .

If a suitable industrial scale gelation procedure were found, there are still possible problem areas which would require further study. In particular, the process of revaporization should be considered. As methane vaporizes from the gel, the gel in turn becomes thicker, increasing in yield stress and apparent viscosity. Flow behavior is very difficult to predict for such conditions of changing composition. Although the yield stress is increasing, slip planes may occur and the actual wall shear stresses may be lower than expected. The fact that natural gas is a mixture rather than pure methane may offer an advantage here. In the case of liquid methane gel, the methane vaporizes from the gel (its temperature remaining constant at the methane boiling point) leaving a packed dry solid. Only after a further temperature rise does the solid clathrate decompose. On the other hand, as methane vaporizes from an LNG gel, the gel becomes more concentrated in the heavier components, resulting in an increase in boiling point. Eventually the temperature of the gel will reach the clathrate decomposition point, and the gel structure will break down. In such cases, the particles have been observed to settle out, thus forming a slurry which would be much easier to pump. This effect could also increase the spread rate in a major spill, thus reducing the safety benefit. However, the decomposition rates are likely to be slow enough that this problem will not occur.

For storage and transport of the gels, the stability of the gels will be important. In the present study, no attempt was made to study the aging properties of the gels. However, Vander Wall (1971) had previously found that liquid methane (both H₂O and CH₃OH) gels were stable, with no appreciable decrease in structure, for 114 hours. Here there are two factors which will affect the structure stability, one being the susceptibility to particle coalescence, the other being particle settling. The former is directly related to the solubility of the gelant in the liquid. However, neither the solubilities nor the rate of coalescence are known, and further study would therefore be necessary to determine the associated rate of gel destabilization. This would be a particularly important consideration for long-term storage. From observations in the present study, particle settling was only noticeable in dilute gels (< 300 dynes/cm²). Some mixing would help to reestablish such a gel provided that particle settling and packing had not been too severe.

Thus, although the gelation of LNG could significantly reduce the hazard associated with LNG transport, there are still a number of possible problems related to large-scale use. These require further study before an overall feasibility assessment can be made.

CHAPTER 8 - CONCLUSIONS AND RECOMMENDATIONS

In the present study, LNG has been gelled using two different gelants, water and methanol, and these gels have been analyzed as to their structural and rheological properties. The gel structure was found to consist of the attractive interactions of small (≈ 150 A) crystalline particles. Analysis of these particles by x-ray diffraction, composition determination, and microscopic observation provided substantial evidence that the particles were crystalline clathrate solids rather than pure solids. A crystal structure was also proposed for the previously unknown methanol clathrate based on the x-ray diffraction data.

The rheological properties of the gels were determined using an oscillating shear technique. The results indicated non-linear viscoelasticity, and analysis of this response at various frequencies gave an apparent Bingham plasticity at the low shear rates studied. Both static and steady state yield stresses were also determined for the gels.

A study on the vaporization rates of LNG gels on water was performed, and these results along with those from the rheological study were used to assess the possible safety benefit of transporting natural gas in a gelled form. Based on confined spill tests, the gels were found to vaporize at a rate which was one-half to one-third that of LNG. To determine the effect of gelation on the spread rate, a simple dam-breaking model was used, and the fluid dynamics was

analyzed using a numerical technique. The results indicated that the gels would spread at a lower rate than LNG, estimated to be approximately 60 percent lower. The combination of reduced spread and boil-off rates give an estimated 80 percent reduction in the maximum distance for flammable gas mixtures for a gel of yield stress 500 dynes/cm^2 .

Although an extensive study has been completed on LNG gels, there are a number of areas which require further study before such gels could be considered feasible for industrial-scale use. In particular, a satisfactory gelation procedure must be developed, and the aging and revaporization properties determined.

From an academic standpoint there are also further gel and clathrate studies which might be of interest. The size of the gelant particles could be determined experimentally, possibly using electron microscopy, and compared with the value estimated in this study. Single crystal x-ray diffraction could be used to clarify the crystal structure of the methanol clathrate and techniques, other than that used in the present study, might be used to determine its composition. It is also not certain whether the guest species for methanol clathrates is limited to very small molecules such as methane. If larger molecules can be enclathrated, the structure may also differ from that proposed for methane.

APPENDIX A - LONDON'S ATTRACTIVE FORCE

Eisenschitz and London (1930) derived the following expression for the London dispersion force between two complex atoms or molecules.

$$B_{12} = \frac{3he^4}{32\pi^4 m_e^2} \sum_i \sum_j \frac{f_{1i} f_{2j}}{\nu_{1i} \nu_{2j} (\nu_{1i} + \nu_{2j})} \quad (A-1)$$

where f_{1i} = oscillator strength corresponding to transition frequency ν_{1i} for molecule 1
 f_{2j} = oscillator strength corresponding to transition frequency ν_{2j} for molecule 2
 h = Planck's constant
 e = charge of electron
 m_e = mass of electron

The summations are taken over all such transitions. These oscillator strengths are related to the polarizability of the molecule at frequency ν .

$$\alpha_1(\nu) = \frac{e^2}{4\pi^2 m_e} \sum_i \frac{f_{1i}}{\nu_{1i}^2 - \nu^2} \quad (A-2)$$

The polarizability is, in turn, related to the molar refraction, R_1 , by the Lorentz-Lorenz equation.

$$R_1 = \frac{n_1^2 - 1}{n_1^2 + 2} \frac{M_1}{\rho_1} = (4/3) \pi N_O \alpha_1(\nu) \quad (A-3)$$

where n_1 = refractive index of material 1 at frequency ν
 M_1 = molecular weight
 ρ_1 = density
 N_O = Avogadro's number

Combining Equations A-2 and A-3 gives

$$\frac{n_1^2 - 1}{n_1^2 + 2} \frac{M_1}{\rho_1} = \frac{e^2 N_o}{3\pi m_e} \sum_1 \frac{f_1}{v_1^2 - v^2} \quad (\text{A-4})$$

This dispersion equation relates the variation of refractive index with frequency. Dispersion refers to electronic oscillations which are responsible for the dispersion of light. Gregory (1969) points out that this expression does not apply at frequencies close to strong absorption bands. In these regions an imaginary damping term must be introduced yielding complex values for the refractive index.

Gregory further suggests that for many materials, the variation of refractive index with frequency can be represented by a dispersion equation with a single term.

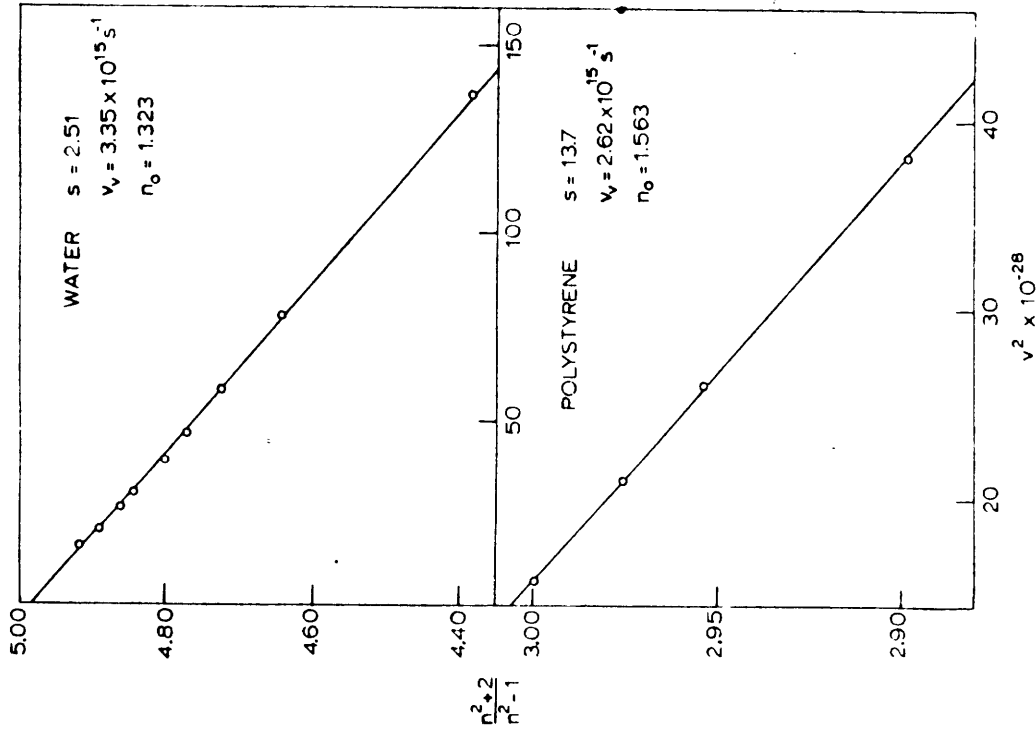
$$\frac{n^2 - 1}{n^2 + 2} \frac{M}{\rho} = \frac{e^2 N_o}{3\pi m_e} \frac{s}{v_v^2 - v^2} \quad (\text{A-5})$$

where $s = \sum f =$ "effective number of dispersion electrons"
 $v_v =$ characteristic frequency

The figure shown on the following page shows the good linear correlation for water and polystyrene (from Gregory, 1969). Materials such as the liquid alkanes, all forms of silica and many inorganic crystals are reported as giving similar straight lines, and some values of s and v_v are given in the subsequent table. The frequency range shown in the figure includes visible to low ultraviolet frequencies. Although not explicitly stated, this same frequency range was, no doubt, used

DISPERSION DATA

Substance	P_r ($\text{sec}^{-1} \times 10^{-13}$)	s	Z
Gases:			
He	6.19	1.22	2
Ne	6.26	2.41	8
Ar	4.12	4.35	8
Kr	3.57	4.93	18
Xe	3.00	5.63	18
H ₂	3.52	1.56	2
O ₂	3.58	3.13	12
N ₂	4.13	4.64	10
CH ₄	3.42	4.83	8
H ₂ O	3.27	2.42	8
Liquids:			
H ₂ O	3.35	2.51	8
C ₆ H ₆	2.54	10.1	30
C ₆ H ₁₂	3.39	19.1	36
n-C ₃ H ₁₂	3.39	17.5	32
n-C ₆ H ₁₄	3.39	20.7	38
n-C ₇ H ₁₆	3.39	23.9	44
n-C ₈ H ₁₈	3.40	27.2	50
n-C ₉ H ₂₀	3.40	30.6	56
n-C ₁₀ H ₂₂	3.39	33.6	62
Solids:			
Diamond	4.19	2.27	4
SiO ₂ (crystalline)	3.89	6.65	16
SiO ₂ (fused)	3.78	6.50	16
Polystyrene	2.62	13.7	40



to determine the characteristic frequencies listed in the table.

Based on a one-term dispersion relation, the resulting London constant for two different molecules having similar characteristic frequencies is

$$B_{12} = \frac{3he^4}{32\pi^4 m_e^2} \frac{s_1 s_2}{v_{1v} v_{2v} (v_{1v} + v_{2v})} \quad (A-6)$$

and for identical molecules

$$B = \frac{3he^4}{64\pi^4 m_e^2} \frac{s^2}{v_v^3} \quad (A-7)$$

If the characteristic energy $h\nu_v$ is equal to the ionization potential, as suggested by London (1937), then B_{12} becomes

$$B_{12} = (3/2)\alpha_1 \alpha_2 \frac{I_1 I_2}{I_1 + I_2} \quad (A-8)$$

Based on the frequencies listed in the preceding table, the characteristic energies are actually quite close to the values for the ionization potentials, thus substantiating London's assumption.

Incorporating the Maxwell relation between refractive index and dielectric constant, $\epsilon = n^2$, gives

$$\frac{\epsilon_o - 1}{\epsilon_o + 2} \frac{M}{\rho} = \frac{e^2 N_o}{3\pi m_e} \frac{s}{v_v^2} \quad (A-9)$$

Here ϵ_o must be taken as the square of the limiting refractive index in the visible wavelength region. The dispersion equation discussed

can be used by setting ν equal to zero. Gregory points out that the static dielectric constant (measured with zero frequency of applied field) must not be used in Hamaker constant calculations as it may include dipole reorientation which does not contribute significantly to dispersion forces. Lifshitz, however, in his macroscopic approach for determining particle-particle interactions, has emphasized that the entire spectrum must be considered, and that dipole reorientation may even be dominant in some cases.

APPENDIX B - CALCULATION USING HAMAKER'S EXPRESSION

$$A_{11} = \pi^2 q_1^2 B_{11} \quad \text{where } q_1 = \rho_1 N_o / M_1$$

$$= (27/64) h\nu_1 \left\{ \frac{\epsilon_1 - 1}{\epsilon_1 + 2} \right\}^2 \quad \text{where } \epsilon_1 = n_1^2 \text{ (} n_1 = \text{index of refraction)}$$

$$h\nu_1 = I_1 \text{ (ionization potential)}$$

For ice $n_1 = 1.31^*$
 $\epsilon_1 = 1.72$
 $I_1 = 12.6 \text{ eV}^*$

*from Handbook of Chemistry and Physics

$$A_{11} = (27/64) (12.6 \text{ eV} \times 1.6 \times 10^{-12} \text{ ergs/eV}) (.72/3.72)^2$$

$$= 3.19 \times 10^{-13} \text{ ergs}$$

For liquid methane $\epsilon_2 = 1.63^{**}$ **(Pan et al., 1975)
 $I_2 = 12.6 \text{ eV}^*$

$$A_{22} = (27/64) (12.6 \text{ eV} \times 1.6 \times 10^{-12} \text{ ergs/eV}) (.63/3.63)^2$$

$$= 2.56 \times 10^{-13} \text{ ergs}$$

$$A_{121} = ((A_{11})^{\frac{1}{2}} - (A_{22})^{\frac{1}{2}})^2 = 3.46 \times 10^{-15} \text{ ergs}$$

For methanol $\epsilon_3 = n_3^2 = 1.7^{***}$
 $I_3 = 10.8 \text{ eV}^*$

***The value for the refractive index of liquid CH_3OH , $n=1.3^*$, was used here, as the value for solid methanol was not known. However, it is quite likely that the refractive index is actually greater than this, as the methanol gelant particles appeared white, while those of H_2O were barely visible. An estimated value for n_3 might be that of Cabosil, 1.5, which also appears white in liquid methane.

$$\begin{aligned} A_{33} &= (27/64) (10.8 \text{ eV} \times 1.6 \times 10^{-12} \text{ ergs/eV}) (.7/3.7)^2 \\ &= 2.6 \times 10^{-13} \text{ ergs} \end{aligned}$$

and $A_{323} = 1.6 \times 10^{-17} \text{ ergs}$

If the higher value for the refractive index is used, the result is

$$A_{33} = 6.3 \times 10^{-13} \text{ ergs} \quad \text{and} \quad A_{323} = 8.3 \times 10^{-14} \text{ ergs}$$

APPENDIX C - APPROXIMATION FOR DIELECTRIC SUSCEPTIBILITY

The approximations, selection of coefficients, etc. used in these calculations follow systematically the procedure used by Ninham and Parsegian (1970b). The following expression for dielectric susceptibility was used for ice.

$$\begin{aligned} \epsilon(i\xi_n) = 1 + \frac{C_{mw}}{1 + \xi_n/\omega_{mw}} + \frac{C_1}{1 + (\xi_n/\omega_1)^2} \\ + \frac{C_2}{1 + (\xi_n/\omega_2)^2} \end{aligned} \quad (C-1)$$

where $C_{mw} = 197.9$

This is the difference between the static dielectric constant, 200 (Johari and Whalley, 1973), and the dielectric constant after Debye relaxation, 3.1 (Franks, 1972).

$C_1 = 1.4$

This is the difference between the dielectric constant at the beginning and end of the infrared region, 3.1 and 1.7 respectively. At the end of the infrared region, the dielectric constant is equal to n^2 where $n=1.3$ (refractive index) from Handbook of Chemistry and Physics.

$C_2 = n^2 - 1 = 0.7$

$\omega_{mw} = 6.0 \times 10^{-2}$ rad/s

This represents an average Debye relaxation frequency (Ruepp, 1973).

$\omega_1 = 3.0 \times 10^{14}$ rad/s

This is an average for the three absorption peaks in the infrared region (Franks, 1972).

$\omega_2 = 1.9 \times 10^{16}$ rad/s

Here $\omega = 2\pi\nu$ and $\nu = I/h$, where I is the ionization potential, 12.6 eV.

For liquid methane, only the ultraviolet is significant (Ninham and Parsegian, 1970b).

$$\epsilon(i\xi_n) = 1 + \frac{C_2}{1 + (\xi_n/\omega_2)^2} \quad (C-2)$$

where $C_2 = n^2 - 1 = 0.63$ $n^2 = \epsilon = 1.6$ (Pan et al., 1975)
 $\omega_2 = 1.9 \times 10^{16}$ Based on ionization potential.

For solid methanol, the complete expression (Equation C-1) was used with the following values.

$$C_{mw} = 60.5$$

$$\omega_{mw} = 10^3 \text{ rad/s}$$

The static dielectric constant for CH_3OH at 160 K, 64 (Handbook of Chemistry and Physics), was used to determine C_{mw} . The relaxation frequency and dielectric susceptibility after relaxation (≈ 3.5) were estimated from data reported by Smyth and McNeight (1936).

$$C_1 = 3.5 - n^2 = 1.8$$

$$\omega_1 = 2.6 \times 10^{14} \text{ rad/s}$$

Based on the liquid refractive index. If the higher suggested refractive index (Appendix B) is used, then C_1 will be equal to 1.25. The associated frequency is an average of the three strongest infrared absorption bands (Herzberg, 1964).

$$C_2 = 0.7$$

$$\omega_2 = 1.6 \times 10^{16} \text{ rad/s}$$

If the higher value for refractive index is used, C_2 will be equal to 1.25. This ultraviolet frequency is based on the ionization potential.

APPENDIX D - CALCULATIONS BASED ON THE LIFSHITZ EXPRESSION

$$G(D,T) = \frac{-A(D,T)}{12\pi D^2} \quad \text{and} \quad A(D,T) = 1.5kT \quad I(\xi_n, D)$$

$$I(\xi_n, D) = \left\{ \frac{2\xi_n D \epsilon_2^{\frac{1}{2}}}{c} \right\}^2 \int_1^{\infty} p \left\{ \ln \left(1 - \bar{\Delta}^2 \exp \left(\frac{-2p\xi_n D \epsilon_2^{\frac{1}{2}}}{c} \right) \right) \right. \\ \left. + \ln \left(1 - \Delta^2 \exp \left(\frac{-2p\xi_n D \epsilon_2^{\frac{1}{2}}}{c} \right) \right) \right\} dp$$

$$\bar{\Delta} = \frac{s\epsilon_2 - p\epsilon_1}{s\epsilon_2 + p\epsilon_1} \quad \Delta = \frac{s - p}{s + p}$$

$$\text{and } s = (p^2 - 1 + \epsilon_1/\epsilon_2)^{\frac{1}{2}}$$

Zero frequency term:

As $\xi_n \rightarrow 0$, $\int () dp \rightarrow \infty$. At small p , the function to be integrated is finite and small. The integral approaches ∞ only as $p \rightarrow \infty$. Thus it is desired to determine the value of I as $\xi_n \rightarrow 0$ and $p \rightarrow \infty$ by letting $\xi_n = \delta$ (a very small value).

$$\text{As } p \rightarrow \infty \quad \bar{\Delta} = \frac{1 - \epsilon_1/\epsilon_2}{1 + \epsilon_1/\epsilon_2} \quad \Delta = \frac{p - p}{2p} \rightarrow 0$$

$$\exp \left(\frac{-2p\delta D \epsilon_2^{\frac{1}{2}}}{c} \right) \rightarrow 0 \quad (\text{or } 1 \text{ for } \delta \rightarrow 0)$$

The second "ln" term reduces to $\ln(1 + 0) = 0$. This leaves

$$\left(\frac{2\xi_n D \epsilon_2^{\frac{1}{2}}}{c} \right)^2 \int_1^{\infty} p \left\{ \ln \left(1 - \bar{\Delta}^2 \exp \left(\frac{-2p\xi_n D \epsilon_2^{\frac{1}{2}}}{c} \right) \right) \right\} dp$$

$$\text{Let } u = \frac{2D\epsilon_2^{\frac{1}{2}}}{c} p \quad du = \frac{2D\epsilon_2^{\frac{1}{2}}}{c} dp$$

$$\delta^2 \int_1^{\infty} u \ln(1 - \bar{\Delta}^2 \exp(-u\delta)) du$$

Let $k = \frac{-2}{\Delta^2}$

Expanding $\ln(1 - ke^{-u\delta}) = -ke^{-u\delta} - (1/2)k^2 e^{-2u\delta} - (1/3)k^3 e^{-3u\delta} - (1/4)k^4 e^{-4u\delta} \dots$

The integral becomes

$$\begin{aligned} & -\delta^2 \int_1^\infty u (ke^{-u\delta} + (1/2)k^2 e^{-2u\delta} + (1/3)k^3 e^{-3u\delta} \dots) du \\ = & -\delta^2 \left[\frac{ke^{-u\delta}}{\delta^2} (-\delta u - 1) + (1/2)k^2 \frac{e^{-2u\delta}}{4\delta^2} (-2\delta u - 1) \right. \\ & \left. + (1/3)k^3 \frac{e^{-3u\delta}}{9\delta^2} \dots \right]_1^\infty \\ = & -(ke^{-\delta}(\delta + 1) + (1/8)k^2 e^{-2\delta}(2\delta + 1) + (1/27)k^3 e^{-3\delta} \dots) \end{aligned}$$

As $\delta \rightarrow 0$, this becomes

$$-(k + k^2/2^3 + k^3/3^3 + k^4/4^3 \dots)$$

This result is also obtained for the zero frequency term in Equation 2-18. Also note that this expression is independent of separation distance.

For the liquid methane/ice system, $\epsilon_1 = 200$ and $\epsilon_2 = 1.6$

(see Appendix C).

$$\begin{aligned} k &= \frac{1 - (200./1.6)}{1 + (200./1.6)}^2 = .9685 \\ k + k^2/2^3 + k^3/3^3 + k^4/4^3 \dots &= .9685 + .11725 + .03365 + \\ & .01375 + .00682 + .00382 + \\ & .00233 + .00151 + .00103 + \\ & .00073 + .00053 + .00039 + \\ & .00030 + .00023 + .00018 \\ & = 1.151 \end{aligned}$$

This zero energy term must then be multiplied by one-half.

$$A(D,T) = 1.2 \times 10^{-14} \text{ ergs} + 1.5kT \quad I(\xi_n, D)$$

Calculation of I for the remaining frequencies was done by computer using the expression for A(0,T).

$$A(0,T) = 2.1 \times 10^{-14} \text{ ergs}$$

For the interaction of solid methanol particles, the results were as follows

$$A(0,100 \text{ K}) = 2.1 \times 10^{-14} \text{ ergs (for refractive index equal to 1.3)}$$

$$A(0,100 \text{ K}) = 1.1 \times 10^{-13} \text{ ergs (for refractive index equal to 1.5)}$$

APPENDIX E - SURFACE POTENTIAL OF ICE IN LIQUID METHANE

The ion concentration in liquid methane can be determined from its electrical conductivity (Adamczewski, 1969).

$$\chi = \sum_i (F/N_o) v_i n_i z_i$$

where v_i = mobility of ion i
 z_i = charge of i
 n_i = number of ions i per unit volume
 N_o = Avagadro's number
 F^o = Faraday constant

The ions are assumed to be CH_4^+ and CH_4^- , and the ionic mobility is assumed to be similar to that of liquid argon ($\approx 10^{-3} \text{ cm}^2/\text{volt-s}$) (Adamczewski, 1969). The conductivity is taken as $10^{-18} \Omega^{-1} \text{ cm}^{-1}$ (White, 1975).

$$10^{-18} \Omega^{-1} \text{ cm}^{-1} = \frac{2 \times 96,493 \text{ coul/equiv.}}{6.02 \times 10^{23} \text{ ionx/equiv.}} \frac{10^{-3} \text{ cm}^2}{\text{volt s}} n$$

$$n = 3.12 \times 10^3 \text{ ions/cm}^3$$

The ionic concentration in an ice particle was estimated using this same expression. Here, the conductivity was estimated from the data of Maeno (1973) to be $10^{-18} \Omega^{-1} \text{ cm}^{-1}$ at 110 K. The mobility was assumed to be $10^{-5} \text{ cm}^2/\text{volt-s}$ (Onsager, 1973). This yields a calculated value of 10^5 ions/cm^3 . To estimate the possible surface charge on an ice particle in liquid methane, it was assumed that 10 percent of the ions present in a 150 Å radius ice sphere did not have counterbalancing ions.

$$N_{\text{ions}} = (4/3) \pi r^3 (10^4)$$

$$\begin{aligned}
 &= 1.4 \times 10^{-13} \text{ ions} \\
 \sigma &= \frac{1.4 \times 10^{-13} \text{ ions}}{4\pi r^2} \\
 &= 5 \times 10^{-3} \text{ ions/cm}^2
 \end{aligned}$$

The surface potential can be calculated from the electrical double layer relation

$$\sigma = \epsilon \epsilon_0 \kappa \phi_0 \qquad \kappa = \frac{2z^2 F^2 c}{\epsilon \epsilon_0 RT}$$

where

- T = absolute temperature
- F = Faraday's constant
- z = charge of ion
- ϵ = dielectric constant of the liquid
- ϵ_0 = permittivity of a vacuum

$$\kappa = \frac{2(96,493 \frac{\text{coul}}{\text{mole}})(23,062 \frac{\text{cal}}{\text{volt mole}})(3.12 \times 10^3 \text{ ions/cm}^3)}{1.6(1.1 \times 10^{-12} \frac{\text{coul}}{\text{volt cm}})(1.987 \frac{\text{cal}}{\text{mole K}})(100 \text{ K})(6.02 \times 10^{23} \frac{\text{ions}}{\text{mole}})}$$

$$\kappa = .26 \text{ cm}^{-1}$$

$$\begin{aligned}
 \phi_0 &= \frac{\sigma}{\epsilon \epsilon_0 \kappa} = \frac{(1.7 \times 10^{-2} \text{ ions/cm}^2)(1.6 \times 10^{-19} \text{ coul/ion})}{1.6(1.1 \times 10^{-12} \text{ coul/volt-cm})(.26 \text{ cm}^{-1})} \\
 &= 5.9 \times 10^{-9} \text{ volt}
 \end{aligned}$$

APPENDIX F - ENERGY OF REPULSION FOR ICE DOUBLE LAYERS

For the interaction of two spherical particles with a small surface potential, ϕ_0 , and a small κr , the repulsive energy is

$$V_R = 4\pi\epsilon\epsilon_0 r^2 \phi_0^2 \frac{\exp(-\kappa D)}{2r + D}$$

where

- r = radius of sphere
- D = smallest distance between the two spherical surfaces
- κ = $.26 \text{ cm}^{-1}$
- ϕ_0 = surface potential (volts)
- ϵ_0 = permittivity of a vacuum
- ϵ = dielectric constant for the liquid
- V_R = energy of repulsion

For $r = 5 \times 10^{-6}$ cm and $D = 10^{-7}$ cm, $V_R = 2 \times 10^{-33}$ joule which is negligible compared to van der Waals attractive energy at all gap widths.

APPENDIX G: EQUILIBRIUM CRITERION BASED ON
VARIATION OF NUCLEUS RADIUS AND ITS
EFFECT ON AVAILABILITY

The variation of availability with nucleus radius is:

$$\left(\frac{\partial(\Delta A)}{\partial r}\right)_{N^\beta} = N^\beta \left(\frac{\partial \mu^\beta}{\partial r}\right)_{N^\beta} - \frac{4}{3} \pi r^3 \left(\frac{\partial P^\beta}{\partial r}\right)_{N^\beta} \\ + (P_o - P^\beta) (4\pi r^2) + 8\pi \sigma r$$

But

$$\left(\frac{\partial \mu^\beta}{\partial r}\right)_{N^\beta} = v^\beta \left(\frac{\partial P^\beta}{\partial r}\right)_{N^\beta} = \frac{4/3 \pi r^3}{N^\beta} \left(\frac{\partial P^\beta}{\partial r}\right)_{N^\beta}$$

which leaves

$$\left(\frac{\partial(\Delta A)}{\partial r}\right)_{N^\beta} = (P_o - P^\beta) (4\pi r^2) + 8\pi \sigma r$$

For equilibrium

$$\left(\frac{\partial(\Delta A)}{\partial r}\right)_{N^\beta} = 0$$

i.e. $r = \partial\sigma / (P^\beta - P_o)$

APPENDIX H - ESTIMATION OF SUPERSATURATIONS

If the vapor is assumed to supersaturate until it reaches -160°C . the maximum supersaturation is therefore P/P_{eq}^{-160} . Vapor pressures for ice and solid methanol are not known at such low temperatures. Ice, however, is known down to -98°C and extrapolation using a general vapor pressure relation based on the Clausius-Clapeyron expression gives

$$P_{\text{eq}}^{-160} = 5.0 \times 10^{-14} \text{ mm Hg. } [6.7 \times 10^{-11} \text{ dynes/cm}^2]$$

$$\text{at } T = -90^{\circ}\text{C (183.2 K)} \quad P_{\text{eq}} = 9.2 \times 10^{-8} \text{ atm. } (9.33 \times 10^{-2} \text{ dynes/cm}^2)$$

$$T = -98^{\circ}\text{C (175.2 K)} \quad P_{\text{eq}} = 1.97 \times 10^{-8} \text{ atm. } (2.0 \times 10^{-2} \text{ dynes/cm}^2)$$

The resulting equation is

$$\log_{10} P = (-2710.2/T) + 7.7619$$

where T = absolute temp (K)

P = pressure (atm.)

$$S = \frac{P}{P_{\text{eq}}^{-160}} = 7 \times 10^{+15}$$

APPENDIX I - NUCLEATION RATES DURING COOLING OF VAPOR MIXTURE

The following table shows the initial time-temperature history of a natural gas vapor with 1 mole percent methanol ($\approx 3 \times 10^{17}$ molecules/cm³). Nucleation rates, J, were calculated using the Becker-Doring expression with surface tension equal to 23 dynes/cm (Handbook of Chemistry and Physics).

<u>Time</u> <u>(sec)</u>	<u>Temp</u> <u>(K)</u>	<u>P_{eg}</u> <u>(dynes/cm²)</u>	<u>Super-</u> <u>sat.</u> <u>(P/P_{eq})</u>	<u>J</u> <u>nuclei/</u> <u>(cm³sec)</u>	<u>No. of</u> <u>nuclei</u> <u>formed</u>	<u>radius</u> <u>of</u> <u>nuclei (A)</u>
0	253	1.01×10^4	1			
5×10^{-6}	246	6.14×10^3	1.65	3.97		
10^{-5}	239	3.60×10^3	2.81	5.09×10^{18}	2.5×10^{13}	8
1.25×10^{-5}	235	2.61×10^3	3.9	8.84×10^{20}	2.2×10^{15}	6
1.5×10^{-5}	232	2.00×10^3	5.1*			

*over maximum supersaturation

APPENDIX J - PARTICLE GROWTH HISTORY BASED ON
CONDENSATION AND COALESCENCE

The rate of change of the total particle concentration, N , is

$$\frac{dN}{dt} = \sum_i \sum_j Z_{ij} N_i N_j$$

where N_i = number conc. for particles containing i molecules

Z_{ij} = collision rate for particles i and j

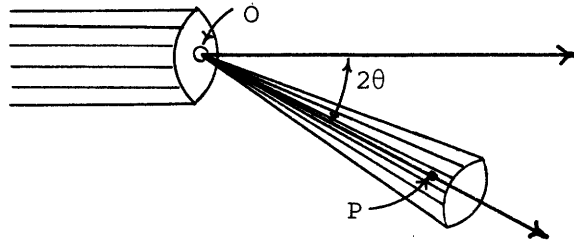
Assuming a monodisperse particle size distribution gives

$$\frac{dN}{dt} = \frac{1}{2} ZN^2$$

<u>Time</u> <u>(sec)</u>	<u>N</u> <u>(part./cm³)</u>	<u>dN/dt</u>	<u>part. radius</u> <u>(A)</u>
0	3×10^{17}	2.2×10^{25}	
10^{-8}	8×10^{16}	1.6×10^{24}	4
5×10^{-8}	1.6×10^{16}	$9. \times 10^{22}$	7
2×10^{-7}	2.5×10^{15}	2.8×10^{21}	12
10^{-6}	2.6×10^{14}	5.1×10^{19}	26
5×10^{-6}	5.6×10^{13}	2.7×10^{18}	44
2×10^{-5}	1.6×10^{13}	2.9×10^{17}	67
7×10^{-5}	1.4×10^{12}	2.7×10^{15}	150
5×10^{-4}	2.4×10^{11}	1.4×10^{14}	271
2×10^{-3}	3×10^{10}	2.7×10^{12}	540
1.2×10^{-2}	3×10^9	9×10^9	1166
.1	2.1×10^9		1313

APPENDIX K - SCATTERING OF X-RAYS

X-ray scattering occurs when the incident radiation is absorbed by a scattering center and subsequently reemitted. Although the incident radiation may be in the form of a parallel beam, the reemitted radiation is scattered in all directions, and the amplitude of this scattered radiation is a function of the scattering angle. For incident radiation falling on a single scattering center, O, the scattering



process can be described as follows. If the incident radiation is in the form of a simple monochromatic wave then the displacement, y , of the incident wave varies with time as

$$y = B \cos(2\pi\nu t)$$

where ν = frequency of radiation
 B = amplitude

At some point of interest, P, a distance D from the scattering center, the scattered wave will have a displacement, y_s , which is a function of the distance D, the scattering process, and the scattering angle.

$$y_s = f_{2\theta} \left(\frac{B}{D} \right) \cos\{2\pi\nu(t - D/c) - \alpha_s\}$$

where c = velocity of propagation of the radiation
 D = distance between P and O
 α_s = phase shift due to scattering process
 $f_{2\theta}$ = scattering length - a proportionality constant with dimension of length; it is a function of the scattering angle

For mathematical convenience, this equation is generally written in complex form.

$$\begin{aligned}
 Y &= Y_o \exp(2\pi i v(t - x/c)) \\
 &= Y_o \cos(2\pi v(t - x/c)) + i Y_o \sin(2\pi v(t - x/c)) \\
 Y_s &= f_{2\theta} \left(\frac{B}{D}\right) \exp(2\pi i v(t - D/c) - i\alpha_s)
 \end{aligned}$$

The amplitude of the disturbance at P is

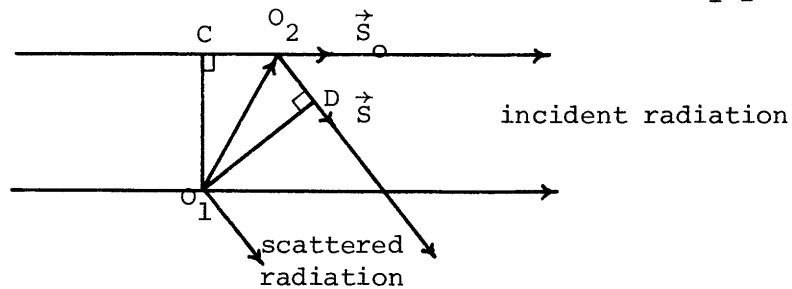
$$A_s = f_{2\theta} \left(\frac{B}{D}\right)$$

and the phase lag is $\alpha_{OP} = 2\pi v D/c + \alpha_s$

The intensity in power per unit solid angle is

$$I_{2\theta} = K A_s^2 \times D^2 = f_{2\theta}^2 K B^2$$

For a pair of identical point scatterers, the radiation arriving at a point P at some very large distance (with respect to $O_1 O_2$) from



O_1 will have been scattered from both O_1 and O_2 through effectively the same angle 2θ . Since the scatterers are identical, the scattering phase shift α_s will be the same for each. Thus the phase difference of radiation scattered at O_2 with respect to O_1 is

$$\alpha_{O_1 O_2} = \frac{-2\pi}{\lambda} (O_2 C + O_2 D)$$

If \vec{S}_0 and \vec{S} are unit vectors in the direction of the incident and the scattered radiation respectively, and \vec{r} is the vector connecting O_1 and O_2

$$\begin{aligned}
 O_2 C &= \vec{r} \cdot \vec{S}_0 & O_2 D &= -\vec{r} \cdot \vec{S} \\
 O_2 C + O_2 D &= 2 \vec{r} \cdot \frac{(\vec{S} - \vec{S}_0)}{\lambda}
 \end{aligned}$$

If \vec{s} is defined as $\frac{(\vec{s} - \vec{s}_0)}{\lambda}$ then $\alpha_{0,0_2} = 2\pi\vec{r}\cdot\vec{s}$

$$\begin{aligned}
 y_s &= f_{2\theta} \left(\frac{B}{D}\right) (\exp(2\pi i v_i(t - D/c) - i\alpha_s) \\
 &\quad + \exp(2\pi i v_i(t - D/c) - i\alpha_s + 2\pi i \vec{r}\cdot\vec{s})) \\
 &= f_{2\theta} \left(\frac{B}{D}\right) \{1 + \exp(2\pi i \vec{r}\cdot\vec{s})\} \exp\{2\pi i v_i(t - D/c) - i\alpha_s\} \\
 A_{2s} &= f_{2\theta} \left(\frac{B}{D}\right) \{1 + \exp(2\pi i \vec{r}\cdot\vec{s})\}
 \end{aligned}$$

As compared with a single unit, this equals

$$A_{2s} = A_s \{1 + \exp(2\pi i \vec{r}\cdot\vec{s})\}$$

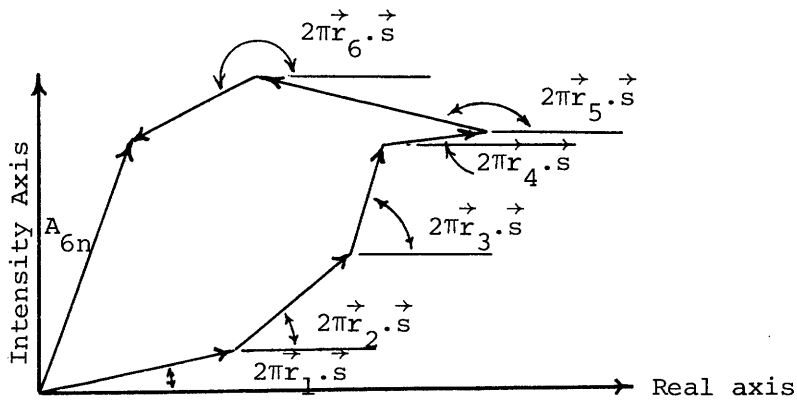
For a general distribution of identical point scatterers

$$A_{ns} = A_s \sum_1^n \exp(2\pi i \vec{r}_j \cdot \vec{s})$$

For non-identical scatterers

$$\begin{aligned}
 A_{ns} &= \sum_1^n A_{sj} \exp(2\pi i \vec{r}_j \cdot \vec{s}) \\
 &= \frac{B}{D} \sum_1^n (f_{2\theta})_j \exp(2\pi i \vec{r}_j \cdot \vec{s})
 \end{aligned}$$

This summation can be illustrated by a phase-vector diagram.



Electrons are the primary scattering units for x-rays. In crystals, however, these electrons are always bound in an atom and thus cannot be treated separately. The scattering must be described by the electron density in the atom. For this reason an atomic scattering factor, f_a , has been defined as the ratio of the amplitude of the coherent radiation from an atom to that from a single electron situated at the atomic center. This scattering factor is the sum of the contributions from all of the electrons in the atom and consequently, the greater the number of electrons in the atom, the greater the amplitude of the scattered radiation. For an array of identical atoms, the amplitude of the scattered radiation with respect to a point electron at the origin is

$$A_n = f_a \sum_1^n \exp(2\pi i \vec{r}_j \cdot \vec{s})$$

APPENDIX L - DIFFRACTION FROM A FINITE ONE-DIMENSIONAL ARRAY

A single row of n identical atoms forms a centrosymmetric arrangement of scatterers if the center of symmetry is taken as the origin. For a centrosymmetric arrangement, the amplitude of the scattered radiation reduces to merely the real component, the sum of the complex components being zero. If n is odd, and the center atom is taken as the origin

$$A_n = f_a \sum_{q=-\frac{1}{2}(n-1)}^{\frac{1}{2}(n-1)} \cos(2\pi q \vec{a} \cdot \vec{s})$$

where a = vector distance between atoms

This expression can be simplified as follows

$$\begin{aligned} A_n &= \frac{f_a}{2\sin(\pi \vec{a} \cdot \vec{s})} \left[2 \cos(2\pi q \vec{a} \cdot \vec{s}) \sin(\pi \vec{a} \cdot \vec{s}) \right. \\ &= \frac{f_a}{2\sin(\pi \vec{a} \cdot \vec{s})} \left\{ \sin(\pi n \vec{a} \cdot \vec{s}) - \sin(\pi(n-2) \vec{a} \cdot \vec{s}) \right. \\ &\quad \left. + \sin(\pi(n-2) \vec{a} \cdot \vec{s}) - \sin(\pi(n-4) \vec{a} \cdot \vec{s}) \right. \\ &\quad \left. + \dots + \sin(\pi(2-n) \vec{a} \cdot \vec{s}) - \sin(\pi(-n) \vec{a} \cdot \vec{s}) \right\} \end{aligned}$$

All the terms on the right cancel except for the first and last which gives

$$A_n = f_a \left(\frac{\sin(\pi n \vec{a} \cdot \vec{s})}{\sin(\pi \vec{a} \cdot \vec{s})} \right)$$

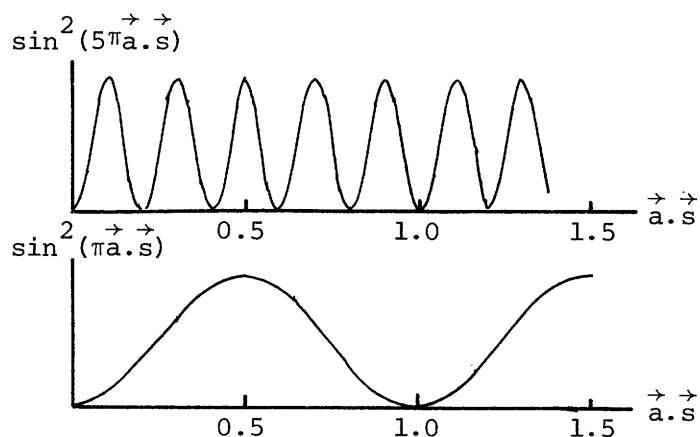
This equation will also hold for n even, provided the center of symmetry is taken as the origin. The intensity of the scattering is

$$(A_n)^2 = f_a^2 \frac{\sin^2(n\pi \vec{a} \cdot \vec{s})}{\sin^2(\pi \vec{a} \cdot \vec{s})} = (K_n)^2 f_a^2$$

When $\vec{a} \cdot \vec{s} = h$, where h is an integer, both $\sin^2(\pi n \vec{a} \cdot \vec{s})$ and $\sin^2(\pi \vec{a} \cdot \vec{s})$ are zero. The limit, however, can be taken as $\vec{a} \cdot \vec{s}$ approaches zero

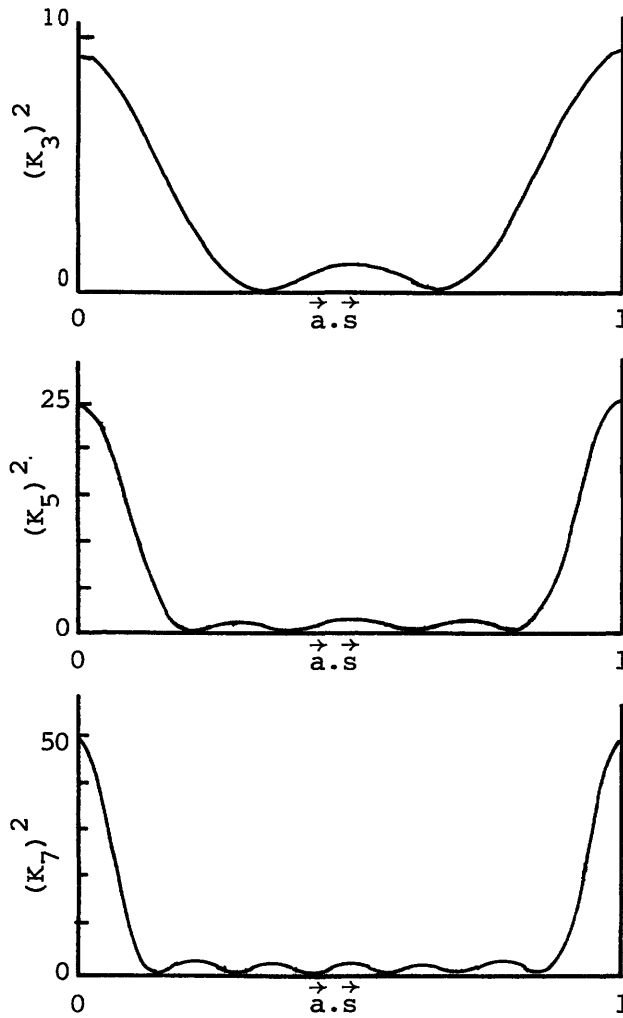
$$\lim_{x \rightarrow 0} \left| \frac{\sin^2(nx)}{\sin^2(x)} \right| = \frac{(nx)^2}{x^2} = n^2$$

The figures below show the two functions $\sin^2(\pi n \vec{a} \cdot \vec{s})$ and $\sin^2(\pi \vec{a} \cdot \vec{s})$ for $n = 5$.



The ratio of these two functions will be periodic, and the following general statements can be made with regard to $(K_n)^2$

- (1) The main maxima of $(K_n)^2$ occur whenever $\vec{a} \cdot \vec{s}$ equals an integer
- (2) Between the main maxima there are $n - 1$ minima, where $(K_n)^2$ is zero, and $n - 2$ subsidiary maxima.
- (3) The width of a main maximum is $2/n$ and the maxima therefore get narrower as n increases.
- (4) The main peak is twice as wide as the subsidiary ones.
- (5) The ratio of the heights of the main to subsidiary maxima increases as n increases.



The maxima of $(K_n)^2$ lie close to the maxima of $\sin^2(\pi n \vec{a} \cdot \vec{s})$ becoming closer the larger the value of n . As n tends to infinity, the positions of the maxima are therefore

$$\vec{a} \cdot \vec{s} = \frac{2m + 1}{2n} \quad m = 1 \text{ to } n-2$$

The height of the first subsidiary peak equals

$$(K_n)^2_{3/2n} = \frac{\sin^2(\pi n((3/2n)))}{\sin^2(\pi 3/2n)} \approx \frac{4n^2}{9}$$

The ratio of this height to the main peak is

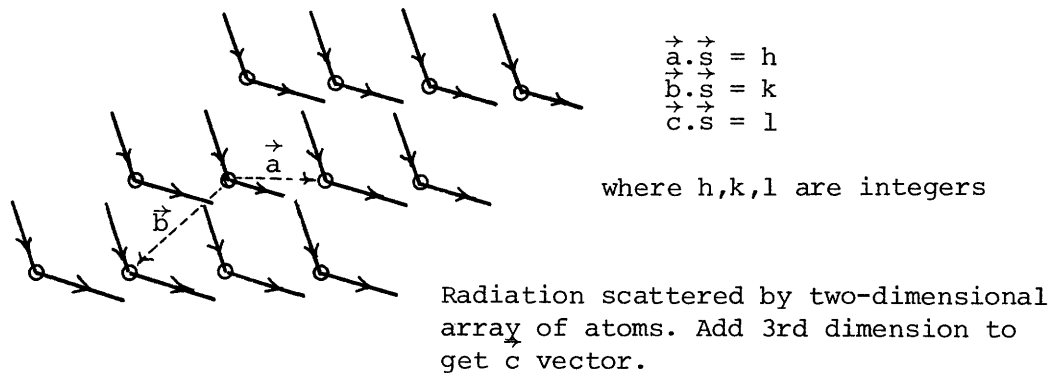
$$\frac{(K_n)^2}{(K_0)^2} \frac{3/2n}{9\pi^2} = \frac{4}{9\pi^2} = 0.045$$

For $n \rightarrow \infty$ there is no significant diffracted intensity except under the condition that $\vec{a} \cdot \vec{s} = h$ (an integer). This is equivalent to the physical argument that reinforcement of scattered radiation from neighboring atoms occurs when the path difference is a multiple of the wavelength.

$$\frac{1}{\lambda} (\vec{r} \cdot \vec{S} - \vec{r} \cdot \vec{S}_0) = h \quad \text{or} \quad \vec{r} \cdot \vec{s} = h$$

APPENDIX M - SCATTERING FROM A 3-DIMENSIONAL ARRAY

In a 3-dimensional array of identical atoms, three non-parallel vectors, \vec{a} , \vec{b} , and \vec{c} , can be used to define the interatomic spacings. For scattered radiation to produce constructive interference, three separate equations must therefore be satisfied simultaneously. These equations are known as the Laue equations.



If three new vectors are defined as follows

$$\begin{aligned} \vec{a} \cdot \vec{a}^* &= 1 & \vec{a}^* \cdot \vec{b} &= \vec{a}^* \cdot \vec{c} = 0 \\ \vec{b} \cdot \vec{b}^* &= 1 & \vec{b}^* \cdot \vec{a} &= \vec{b}^* \cdot \vec{c} = 0 \\ \vec{c} \cdot \vec{c}^* &= 1 & \vec{c}^* \cdot \vec{a} &= \vec{c}^* \cdot \vec{b} = 0 \end{aligned}$$

These three vectors will define a space lattice which is given the name reciprocal lattice. A reciprocal lattice point can be defined by the vector $h\vec{a}^* + k\vec{b}^* + l\vec{c}^*$ where h , k , and l are three integers (Miller indices). From the above definitions, the following relations must be true.

$$\begin{aligned} (h\vec{a}^* + k\vec{b}^* + l\vec{c}^*) \cdot \vec{a} &= h \\ (h\vec{a}^* + k\vec{b}^* + l\vec{c}^*) \cdot \vec{b} &= k \end{aligned}$$

$$(\vec{h}\vec{a}^* + \vec{k}\vec{b}^* + \vec{l}\vec{c}^*) \cdot \vec{c} = 1$$

Comparing these relations to the Laue equations indicates that $\vec{h}\vec{a}^* + \vec{k}\vec{b}^* + \vec{l}\vec{c}^*$ is a possible value of \vec{s} satisfying the Laue equations for the indices (hkl).

The past discussion has considered only arrays of identical atoms. In a 3-dimensional crystal structure there may be several different atoms per unit cell, and the crystal can be pictured as a close-packed 3-dimensional array of these unit cells. The scattering of any atom A with respect to an electron at the origin of the cell it occupies is $f_A \exp(2\pi i \vec{r}_A \cdot \vec{s})$, and this same ratio will hold for all atoms A with respect to electrons at the respective origins. The total scattered amplitude from the crystal will thus be that from an array of electrons, one at each unit cell origin, multiplied by a factor.

$$f_A \exp(2\pi i \vec{r}_A \cdot \vec{s}) + f_B \exp(2\pi i \vec{r}_B \cdot \vec{s}) + f_C \exp(2\pi i \vec{r}_C \cdot \vec{s}) \text{ etc.}$$

where A, B, C are atoms in the unit cell.

This leads to the definition of the structure factor F_{hkl}

$$F_{hkl} = \sum_1^N f_j \exp(2\pi i \vec{r}_j \cdot \vec{s})$$

where N = number of atoms in the unit cell

The unit cell edges have been previously defined by vectors a, b, and c, and the vector position of an atom in the unit cell can therefore be given as

$$\vec{r} = x\vec{a} + y\vec{b} + z\vec{c}$$

Using this equation plus the previous equation for s results in

$$F_{hkl} = \sum_1^N f_j \exp(2\pi i \vec{r}_j \cdot \vec{s})$$

$$= \sum_1^N f_j \exp(2\pi i(x_j \vec{a} + y_j \vec{b} + z_m \vec{c}) \cdot (h\vec{a}^* + k\vec{b}^* + l\vec{c}^*))$$

which reduces to

$$F_{hkl} = \sum_1^N f_j \exp(2\pi i(hx_j + ky_j + lz_j))$$

APPENDIX N - ABBERATIONS IN PEAK POSITION DUE TO ABSORPTION AND FLAT SPECIMEN

For a crystalline material with known molecular composition and unit cell, the total absorption coefficient, μ , is given as

$$\mu = \frac{n}{V_c} \sum (\mu_a)_i$$

where V_c = volume of unit cell (cm^3)

n = number of molecules in unit cell

μ_a = atomic absorption coefficient (these are tabulated in International Tables for X-ray Crystallography, Vol. III)

For carbon, $\mu_C = 9.17 \times 10^{-23} \text{ cm}^2$; oxygen, $\mu_O = 30.5 \times 10^{-23} \text{ cm}^2$; and hydrogen, $\mu_H = 0.073 \times 10^{-23} \text{ cm}^2$. (n/V_c) is nearly equal for both the pure solid and the clathrate, thus the calculations will be made for the pure solids where $(n/V_c)_{\text{H}_2\text{O}} = 3.1 \times 10^{22} \text{ cm}^{-3}$ and $(n/V_c)_{\text{CH}_3\text{OH}} = 1.9 \times 10^{22} \text{ cm}^{-3}$. This results in $\mu_{\text{H}_2\text{O}} = 9.5$ and $\mu_{\text{CH}_3\text{OH}} = 7.6$.

To determine the shift in the peak position due to absorption and flat specimen aberrations, Wilson (1950) gives the following solution. The shift of the peak to smaller 2θ expressed in radians is given by the smallest value of the three expressions.

$$\Delta 2\theta \begin{cases} = L^2 \sin(2\theta/4R^2) & L = 2\alpha R/\sin\theta \\ = 0.428 \sin(2\theta/\mu R) \\ = 2t \cos(\theta/R) \end{cases}$$

where $\Delta 2\theta$ = shift in position of peak maximum in radians
 μ = total absorption coefficient as calculated above
 R = distance from specimen to radiation detector
 (15 cm for the diffractometer in this study)

2α = (radians) full angle aperture of the primary beam in the plane of Bragg focusing ($3^\circ = 0.0524$ rad. for this study)

t = thickness of specimen (0.1 cm)

For both ice and solid methanol, the second expression is dominant.

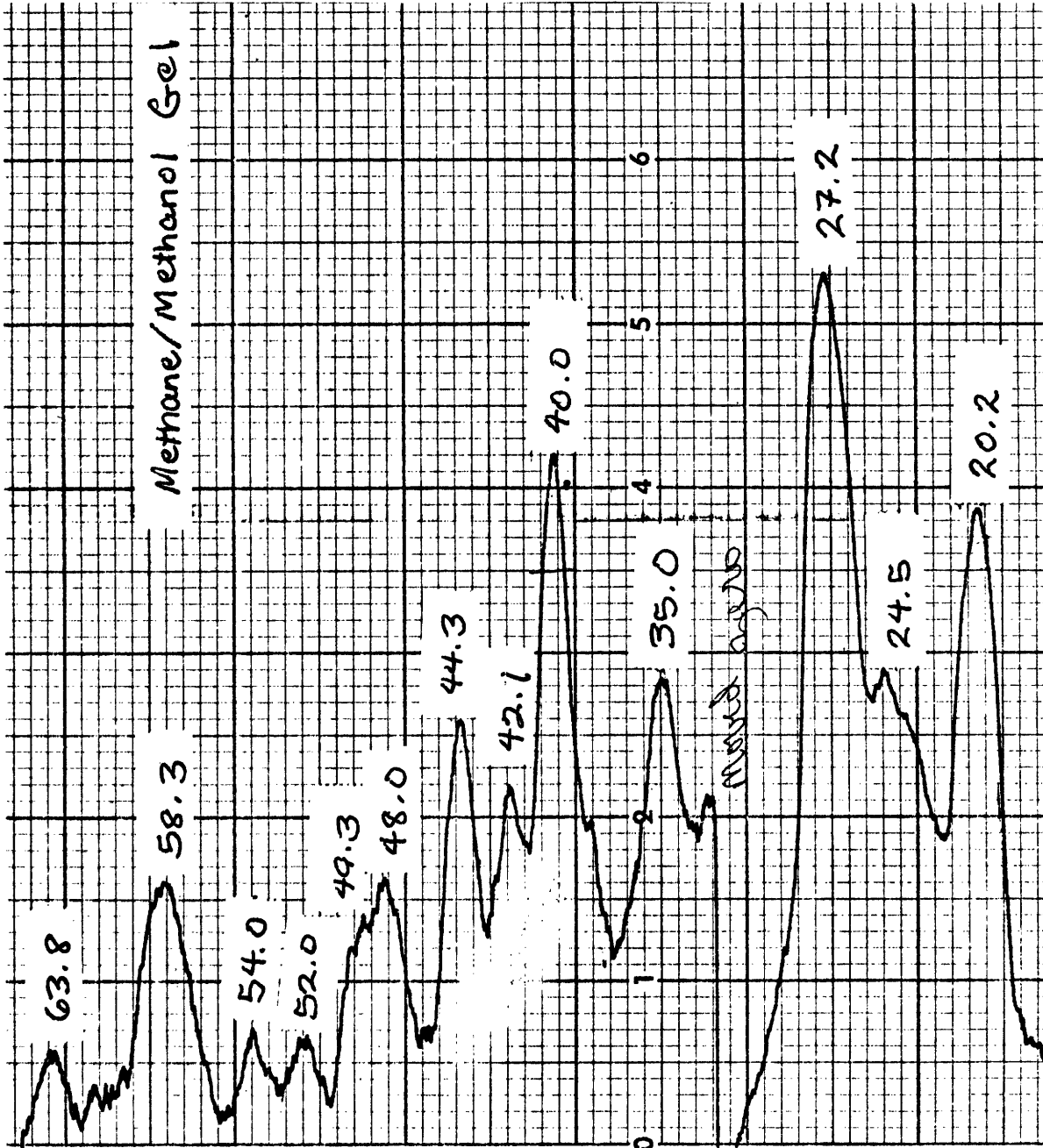
The range of $\Delta 2\theta$ for ice is 0.06° @ $2\theta = 20^\circ$ and 0.13° @ $2\theta = 50^\circ$,

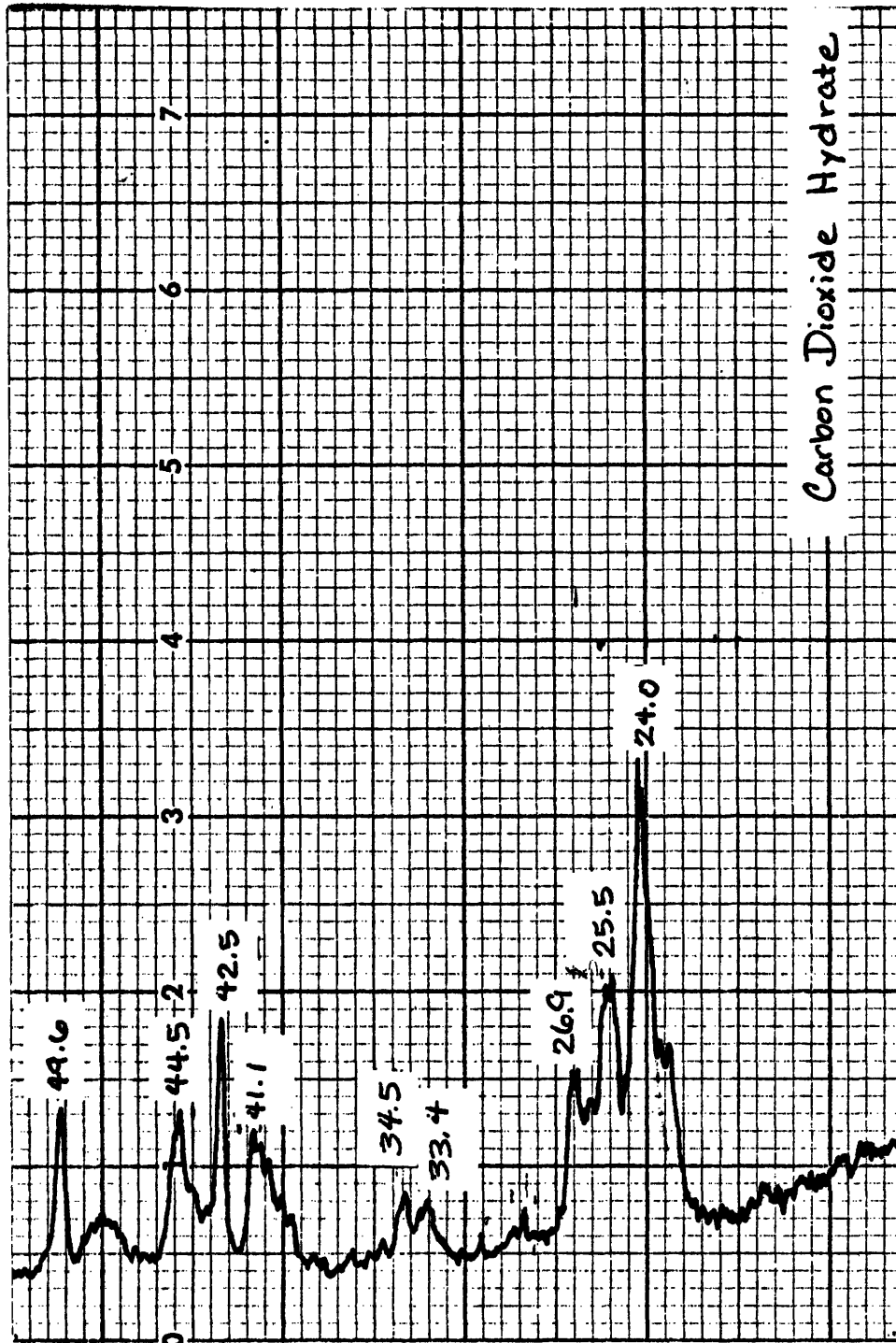
for solid methanol is 0.07° @ $2\theta = 20^\circ$ and 0.19 @ $2\theta = 60^\circ$.

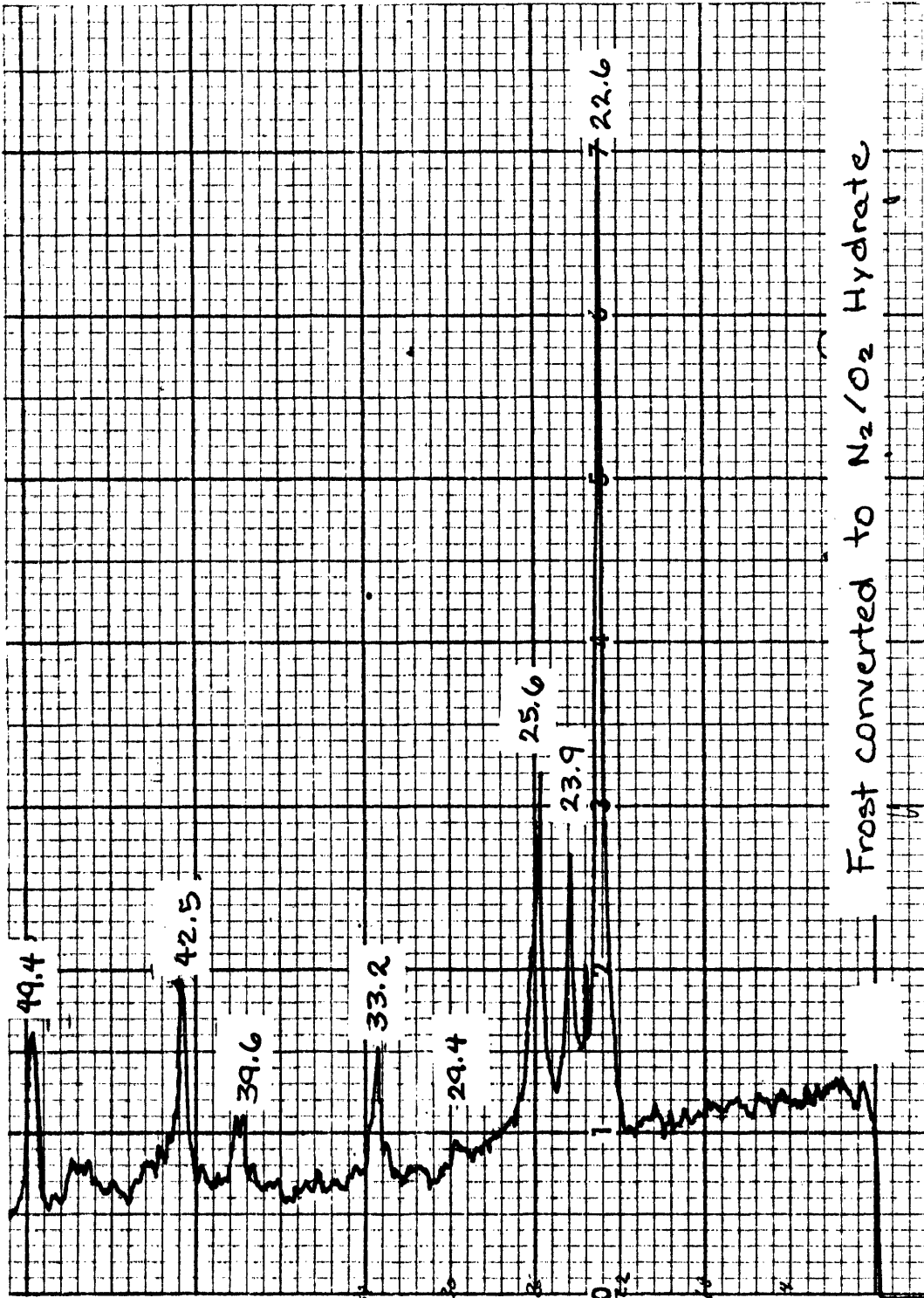
APPENDIX O - X-RAY DIFFRACTION DATA FOR LNG GELS

The following pages contain the x-ray diffraction patterns obtained for liquid methane/water and liquid methane/methanol gels. Also included are the patterns obtained for the carbon dioxide/water clathrate and air/water clathrate. The value associated with each peak is its reflection angle, 2θ .









APPENDIX P - ESTIMATION OF DIFFUSION EFFECTS

$$\begin{aligned} \text{Flux} &= AD \left(\frac{dc}{dx} \right) \leq 1 \text{ cm}^3/\text{hr} \text{ (273 K, 1 atm.)} = 8.2 \times 10^{18} \text{ molecules/hr} \\ &= 2.3 \times 10^{15} \text{ molecules/sec} \end{aligned}$$

Near equilibrium the concentration difference within the pore is likely to be the same order of magnitude as the concentration outside of the pore.

$$\begin{aligned} \Delta c &= \frac{(250/760) \text{ atm } 6.02 \times 10^{23} \text{ molecules/mole}}{(82 \text{ atm cm}^3/\text{mole K}) (163 \text{ K})} \\ &= 1.48 \times 10^{19} \text{ molecules/cm}^3 \end{aligned}$$

$$\begin{aligned} \text{Flux} = 2.3 \times 10^{15} \text{ molecules/sec} &= \left(\frac{A}{L} \right) \text{ cm } D (\text{cm}^2/\text{sec}) (1.48 \\ &\quad \times 10^{19} \text{ molecules/cm}^3) \end{aligned}$$

The diffusion coefficient, D, was estimated using the following expression.

$$\frac{PD}{(P_c)^{2/3} (T_c)^{5/6} (2/M)^{1/2}} = 2.75 \times 10^{-4} \left(\frac{T}{T_c} \right)^{1.82}$$

(Bird, Steward, and Lightfoot,
1960)

For P = .333 atm. and T = 163 K

$$D = .22 \text{ cm}^2/\text{sec}$$

$$2.3 \times 10^{15} = \frac{A}{L} (.22) (1.48 \times 10^{19})$$

$$\frac{A}{L} = 7.06 \times 10^{-4}$$

A maximum pore length of 1 cm is assumed resulting in

$$A = 7.06 \times 10^{-4} \text{ cm}^2 \quad (\text{total pore cross-sectional area})$$

$$\text{Total pore volume} = AL = 7.06 \times 10^{-4} \text{ cm}^3$$

For an average pore concentration of 1.5 (1.48×10^{19})

$$1.5(7.06 \times 10^{-4})(1.48 \times 10^{19}) = 1.57 \times 10^{16} \text{ molecules withheld in pores}$$

The total number of enclathrated molecules for a .1 gm. sample of H_2O is

$$\frac{.1 \text{ gm} (6.02 \times 10^{23} \text{ molecules/mole})}{(18 \text{ gm/g mole}) (7 \text{ moles } \text{H}_2\text{O/mole } \text{CH}_4)} = 4.8 \times 10^{20} \text{ molecules in sample}$$

Thus possible pore entrapment is negligible.

To estimate possible multilayer adsorption within pores, a cylindrical pore is assumed. Also a small pore radius is likely, and is assumed to be 20 Å.

$$\# \text{ of pores} = \frac{7.06 \times 10^{-4} \text{ cm}^2}{\pi (2.0 \times 10^{-7} \text{ cm})^2} = 5.62 \times 10^9 \text{ pores}$$

$$\begin{aligned} \text{total pore surface area} &= (5.6 \times 10^9) 2\pi (1.5 \times 10^{-7} \text{ cm}) (1 \text{ cm}) \\ &= 7.0 \times 10^3 \text{ cm}^2 \end{aligned}$$

If an extra layer is adsorbed on this area because diffusion has hindered the emptying of the pores, the number of extra adsorbed molecules would be

$$\frac{7.0 \times 10^3 \text{ cm}^2}{1.6 \times 10^{-15} \text{ cm}^2/\text{CH}_4 \text{ molecule}} = 4.4 \times 10^{18} \text{ molecules}$$

APPENDIX Q - BINGHAM YIELD STRESS FUNCTIONALITY

WHEN HYDROGEN BONDING IS THE PRIMARY ATTRACTIVE INTERACTION

The proportionality for τ_B based on van der Waals attraction was given as

$$\tau_B \propto \frac{A \phi_p^2}{D^2 r}$$

Van der Waals attractive energy (Chapter 2) was given as

$$V_v = \frac{-Ar}{12D}$$

Van der Waals attractive force can be obtained by taking the derivative of V_v with respect to D .

$$F_v = \frac{Ar}{12D^2}$$

Therefore,

$$\tau_B \propto \frac{F_v \phi_p^2}{r^2} = \frac{V_v \phi_p^2}{r^2 D}$$

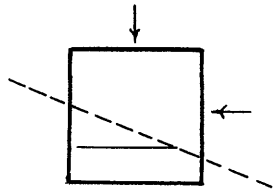
If hydrogen bonding dominates, then V_v can be replaced by a multiple of the hydrogen bond energy

$$\tau_B \propto \frac{n(E_{HY}) \phi_p^2}{r^2 D}$$

where n = number of hydrogen bonds formed between two particles

APPENDIX R - MAXIMUM SHEAR FORCE MEASURED BY BUILDUP ON A DISK

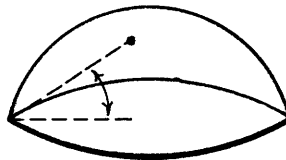
Gel buildup on a disk will be similar to a pile of sand except for one basic difference. For a gel peak, both the radial stress and the angular stress are expected to be negligible in comparison to the vertical component, ρgH , where H is the hydrostatic head above the differential element. Although such angular forces may be transmitted through interparticle contacts, it is likely to be quite small due to the small particle volume fraction in the gel. In two-dimensional geometry, the shear for an arbitrary plane is given as follows



$$\sigma_{\alpha} = \frac{\sigma_1 + \sigma_3}{2} + \frac{\sigma_1 - \sigma_3}{2} \cos 2\alpha$$

$$\tau_{\alpha} = \frac{\sigma_1 - \sigma_3}{2} \sin 2\alpha$$

The shear planes of interest will be those accessible to rupture or sliding flow. For any point within the gel peak, the maximum angle plane will be defined by the line connecting this point and the edge, i.e. the plane angle must be $\leq \beta$.



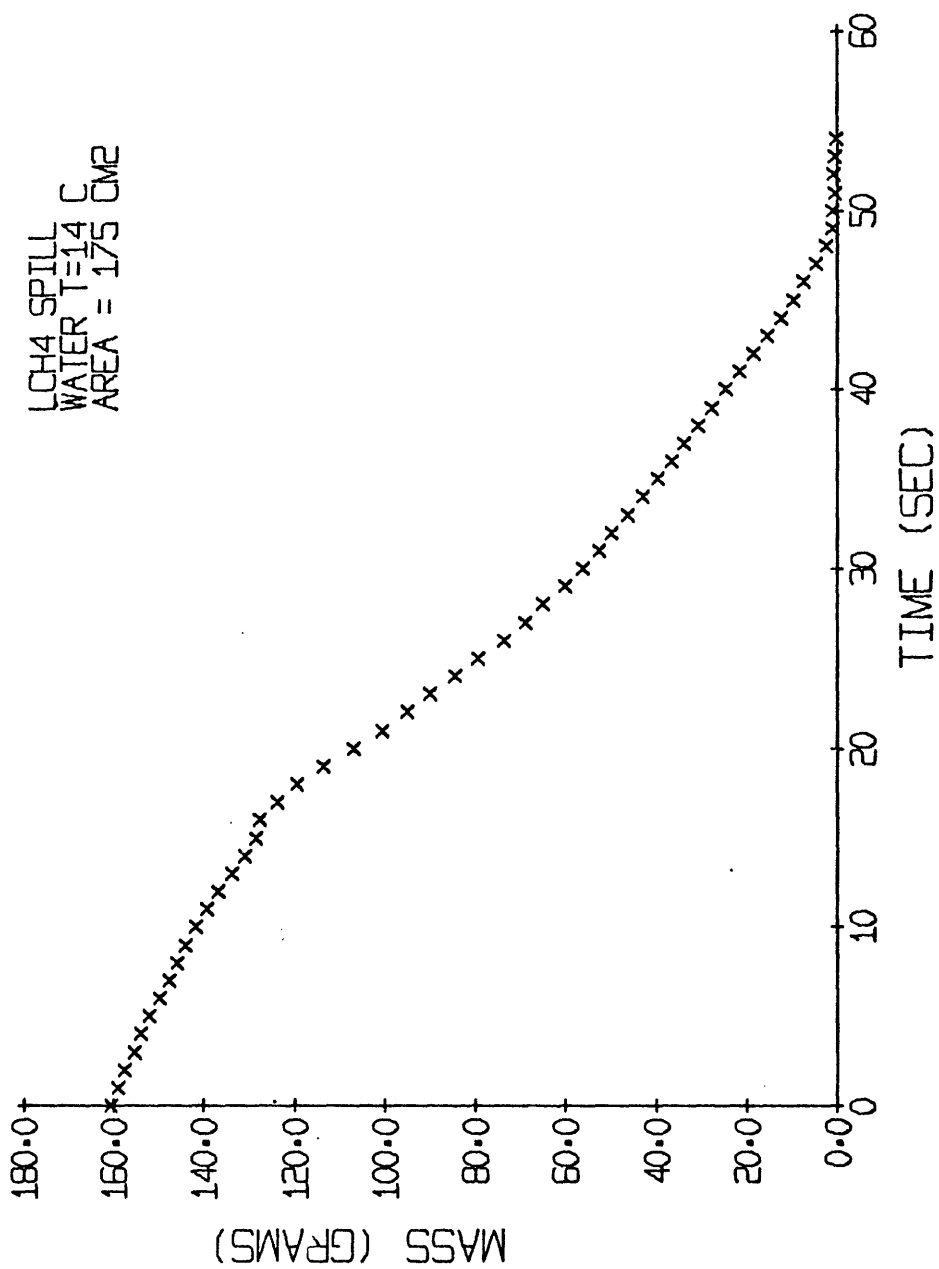
The maximum shear at any given depth will correspond to a 45° angle.

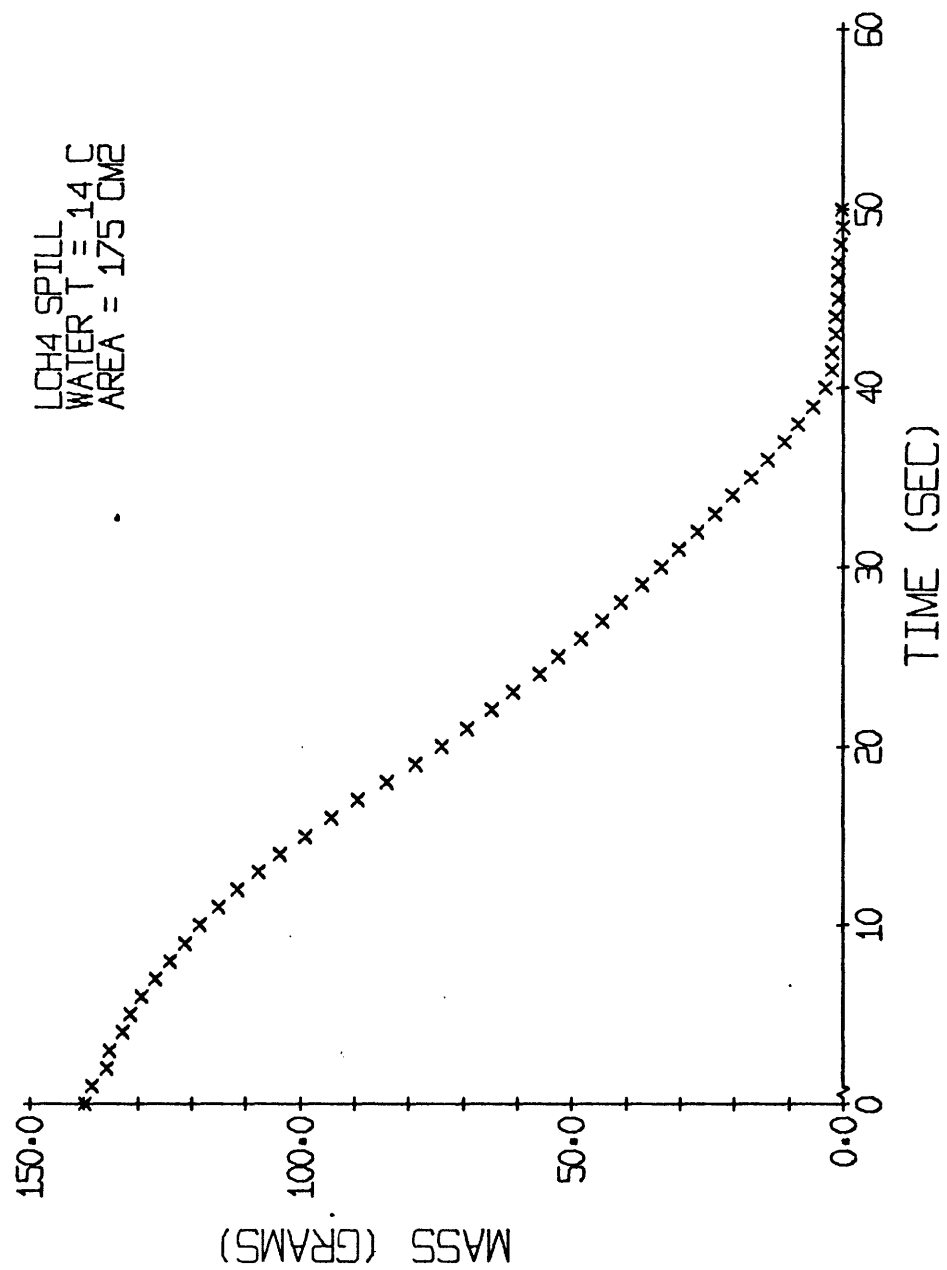
For the simplest geometry, a cylinder of gel, the maximum hydrostatic head will be ρgH , and the maximum shear will then be $0.49 \rho gH$. For a geometry other than a cylinder, the maximum shear stress will be less than this. If the geometry is spherical the maximum shear stress will be $\approx 0.36 \rho gH$. The actual geometries observed were in between these two, and thus the expected maximum shear stress was $0.36 \rho gH \leq \tau \leq 0.49 \rho gH$.

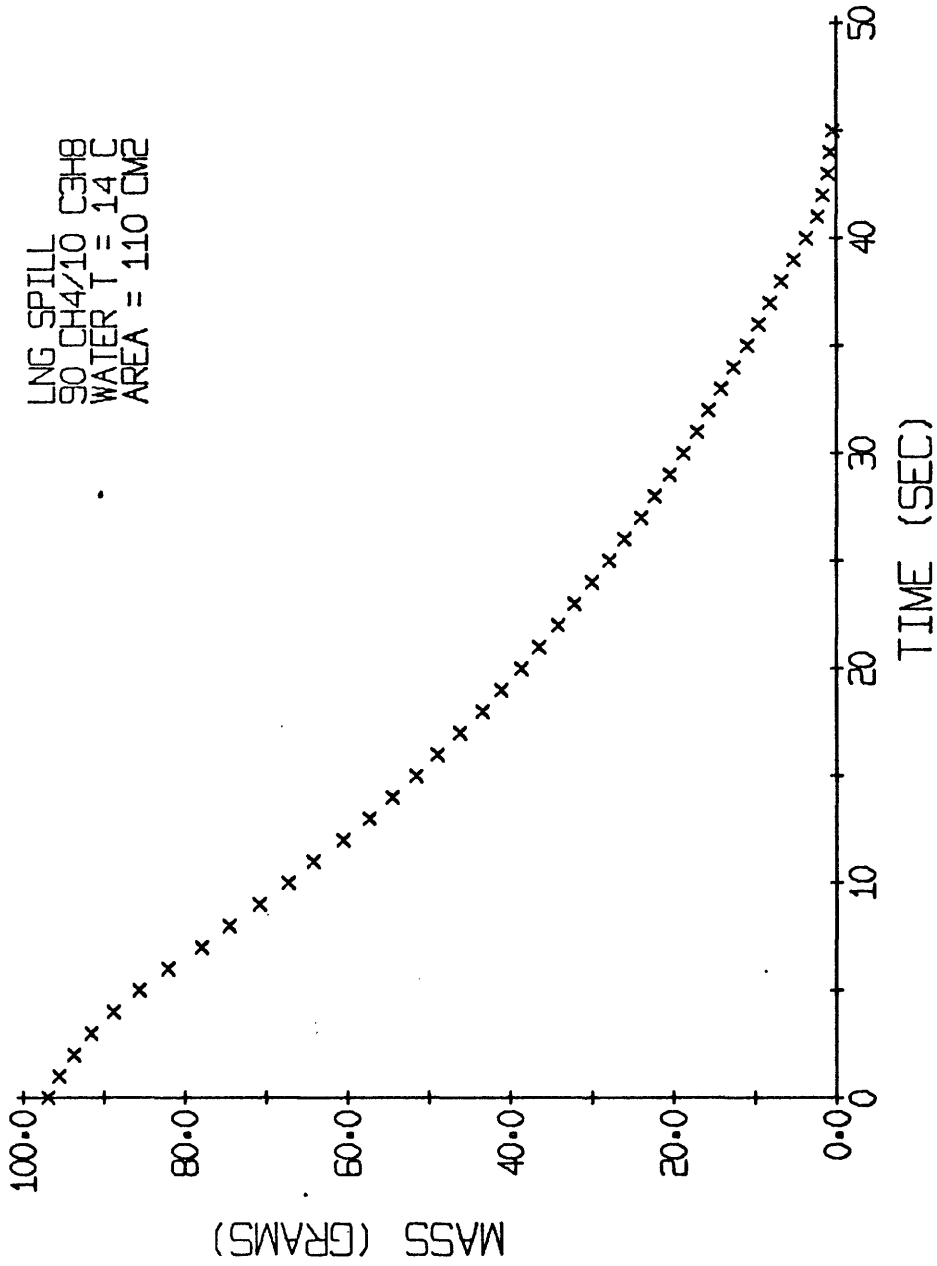
APPENDIX S - BOIL-OFF DATA FOR LNG GELS

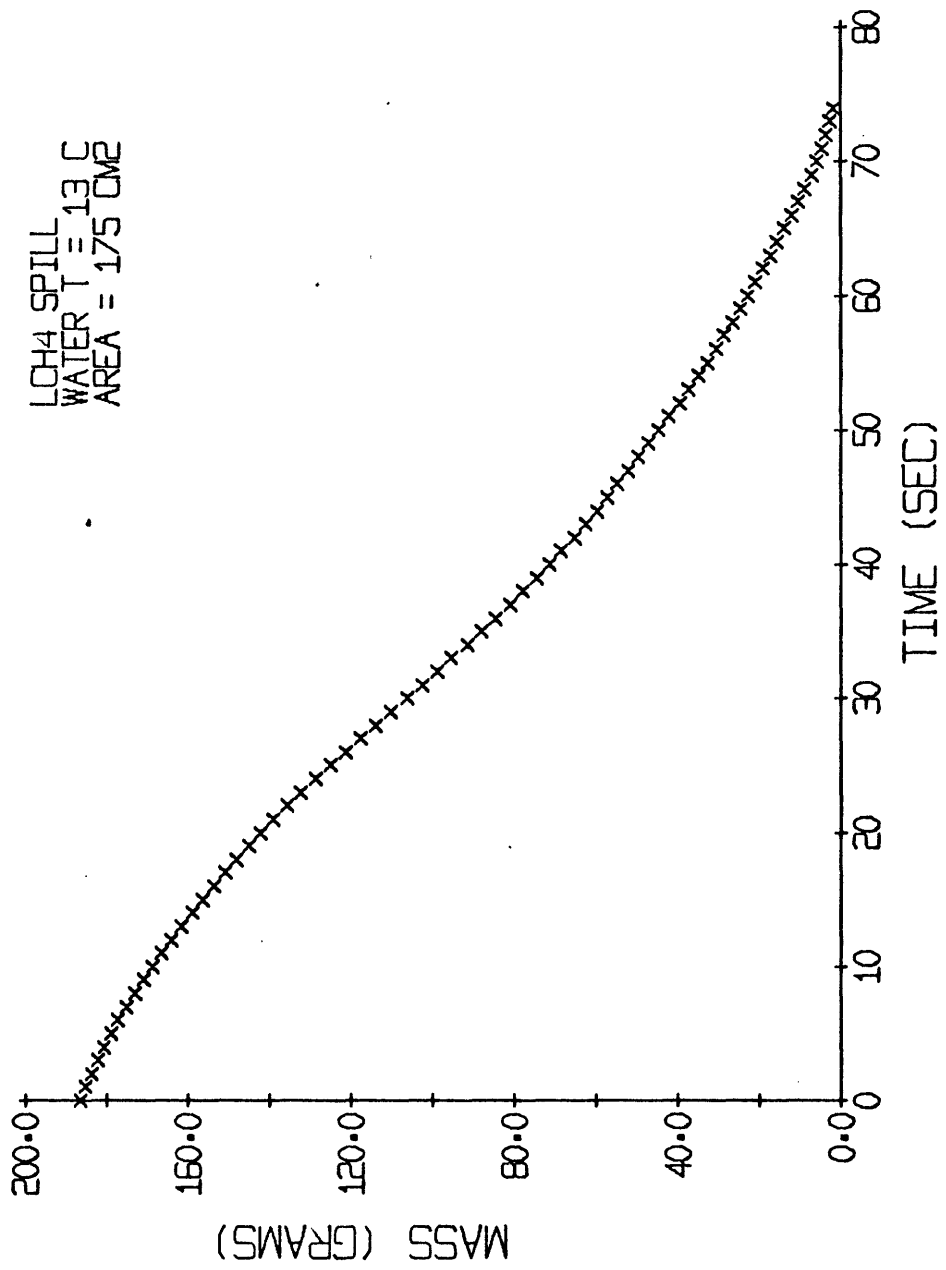
The succeeding pages contain the original mass versus time data for liquid methane, LNG, and LNG gels spilled on water.

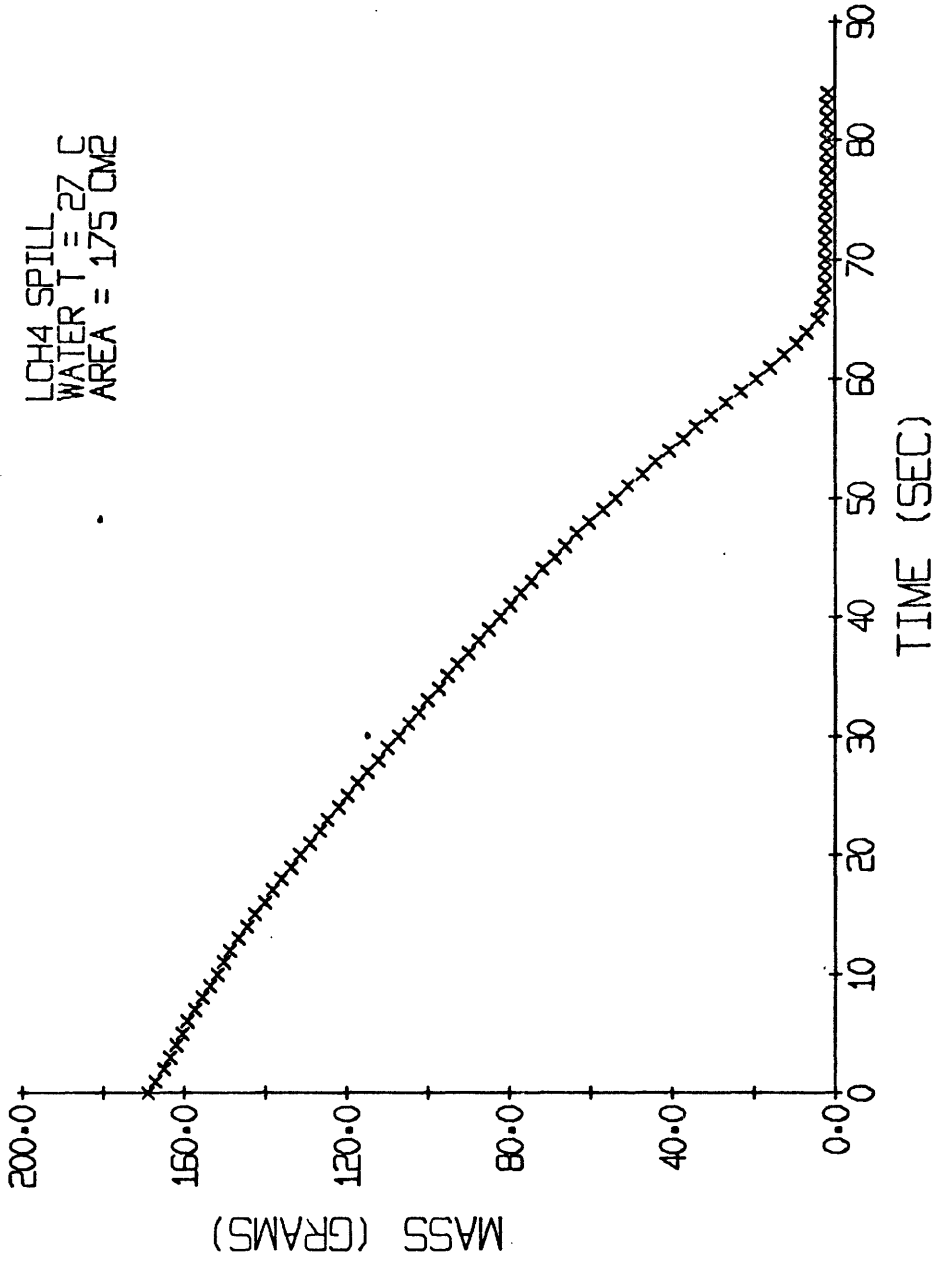
Notation: PT = percent
 YS = yield stress (static)



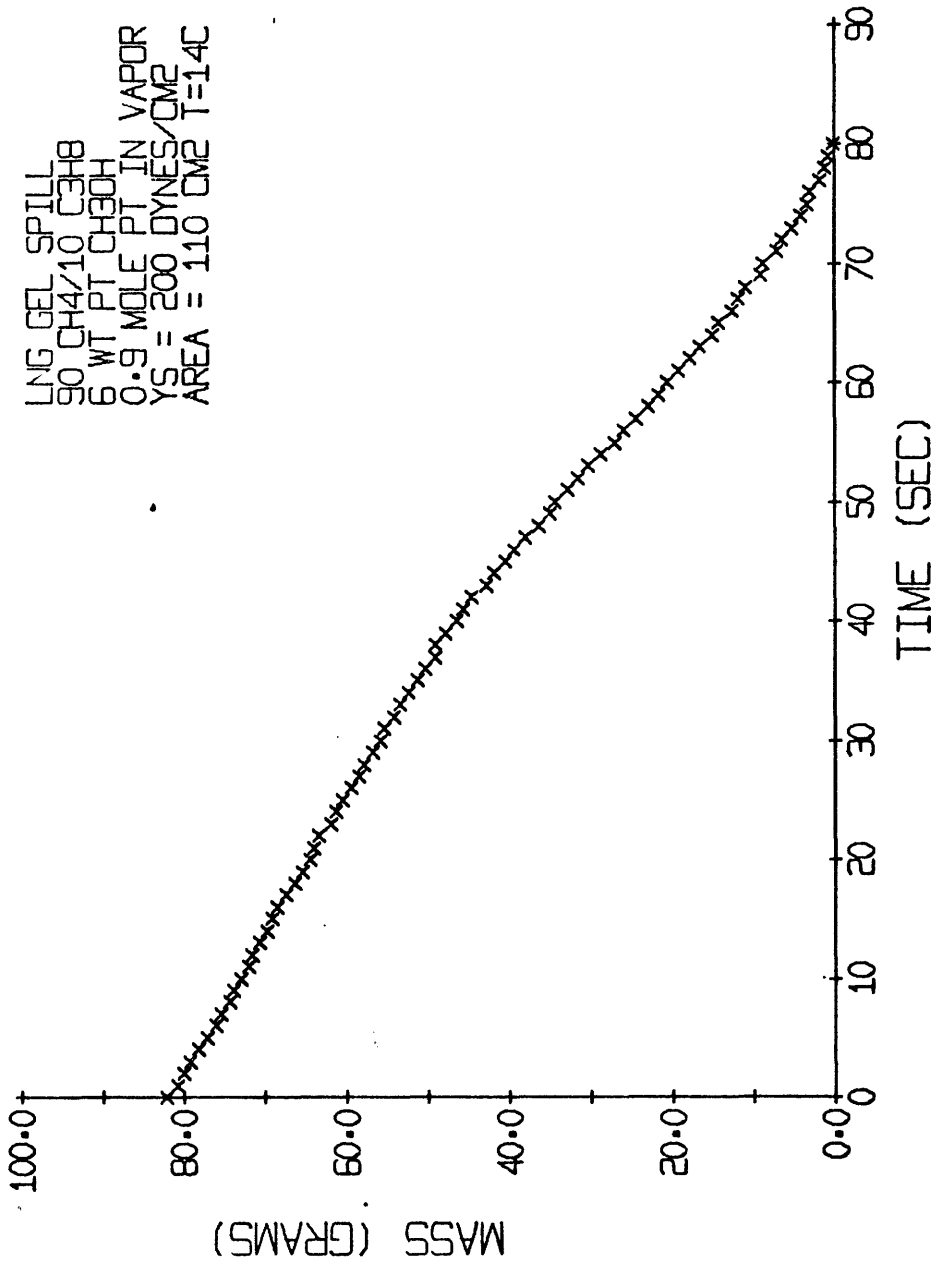


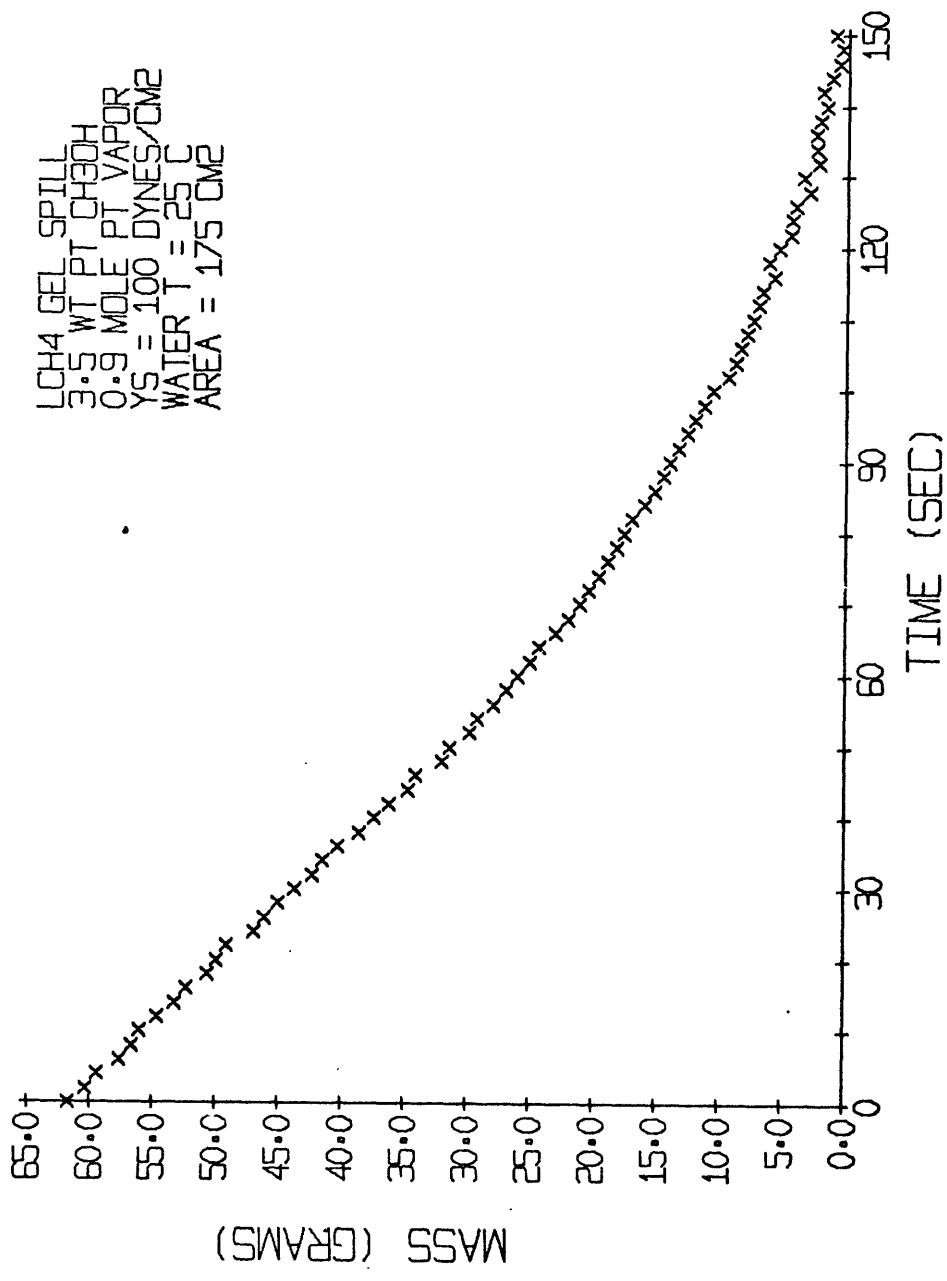


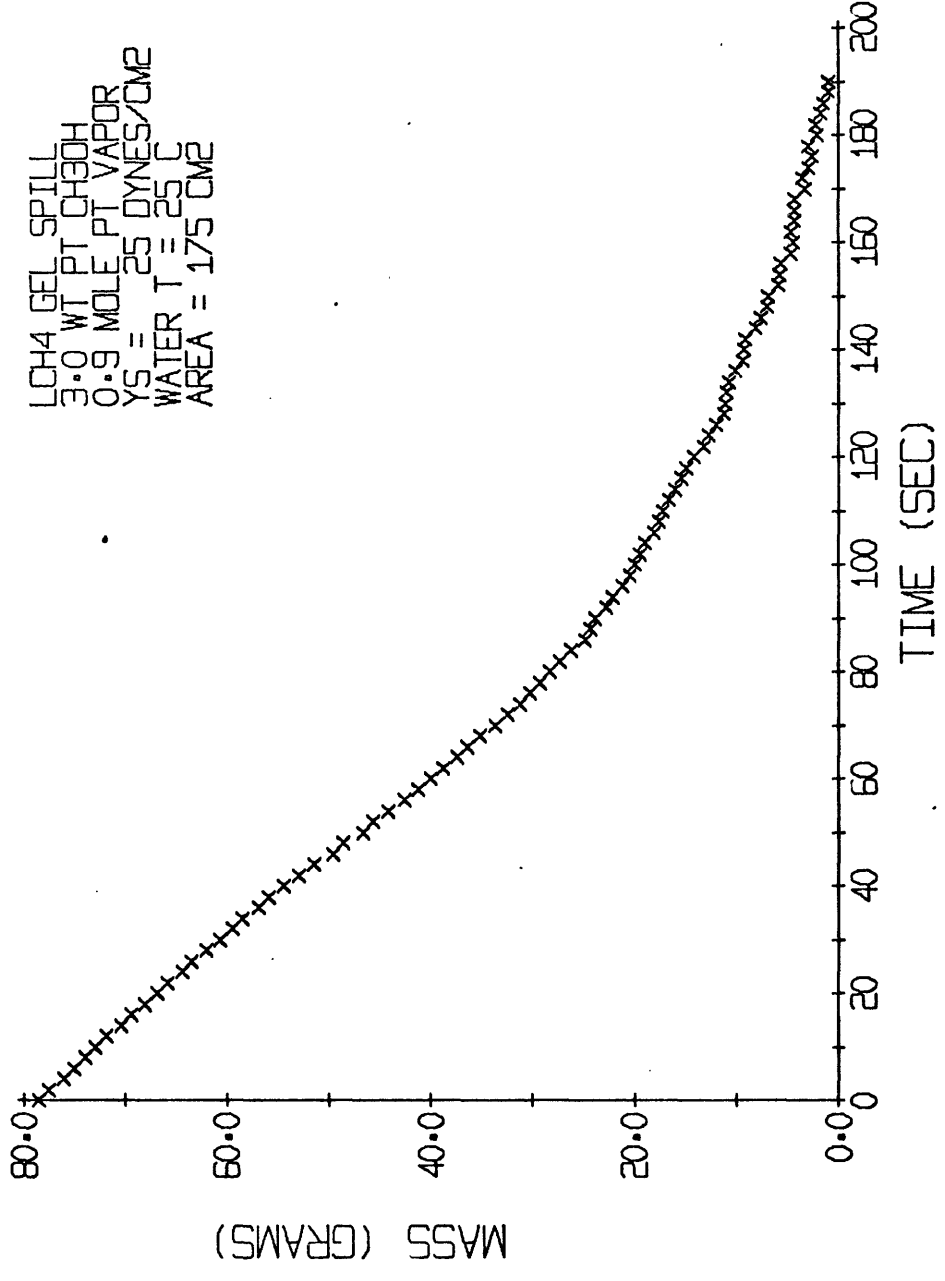




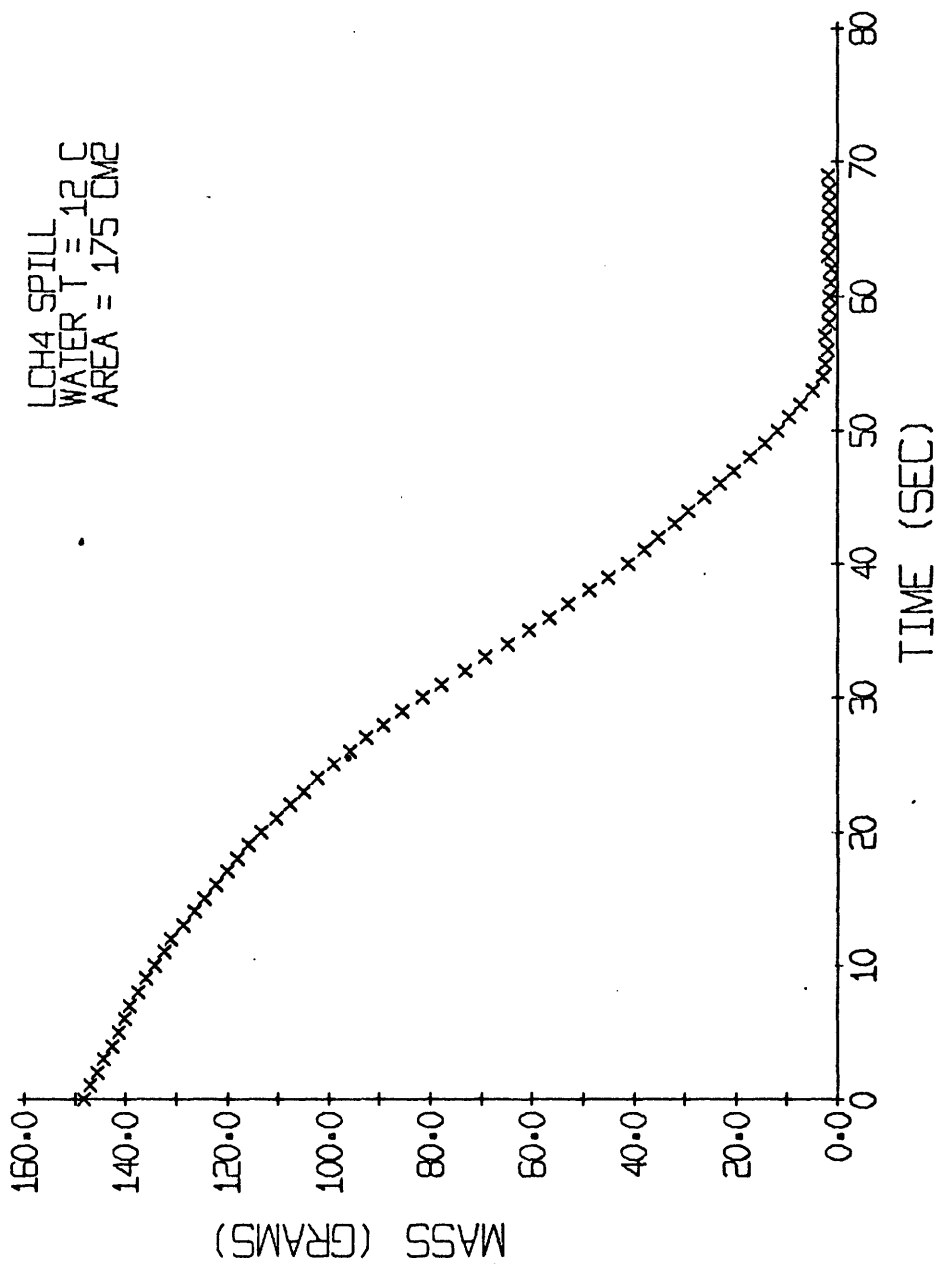
LNG GEL SPILL
90 CH4/10 C3H8
6 WT PT CH3OH
0.9 MOLE PT IN VAPOR
YS = 200 DYNES/CM2
AREA = 110 CM2 T=14C



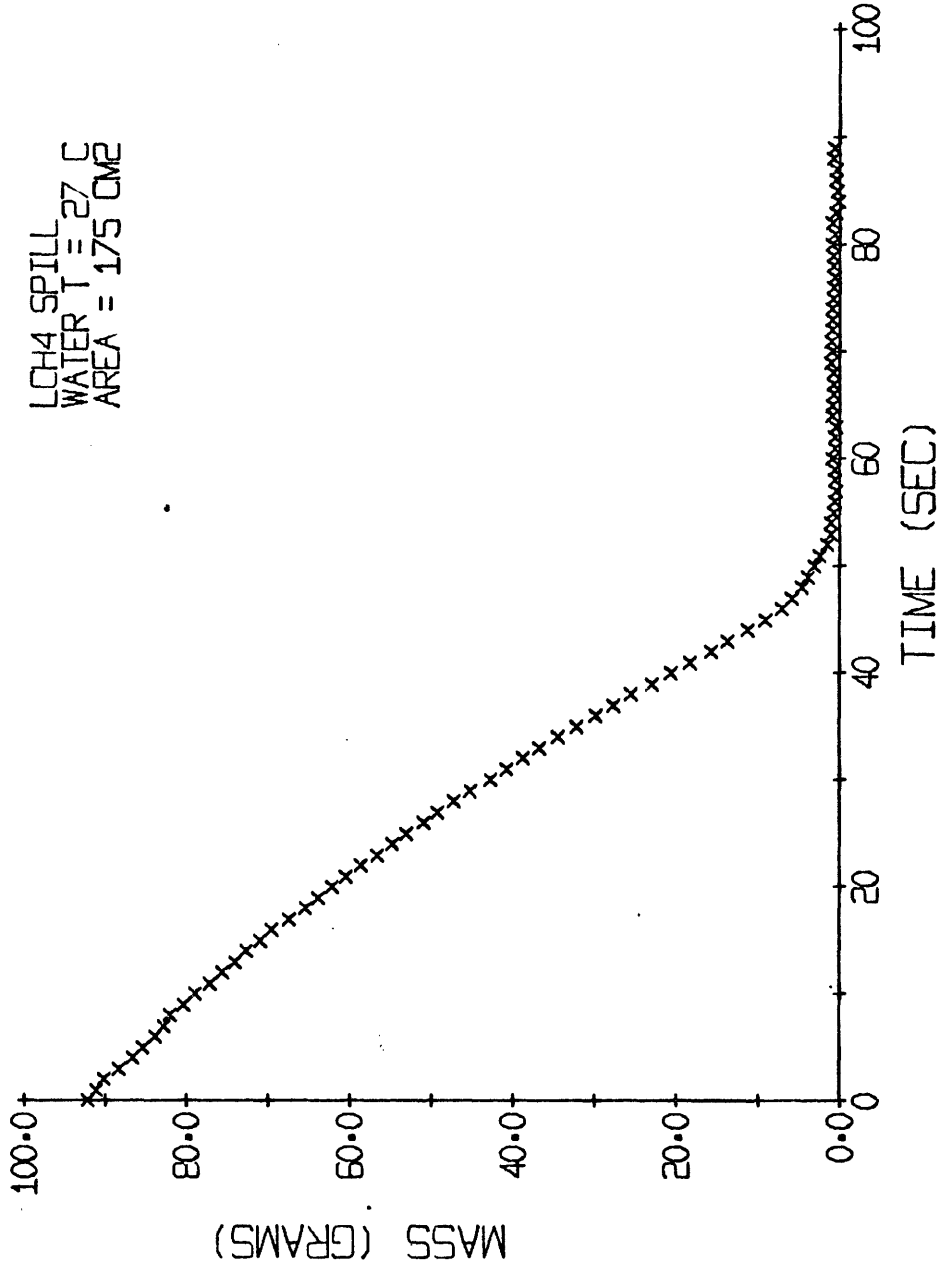


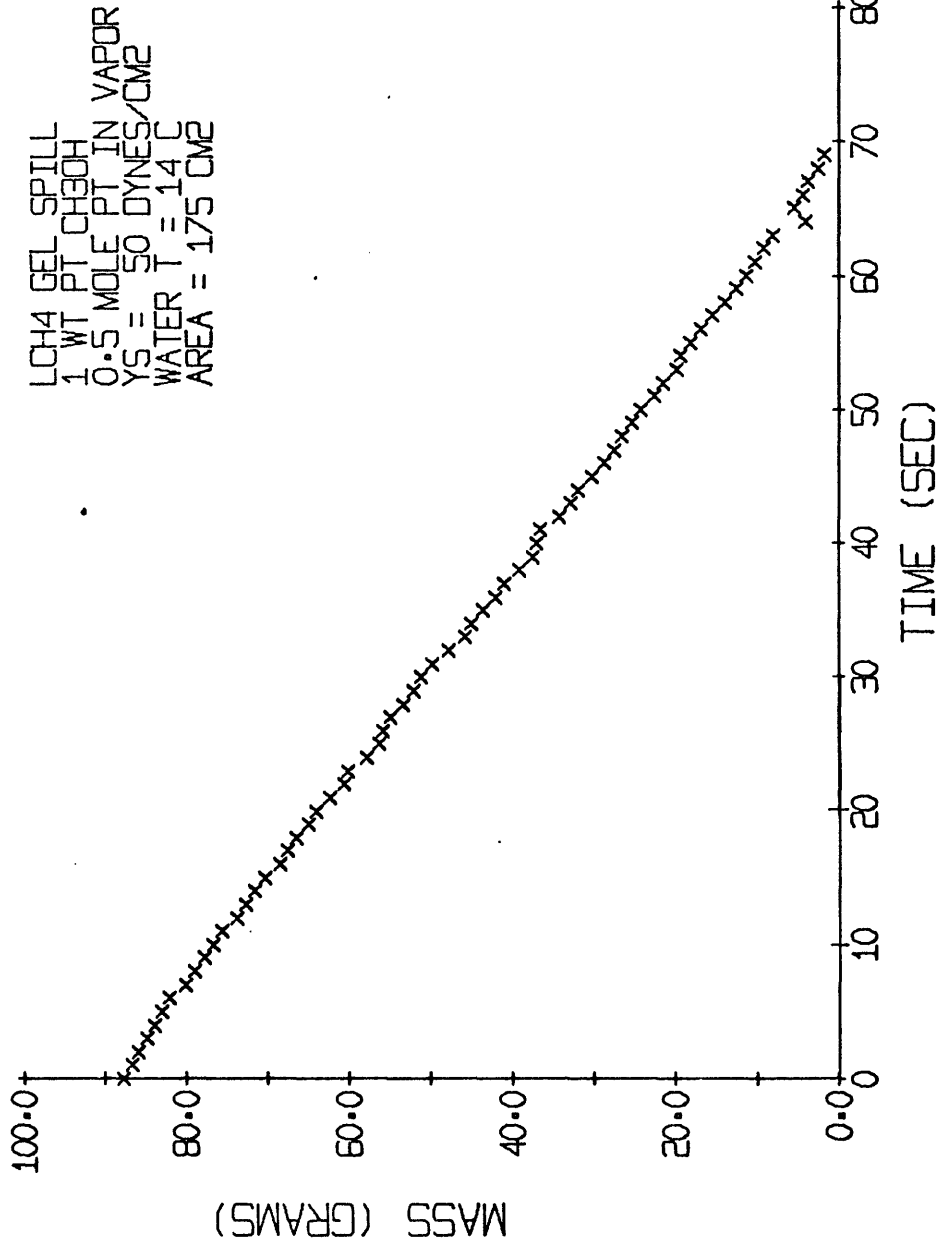


LCH4 SPILL
WATER T = 12 C
AREA = 175 CM2

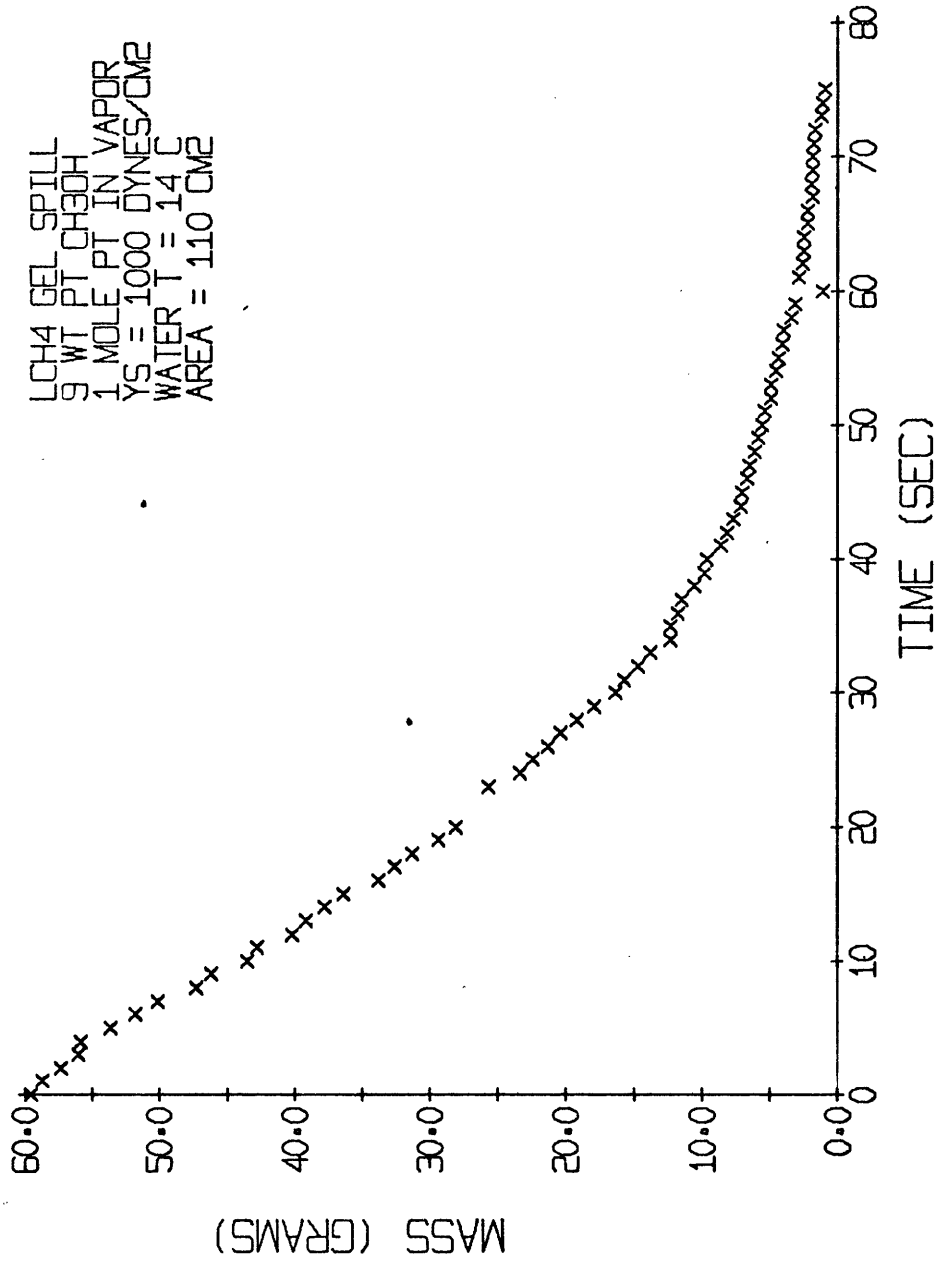


LCH4 SPILL
WATER T = 27 C
AREA = 175 CM2

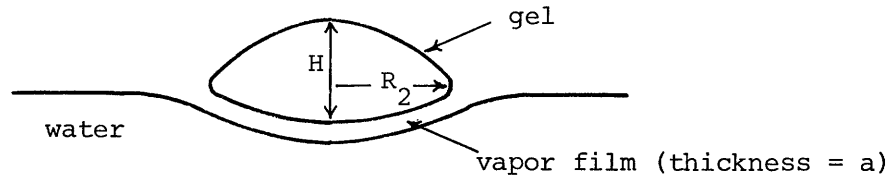




LCH4 GEL SPILL
9 WT PT CH3OH
1 MOLE PT IN VAPOR
YS = 1000 DYNES/CM2
WATER T = 14 C
AREA = 110 CM2



APPENDIX T - LNG GEL MODELED AS A VAPORIZING SOLID



Assumption: Vapor film thickness, a , is constant over entire contact area.

The total heat flux is $q = \pi R_1^2 k a \Delta T$

where R_1 represents the length of the vapor film in the radial direction. This will be slightly greater (10 to 20 percent) than the radius of the gel.

The total vapor generated must equal the outflow.

$$q = 2\pi R_2 V_o \Delta h$$

where R_2 is the radius of the gel, and Δh is the heat of vaporization plus any sensible heat effect

The flow in the vapor film is

$$\frac{dP}{dr} = \frac{12\mu_f V}{ga^2} \approx \frac{\rho g H}{R_1}$$

At the outer edge, a good approximation is

$$\frac{\rho g H}{R_1} = \frac{12\mu_f V_o}{ga^2}$$

For the present purposes R_1 and R_2 will be assumed equal.

$$\begin{aligned} \pi R_1^2 k a \Delta T &= 2\pi R_1 V_o \Delta h \\ &= 2\pi \Delta h \frac{\rho g a^2 H}{12\mu_f} \end{aligned}$$

$$a = \frac{6R_1^2 k \Delta T \mu_f}{\rho g^2_H \Delta h}$$

$$q = \frac{6\pi R_1^4 k^2 \Delta T^2}{\rho g^2_H \Delta h}$$

$$\frac{q}{A} = \frac{q}{\pi R_1^2} = \frac{6R_1^2 k^2 (\Delta T)^2}{\rho g^2_H \Delta h}$$

APPENDIX U - ESTIMATION OF FROTHING CAPABILITY

Marruci (1969) has suggested that the value of (crk^2/σ) determines whether a mixture will froth. The following calculation estimates the value of this ratio for a 90 percent CH_4 and 10 percent C_2H_6 LNG mixture.

$$C = \frac{2a_1}{RT} \left(\frac{d\sigma}{da_1} \right) \left(\frac{d\sigma}{dc_1} \right) \left(\frac{1}{1 + x_1v_1/x_2v_2} \right)$$
$$\approx \frac{2c_1}{RT} \left(\frac{d\sigma}{dc_1} \right)^2 \left(\frac{1}{1 + x_1v_1/x_2v_2} \right)$$

CH_4 is component 1

$$x_1 = 0.9$$

$$v_1 = 0.02625 \text{ moles/cm}^3$$

$$c_1 = 0.02363 \text{ moles/cm}^3$$

C_2H_6 is component 2

$$x_2 = 0.1$$

$$v_2 = 0.01667 \text{ moles/cm}^3$$

$$c_2 = 0.00167 \text{ moles/cm}^3$$

The surface tension for the mixture was estimated using a mole fraction average.

$$\sigma_m = x_1\sigma_1 + x_2\sigma_2$$

At 112 K, $\sigma_1 = 13.3$ dynes/cm

$\sigma_2 = 28.2$ dynes/cm

(Yaws, 1976)

$\sigma_m = 14.8$ dynes/cm

For an LNG mixture which is 80 percent CH_4 /20 percent C_2H_6 , the surface tension will be 16.2 dyne/cm.

Therefore, $\left(\frac{d\sigma_m}{dc_1}\right) = \frac{1.4}{(0.1)(.00167)} = 8383.$

and $C = 1.15 \times 10^{-7}$

Estimation of k:

$$k = \left(\frac{12\pi\sigma}{Ar}\right)^{1/3}$$

Assumptions: $r = 10^{-1}$ cm

$A = 10^{-13}$ ergs (this may be a little high for gas bubbles but a lower value will increase the ratio (crk^2/σ)).

Thus, $k = 3.66 \times 10^5$ and $\frac{crk^2}{\sigma} = 11.8$

APPENDIX V - VAPOR DISPERSION

The general dispersion equation for a continuous ground line source is:

$$C(x,y,z) = \frac{\dot{m}}{LU} Z^* Y^*$$

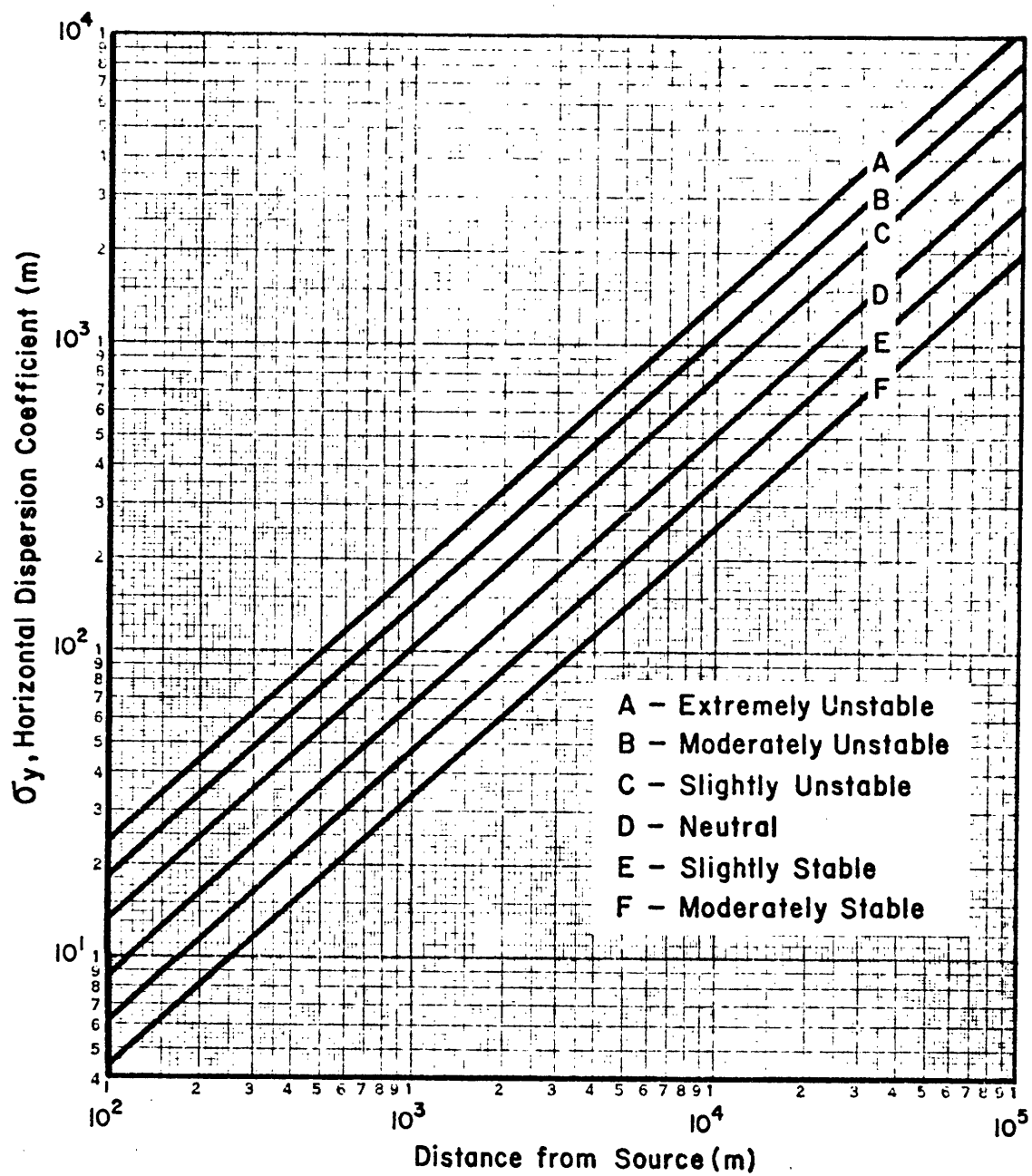
$$\text{and } Z^* = \frac{2}{\sqrt{2\pi} \sigma_z} \exp\left(\frac{-z^2}{2\sigma_z^2}\right)$$

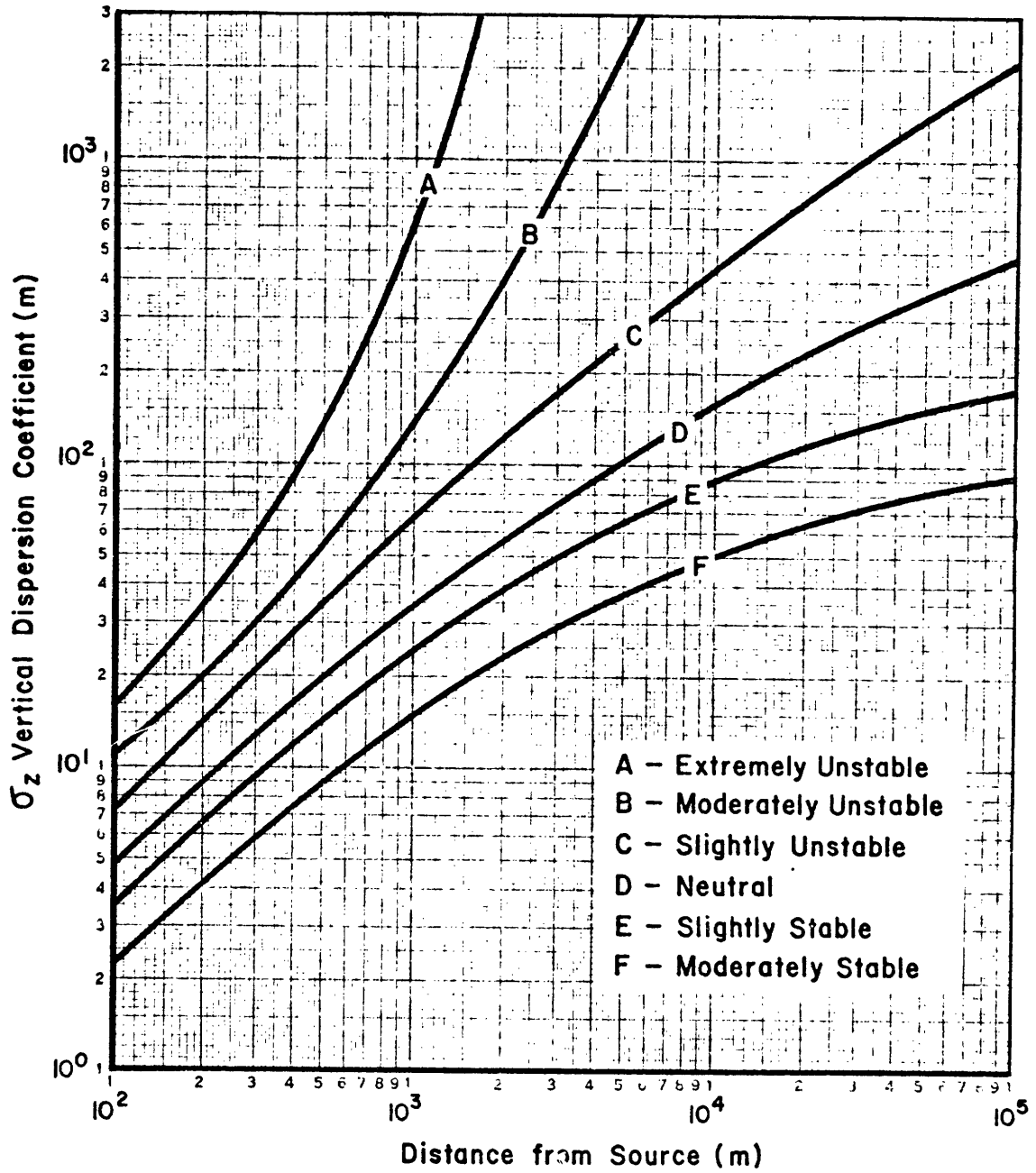
$$Y^* = 1/2 \left\{ \operatorname{erf} \left(\frac{L/2 - y}{\sqrt{2} \sigma_y} \right) + \operatorname{erf} \left(\frac{L/2 + y}{\sqrt{2} \sigma_y} \right) \right\}$$

where z = vertical distance from vapor source

y = lateral distance from vapor source

To estimate the maximum distance, x , for flammable mixtures, y and z are set equal to zero. Both σ_z and σ_y will be a function of atmospheric conditions as well as distance from the vapor source. Generalized curves for these values have been obtained, using a Gifford-Pasquill Correlation, and the figures are shown on the two pages following.





APPENDIX W - ANALYSIS OF PLUG FLOW ASSUMPTION

The length of the viscous boundary layer can be approximated as $\sqrt{v_{\omega}t}$. The shear stress due to the water surface velocity can therefore be estimated as $\mu_{\omega} \frac{U}{\sqrt{v_{\omega}t}}$. The shear stress due to the viscosity of the spreading liquid is $\mu_L \frac{\Delta U}{h}$ where h is the pool height. To approximate h, the relation for gravity-inertia spreading can be used.

$$h = \frac{V}{\pi r^2} = \frac{V}{\pi (1.14)^2 (GV)^{1/2} t}$$
$$= \frac{V^{1/2}}{97 t}$$

If the liquid viscosity effect is to be insignificant, then

$$\mu_L \frac{\Delta U (97) t}{V^{1/2}} \ll \mu_{\omega} \frac{U}{\sqrt{v_{\omega}t}} = .1 \frac{U}{\sqrt{t}}$$

$$\frac{\Delta U}{U} \ll \frac{.001V^{1/2}}{\mu_L t^{3/2}}$$

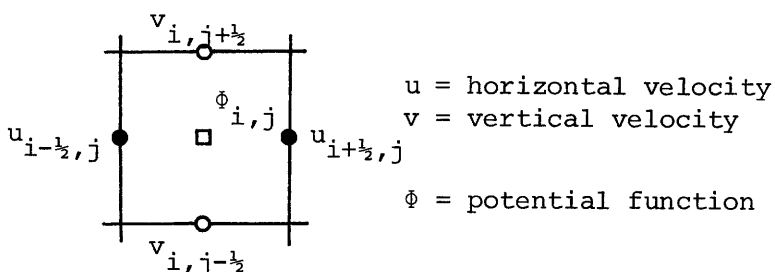
where μ_L [=] poise

t [=] sec

V [=] cm³

APPENDIX X - NUMERICAL TECHNIQUE USED TO ASSESS THE
SPREADING BEHAVIOR OF LNG GELS

The SMAC (Simplified Marker-and-Cell) method developed by Amsden and Harlow (1970) was used in the present study. Here the fluid behavior is determined by the complete two-dimensional Navier-Stokes equations, and the fluid itself is represented by a system of particles (massless markers) whose motions describe the trajectories of the fluid elements. The purpose of these particles is two-fold. First, they indicate which cells are surface cells, i.e. where the surface boundary conditions should be applied. Second, they show the fluid motion within the entire computing region. The actual dynamics of the fluid, however, is determined by a numerical representation of the Navier-Stokes equations using a rectangular grid of cells with the field variable layout as shown below.



The numerical expressions are given in the previously-mentioned reference along with a detailed discussion of the solution sequence. Briefly, however, the sequence was as follows. A tentative field of advanced time velocities was calculated using an arbitrary pressure

field within the fluid except for the pressure boundary condition at the free surface which precisely satisfied the normal stress condition. By using correct velocity boundary conditions, they have assured that this tentative velocity field contains the correct vorticity at all interior points in the fluid. However, the continuity equation has not been satisfied. Final modification of these tentative velocities is done in such a way as to preserve the vorticity at every point while further satisfying the continuity expression for an incompressible fluid. Once the dynamics of the fluid have been solved, the particles are then moved according to a weighted average of the nearest velocities. The results shown in Chapter 7 are the particle marker locations after the specified time lapse.

BIBLIOGRAPHY

- Abramovich, The Theory of Turbulent Jets, trans. by Scripta Technica, MIT Press, Cambridge, Mass., 1963
- Adamczewski, I., Ionization, Conductivity and Breakdown in Dielectric Liquids, Taylor and Francis Ltd., London, 1969.
- Adamson, A.W., Dormant, L.M., and Orem, M., "Physical Adsorption of Vapors on Ice", J. Colloid Interface Sci., 25, 206, 1967.
- Allen, K.W., and Jeffrey, G.A., "On the Structure of Bromine Hydrate", J. Chem. Phys., 38, 2304, 1963.
- Allen, L.B. and Kassner, J.L., Jr., "The Nucleation of Water Vapor in the Absence of Particulate Matter and Ions", J. Colloid Interface Sci., 30, No. 1, 81, 1969.
- Allen, Leland C., "Structural Models for Vitreous Ice", Physics and Chemistry of Ice, Ed. E. Whalley, S. J. Jones, L. W. Gold, 1973, p. 13.
- Amsden, A.A. and Harlow, F.H., "The SMAC Method: A numerical Technique for Calculating Incompressible Fluid Flows", Los Alamos Scientific Laboratory, Technical Report LA-4370, 1970.
- Andrew, S.P.S. "Frothing in Two-Component Mixtures", Inst. Chem. Engrs. Int. Symp. on Distillation, Brighton, England, 73, 1960.
- Arnold, G.P., Wenzel, R.G., Rabideau, S.W., Nerenson, N.G., and Bowman, A.L., "Neutron Diffraction Study of Ice Polymorphs under Helium Pressure", J. Chem. Phys., 55, 589, 1971.
- Astbury, N.F. and Moore, F., "Torsional Hysteresis in Plastic Clay", Rheol. Acta, 9, 124, 1970.
- Bantoft, E., "Some Measurements on Pigment-Plasticizer Dispersions", Rheology of Disperse Systems, p. 105, C.C. Mill, editor, Pergamon, London, 1959.
- Barrer, R.M. and Edge, A.V.J., "Gas Hydrates containing Argon, Krypton, and Xenon: Kinetics and Energetics of Formation and Equilibria", Proc. Roy. Soc., Ser. A, 300, 1, 1967.
- Barrer, R.M. and Ruzicka, D.J., "Non-Stoichiometric Clathrate Compounds of Water", Trans. Faraday Soc., 58, 2239, 1962.
- Becker, R. and Doring, W., Ann. Physik, 24, 719, 1935.
- Berenson, P.J., "Film-Boiling Heat Transfer From a Horizontal Surface", Journal of Heat Transfer, 83, 351, 1961.

- Bertie, J.E., Calvert, L.D., and Whalley, E., "Transformations of Ice II, Ice III, and Ice V at Atmospheric Pressure", J. Chem. Phys. 38, (4), 840, 1963.
- Bertie, J.E., Othen, D.A., and Solinas, M., "The Infrared Spectra of Ethylene Oxide Hydrate and Hexamethylenetetramine Hydrate at 100K", Physics and Chemistry of Ice, p. 61, Royal Society of Canada, Ottawa, 1973, Ed.: Whalley, E., Jones, S.J., Gold, L.W.
- Bertie, J.E. and Whalley, E., "Infrared Spectra of Ices Ih and Ic in the Range 4000 to 350 cm⁻¹", J. Chem. Phys., 40, 1937, 1964.
- Beaumont, R.H., Chihara, H. and Morrison, J.A., "Transitions between Different Forms of Ice", J. Chem. Phys., 26, 1456, 1961.
- Beurskens, G., Jeffrey, G.A., and McMullan, R.K., "Polyhedral Clathrate Hydrates. VI. Lattice Type and Ion Distribution in Some New Peralkyl Ammonium, Phosphonium, and Sulfonium Salt Hydrates", J. Chem. Phys., 39, 3311, 1963.
- Bellman, R. and Pennington, R.H., "Effects of Surface Tension and Viscosity on Taylor Instability", Quarterly of Applied Mathematics, 12, 151, 1954.
- Blackman, M. and Lisgarten, N.D., "The Cubic and Other Structural Forms of Ice at Low Temperature and Pressure", Proc. Roy. Soc. (London), A239, 93, 1957.
- Bode, H. and Teufer, G., "Die Kristallstruktur der Hexafluorophosphorsäure", Acta Cryst., 8, 611, 1955.
- Bonamico, M., Jeffrey, G.A., and McMullan, R.K., "Polyhedral Clathrate Hydrates III. Structure of the Tetra-n-Butyl Ammonium Benzoate Hydrate", J. Chem. Phys., 37, 2219, 1962.
- Booth, D.A., Bulsura, A., Joyce, F.G., Morton, I.P. and Scurlock, R.G., "Wall Film Flow Effects with Liquefied Natural Gas", Cryogenics, 562, 1974.
- Boyle, G.J. and Kneebone, A., "Laboratory Investigations into the Characteristics of LNG Spills on Water. Evaporation, Spreading and Vapor Dispersion", Shell Research Ltd., Thornton Research Centre, Chester, England, March 1973.
- Brown, L.E. and Colver, C.P., "Nucleate and Film Boiling Heat Transfer to Liquefied Natural Gas", Advances in Cryogenic Engineering, 13, 647, 1968.
- Burgess, D.S., Murphy, J.N., and Zabetakis, M.G., "Hazards of LNG Spillage in Marine Transportation", U.S. Bureau of Mines, February 1970.
- Bykov, A.G. and Teverovskii, E.N., JETP, 19, 328, 1949.

- Carson, D.B. and Katz, D.L., "Natural Gas Hydrates", Trans. Am. Inst. Mech. Engrs., 146, 150, 1941.
- Casson, N., "A Flow Equation for Pigment-Oil Suspensions of the Printing Ink Type", Rheology of Disperse Systems, p. 84, C.C. Mill, editor, Pergamon, London, 1959.
- Claussen, W.F., "Suggested Structures of Water in Inert Gas Hydrates", J. Chem. Phys., 19, 259, 1951a.
- Claussen, W.F., "A Second Water Structure for Inert Gas Hydrates", J. Chem. Phys., 19, 1425, 1951b.
- Courtney, W.G., J. Chem. Phys., 36, 2009, 1962a.
- Courtney, W.G., "Kinetics of Condensation of Water Vapor", J. Chem. Phys., 36, 2018, 1962b.
- Cross, M.M., "Rheology of Non-Newtonian Fluids: A New Flow Equation For Pseudoplastic Systems", J. Colloid Sci., 20, 417, 1965.
- Daney, D.E. and Rapial, A.S., "Preparation and Characterization of Slush Hydrogen and Nitrogen Gels", Adv. in Cryogenic Engineering, 15, 467, 1969.
- Davis, S.S., "Rheological Evaluation of Semi-Solid Materials", American Perfumer and Cosmetics, 85, 45, 1970.
- Davis, S.S. "Rheological Properties of Semi-Solid Foodstuffs", Journal of Texture Studies, 4, 15, 1973.
- Deaton, W.M. and Frost, E.M., "Gas Hydrates in Natural Gas Pipe Lines", The Oil and Gas Journal, 36, 75, 1937.
- Deaton, W.M. and Frost, E.M., "Gas Hydrates", Gas Age, 81, #11, 33, 1938.
- Deaton, W.M. and Frost, E.M., "The Hydrates of Natural Gas, Pure Gas and Synthetic Gas Mixtures", Gas, 16, #6, 28, 1940.
- Derjaquin, B.V., Abrikosova, I.I., and Lifshitz, E.M., "Direct Measurement of Molecular Attraction Between Solids Separated by a Narrow Gap", Quat. Revs. (London), 10, 295, 1956.
- Dowell, L.G., and Rinfret, A.P., "Low-Temperature Forms of Ice as Studied by X-ray Diffraction", Nature, 188, 1144, 1960.
- Drake, E., Jeje, A.A., and Reid, R.C., "Transient Boiling of Liquefied Cryogenics on a Water Surface", Int. J. Heat and Mass Transfer, 1975.
- Dzyaloshinskii, I.E., Lifshitz, E.M., and Pitaevskii, L.P., Advan. Phys., 10, 165, 1959.

- Efremov, I.F. and Usyarov, O.G., "The Long-range Interaction Between Colloid and Other Particles and the Formation of Periodic Colloid Structures", Russian Chemical Reviews, 45, (5), 435, 1976.
- Eisenschitz, R. and London, F., Z. Physik, 60, 491, 1930.
- Elliott, J.H. and A.J. Ganz, "Modification of Food Characteristics with Cellulose Hydrocolloids", Journal of Texture Studies, 2, 220, 1971.
- Elliott, J.H. and Ganz, A.J., "Some Rheological Properties of Sodium Carboxymethylcellulose Solutions and Gels", Rheol. Acta, 13, 670, 1974.
- Elliott, J.H. and Ganz, A.J., "Gel Characterization with the Weissenberg Rheogoniometer: Application to Carrageenan Gels", Journal of Food Science, 40, 394, 1975.
- Elliott, J.H. and Green, C.E., "Modification of Food Characteristics with Cellulose Hydrocolloids. II. The Modified Bingham Body - A Useful Rheological Model", Journal of Texture Studies, 3, 194, 1972.
- Falabella, B.J. and Vanpee, M., "Experimental Determination of Gas Hydrate Equilibrium Below the Ice Point", Ind. Eng. Chem. Fundam., 13, 228, 1974.
- Fannelop, T.K. and Waldman, G.D., "Dynamics of Oil Slicks", AIAA Journal, 10, 506, 1972.
- Firth, B.A., "Flow Properties of Coagulated Colloidal Suspensions. II. Experimental Properties of the Flow Curve Parameters", J. Colloid Interface Sci., 57, 257, 1976.
- Firth, B.A., and Hunter, R.J., "Flow Properties of Coagulated Colloidal Suspensions. I. Energy Dissipation in the Flow Units", J. Colloid Interface Sci., 57, 248, 1976.
- Fisher, J.C., Hollomon, J.H., and Turnbull, D., "Nucleation", Journal of Applied Physics, 19, 775, 1948.
- Flippen, J.L., Karle, J. and Karle, I.L., "The Crystal Structure of a Versatile Organic Clathrate. 4-p-Hydroxyphenyl-2,2,4-trimethylchroman (Dianin's Compound)", Journal of the American Chemical Society, 92, (12), 3749, 1970.
- Franks, F., "The Properties of Ice", Water: A Comprehensive Treatise, Vol. 1, p. 115, 1972, Plenum Press, New York.
- Frenkel, J., "A General Theory of Heterophase Fluctuations and Pretransition Phenomena", J. Chem. Phys., 7, 538, 1939.
- Frenkel, J., Kinetic Theory of Liquids, Dover Publications, New York, 1955.

- Frost, E.M. and Deaton, W.M., "Gas Hydrate Composition and Equilibrium Data", Oil Gas Journal, 45, 170, 1946.
- Gibbs, J.W., Collected Works, p. 3020, Longmans, Green, 1928.
- Gillespie, T., "An Extension of Goodeve's Impulse Theory of Viscosity to Pseudoplastic Systems", J. Colloid Sci., 15, 219, 1960.
- Goodrich, F.C., "Nucleation Rates and the Kinetics of Particle Growth I. The Pure Birth Process". Proc. Roy. Soc. (London), A 277 (1369) p. 155, 1964.
- Gordon, K.F., Singh, T., and Weissman, E.Y. (et al), "Boiling Heat Transfer Between Immiscible Liquids", Int. J. Heat Mass Transfer, 3, 90, 1961.
- Goren, S.L., J. Colloid Interface Sci., 36, 94, 1971.
- Gough, S.R. and Davidson, D.W., "Dielectric Properties of Clathrate Ices", Physics and Chemistry of Ice, p. 51, Royal Society of Canada, Ottawa, 1973. Ed.: E. Whalley, S.J. Jones, L.W. Gold.
- Gregory, J., "The Calculation of Hamaker Constants", Advan. Colloid Interface Sci., 2, 396, 1969.
- Hafemann, D.R. and Miller, S.L., "The Clathrate Hydrates of Cyclopropane", J. Phys. Chem., 73, 1392, 1969.
- Hanamaker, H.C., "The London-Van der Waals Attraction Between Spherical Particles", Physica (Utrecht), 4, 1058, 1937.
- Hammerschmidt, E.G., "Formation of Gas Hydrates in Natural Gas Transmission Lines", Industrial and Engineering Chemistry, 26, 851, 1934.
- Hammerschmidt, E.G., "Gas Hydrates", American Gas Association Monthly, 18, 273, 1936.
- Hammerschmidt, E.G., "Elimination of Hydrate Troubles", The Oil and Gas Journal, 39, 61, 1940.
- Hardy, A.D.U., McKendrick, J.J., and MacNicol, D.D., "Synthesis and Clathrate Geometry of a 2-Nor-analogue of Dianin's Compound; X-ray Crystal Structure", J.C.S. Chem. Comm., 355, 1976.
- Hartgerink, R., Fuller, E.J., and Chianelli, R.R., Personal Communication, Exxon Research and Eng. Co., Linden, N.J.
- Haydon, D.A. and Taylor, J.L., Nature (London), 217, 739, 1969.
- Heist, R.H. and Reiss, H., "Investigation of the Homogeneous Nucleation of Water Vapor Using a Diffusion Cloud Chamber", J. Chem. Phys., 59, 665, 1973.

- Herzberg, G., Molecular Spectra and Molecular Structure, II. Infrared and Raman Spectra of Polyatomic Molecules, D. Van Nostrand Company, Inc., Princeton, New Jersey, p. 335, 1964.
- Holder, G.D. and Hand, J.H., "Multiple Phase Equilibria in Hydrate Forming Mixtures of Methane, Ethane, and Propane", paper presented at the 83rd National Meeting, American Inst. of Chem. Eng., Houston, Texas, March 20-24, 1977.
- Hoult, D.P. and Suchon, W., "The Spread of Oil in a Channel", Fluid Mechanics Lab Report, MIT, May, 1970.
- Hovestreydt, J., "The Influence of the Surface Tension Difference on the Boiling of Mixtures", Chem. Eng. Sci., 18, 631, 1963.
- Hunter, R.J. and Nicol, S.K., "The Dependence of Plastic Flow Behavior of Clay Suspensions on Surface Properties", J. Colloid Interface Sci., 28, 250, 1968.
- Jachimiak, P.D., Song, Y.S., and Brodkey, R.S., "Time-dependent, Non-Newtonian Behavior of Viscoelastic Materials", Rheol. Acta, 13, 745, 1974.
- Jaeger, H.L., Willson, E.J., Hill, P.G., and Russell, K.C., "Nucleation of Supersaturated Vapors in Nozzles. I. H_2O and NH_3 ", J. Chem. Phys., 51, 5380, 1969.
- Johari, G.P. and Whalley, E., "Orientational Order in Ice I, V, VI, and VII", Physics and Chemistry of Ice, p. 278, Royal Society of Canada, Ottawa, 1973. Ed.: E. Whalley, S.J. Jones, L.W. Gold.
- Kamb, B., "Crystallography of Ice", Physics and Chemistry of Ice, p. 28, Royal Society of Canada, 1973, Ed.: E. Whalley, S.J. Jones, L.W. Gold.
- Kamb, Barclay and Anand Prakash, "Structure of Ice III", Acta Cryst. B24, 1317, 1968.
- Kaiser, R.L., Sc.D. thesis, Dept. of Chemical Engineering, MIT, 1961.
- Katz, D.L., "Prediction of Conditions for Hydrate Formation in Natural Gases", AIME Tech. Paper No. 1748, 1944.
- Katz, J.L., "Condensation of a Supersaturated Vapor. I. The Homogeneous Nucleation of the n-Alkanes", J. Chem. Phys., 52, 4733, 1970.
- Katz, J.L. and Ostermier, B.J., "Diffusion Cloud-Chamber Investigation of Homogeneous Nucleation", J. Chem. Phys., 47, 478, 1967.
- Kennedy, T.D.A. and Collier, J.G., "The Structure of an Impinging Gas Jet Submerged in a Liquid", Multi-phase Flow Systems, Vol. II, The Institution of Chemical Engineers Symposium Series No. 38, April, 1974.

- Kirkwood, J.G. and Buff, F.P., J. Chem. Phys., 17, 338, 1949.
- Kitchener, J.A. and Prosser, A.P., "Direct Measurement of the Long-range van der Waals Forces", Proc. Roy. Soc., A242, 403, 1957.
- Komatsu, H. and Mitsui, T., "Nonlinear Viscoelastic Properties of Semisolid Emulsions", Trans. Soc. Rheol., 17, 351, 1973.
- Krieger, I.M., Advan. Colloid Interface Sci., 3, 111, 1972.
- Krishna Murti, G.S.R. and Sen, S.N., "On the Crystal Structure of Para Dichlorobenzene at Different Temperatures", Ind. J. Phys., 30, 242, 1956.
- Krupp, H., "Particle Adhesion: Theory and Experiment", Adv. Colloid Interface Sci., 1, 111, 1967.
- Landau, L.D. and Lifshitz, E.M., Electrodynamics of Continuous Media, Addison-Wesley Publ. Co. Inc., Reading, Mass., 1960.
- Lifshitz, E.M., "The Theory of Molecular Attractive Forces Between Solids", Sov. Phys. JETP, 2, 73, 1956.
- Lippe, R.J., "Some Factors Affecting Thixotropy Recovery Rates", Cabot Research Paper, 112-181, 1976.
- London, F., Trans. Faraday Soc., 33, 8, 1937.
- Maeno, N., "Measurements of Surface and Volume Conductivities of Single Ice Crystals", Physics and Chemistry of Ice, p. 140, Royal Soc. of Canada, 1973.
- Mak, T.C.W. and McMullan, R.K., "Polyhedral Clathrate Hydrates. X. Structure of the Double Hydrate of Tetrahydrofuran and Hydrogen Sulfide", J. Chem. Phys., 42, 2732, 1965.
- Mak, T.C.W., Tse, J.S., Tse, C., Lee, K., and Chong, Y., "Crystal Structure of a Clathrate Inclusion Compound of Hydroquinone and Hydrogen Sulfide", J.C.S. Perkin II, 1169, 1976.
- Manley, R. St. J. and Mason, S.G., Canad. J. Chem., 32, 763, 1954.
- Marrucci, G., "A Theory of Coalescence", Chem. Eng. Sci., 24, 975, 1969.
- Marrucci, G., Nocodemo, L., and Acierno, D., "Bubble Coalescence Under Controlled Conditions", International Symposium on Research in Co-current Gas-Liquid Flow, Waterloo, Canada, 1968.
- Mason, S.G., Pulp Paper Mag. Canada, 49, 99, 1948.
- Matsumoto, T., Segawa, Y., Warashina, Y. and Onogi, S., "Nonlinear Behavior

- of Viscoelastic Materials. II. The Method of Analysis and Temperature Dependence of Nonlinear Viscoelastic Functions", Trans. Soc. Rheol., 17, 47, 1973.
- McFarlan, R.L., "The Structure of Ice II", J. Chem. Phys., 4, 60, 1936a.
- McFarlan, R.L., "The Structure of Ice III", J. Chem. Phys., 4, 253, 1936b.
- McLennan, J.C. and Plummer, W.G., "The Crystal Structure of Solid Methane", Phil. Mag., 7, 761, 1929.
- McMullan, R.K., Bonamico, M., and Jeffrey, G.A., "Polyhedral Clathrate Hydrates. V. Structure of the Tetra-n-butyl Ammonium Fluoride Hydrate", J. Chem. Phys., 39, 3295, 1963.
- McMullan, R.K. and Jeffrey, G.A., "Polyhedral Clathrate Hydrates. IX. Structure of Ethylene Oxide Hydrate", J. Chem. Phys., 42, 2725, 1965.
- Mercer, H.A. and Weymann, H.D., "Structure of Thixotropic Suspensions in Shear Flow. III. Time-Dependent Behavior", Trans. Soc. Rheol., 18, 199, 1974.
- Michaels, A.S. and Bolger, J.C., "The Plastic Flow Behavior of Flocculated Suspensions", I & EC Fundamentals, 1 (3), 153, 1962.
- Miller, B. and Strong, E.R., Proceedings, Natural Gas Department, American Gas Association, 80, 1945.
- Miller, B. and Strong, E.R., American Gas Association Monthly, 28, 63, 1946.
- Mitchell, D.J. and Ninham, B.W., "Van der Waals Forces Between Two Spheres", J. Chem. Phys., 56, 1117, 1972.
- Moelwyn-Hughes, E.A., "Physical Chemistry", 2nd ed., p. 383, Pergamon, London, 1961.
- Murti, G.S.R. Krishna, "On the Crystal Structure of Methanol at -180°C ", Ind. J. Phys., 1959.
- Nagata, I. and Kobayashi, R., "Prediction of Dissociation Pressures of Mixed Gas Hydrates From Data for Hydrates of Pure Gases with Water", I and EC Fundamentals, 5, 466, 1966.
- Nakanishi, E. and Reid, R.C., "Liquid Natural Gas-Water Reactions", Chem. Eng. Prog., 67 (12), 36, 1971.
- Napper, D.H. and Netschey, A., "Studies of the Steric Stabilization of Colloidal Particles", J. Colloid Interface Sci., 37, 528, 1971.
- Navokovic, M., and Stefanovic, M., "Boiling From a Mercury Surface", Int. J. Heat Mass Transfer, 7, 801, 1964.

- Netzel, D.A., Hoch, G., and Marx, T.I., "Adsorption Studies of Surfactants at the Liquid-Vapor Interface: Apparatus and Method for Rapidly Determining the Dynamic Surface Tension", J. Colloid Sci., 19, 774, 1964.
- Neugebauer, Th., Z. Phys., 107, 785, 1937.
- Ninham, B.W. and Parsegian, V.A., "van der Waals Forces across Triple-Layer Films", J. Chem. Phys., 52, 4578, 1970a.
- Ninham, B.W., and Parsegian, V.A., "vander Waals Forces: Special Characteristics in Lipid-Water Systems and a General Method of Calculation Based on the Lifshitz Theory", Biophys. J., 10, 646, 1970b.
- Oldroyd, J.G., "Complicated Rheological Properties", Rheology of Disperse Systems, p.1, C.C. Mill, editor, Pergamon Press, N.Y., 1959.
- Onogi, S., Masuda, T., and Matsumoto, T., "Non-Linear Behavior of Viscoelastic Materials. I. Disperse Systems of Polystyrene Solution and Carbon Black", Trans. Soc. Rheol., 14, 275, 1970.
- Onsager, L., "Introductory Lecture", Physics and Chemistry of Ice, p. 7, Royal Society of Canada, Ottawa, 1973. Ed.: E. Whalley, S.J. Jones, L.W. Gold.
- Owston, P.G., "The Structure of Ice-I, as Determined by X-ray and Neutron Diffraction Analysis", Advances in Physics, 7, 171, 1958.
- Palin, D.E. and Powell, H.M., "Hydrogen Bond Linking of Quinol Molecules", Nature, 156, 334, 1945.
- Palin, E.D. and Powell, H.M., "The Structure of Molecular Compounds. Part III. Crystal Structure of Addition Complexes of Quinol With Certain Volatile Compounds", J. Chem. Soc. (London), 208, 1947.
- Palin, D.E. and Powell, H.M., "The Structure of Molecular Compounds. Part V. The Clathrate Compound of Quinol and Methanol.", J. Chem. Soc. (London), 571, 1948.
- Palin, D.E. and Powell, H.M., "The Structure of Molecular Compounds. Part VI. The B-Type Clathrate Compounds of Quinol." J. Chem. Soc., (London), 815, 1948b.
- Pan, W.P., Mady, M.H., and Miller, R.C., "Dielectric Constants and Clausius-Mossotti Functions for Simple Liquid Mixtures: Systems Containing Nitrogen, Argon and Light Hydrocarbons", AIChE Journal, 21, 283, 1975.
- Papenhuijzen, J.M.P., "The Role of Particle Interactions in the Rheology of Dispersed Systems", Rheol. Acta, 11, 73, 1972.

- Parsegian, V.A. and Ninham, B.W., "Toward the Correct Calculation of van der Waals Interactions Between Lyophobic Colloids in an Aqueous Medium", J. Colloid Interface Sci., 37, No. 2, 332, 1971.
- Pauling, L. and Marsh, R.E., "The Structure of Chlorine Hydrate", Proc. Nat. Acad. Sci., 38, 112, 1952.
- Payne, A.R. and Whittaker, R.E., "Dynamic Properties of Materials. Part I. Dynamic Behavior of Clay-Water Systems", Rheol. Acta, 9, 91, 1970.
- Petz, J.I., "X-ray Determination of the Structure of Liquid Methane", J. Chem. Phys., 43, 2238, 1965.
- Pieroen, A.P., "Gas Hydrates - Approximate Relations Between Heat of Formation, Composition and Equilibrium Temperature Lowering by Inhibitors", Recueil, 74, 995, 1955.
- Pound, G.M., "Selected Values of Evaporation and Condensation Coefficients for Simple Substances", J. Phys. Chem. Ref. Data 1, No. 1, 135, 1972.
- Powell, H.M. and Wetters, B.D.P., "Crystallographic Examination of Some Inclusion Compounds", Chemistry and Industry, 256, 1955.
- Quist, A.S. and Frank, H.S., "Ice VIII - An Acetone Hydrate?", J. Phys. Chem., 65, 560, 1961.
- Raj, P.P.K. and Kalelkar, A.S., Chemical Hazard Response Information System, Manual 3, Arthur D. Little, Inc., 1973.
- Reich, I. and Vold, R.D., "Flocculation-Deflocculation in Agitated Suspensions. I. Carbon and Ferric Oxide in Water", J. Phys. Chem., 63, 1497, 1959.
- Roberts, O.L., Brownscombe, E.R. and Howe, L.S., "Constitution Diagrams and Composition of Methane and Ethane Hydrates", The Oil and Gas Journal, 39, 37, 1940.
- Ruepp, R., "Electrical Properties of Ice Ih Single Crystals", Physics and Chemistry of Ice, p. 179, Royal Society of Canada, Ottawa, 1973, Ed: E. Whalley, S.J. Jones, L.W. Gold.
- Sargent, D.F. and Calvert, L.D., "Crystallographic Data for Some New Type II Clathrate Hydrates", J. Phys. Chem., 70, 2689, 1966.
- Science, C.T., Colver, C.P., and Sliepcevich, C.M., "Pool Boiling of Methane Between Atmospheric Pressure and the Critical Pressure", Advances in Cryogenic Engineering, 12, 395, 1967.
- Shallcross, F.V. and Carpenter, G.B., "X-ray Diffraction Study of the Cubic Phase of Ice", J. Chem. Phys., 26, 782, 1957.

- Shcherbakov, L.M., Kolloidnyi Zhurnal, 33, 759, 1958.
- Shcherbakov, L.M., Ryazantsev, P.P., and Fillipova, N.P., "The Homogeneous Formation of Nuclei During Vapor Condensation and the Absolute (limiting) Critical Supersaturation", Kolloidnyi Zhurnal, 23, 338, 1961.
- Slater, J.C. and Kirkwood, J.G., Phys. Rev., 37, 682, 1931.
- Smyth, C.P. and McNeight, S.A., "Molecular Rotation in Solid Aliphatic Alcohols", 58, 1597, 1936.
- Sparnaay, M.J., "On the Additivity of London-Van der Waals Forces", Physica (Utrecht), 25, 217, 1959.
- Srivastava, S.N. and Haydon, D.A., Trans. Faraday Soc., 60, 971, 1964.
- Stein, G.D. and Wegener, P.P., "Experiments on the number of Particles Formed by Homogeneous Nucleation in the Vapor Phase", J. Chem. Phys., 46, 3685, 1967.
- Tabor, D. and Winterton, R.H.S., Proc. Royal Society, A312, 435, 1969.
- Tauer, K.J. and Lipscomb, W.N., "On the Crystal Structures, Residual Entropy and Dielectric Anomaly of Methanol", Acta Cryst., 5, 606, 1952.
- Tester, J.W., Bivins, R.L., and Herrick, C.C., "Use of Monte Carlo in Calculating the Thermodynamic Properties of Water Clathrates", AIChE Journal, 18, 1220, 1972.
- Thomas, D.G., "Transport Characteristics of Suspensions: Part III. Laminar-Flow Properties of Flocculated Suspensions", AIChE Journal, 7, 431, 1961.
- Thomas, D.G., J. Colloid Sci., 20, 267, 1965.
- Vander Wall, E.M., "Investigation of the Stability of Gelled Methane for Use in a Jet Engine", Technical Report NASA CR-72876, March 1971.
- Van Olphe, H., An Introduction to Clay Colloid Chemistry, Interscience Publishers, New York, 1963.
- van Silfhout, A., Proc. Kon. Ned. Akad. Wetensch., B69, 501, 1966.
- van Stralen, S.J.D., "The Mechanism of Nucleate Boiling in Pure Liquids and in Binary Mixtures - Parts I and II", Int. J. Heat Mass Transfer, 9, 995, 1966.
- van Stralen, S.J.D., "The Mechanism of Nucleate Boiling in Pure Liquids and in Binary Mixtures - Parts III and IV", Int. J. Heat Mass Transfer, 10, 1469, 1967.

- van Stralen, S.J.D., "The Boiling Paradox in Binary Mixtures", Chem. Eng. Sci., 25, 149, 1970.
- van Stralen, S.J.D., Sohal, M.S., Cole, R., and Sluyter, W.M., "Bubble Growth Rates in Pure and Binary Systems: Combined Effect of Relaxation and Evaporation Microlayers", Int. J. Heat Mass Transfer, 18, 453, 1975.
- Van Wazer, J.R., Lyons, J.W., Kim, K.Y., and Colwell, R.E., Viscosity and Flow Measurement: A Laboratory Handbook of Rheology, Interscience, New York, 1963.
- Verwey, E.J.W. and Overbeek, J. Th. G., Theory of the Stability of Lyophobic Colloids, Elsevier Publishing Company, Amsterdam, 1948.
- Viskanta and Lottes, "Nucleation and Boiling from a Liquid-Liquid Interface", Proc. Heat Transfer Fluid Mech. Inst., p. 171, 1962.
- Visser, J., "On Hamaker Constants: A comparison Between Hamaker and Lifshitz-Van der Waals Constants", Advan. Colloid Interface Sci., 3, 331, 1972.
- Visser, J., "Adhesion of Colloidal Particles", Surface and Colloid Science, Vol. 8, Ed. E. Matijevic, John Wiley and Sons, New York, 1976.
- Vlahakis, J.G., Chen, H., Suwandi, M.S. and Barduhn, A.J., "The Growth Rate of Ice Crystals; The Properties of Carbon Dioxide Hydrate; A Review of Properties of 51 Gas Hydrates", Technical Report Int.-OSW-RDPR-72-830, 1972.
- Volmer, M. and Weber, A., Z. Physik. Chem., 119, 277, 1925.
- Von Smoluchowski, M., Physik Z., 17, 557, 1916.
- von Stackelberg, M. and Muller, H.R., "On the Structure of Gas Hydrates", J. Chem. Phys., 19, 1319, 1951.
- von Stackelberg, M., "Die Struktur der Einschlussverbindungen des Wassers (Gas hydrate) und des Phenols", Recueil, 75, 902, 1956.
- Vrij, A., Discuss. Faraday Soc., 42, 23, 1966.
- Waals, J.H. van der and Platteeuw, J.C., "Clathrate Solutions", Advances in Chemical Physics, 2, Interscience, New York, 1959.
- White, M., "Electrical Conductivity of Low Dielectric Constant Liquids", MS Thesis, MIT, 1975.
- Wilcox, W.I., Carson, D.B., and Katz, D.L., "Natural Gas Hydrates", Industrial and Engineering Chemistry, 33, 662, 1941.
- Wilson, A.J.C., J. Sci. Instr., 27, 321, 1950.

Yaws, C.L., "Correlation Constants for Liquids", Chemical Engineering,
83 (23), 127, 1976.

Zeldovich, J., J.E.T.P., 12, 525, 1942.

ADDENDUM

Bird, R. B., W. E. Steward, and E. N. Lightfoot, Transport Phenomena,
John Wiley and Sons, Inc., New York, p. 505, 1960.

Norton, F. H., A. L. Johnson, and W. G. Lawrence, "Fundamental Study
of Clay: VI. Flow Properties of Kaolinite-Water Suspensions",
J. Am. Ceram. Soc., 27, 149, 1944.

Parrish, W. R. and J. M. Prausnitz, "Dissociation Pressures of Gas
Hydrates Formed by Gas Mixtures", Ind. Eng. Chem. Fundamentals,
11, 26, 1972.

Saito, S., D. R. Marshall, and R. Kobayashi, "Hydrates at High
Pressures: Part II. Application of Statistical Mechanics to
the Study of the Hydrates of Methane, Argon, and Nitrogen",
AIChE J., 10, 734, 1964.

Unruh, C. H. and D. L. Katz, "Gas Hydrates of Carbon Dioxide-Methane
Mixtures", AIME Petrol. Trans., 186, 83, 1949.

van Cleef, A. and G. A. M. Diepen, "Gas Hydrates of Nitrogen and
Oxygen, II", Rec. Trav. Chim., 84, 1085, 1965.

von Stackelberg, M. and H. R. Muller, "Feste Gashydrate II",
Z. Electrochem., 58, 25, 1954.

LOCATION OF ORIGINAL DATA

The original data, computer programs, and photograph negatives and prints used in this investigation are in the possession of the author.

BIOGRAPHICAL NOTE

Lucile Shanes was born on May 19, 1950 in Kansas City, Missouri. She received her secondary education at Southwest High School in Kansas City. In September, 1968, she entered Washington University (St. Louis), and was awarded a Bachelor of Science degree in chemical engineering in May of 1972. She entered M.I.T. in September, 1972 to pursue a doctorate degree in chemical engineering. On April 9, 1977, the author married John A. Wilkens, also a graduate student in the chemical engineering department at that time. Present plans of the author are to continue in chemical engineering as a professional employee of duPont, Wilmington, Delaware.

The author is a member of the American Institute of Chemical Engineers, the American Chemical Society and the Society of Sigma Xi.